Quantum boomerang effect in disordered ultra-cold atomic gases

Jakub Janarek

DOCTORAL THESIS
JAGIELLONIAN UNIVERSITY AND SORBONNE UNIVERSITY

Speciality : physics

realized

in Institute of Theoretical Physics and Laboratoire Kastler Brossel

presented by

Jakub Janarek

to obtain the degree of :

DOCTOR OF PHYSICS

Subject of the thesis :

Quantum boomerang effect in disordered ultra-cold atomic gases

defended December 2021

in front of the jury composed of :

Mr	Maciej A. Nowak	Chairman of the jury
Mr	Benoît Grémaud	Reviewer
Mr	Krzysztof Pawłowski	Reviewer
Mr	Dominique Delande	Thesis supervisor
Mr	Jakub Zakrzewski	Thesis supervisor
Mr	Jean-Noël Fuchs	Examiner
Mr	Szymon Pustelny	Examiner
Mrs	Alice Sinatra	Examiner

Wydział Fizyki, Astronomii i Informatyki Stosowanej
Uniwersytet Jagielloński

Oświadczenie

Ja niżej podpisany Jakub Janarek (nr indeksu: 1089010) doktorant Wydziału Fizyki, Astronomii i Informatyki Stosowanej Uniwersytetu Jagiellońskiego oświadczam, że przedłożona przeze mnie rozprawa doktorska pt. „Quantum boomerang effect in disordered ultra-cold atomic gases" jest oryginalna i przedstawia wyniki badań wykonanych przeze mnie osobiście, pod kierunkiem dr. hab. Dominique'a Delande'a oraz prof. dr. hab. Jakuba Zakrzewskiego. Pracę napisałem samodzielnie.

Oświadczam, że moja rozprawa doktorska została opracowana zgodnie z Ustawą o prawie autorskim i prawach pokrewnych z dnia 4 lutego 1994 r. (Dziennik Ustaw 1994 nr 24 poz. 83 wraz z późniejszymi zmianami).

Jestem świadom, że niezgodność niniejszego oświadczenia z prawdą ujawniona w dowolnym czasie, niezależnie od skutków prawnych wynikających z ww. ustawy, może spowodować unieważnienie stopnia nabytego na podstawie tej rozprawy.

Kraków, dnia 4 listpada 2021

Abstract

In this thesis, we theoretically and numerically investigate the quantum boomerang effect – i.e. the return of a wave packet launched with a nonzero velocity to its initial position – in ultra-cold disordered atomic gases. We address three main problems.

We study the effect of the time-reversal symmetry breaking on the existence of the quantum boomerang phenomenon. We show that time-reversal symmetry is not a necessary condition for the presence of the quantum boomerang. Next, we investigate the impact of interactions on the quantum boomerang effect, using the mean-field approximation. The interactions lead to partial destruction of the boomerang effect. Within the framework of the Gross-Pitaevskii equation, we identify a universal parameter that describes the observed destruction of the particle's return to the origin. Finally, we numerically study the effect of interactions using a quasi-exact approach. To this end, we study weakly interacting bosons, the Tonks-Girardeau gas, and strongly interacting bosons, which map to weakly interacting fermions. We find that weakly interacting bosons exhibit stronger destruction of the boomerang effect than in the case of the mean-field approach, thus that quantum fluctuations play a major role. Results for the Tonks-Girardeau gas show the existence of the full quantum boomerang phenomenon. Moreover, the results for strongly interacting bosons, where the boomerang is also only partial, provide evidence that the destruction of the quantum boomerang effect does not depend on the details of the interactions between particles.

Acknowledgements

This Ph.D. was carried out in two institutions: the Institute of Theoretical Physics (Jagiellonian University) in Kraków and the Laboratoire Kastler Brossel (Sorbonne Université) in Paris. Bilateral doctoral studies were possible thanks to Bourse de Gouvernement Français, which was granted by the French Embassy in Warsaw and administrated by Campus France. I would like to thank all these institutions and their staff.

I also acknowledge the support of the Polish National Science Centre (grant no. OPUS11 2016/21/B/ST2/01086) and the support of the PL-Grid structure. This work was also supported by the Foundation for Polish Science for the polish-french Maria Skłodowska and Pierre Curie reward received by Dominique Delande and Jakub Zakrzewski.

I would like to express my gratitude to my supervisors Dominique Delande (LKB) and Jakub Zakrzewski (IFT UJ). Without their support and guidance, none of the presented results would have been possible. I would like to thank them for their advice in carrying out the research. I am deeply grateful for showing me scientific craftsmanship. In addition, I would like to thank Dominique for his warm welcome in Paris. Without his help, the frequent changes between Kraków and Paris would have been much more difficult.

I would also like to thank Krzysztof Sacha, Bogdan Damski, Mateusz Łącki, Nicolas Cherroret, Giovanni Martone, and Pierre-Élie Larré. Discussions, not only about the subject of the thesis, helped me grow academically. Moreover, I would like to express my gratitude to father Marian Falenczyk, Iwona Szleper, and Zbyszek Falenczyk for their hospitality and for allowing me to stay in the students' residence in Arcueil. Every year I could count on a warm welcome and help in solving any problems.

My appreciation also goes out to all my colleagues from Kraków and Paris. I would like to thank Piotr (Picek), Lili, Krzysiek, and Magda for keeping my spirits up during tough moments. I would also like to offer my thanks to Oskar and Alice, who, unfortunately, left Kraków during my doctoral studies. Besides, I am grateful to all other Ph.D. students of the two departments for the time spent together: Piotr, Weronika, Staszek, and Tomek (who worked with me in "Kołchoz"), Thibault, Tamara, Panayotis, and Federico.

I cannot omit my colleagues from the Jagiellonian University Ph.D. Students' Association: Ania, Nadia, Monika, Aron, and Filip. With each of us pursuing a different field of study, our discussions have always broadened our horizons.

Finally, I am truly grateful to my friend Filip, who is always ready and willing to help me. I would like to thank for our endless discussions, solving problems (not necessarily scientific) together, and advice. All these things allowed me to go through the various stages of my studies.

At the very end, I would like to express my sincere gratitude to my parents: Krystyna and Józef. They patiently supported me from the very beginning, through many stages of school, until the end of my Ph.D. Thanks to them, I was able to undertake all these things. I would especially like to thank my mother, Krystyna, for her care, help, and inspiration for scientific work, without which I would not have been able to reach this stage.

Paris, August 2021
Kraków, November 2021

Contents

Introduction

Anderson localization is one of the most famous phenomena in quantum disordered systems. The destructive interference of the partial wave scattered by the disorder may lead to the inhibition of transport at long time over long distances, a phenomenon known as Anderson or strong localization. The phenomenon, predicted over 50 years ago [1], has waited a very long time for direct experimental observation. It was only the development of cold atomic experimental techniques that allowed full experimental confirmation of Anderson localization.

Despite the extensive experimental and theoretical works devoted to Anderson localization, it continues to surprise. It was not until 2017 when a new phenomenon, resulting from Anderson localization, was disordered: the quantum boomerang effect [2, 3]. The present thesis theoretically investigates the quantum boomerang effect in various systems.

Consider the evolution of a classical particle that initially has a nonzero velocity in a disordered system. After the initial ballistic motion, the particle will randomize its velocity due to scattering. After traveling, on average, one mean free path, the particle will stop its movement. The quantum evolution of a wave packet with nonzero initial velocity in the Anderson localized system is drastically different. For a short time, the wave packet moves ballistically, similarly to the classical counterpart. Then, on average, the wave packet makes a U-turn and slowly returns to its initial position. This unexpected behavior was dubbed quantum boomerang effect.

The quantum boomerang effect requires Anderson localization. It was studied numerically in one-, two-, and three-dimensional single-particle systems. In localized systems, the center of mass always returns to the origin. In the diffusive regime, the effect is only partial. The quantum boomerang effect can be used for pinpointing the Anderson transition [3]. Using time reversal invariance, it is possible to show that the boomerang effect exists in Anderson localized systems. An exact analytical solution of the problem is known in a one-dimensional system, where a diagrammatic technique can be used, see chapter 2. Until the start of this Ph.D., there was little research on the topic of the quantum boomerang effect.

The present thesis is expected to contribute to our understanding of the quantum boomerang effect. We answer two important questions. Is time reversal invariance a necessary condition for the quantum boomerang effect? What is the fate of the boomerang effect in the presence of interactions? Although we present theoretical results, we are focused on problems realizable in cold atomic experiments.

Thesis outline

The thesis is divided into several chapters. We begin chapter 1 with a brief introduction to Anderson localization and disordered quantum systems. Then, we show the state of the art for

the quantum boomerang effect. The chapter also includes examples of cold atomic experiments on Anderson localization and introduces the numerical methods used in this thesis.

Chapter 2 is concerned with the problem of time reversal symmetry breaking. We study a one-dimensional system with an effective spin-orbit coupling, which breaks time reversal invariance. We investigate the problem using an approach in which we directly test the influence of time reversal invariance on the presence of the boomerang effect. We study the classical solution and show that it is very similar to the classical approach in systems with time reversal invariance. Then, the results of our simulations unambiguously confirm the existence of the quantum boomerang effect in systems without time reversal invariance. Generalizing the Berezinskii diagrammatic technique [4], we calculate the theoretical prediction for temporal evolution of the center of mass. Our prediction agrees perfectly with the numerical simulations. The presence of the full quantum boomerang effect without time reversal symmetry is one of the most important results of this thesis.

In chapter 3, we introduce interactions in the problem under the form of a nonlinearity. We investigate the quantum boomerang effect in the framework of the one-dimensional Gross-Pitaevskii equation. Our analysis is focused on the regime of weak interactions. We show that interactions partially destroy the quantum boomerang effect. The average center of mass does not return to the origin but saturates at some finite position. We investigate this effect numerically and find a universal parameter that characterizes the destruction of the boomerang effect. Although we study a one-dimensional system, the same conclusions should be valid in higher dimensions. Additionally, we introduce the quantum boomerang effect for plane waves which goes beyond the original idea of the previous studies.

Finally, in chapter 4, we numerically study the impact of interactions treated at the full many-body level. For this purpose, we consider weakly interacting bosons, strongly interacting bosons (which map to weakly interacting fermions), and the Tonks-Girardeau gas. We perform the simulations using a quasi-exact approach: the time-evolving block decimation algorithm [5, 6]. Even though we study only one-dimensional systems, the simulations are demanding. The results for weakly interacting bosons are qualitatively similar to the results in the mean-field approximation. However, the destruction of the boomerang is more pronounced. Our analysis also shows that the system's state at long time is far from a Bose-Einstein condensate. This implies that the quantum fluctuations (depletion of the condensate) play a major role in the destruction of the quantum boomerang effect.

The simulations display the full boomerang effect in the Tonks-Girardeau gas, which is expected because particles of the Tonks-Girardeau gas in a disordered potential are Anderson localized. In the last part of chapter 4, we investigate strongly interacting bosons, which map to weakly interacting fermions. In this scenario, we also observe the weakening of the boomerang effect. The analysis demonstrates that this phenomenon may be grasped by the same tools as in the mean-field study. It shows that the destruction of the boomerang effect by interactions is largely independent of microscopic details.

The results presented in chapter 3 have been published in J. Janarek, D. Delande, N. Cherroret, and J. Zakrzewski, "Quantum boomerang effect for interacting particles", *Physical Review A* **102**, 013303, 2020. The findings of chapter 2 and chapter 4 are not yet published.

Chapter 1

An introduction to Anderson localization

The properties of quantum disordered systems have been studied for more than 50 years with many great theoretical and experimental successes. Transport in disordered systems is one of the greatly explored topics. Nevertheless, very recently, in 2017, a new dynamical phenomenon was revealed – the quantum boomerang effect. The present thesis studies this effect in many different scenarios, from non-interacting to many-body systems.

This chapter serves as a general introduction to the subject of disordered systems and Anderson localization. In section 1.1, we give a basic intuition of the disordered systems and the main concept of Anderson localization. Afterwards, in section 1.2, we present a short introduction to disordered systems, where we define the most important theoretical tools. In section 1.3, we present the quantum boomerang effect and discuss its most important features. Section 1.4 includes a few examples of observations of Anderson localization in disordered cold atomic systems. The last part of the chapter, section 1.5, describes the numerical tools and methods used in the thesis.

1.1 Disorder and Anderson localization

Disorder is ubiquitous in nature. Although this may sound vague, disorder is present in various physical systems. To make disorder less abstract, we can associate it with some lack of regularity. For example, in doped crystals, dopant atoms may be arranged randomly, or scatterers can be positioned randomly in some medium (e.g. droplets of lipids and proteins in a glass of milk). This randomness is realized differently each time, that is, there is no precise control over it. Thus, to study disordered systems, we have to give up the idea of learning all details which depend on the specific realization of this randomness.

In most cases, we are interested in some typical or average features of the problem. For example, the maximal concentration of dopant may vary considerably between different realizations of disorder, but usually the average does not change from one realization to another. To describe disordered systems, we focus on distributions, averages, or correlations of the interesting observables. The aim is not to describe the system as accurately as possible, but rather to predict some behaviors which may be observed in the whole ensemble of disorder realizations. Because this average or typical feature does not depend on the specific details of a single disorder realization, it may be considered universal. Moreover, because of the omnipresence of disorder, the phenomena originating in randomness exist in many different physical systems.

This thesis is devoted to the topic of quantum disordered systems. The quantum mechanical description of the world is based on the waves representing quantum particles. Disorder combined with the wave nature of particles leads to many fascinating phenomena. A primary focus of our interest is the quantum boomerang effect, occurring in systems with Anderson localization.

Anderson localization

One of the most important phenomena occurring in quantum disordered systems is Anderson localization, which is the absence of diffusion for waves propagating in a disordered medium. It was named after Philip Warren Anderson, who was the first to suggest this curious phenomenon in 1958 [1].

Consider a single particle problem, where the system is described by Hamiltonian H:

$$H = \frac{p^2}{2m} + V(x), \tag{1.1}$$

where $V(x)$ is a time-independent disordered potential. By "disordered potential", we understand that $V(x)$ is position-dependent and its values are a realization of some random process. We are interested in the temporal evolution of particles in such a system.

From the classical perspective, a moving particle will scatter from the potential in different directions. Between the scattering events, it will move ballistically. The evolution will be similar to a random walk. Depending on the details of the potential and the particle's energy, it will explore the whole system or remain trapped in some finite region. On average, looking at long times and large distances, the dynamics may be regarded as a diffusion. This conclusion is not always true: if the particle's energy is higher than the maximal height of the potential $V(x)$ in a one-dimensional system, it will continue its ballistic motion forever. Even so, here we want to study cases where the particle does interact with the potential.

The quantum mechanical picture is very different. To make an analogy with the classical case, we assume that the initial state is localized in space, for example, the initial wave function $\psi(x, t = 0)$ is a Gaussian wave packet. In the quantum description, the particle can be transmitted through a barrier, even if its energy is lower than the barrier's height. This is known as quantum tunneling. Moreover, a similar thing applies to the reflection: the particle may be reflected from the barrier even if it has higher energy than the barrier's height. After many scattering events, this situation naively looks diffusive as in the classical case.

The actual time evolution of the quantum particle is more complicated. It is well known that, when $V(x)$ is zero, the wave packet will spread: for the Gaussian wave packet, its width increases linearly in time. When the random potential is nonzero, the result is completely counter-intuitive. The average density profile initially spreads but, after some time, dubbed localization time, its dynamics freezes. The long-time average density has exponentially decaying tails:

$$|\psi(x, t)|^2 \propto e^{-|x|/\xi_{\mathrm{loc}}}, \tag{1.2}$$

where ξ_{loc} is called localization length – a characteristic length scale usually depending on the state's initial energy and the average strength of the disorder.

This strange inhibition of transport, due to the exponential decay of the density, is called Ander-

son localization (sometimes also strong localization). Even though it was discovered in the late fifties of XX$^{\text{th}}$ century, it had to wait 50 years for a direct experimental observation, which we describe in section 1.4. The localization depends on the features of the system, for example, all states in one- and two-dimensional quantum systems (described by the Hamiltonian H, Eq. (1.1)) are localized. In three-dimensional systems, not all states are localized, there exists a transition point between localized and delocalized phases (Anderson transition). Whether the state is localized or not depends on its energy and the average disorder strength.

1.2 Introduction to disordered quantum systems

In this section, we introduce all important tools used throughout the thesis. For this purpose, we closely follow [7] and [8] which may serve as much more detailed resources.

Most tools presented in this section are simple for non-interacting, linear systems, but may be generalized for interacting and more complex cases. The presented theory is general by construction and does not depend on the details of the system.

1.2.1 Green's functions

Green's function is an essential tool: it is defined as the impulse response of a differential operator. Thus, from a physical point of view, it includes all the necessary information about the system to calculate its time dynamics. Green's functions are widely used in disordered systems allowing for calculation of many important characteristic features. In the generic situation we are interested, the system is described by Hamiltonian H:

$$H = H_0 + V, \tag{1.3}$$

where H_0 is responsible for the evolution of the system without any disorder, while V represents the disordered potential. For simplicity, we assume that V is a static or quenched disorder, i.e. it does not evolve in time. Then, the Green's function is defined by the equation:

$$(i\hbar\partial_t - H)G(t,t') = \delta(t'-t). \tag{1.4}$$

Additionally, Eq. (1.4) is accompanied by boundary conditions. We define *retarded* and *advanced* Green's functions. The retarded Green's function is responsible for the forward-time evolution, the advanced Green's function for the backward-time evolution. On the practical basis, Green's functions are commonly defined using the evolution operator $U(t,t')$:

$$\begin{aligned} G^R(t,t') &= -\frac{i}{\hbar}\theta(t-t')U(t,t'), \\ G^A(t,t') &= \frac{i}{\hbar}\theta(t'-t)U(t,t'), \end{aligned} \tag{1.5}$$

where $\theta(t)$ is Heaviside step function which ensures that the retarded Green's function vanishes for $t - t' < 0$ and vice versa for advanced Green's function. The evolution operator is defined in the following way:

$$U(t,t') = e^{-iH(t-t')/\hbar}. \tag{1.6}$$

Because Green's functions depend only on the time difference $t' - t$, we use

$$G^R(t) = -\frac{i}{\hbar}\theta(t)e^{-iHt/\hbar}, \quad G^A(t) = \frac{i}{\hbar}\theta(-t)e^{-iHt/\hbar}. \tag{1.7}$$

It is convenient to introduce the energy representation using Fourier transform and exploit Heaviside step function representation in the frequency domain $\theta(\epsilon) = i(\epsilon - i\eta)^{-1}$, where η is an infinitesimal positive element:

$$G^{R/A}(t) = \frac{1}{2\pi\hbar}\int_{-\infty}^{+\infty} \mathrm{d}\epsilon \, \frac{e^{-iHt/\hbar}}{\epsilon - H \pm i\eta}. \tag{1.8}$$

From this one can easily find:

$$G^{R/A}(\epsilon) = \frac{1}{\epsilon - H \pm i\eta} = \frac{1}{\epsilon - H \pm i0^+}. \tag{1.9}$$

This operator is commonly called as a resolvent of H. The resolvent is extremely useful, e.g. if we know the eigensystem of the Hamiltonian H, $\{|\phi_n\rangle, \epsilon_n\}$, the resolvent may be decomposed spectrally:

$$G^{R/A}(\epsilon) = \sum_n \frac{|\phi_n\rangle \langle\phi_n|}{\epsilon - \epsilon_n \pm i0^+}. \tag{1.10}$$

This may be utilized in many ways, for example:

$$G^{R/A}(x, x', \epsilon) = \langle x| G^{R/A}(\epsilon) |x'\rangle = \sum_n \frac{\phi_n(x)\phi_n^*(x')}{\epsilon - \epsilon_n \pm i0^+}. \tag{1.11}$$

The Hamiltonian H contains both the unperturbed part H_0 and the disorder V (cf. Eq. (1.3)). To express the full resolvent, we can use the Green's function of the free system: $G_0^{R/A}(\epsilon) = (\epsilon - H_0 \pm i0^+)^{-1}$. A simple manipulation leads to

$$G^{R/A}(\epsilon) = G_0^{R/A}(\epsilon) + G_0^{R/A}(\epsilon) V G^{R/A}(\epsilon). \tag{1.12}$$

Eq. (1.12) is called Lippmann-Schwinger equation [9]. The equation can be nested and iterated which leads to an expression for G in terms of powers of VG_0:

$$G(\epsilon) = G_0(\epsilon) + G_0(\epsilon)VG_0(\epsilon) + G_0(\epsilon)VG_0(\epsilon)VG_0(\epsilon) + \ldots = G_0(\epsilon)\big[1 + \sum_{n=1}^{\infty}(VG_0(\epsilon))^n\big], \tag{1.13}$$

where for clearer notation we drop the upper index R/A. This perturbative expansion in powers of V is called the Born series. The series can be expressed in any basis. From now, we assume that the Hamiltonian H_0 from Eq. (1.3) is translationally invariant. This means that momentum space is much more convenient to express relevant quantities, for example $G_0(\epsilon)$ is diagonal in momentum space, $\langle \boldsymbol{k}| G_0(\epsilon) |\boldsymbol{k}'\rangle = \delta_{\boldsymbol{k},\boldsymbol{k}'} G_0(\epsilon, \boldsymbol{k})$. Hence, we can easily express the full Green's function $G(\epsilon)$ in momentum space:

$$\langle \boldsymbol{k}| G(\epsilon) |\boldsymbol{k}'\rangle = \delta_{\boldsymbol{k},\boldsymbol{k}'} G_0(\epsilon, \boldsymbol{k}) + G_0(\epsilon, \boldsymbol{k}) V_{\boldsymbol{k}'-\boldsymbol{k}} G_0(\epsilon, \boldsymbol{k}') + \sum_{\boldsymbol{k}''} G_0(\epsilon, \boldsymbol{k}) V_{\boldsymbol{k}-\boldsymbol{k}''} G_0(\epsilon, \boldsymbol{k}'') V_{\boldsymbol{k}''-\boldsymbol{k}'} G_0(\epsilon, \boldsymbol{k}') + \ldots \tag{1.14}$$

where $V_{\boldsymbol{k}}$ is the potential component in the momentum basis. In this form, however, the Born series seems to get complicated and the simplicity of the initial equation seems to be lost. Here another trick proves to be helpful: expression of Eq. (1.14) in terms of diagrams graphically representing free propagation and scattering events:

$$\langle \boldsymbol{k}| \, G(\epsilon) \, |\boldsymbol{k}'\rangle = \delta_{\boldsymbol{k},\boldsymbol{k}'}$$ 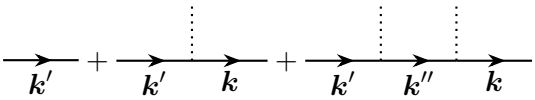

(1.15)

In the above equation, the solid lines represent the free Green's function $G_0(\epsilon, \boldsymbol{k})$ and dotted lines represent scattering events.

Using Eqs. (1.13)–(1.15), one can compute the full Green's function for a given system in a perturbative way. This already enables the calculation of many interesting features of the system. The results, however, depend on the specific realization of disorder, thus observables calculated using this Green's function would change from one disorder realization to another. In the very end, we want to calculate average values of interesting observables, which will depend only on global and average characteristics of the disordered potential.

1.2.2 Dyson equation and self-energy

The disorder, which in our Hamiltonian comes in the form of a disordered potential $V(x_i) = V_i$, is a realization of some random process. We can fully characterize the disorder by its moments: $\overline{V_i}$, $\overline{V_i V_j}$, $\overline{V_i V_j V_k}$, ... where $\overline{(\dots)}$ denotes average over different realizations of the process [1]. Moreover, if we can assume that the random process is stationary and statistically homogeneous, then its correlation functions depend only on the relative distance between the points [10]. We can always set the average of the disorder to zero by shifting it by its average value, $V \to V - \overline{V}$.

Now, if we want to compute the average Green's function $\overline{G}(\epsilon)$ we can simply average the Born series, Eq. (1.13):

$$\overline{G}(\epsilon) = G_0 + G_0\overline{(VG_0V)}G_0 + G_0\overline{(VG_0VG_0V)}G_0 + \dots \tag{1.16}$$

where we used $\overline{V} = 0$ and the fact that $\overline{G_0} = G_0$. This way we generate all possible correlation functions of the disorder, which depend on its details. To proceed, we will turn to a very useful, from a theoretical point of view, type of disorder: *Gaussian disorder*, where $V(r)$ at each point has a Gaussian distribution:

$$P(V) = \frac{1}{\sqrt{2\pi V_0^2}} \exp\left(\frac{V^2}{2V_0^2}\right). \tag{1.17}$$

This model is fully characterized by its first two moments, $\overline{V} = 0$ and $\overline{V(r_1)V(r_2)} = V_0^2 P(r)$ with $r = r_1 - r_2$. Analogously to a scalar Gaussian random variable, whose odd moments vanish and even moments are expressed in terms of the second moment

$$\overline{X^{2n}} = C_n \overline{X^2}, \quad C_n = \frac{(2n)!}{2^n n!}, \tag{1.18}$$

in the case of Gaussian disorder all higher order correlation functions completely factorize into pair

1. Later we will call it an average over disorder realizations.

correlations

$$\overline{V_1 \dots V_{2n}} = \frac{1}{2^n n!} \sum_{\pi} \overline{V_{\pi(1)} V_{\pi(2)}} \dots \overline{V_{\pi(2n-1)} V_{\pi(2n)}}, \tag{1.19}$$

where the sum is performed over all possible permutations. This is a manifestation of Wick's theorem [11], which is also called by statisticians Isserlis' theorem. To demonstrate its application, we present an example for $2n = 4$:

(1.20)

where dotted lines between the points denote the average correlation functions of the disorder. This diagrammatic notation will be used in the following of this chapter.

Gaussian potentials can be constructed with arbitrary spatial correlation functions $P(r)$. One very common choice is $P(r) = \delta(r)$. Such a model is called Gaussian uncorrelated disorder. The model extremely simplifies all calculations due to the presence of Dirac's delta function, which facilitates the computation of all integrals. The other typical choice is a Gaussian correlation, e.g. $P(r) = \exp(-r^2/2\sigma^2)$ with the σ parameter called correlation length.

Another common model comes from experiments – *speckle disorder model*, used for example in [12]. Shining a far-detuned light on a mate glass plate, it is possible to generate a speckle pattern. At some large distance, the electric field $E(r)$ is the sum of a large number of complex amplitudes. Those random fields originate from the randomly distributed grains of the mate plate. The resulting field is a random complex Gaussian variable which is described by a pair correlation, e.g. for a one-dimensional system, taking the characteristic form [13]:

$$P(r) = \frac{\sin^2(r/\sigma)}{(r/\sigma)^2}. \tag{1.21}$$

Now we can proceed and calculate the average Green's function [2] $\overline{G}(\epsilon)$. Using the diagrammatic representation of the Green's function we may write:

(1.22)

Details of the calculation depend on the type of the disordered potential, but if we restrict ourselves to Gaussian disorder, the infinite sum consists of all possible pair correlations. This greatly simplifies the following steps. The diagrams occurring in Eq. (1.22) can be divided into two groups. The first one, called *reducible*, consists of diagrams which can be divided into simpler diagrams without cutting through any correlation line. For example, the third diagram in Eq. (1.22) can be split into two diagrams which coincide with the second diagram from Eq. (1.22):

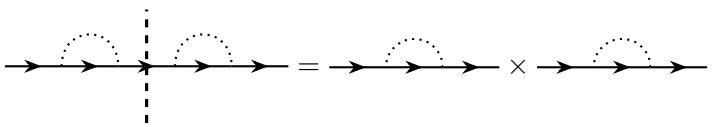

(1.23)

The second type of diagrams are called *irreducible*, for example the second (*rainbow*) and the fourth (*double rainbow*) diagrams from Eq. (1.22). All reducible diagrams are products of irreducible

2. For simplicity, we work here only with the retarded Green's function.

diagrams. We call the sum of all possible irreducible diagrams *self-energy* Σ. Because we concentrate on the inner parts of the diagrams, we factor out the initial and final $G_0(\epsilon)$. Self-energy $\Sigma(\epsilon)$ is given by:

$\Sigma(\epsilon) =$ 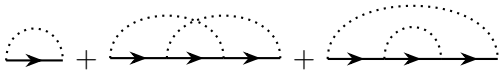 $+ \ldots$ (1.24)

The average Green's function can be expressed as a sum of a geometric series:

$$\overline{G}(\epsilon) = G_0(\epsilon) + G_0(\epsilon) \sum_n \left[\Sigma(\epsilon) G_0(\epsilon)\right]^n . \tag{1.25}$$

This way, we are sure that the average Green's function includes all possible products of irreducible diagrams. In Eq. (1.24) we do not include incoming and outgoing free lines into diagrams, hence G_0 is incorporated into the series. The geometric series in Eq. (1.25) may be summed yielding:

$$\overline{G}(\epsilon) = \frac{1}{1 - G_0(\epsilon)\Sigma(\epsilon)} G_0(\epsilon). \tag{1.26}$$

Simple manipulation leads to the, so-called, Dyson equation:

$$\overline{G}(\epsilon) = G_0(\epsilon) + G_0(\epsilon)\Sigma(\epsilon)\overline{G}(\epsilon). \tag{1.27}$$

We can calculate the formal solution of this equation, which has the following form:

$$\overline{G}(\epsilon) = \frac{1}{\epsilon - H_0 - \Sigma(\epsilon)}, \tag{1.28}$$

where we use $G_0(\epsilon) = [\epsilon - H_0 \pm i0^+]^{-1}$. If H_0 is diagonal in the momentum representation, then the free Green's function and the average Green's function are also diagonal [3]. As a consequence, from Eq. (1.28) the self-energy is diagonal as well. Then, the average Green's function in the momentum representation may be written as:

$$\overline{G}(\epsilon, \boldsymbol{k}) = \langle \boldsymbol{k} | \, \overline{G}(\epsilon) \, | \boldsymbol{k} \rangle = \frac{1}{\epsilon - \epsilon_{\boldsymbol{k}} - \Sigma(\epsilon, \boldsymbol{k})}. \tag{1.29}$$

This leads us to an essential conclusion: disorder changes the free dispersion relation of the system and the eigenstates. In general, the self-energy is a complex-valued function. Its real part is responsible for energy shifts. Because of causality, the retarded Green's function has to vanish for time $t < 0$, hence it cannot have poles in the upper complex plane. Therefore, the imaginary part of the self-energy is negative, $\mathrm{Im}(\Sigma(\epsilon, \boldsymbol{k})) \leq 0$.

This way, we reduced the problem of calculating the average Green's function to finding the self-energy Σ. It, however, can be a formidable task: the self-energy contains an infinite number of diagrams. The problem can be approached from a perturbative point of view. The simplest estimation of the self-energy is called Born approximation, where we include only the first diagram shown in Eq. (1.24):

$$\Sigma(\epsilon, \boldsymbol{k}) = \int \frac{\mathrm{d}\boldsymbol{k}'}{(2\pi)^d} V_0^2 P(\boldsymbol{k} - \boldsymbol{k}') G_0(\epsilon, \boldsymbol{k}'), \tag{1.30}$$

where d is the dimension of the system, and $P(\boldsymbol{k})$ is the disorder correlation function expressed in

3. Due to homogeneity of the random process – the disorder is statistically translational invariant.

momentum space:

$$P(\boldsymbol{k}) = \int \mathrm{d}\boldsymbol{r}\, e^{-i\boldsymbol{k}\cdot\boldsymbol{r}} P(\boldsymbol{r}). \tag{1.31}$$

Usually one is more interested in the imaginary part of the self-energy, which may be computed with the help of the Sokhotski-Plemelj formula (cf. Appendix A) for integrals over the real axis:

$$\operatorname{Im}\Sigma(\epsilon, \boldsymbol{k}) = -\pi \int \frac{\mathrm{d}\boldsymbol{k}'}{(2\pi)^d} V_0^2 P(\boldsymbol{k} - \boldsymbol{k}')\delta(\epsilon - \epsilon_{\boldsymbol{k}'}). \tag{1.32}$$

We see that the integral in the equation is nothing more but a representation of the Fermi golden rule applied to the scattering of modes with momentum $\boldsymbol{k}$ on a disordered potential V. Within this interpretation, we introduce an average lifetime of plane waves in the presence of disorder, denoted τ :

$$\frac{\hbar}{\tau} = -2\operatorname{Im}(\Sigma(\epsilon, \boldsymbol{k})). \tag{1.33}$$

This characteristic time scale is called scattering mean free time. In a one-dimensional system, where the free retarded Green's function reads:

$$G_0(\epsilon, x - x') = -\frac{im}{\hbar^2 k} e^{ik|x-x'|}, \tag{1.34}$$

in the Born approximation for Gaussian uncorrelated disorder, $\overline{V(x)V(x')} = \gamma\delta(x - x')$, the imaginary part of the self-energy is

$$\operatorname{Im}\Sigma(\epsilon) = -\frac{m\gamma}{\hbar^2 k}, \tag{1.35}$$

where k is the momentum of the state with energy ϵ. In such a system (at the level of the Born approximation), the scattering mean free time is

$$\tau_0 = \frac{\hbar^3 k}{2m\gamma}. \tag{1.36}$$

For the last important observation, we focus on the average Green's function in position space. Let us also assume that our disorder-free system has a quadratic dispersion relation, $\epsilon_{\boldsymbol{k}} = \hbar^2 k^2/2m$. The average Green's function reads

$$\overline{G}(\epsilon, \boldsymbol{r} - \boldsymbol{r}') = \int \frac{\mathrm{d}\boldsymbol{k}}{(2\pi)^d} \frac{e^{i\boldsymbol{k}\cdot(\boldsymbol{r}-\boldsymbol{r}')}}{\epsilon - \epsilon_{\boldsymbol{k}} - \Sigma(\epsilon, \boldsymbol{k})}. \tag{1.37}$$

The integral has a pole at $\tilde{k} = \sqrt{2m/\hbar^2(\epsilon - \operatorname{Re}\Sigma - i\operatorname{Im}\Sigma)}$. We put $\tilde{\epsilon} = \epsilon - \operatorname{Re}\Sigma$, then

$$\tilde{k} \approx k_{\tilde{\epsilon}} \left(1 - \frac{i\operatorname{Im}\Sigma}{2\tilde{\epsilon}}\right). \tag{1.38}$$

The self-energy shifts the energy argument of the Green's function and its imaginary part amounts to an exponentially decaying factor:

$$\overline{G}(\epsilon, \boldsymbol{r} - \boldsymbol{r}') = G_0(\tilde{\epsilon}, \boldsymbol{r} - \boldsymbol{r}') e^{|\boldsymbol{r}-\boldsymbol{r}'| k_{\tilde{\epsilon}} \operatorname{Im}\Sigma/2\tilde{\epsilon}} = G_0(\tilde{\epsilon}, \boldsymbol{r} - \boldsymbol{r}') e^{-|\boldsymbol{r}-\boldsymbol{r}'|/2\ell}, \tag{1.39}$$

where we introduce $\ell = -\tilde{\epsilon}/(k_{\tilde{\epsilon}} \operatorname{Im}\Sigma)$, a characteristic length scale called scattering mean free path.

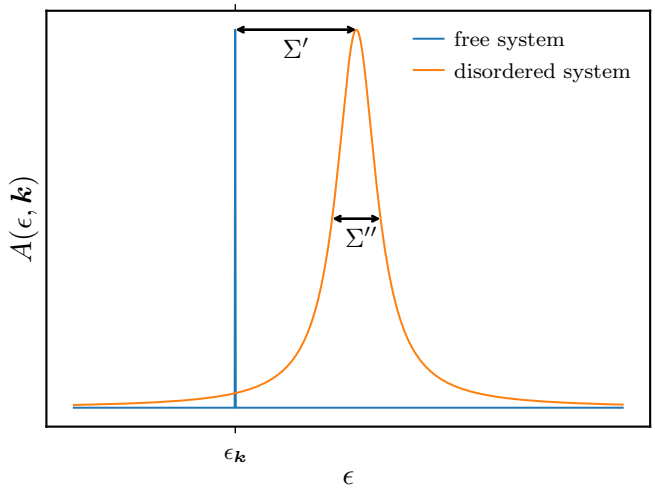

Figure 1.1. Graphical representation of the spectral function $A(\epsilon, \boldsymbol{k})$ as a function of energy ϵ. In a free system (blue curve) the spectral function is given by a Dirac delta function $\delta(\epsilon - \epsilon_{\boldsymbol{k}})$ with $\epsilon_{\boldsymbol{k}} = (\hbar k)^2/2m$. In a weakly disordered system (orange curve), the spectral function is given by Eq (1.42). The shift from the energy ϵ_0 is $\Sigma' = \operatorname{Re}\Sigma(\epsilon_{\boldsymbol{k}}, \boldsymbol{k}))$, whereas the full width at half maximum is $\Sigma'' = |\operatorname{Im}\Sigma(\epsilon_{\boldsymbol{k}}, \boldsymbol{k})|$.

Using this length scale, we may define the weak disorder criterion: $k\ell \gg 1$. For weak disorder, the self-energy may be safely approximated using the Born approximation, Eq. (1.30). The contributions of the next terms in the self-energy are usually of higher order in $(k\ell)^{-1}$. The scattering mean free path is also connected with the localization length. In one-dimensional systems $\xi_{\text{loc}} = 2\ell$ [14]. However, in higher dimensions the connection is more complicated.

The scattering mean free path ℓ is connected with the scattering mean free time τ via group velocity $v = \hbar^{-1}\vec{\nabla}_{\boldsymbol{k}}\tilde{\epsilon}_{\boldsymbol{k}}$, i.e. $\ell = v\tau$. For an one-dimensional system with Gaussian uncorrelated disorder, the scattering mean free path, at the level of the Born approximation (cf. the scattering mean free time τ_0, Eq. (1.36)), is :

$$\ell_0 = v\tau_0 = \frac{\hbar k}{m}\tau_0 = \frac{\hbar^4 k^2}{2m^2\gamma}. \tag{1.40}$$

Another important length scale in disordered systems is the transport mean free path, ℓ_t. The scattering mean free path ℓ measures the average distance between the scattering events (a measure of phase coherence). The transport mean free path is the distance over which the memory of the incident direction of motion is lost. Only the latter is relevant for the quantum boomerang effect described in section 1.3. The scattering mean free path and transport mean free path are equal only in the case of uncorrelated disorder. In correlated disorders, usually, the transport mean free path is longer than the scattering mean free path. The effect is especially large for anisotropic scattering potentials (see [7]).

1.2.3 Spectral function and density of states

To better understand the self-energy, we can study the spectral function $A(\epsilon, \boldsymbol{k})$. It represents the probability of finding a state with momentum $\boldsymbol{k}$ at energy ϵ. In a disorder-free case, it is equal

$A_0(\epsilon, \boldsymbol{k}) = \delta(\epsilon - \epsilon_{\boldsymbol{k}})$. In disordered systems, we are interested in the average spectral function:

$$A(\epsilon, \boldsymbol{k}) = \overline{\langle \boldsymbol{k}| \, \delta(\epsilon - H) \, |\boldsymbol{k}\rangle} = -\frac{1}{\pi} \overline{\langle \boldsymbol{k}| \operatorname{Im} \frac{1}{\epsilon - H + i0^+} \, |\boldsymbol{k}\rangle} = -\frac{1}{\pi} \operatorname{Im} \overline{G}^R(\epsilon, \boldsymbol{k}). \tag{1.41}$$

The spectral function can be interpreted as a function of momentum $\boldsymbol{k}$ and energy ϵ. In the presence of disorder, it is no longer represented by the Dirac delta, the spectral function is broadened and shifted by disorder. In the weak disorder limit, the spectral function becomes a Lorentzian [15] (cf. Eq. (1.41) and Eq. (1.29)):

$$A(\epsilon, \boldsymbol{k}) = \frac{|\operatorname{Im} \Sigma(\epsilon, \boldsymbol{k})|}{\pi} \frac{1}{(\epsilon - \epsilon_{\boldsymbol{k}} - \operatorname{Re} \Sigma(\epsilon, \boldsymbol{k}))^2 + (\operatorname{Im} \Sigma(\epsilon, \boldsymbol{k}))^2}. \tag{1.42}$$

From Eq. (1.42) we can clearly see the effect of disorder on the spectral function. The spectral function is shifted by the real part of the self-energy, which represents the disorder effect on the dispersion relation, and broadened by the imaginary part of the self-energy. This broadening is strictly connected with a finite lifetime of the states with momentum $\boldsymbol{k}$. The effect of nonzero self-energy $\Sigma(\epsilon, \boldsymbol{k})$ is illustrated in Fig. 1.1. From Eq. (1.42) we see that the spectral function may be used to extract both the mean free time τ as well as the mean free path ℓ.

Knowing the average Green's function, we can compute numerous important quantities, like the average density of states. To show its connection with the Green's function, we begin with the density of states per unit volume:

$$\nu(\epsilon) = \frac{1}{V} \sum_n \delta(\epsilon - \epsilon_n), \tag{1.43}$$

where V is the volume of the system. Then, the local density of states is given by:

$$\nu(\epsilon, \boldsymbol{r}) = \frac{1}{V} \sum_n |\phi_n(\boldsymbol{r})|^2 \delta(\epsilon - \epsilon_n). \tag{1.44}$$

Using once again the Sokhotski-Plemelj formula, we can write:

$$\nu(\epsilon, \boldsymbol{r}) = -\frac{1}{V\pi} \operatorname{Im} \overline{G}^R(\boldsymbol{r}, \boldsymbol{r}, \epsilon) \tag{1.45}$$

To finally compute the density of states (per unit volume), it is enough to integrate $\nu(\epsilon, \boldsymbol{r})$ over configuration space:

$$\nu(\epsilon) = -\frac{1}{V\pi} \operatorname{Im} \int \overline{G}^R(\epsilon, \boldsymbol{r}, \boldsymbol{r}) \mathrm{d}\boldsymbol{r} \, . \tag{1.46}$$

The integral in Eq. (1.46) is nothing but the trace of the Green's function:

$$\nu(\epsilon) = -\frac{1}{V\pi} \operatorname{Im} \operatorname{Tr} \overline{G}^R(\epsilon). \tag{1.47}$$

The trace can also be computed in momentum space, yielding, with the help of Eq (1.41),

$$\nu(\epsilon) = \int \frac{\mathrm{d}\boldsymbol{k}}{(2\pi)^d} A(\epsilon, \boldsymbol{k}). \tag{1.48}$$

From Eq. (1.48), we infer that when disorder only slightly perturbs the spectral function, the density of states may be approximated by the free density of states.

It is also worth mentioning, in the spirit of section 1.4, that spectral function was successfully measured in a cold atomic experiment where a three-dimensional gas was subjected to a speckle potential [16].

1.2.4 Scaling theory of localization

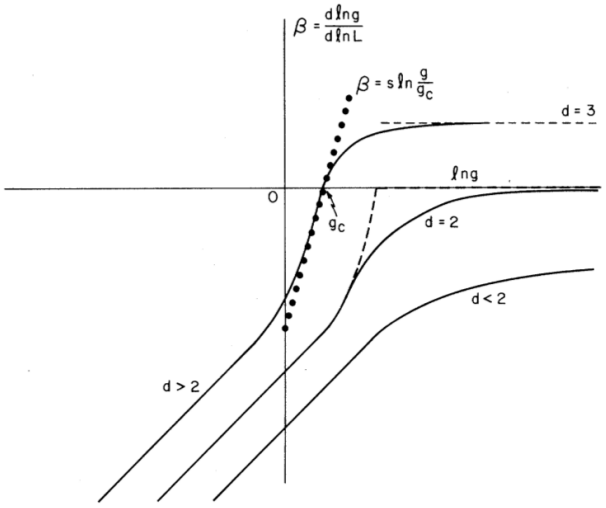

Figure 1.2. Approximations of $\beta(g)$ versus $\ln(g)$ from [17] for $d < 2$, $d = 2$, and $d = 3$. The plot is obtained as a smooth transition between the asymptotic behaviors Eq. (1.51) and Eq. (1.50). For $d = 1$ and $d < 2$ the function is negative, while for $d = 3$ it changes sign at some critical value g_c. The solid-circled line shows the approximation $\beta(g) = s \ln(g/g_c)$ near the critical point.

Although our studies are focused on one-dimensional systems, we will now briefly describe a very powerful tool capturing the main features of localization in higher dimensional systems: the scaling theory of localization. The primary aim of any scaling theory is to analyze how the chosen parameter evolves with the changes of the system size. This idea was firstly used in quantum field theory. The concept was introduced to disordered systems by Wegner [18], and the scaling theory of localization was proposed by Abrahams, Anderson, Licciardello, and Ramakrishnan in 1979 [17]. The scaling theory studies systems on a macroscopic level, hence its predictions are only qualitative. However, they may be quite general and universal.

The theory describes the scaling of the dimensionless conductance g of a disordered system, with the system size L^d. The dimensionless conductance is defined in such a way that when the transmission of the system is perfect, the conductance $g \to \infty$, and when the system is perfectly resisting, the conductance $g = 0$. The main object of interest is the scaling β-function. Based on a scaling hypothesis that it is a function of only g, it is defined as:

$$\beta = \frac{\mathrm{d}\ln(g(L))}{\mathrm{d}\ln(L)}. \tag{1.49}$$

Which is the Gell-Mann-Low function introduced by Callan and Symanzik in studies of the running coupling constant in the renormalization of the quantum field theory [19]. The scaling theory of

localization is a single parameter theory, because β depends solely on g. For very large and small g it is possible to get the asymptotic behavior of β. For large values of g, starting from the microscopic theory of transport [17]

$$\beta(g) \approx d - 2 - \frac{a}{g} + \mathcal{O}(g^{-2}), \tag{1.50}$$

where a denotes microscopic corrections. For small values of g, where localization takes place, g falls off exponentially and the asymptotic behavior of β is

$$\beta(g) \approx \ln(g/g_a), \tag{1.51}$$

with a constant g_a of order unity. Assuming that the function $\beta(g)$ is smooth and regular, it is possible to sketch it, what is shown in Fig. 1.2.

Based on Fig. 1.2, it is possible to draw several important conclusions about the disordered systems. For $d < 2$ the function is always negative, meaning that $g(L \to \infty) = 0$. The one-dimensional systems are always localized. When $d = 2$, where $\beta(g)$ is also negative but its value may be very close to zero. It means that, when $g \gg 1$, the localization length may be exponentially large, although the systems remain also localized.

For $d > 2$, the situation is more complicated. The β-function has a zero at some critical value g_c, $\beta(g_c) = 0$. This point reveals a transition between localized and delocalized regimes. If, initially $g > g_c$, the flow of the renormalization will make the conductance even higher, i.e. $g(L \to \infty) = \infty$, hence we will end up in a metallic regime. On the contrary, if the initial $g < g_c$, we will arrive finally with the opposite situation, $g(L \to 0) = 0$, meaning an insulating phase. The critical value g_c, shows a metal-insulator phase transition. Near the critical point g_c the β-function can be approximated by

$$\beta \approx s \ln\left(\frac{g}{g_c}\right). \tag{1.52}$$

Using this approximation, Abrahams et al. [17] showed that the critical exponent ν associated with the metal-insulator transition,

$$\xi_{\text{loc}} \sim \frac{1}{(g - g_c)^{\nu}}, \tag{1.53}$$

is connected with the slope s, i.e. $\nu = 1/s$.

This seemingly simple idea allows us to describe the dependence of localization phenomena on the dimensionality of the system. It unambiguously shows that one- and two-dimensional systems remain in the localized regime, albeit the localization length in the two-dimensional systems may be very large. Moreover, in three-dimensional systems, it predicts the existence of the mobility edge where metal-insulator transition occurs.

1.3 Quantum boomerang effect

In section 1.2 we have described the general features of Anderson localization. Now we turn to a newly discovered phenomenon which can be observed during the time evolution of a disordered quantum system. Below we present the state of the research regarding the quantum boomerang effect at the beginning of this Ph.D. studies. The section closely follows [2].

Let us consider the time evolution of a Gaussian wave packet with an initial nonzero velocity,

$$\psi(x, t = 0) = \left(\frac{1}{\pi\sigma^2}\right)^{1/4} e^{-x^2/2\sigma^2 + ik_0 x}, \tag{1.54}$$

where σ is the packet's width, and its velocity is $v_0 = \hbar k_0/m$. For now, we assume only that $k_0\sigma \gg 1$, i.e. the wave packet is quasi-monochromatic. We refer to such a wave packet as a *kicked wave packet* with velocity v_0. The Hamiltonian governing its dynamics is

$$H = \frac{p^2}{2m} + V(x), \tag{1.55}$$

where $V(x)$ is a disordered potential. For simplicity, we assume that $V(x)$ is a Gaussian uncorrelated disorder, i.e. $\overline{V(x)} = 0$, $\overline{V(x)V(x')} = \gamma\delta(x - x')$.

If the initial velocity is zero, we can easily predict the behavior of the Gaussian wave packet in a localized one-dimensional system. For a short time, the wave packet spreads around its initial position and then, after several scattering mean free times, becomes localized. The wave packet's density freezes – its dynamics completely ceases.

What will change for a nonzero initial velocity? The first guess is, that for a very short time, the packet will move ballistically and, after a few scattering events, its velocity will randomize. It means that, after an initial motion in the direction of the initial velocity, it will stop its movement, traveling, on average, a transport mean free path. Then the localization will set on, stopping any further evolution. It turns out that this prediction agrees with the classical picture.

1.3.1 Classical solution

We begin the classical approach with a study of the position of the center of mass $\langle x(t)\rangle$, as a function of time t. We start by using the classical equation:

$$\partial_t \langle x(t)\rangle = \frac{\langle p(t)\rangle}{m}, \tag{1.56}$$

which conveniently expresses the time evolution of the center of mass in terms of the average momentum. Here, notation $\langle\cdot\rangle$ denotes disorder averaging. To solve this equation, we assume that disorder is weak and the scattering happens only between two momenta $\pm\hbar k_0$ – the spectral function $A(k, \epsilon)$ is sharply peaked only around $k = \pm\sqrt{2m\epsilon}/\hbar$. Each momentum has its own population $n_\pm(t)$. We use a normalization condition $n_-(t) + n_+(t) = 1$. Scattering between populations occurs at a constant rate $1/2\tau$, τ being the transport mean free time. Population dynamics is described by a system of coupled Boltzmann equations:

$$\begin{cases} \dfrac{\mathrm{d}n_+}{\mathrm{d}t} &= \dfrac{n_-}{2\tau} - \dfrac{n_+}{2\tau}, \\ \dfrac{\mathrm{d}n_-}{\mathrm{d}t} &= \dfrac{n_+}{2\tau} - \dfrac{n_-}{2\tau}. \end{cases} \tag{1.57}$$

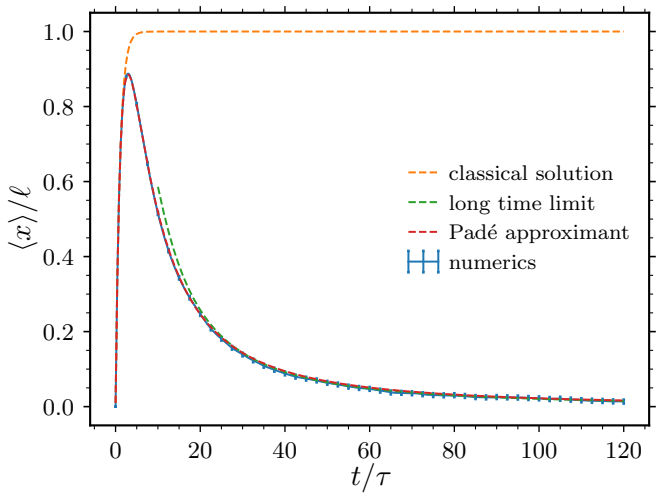

Figure 1.3. Temporal evolution of the center of mass obtained in a numerical simulation of the quantum wave packet (blue solid line with error bars), classical Botlzmann solution Eq. (1.59) (orange dashed line). The plot shows also the quantum long-time limit Eq. (1.77) (green dashed line) and the full quantum solution obtained using a Padé approximant of order $n = 7$, Eq. (1.80) (red dashed line) which are defined later in the text. The classical solution is very different from the numerical simulations of the quantum system where the center of mass returns to its initial position. The quantum long-time limit and Padé approximated solution coincide very well with the numerical data.

As an initial condition, we choose $n_+(0) = 1$, i.e. the wave packet has a positive initial velocity. The solution is straightforward and reads:

$$n_+(t) = \frac{1}{2}\big(1 + e^{-t/\tau}\big), \quad n_-(t) = \frac{1}{2}\big(1 - e^{-t/\tau}\big). \tag{1.58}$$

It means that, after several scattering events, the populations equalize, $n_\pm(t \gg \tau) = 1/2$. As a consequence, the average velocity is zero. Using Eq. (1.56) we calculate the center of mass position $\langle x(t) \rangle$:

$$\langle x(t) \rangle = \ell\big(1 - e^{-t/\tau}\big), \tag{1.59}$$

where ℓ is the mean free path, $\ell = \hbar k_0 \tau / m$. The solution agrees with the naive analysis presented above. After a short period of ballistic evolution, the center of mass stops its movement and remains localized forever. The classical result, Eq. (1.59), is valid in any dimension and for any statistically homogeneous and isotropic disorder. Moreover, it does not require the presence of Anderson localization in the system.

1.3.2 Quantum return to the origin

Numerical simulations reveal that the behaviour of a quantum system is very different. The simulations are performed using the Chebyshev kernel method described in section 1.5.3. Here, we present results obtained for a system of length $20000/k_0$ divided into 10^5 grid points with negligible discretization effects. The disorder strength is chosen such that $k_0 \ell = 20$, so we can safely assume that we are in the weak disorder limit. The initial width of the wave packet is $\sigma = 10/k_0$. In numerical simulations $k_0 = 1$ is used. The results are averaged over 50000 disorder realizations.

In order to calculate the center of mass time evolution, we propagate the wave function $\psi(x,t)$ and compute the center of mass in the following way:

$$\langle x(t)\rangle = \int x\overline{|\psi(x,t)|^2}\mathrm{d}x\,, \tag{1.60}$$

where $\overline{(\ldots)}$ is the disorder average. The outcome of the simulations is presented in Fig. 1.3. The quantum behavior is extremely different from the classical prediction. After the initial ballistic motion, at around $t = 3\tau$ the center of mass is reflected and begins a slow return to its origin. This phenomenon, called the quantum boomerang effect, was discovered and thoroughly studied in [3].

The quantum return to the origin can be simply proven using a time reversal invariance (TRI) symmetry argument. At any time, the wave function density can be calculated using the eigenbasis $\{\epsilon_n, \phi_n(x)\}$:

$$|\psi(x,t)|^2 = \sum_{n,m} \langle\phi_n|\psi_0\rangle \langle\psi_0|\phi_m\rangle \phi_n(x)\phi_m^*(x)e^{-i(\epsilon_n-\epsilon_m)t/\hbar}. \tag{1.61}$$

In localized systems, only states localized within the localization length ξ_{loc} from the initial wave function matter. Thus, the dynamics is restricted to a finite volume ξ_{loc}^d. This fact is used to define a typical mean level spacing, $\Delta = 1/\rho\xi_{\mathrm{loc}}^d$, where ρ is the density of states per unit volume, and a characteristic time scale, the Heisenberg time $\tau_{\mathrm{H}} = 2\pi\hbar/\Delta$. Beyond the Heisenberg time, the superposition of the oscillatory terms average out, allowing for the diagonal approximation:

$$|\psi(x,t=\infty)|^2 \approx \sum_n |\langle\phi_n|\psi_0\rangle|^2 |\phi_n(x)|^2. \tag{1.62}$$

In a time reversal invariant system, the eigenbasis can always be chosen real. Then, factors $|\langle\phi_n|\psi_0\rangle|^2$ do not depend on the initial sign of k_0, i.e. $|\langle\phi_n|\psi_{k_0}\rangle|^2 = |\langle\phi_n|\psi_{-k_0}\rangle|^2$. From this, we can infer that the long-time wave function density is independent of the initial velocity. Thus, the average infinite-time density has to coincide with a symmetric density profile both in configuration and momentum spaces, and the average center of mass has to be zero, $\langle x(t=\infty)\rangle = 0$. It means that the center of mass has to return to the initial point due to Anderson localization. In systems which are not Anderson localized, this analysis is not valid: when the localization length ξ_{loc} is infinite, also the Heisenberg time τ_{H} is infinite. Consequently, the diagonal approximation cannot be used.

The infinite time density profile is known analytically. It is derived in [20] by Gogolin using the diagrammatic technique developed by Berezinskii [4], see section 2.6 for a detailed description of this technique. The density is given by:

$$\overline{|\psi^{\mathrm{Gogolin}}(x,t=\infty)|^2} = \int_0^\infty \frac{\mathrm{d}\eta\,\pi^2}{32\ell} \frac{\eta(1+\eta^2)^2\sinh(\pi\eta)e^{-(1+\eta^2)|x|/8\ell}}{(1+\cosh(\pi\eta))^2}, \tag{1.63}$$

and is called *Gogolin profile*. The Gogolin profile may be interpreted as an average of exponentially localized profiles $\sim e^{-|x|/\xi}$, where η dependence represents the distribution of localization lengths ξ. The authors of [3] showed that the long-time average density of a wave packet with the initial nonzero velocity coincides very well with the Gogolin profile.

1.3.3 Symmetry of the initial state

In section 1.3.2, we have used only the time-reversal symmetry of the Hamiltonian. It turns out that the symmetry of the initial state is also important for the existence of the quantum boomerang effect. The analysis of the symmetries of the initial state is inspired by the preprint [21]. We assume that the Hamiltonian of the system $H = p^2/2m + V(x)$ is time reversal invariant. We will use the following symmetries:

$$\mathcal{P}\text{ (parity)}: \begin{cases} x \to -x \\ p \to -p \\ t \to t \end{cases} \qquad \mathcal{T}\text{ (time-reversal)}: \begin{cases} x \to x \\ p \to -p \\ t \to -t \end{cases} \tag{1.64}$$

where $\mathcal{P}^2 = 1$ and $\mathcal{T}^2 = 1$. Unlike the parity operator $\mathcal{P}$, the time reversal operator $\mathcal{T}$ is anti-unitary, i.e.

$$\mathcal{T} : \phi(x) \to \phi^*(x).$$

The Hamiltonian H is time-reversal symmetric, however

$$\mathcal{P}H\mathcal{P}^{-1} = \frac{p^2}{2m} + V(-x) = \tilde{H} \neq H, \tag{1.65}$$

thus it is not symmetric under the parity transformation. We use the eigenbasis $\{\epsilon_n, \phi_n(x)\}$, which due to the time-reversal invariance of H may be chosen real, $\mathcal{T}\,|\phi_i\rangle = |\phi_i\rangle$. The infinite-time value of the center of mass position may be computed using the diagonal approximation, similarly to Eq. (1.62):

$$\langle x^H(t=\infty)\rangle = \sum_i \langle\phi_i|\, x\, |\phi_i\rangle\, |\, \langle\phi_i|\psi_0\rangle\, |^2 = \sum_i \langle\phi_i|\, x\, |\phi_i\rangle\, |\, \langle\phi_i|\mathcal{P}\mathcal{T}\,\mathcal{P}\mathcal{T}|\psi_0\rangle\, |^2. \tag{1.66}$$

Due to time-reversal invariance of H:

$$\mathcal{P}\mathcal{T}\,|\phi_i\rangle = \mathcal{P}\,|\phi_i\rangle = |\tilde{\phi}_i\rangle\,, \tag{1.67}$$

where $|\tilde{\phi}_i\rangle$ is an eigenstate of the Hamiltonian $\tilde{H}$. Because $\mathcal{P}H\mathcal{P}^{-1} = \tilde{H}$ we can also write:

$$\langle\phi_i|x|\phi_i\rangle = -\,\langle\tilde{\phi}_i|x|\tilde{\phi}_i\rangle\,. \tag{1.68}$$

Thus, if we use Eq. (1.68) in Eq. (1.66), we get:

$$\langle x^H(t=\infty)\rangle = -\sum_i \langle\tilde{\phi}_i|\, x\, |\tilde{\phi}_i\rangle\, |\, \langle\tilde{\phi}_i|\mathcal{P}\mathcal{T}|\psi_0\rangle\, |^2. \tag{1.69}$$

If $\mathcal{P}\mathcal{T}\,|\psi_0\rangle = |\psi_0\rangle$ then

$$\langle x^H(t=\infty)\rangle = -\langle x^{\tilde{H}}(t=\infty)\rangle. \tag{1.70}$$

For a single disorder realization, $\langle x(t=\infty)\rangle$ is generically nonzero, making the quantum boomerang effect an average phenomenon. Because H and $\tilde{H}$ cover the same disorder space, after disorder averaging

$$\overline{\langle x(t=\infty)\rangle} = -\overline{\langle x(t=\infty)\rangle} = 0, \tag{1.71}$$

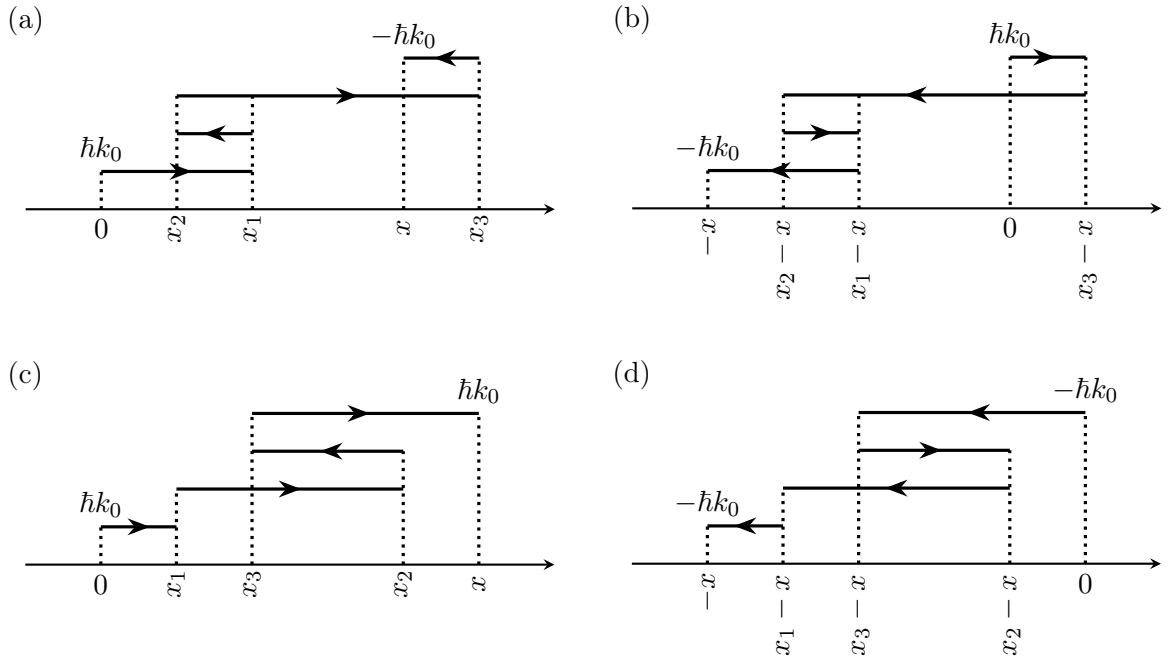

Figure 1.4. Different examples of scattering paths contributing to the center of mass $\langle x \rangle$. (a) A typical path going from the initial point to x contributing to $\langle x \rangle_-$ (defined in the text below). (b) Time reversed and translated by $-x$ version of path (a). This path gives opposite contribution to path a), hence $\langle x \rangle_-$ vanishes. (c) Example of path contributing to $\langle x \rangle_+$. (d) Time reversed and translated by $-x$ path (c). Such path starts with negative velocity, which is initially unpopulated, so that $\langle x \rangle_+ \neq 0$.

which means the presence of the full boomerang effect. Thus, we conclude that $\mathcal{PT} |\psi_0\rangle = |\psi_0\rangle$ is a sufficient condition for the full boomerang effect.

In the configuration space $\langle x| \mathcal{PT} |\psi_0\rangle = \psi_0^*(-x)$. For example, plane waves or Gaussian wave packets (kicked and non-kicked) have $\mathcal{PT}$-symmetry. However, for a chirped wave packet:

$$\begin{aligned} \psi_0(x) &\sim \mathcal{N} e^{ik_0 x} e^{-x^2/2\sigma^2} e^{i\alpha x^2} \\ \psi_0^*(-x) &\sim \mathcal{N} e^{ik_0 x} e^{-x^2/2\sigma^2} e^{-i\alpha x^2}. \end{aligned} \tag{1.72}$$

and, as a consequence, for such a state, we should not observe the full quantum boomerang effect, which is confirmed by numerical simulations.

1.3.4 Long-time behavior of the quantum boomerang effect

We here give another argument based on TRI indicating that, in localized systems, the center of mass should always return to its origin. Using Ehrenfest theorem, it is possible to connect the center of mass $\langle x \rangle$ with the mean squared displacement $\langle x^2 \rangle$:

$$\partial_t \langle x^2 \rangle = \frac{1}{2i\hbar m} \langle [x^2, p^2] \rangle = \frac{\langle xp + px \rangle}{m}. \tag{1.73}$$

Similarly to the classical solution, we split the whole average spatial density into two separate components with positive and negative velocities:

$$\overline{|\psi(x,t)|^2} = n_+(x,t) + n_-(x,t). \tag{1.74}$$

This simplification may be justified more rigorously using the average Wigner's functions $\overline{W(x,p,t)}$. In the weak disorder approximation the average Wigner's function may be split into two parts corresponding to the velocity components: $\overline{W(x,p,t)} \approx n_+(x,t)\delta(p-\hbar k_0) + n_-(x,t)\delta(p+\hbar k_0)$ With this approximation, Eq (1.73) becomes

$$\partial_t \langle x^2(t)\rangle = 2v_0\langle x(t)\rangle_+ - 2v_0\langle x(t)\rangle_-, \tag{1.75}$$

where $\langle x\rangle_\pm$ are the center of mass positions of the respective wave function components, the total center of mass is $\langle x\rangle = \langle x\rangle_+ + \langle x\rangle_-$, and $v_0 = \hbar k_0/m$. Now, by using the time reversal invariance, we can demonstrate that, if the initial velocity is positive, then, at any time, $\langle x(t)\rangle_- = 0$. For this purpose, we use the diagrams shown in Fig. 1.4, which represent examples of multiple scattering paths for different initial and final scenarios. For clarity, the paths are unfolded to top, the unfolding does not have any physical meaning. Diagram (a) shows a path contributing to $\langle x\rangle_-$: the path starts with the positive velocity and reaches the final point x with the negative velocity. By using the time reversal and translating the path by $-x$ we can obtain exactly the path shown in panel (b). This path also belongs to $\langle x\rangle_-$, however with precisely opposite contribution $-x$. The studied system is time reversal and statistically translation invariant, hence we have shown that each path belonging to $\langle x\rangle_-$ has an opposite counterpart with another realization of disorder with the same weight, so that $\langle x\rangle_-$ is zero. Analogous analysis can be performed for a path shown in (c) which belongs to $\langle x\rangle_+$. Time reversal and translation by $-x$ result in the path (d). However, path (d) starts with the negative velocity, which is not populated initially. Paths contributing to $\langle x\rangle_+$, similar to (c), are not cancelled out due to time reversal and translational invariance, and $\langle x\rangle_+ \neq 0$. We can now write that:

$$\partial_t \langle x^2(t)\rangle = 2v_0\langle x(t)\rangle. \tag{1.76}$$

From this it is clear that in localized systems, where the diffusion is fully suppressed, the infinite time value of the center of mass position has to be zero. What is more, the result can also be used to infer the long-time limit of $\langle x(t)\rangle$. The mean squared displacement long-time behavior was analyzed previously in [22]. Together with the corrections explained in [3], the long-time limit for the center of mass position is given by

$$\langle x(t)\rangle = 64\ell\frac{\ln(t/4\tau)\tau^2}{t^2} + \mathcal{O}\big(t^{-2}\big). \tag{1.77}$$

1.3.5 General solution of the quantum boomerang effect

In subsections 1.3.2-1.3.4 we have shown that the wave packet with nonzero initial velocity has to return to its origin due to Anderson localization. Equation (1.77) gives the prediction for the long-time behavior. The problem can be studied also for short times. This result can be then extended for intermediate time using a Padé approximant. The technical aspects will be presented in thorough detail in chapter 2.

In order to compute the time evolution of the center of mass $\langle x(t)\rangle$, we start by expressing it through the initial state and the Green's functions:

$$\langle x(t)\rangle = \int \mathrm{d}x\,\mathrm{d}x'\,\mathrm{d}x''\,x\,\overline{G^R(x,x',t)G^A(x'',x,-t)}\psi_0(x')\psi_0^*(x''). \tag{1.78}$$

The most difficult ingredient of this integral is the average product of the Green's functions. In one-dimensional systems, this object can be computed with the help of a diagrammatic approach, the aforementioned Berezinskii technique (see [4]). This theoretical tool is thoroughly described in the next chapter of the thesis, so here we do not explain the details of it. In the Berezinskii technique, all possible scattering paths are systematically included into the calculations. In principle, this approach gives results beyond the Born approximation. The final result consists of an algebraic equation allowing for calculation of $\langle x(t)\rangle$ as a power series in t. For practical purposes, this series is cut at finite order giving the following result in time domain:

$$\langle x(t)\rangle = \ell\left[\frac{t}{\tau} - \frac{t^2}{2\tau} + \frac{t^3}{6\tau^3} - \frac{3t^4}{64\tau^4} + \frac{7t^5}{576\tau^5}\right] + \mathcal{O}(t^6). \tag{1.79}$$

The time series has a finite radius of convergence, estimated at $t = 4\tau$. To infer the intermediate time behavior, the time series can be written as:

$$\langle x(t)\rangle = \ell\frac{\ln(1+t/4\tau)\tau^2}{t^2}\lim_{n\to\infty} R_n(t), \tag{1.80}$$

where $R_n(t)$ is a diagonal Padé approximant of n-th order, see [23]. The time series Eq. (1.79) agrees with the classical Boltzmann solution, Eq. (1.59) up to third order in time. Quantum corrections are visible starting from fourth order. In [2] the calculation of $\langle x(t)\rangle$ involved the use the Ehrenfest theorem and simplifications of the Berezinskii approach based on TRI. However, it can be shown that the same results may be obtained without this two ingredients.

The comparison of numerical simulations of the quantum particle with the long-time solution and the Padé approximated solution as well as the classical prediction are presented in Fig. 1.3. The agreement of the long-time limit is very good starting from $t = 30\tau$, and the Padé approximated solution with the approximant order $n = 7$ agrees perfectly with the numerical simulation of the quantum particle for any time.

The full solution works well not only for Gaussian uncorrelated disorder and initially narrow wave packets. Different disorder types, as long as homogeneous and isotropic, can be described with the same curve if proper time and length scales are used, e.g. the transport mean free time and transport mean free path in the case of correlated potentials. This means that the function $\langle x(t/\tau)\rangle/\ell$ is a universal quantum boomerang curve. For initially broad wave packets, the behavior does not change. In the presented analysis, we only assumed that the wave packet is quasi-monochromatic, i.e. $k_0\sigma \gg 1$. There is no condition between σ and ℓ. Broad wave packets in configuration space are in fact better approximations of the monochromatic waves. We will return to this as to *plane wave boomerang effect* described in section 3.4. It turns out that the opposite situation, when the wave packet is very narrow, may be more cumbersome. In such a case, the initial wave packet consists of many momentum components. Then, each component is characterized by its own transport mean free time and path, which may complicate the resulting $\langle x(t)\rangle$ curve. However, this should not

change the return to the origin.

1.4 Experimental observations of Anderson localization with cold atoms

After initial theoretical works, which included many predictions, the experimental observations of Anderson localization were desired. Consequences of disorder in experimental systems were firstly explored by Mott in 1968 [24]. After publication of this seminal work, many experimentalists started their investigations. Experimental setups were mainly based on the electronic systems, like quasi one-dimensional wires and thin films, where anomalies in conductance or magneto-resistance were measured (see review [25]). For electrons, however, there are numerous phenomena that make the observation of localization difficult. Electrons interact with each other repulsively, this makes them difficult to control and masks single particle behaviour. They also are affected by lattice vibrations – a kind of disorder which is not static, hence may break Anderson localization. Lastly, the electronic wave function is difficult to observe, so the localization effects can be accessed only indirectly. These facts significantly increase the difficulty of both the experimental and theoretical tasks in the analysis of localization effects. Thus, the main focus turned to the observation of the disorder effects in classical waves. The first results were published in 1985 for the coherent backscattering phenomenon, a weak localization effect, which may be thought of as a precursor to the strong localization [26, 27].

The end of XX$^{\text{th}}$ century was marked by a breakthrough: experimental realization of Bose-Einstein condensates [28, 29]. Dilute ultra cold matter, representing many independent quantum particles quickly started to be a standard experimental platform for quantum mechanics. Interaction effects may be diminished via precise control on their strength. Cold atoms allow for easy visualization, thanks to absorption or fluorescence imaging and time of flight techniques. Using different kinds of light, it is easy to control the dimensionality of the system and the type of disordered potential. The disorder may be created using masks [30] or speckle patterns [12], and even only using incommensurate laser wavelengths [31].

Advances in the field of cold atoms enabled many experimental studies of disorder and localization effects both in non-interacting and many-body quantum systems. In the following subsections, we briefly discuss some of the most important results.

1.4.1 Direct observation of Anderson localization of matter waves in a controlled disorder

The experiment conducted by the group of Alain Aspect and Vincent Josse in Orsay [32] has a very special feature: the possibility of the direct observation of the exponential decay of the density profile. The main idea of the experiment is presented in Fig. 1.5. Atoms are initially prepared in a one-dimensional tube, due to the far off-resonance confining laser beam (pink tube in Fig. 1.5). They are also trapped in a harmonic potential at the center of the system (grey harmonic potential in Fig. 1.5a). If there is no disorder, after switching off the trap, atoms can freely expand in the tube. At any time, it is possible to image the atoms' density using fluorescence.

The disorder is created using a speckle pattern, represented as a purple-blue field in Fig. 1.5. In the presence of disorder, after switching off the trap, the atoms start to expand. The expansion

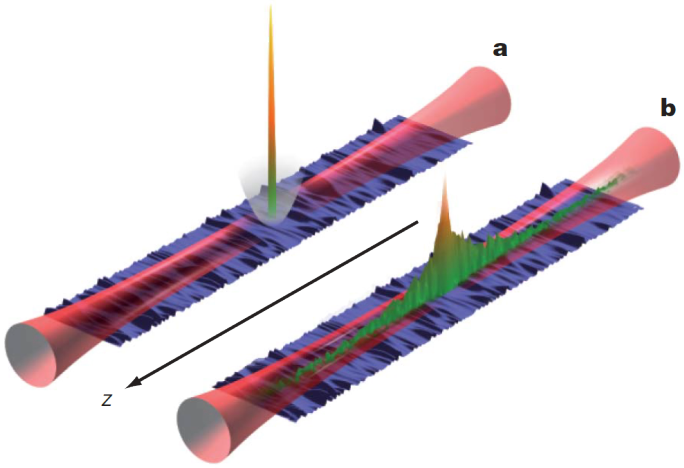

Figure 1.5. Sketch of the experiment presented in [32]. Due to the confining laser (pink) the atoms can move freely only in the z direction. (a) Initially the atoms are prepared in a harmonic trap (grey potential). The disordered potential is created by a speckle pattern (purple-blue). (b) When the trap is switched off, atoms initially expand but, after some time, they reach a stationary state, where the size of the atomic density does not evolve in time. Figure extracted from [32].

slows down and, at a long time, the atomic density freezes. This saturation of the density width is consistent with the theory of Anderson localization. The total duration of the experiment is much longer than the time needed to observe the onset of localization. Observation of the stationary, exponentially localized wave function is a direct proof of Anderson localization (Fig. 1.5b). Thanks to the long exponential wings of the density, experimentalists could extract also the localization length.

1.4.2 Experimental observation of the Anderson metal-insulator transition with atomic matter waves

Although observations of Anderson localization were also done in three-dimensional systems [34–36] [4] the most interesting phenomenon in 3D is the metal-insulator transition. It was observed for the first time in a kicked rotor system using cold Caesium atoms in 2008 [33] (in solid state experiments the transition was studied earlier, e.g. [38, 39]). The experimental realization of the kicked rotor is a system where atoms are periodically kicked by a laser pulse (first realization in cold atoms [40]). The theoretical model of the kicked rotor exhibits dynamical localization – the Anderson localization counterpart in momentum space. Although the atoms are periodically kicked, the wave function is exponentially localized. Addition of more incommensurate frequencies to the kicked rotor allows to study localization in more than one dimension. In such a system, the role of time is taken over by the total number of applied kicks.

The atoms are initially prepared in a Gaussian state where their momentum density is much narrower than the expected localization length. In the localized regime, after several initial kicks, the density is effectively frozen, with an exponential decay. On the other side of the transition, in the

4. We have to note that the results of [34] on the position of the metal-insulator transition are highly questionable, cf. [37].

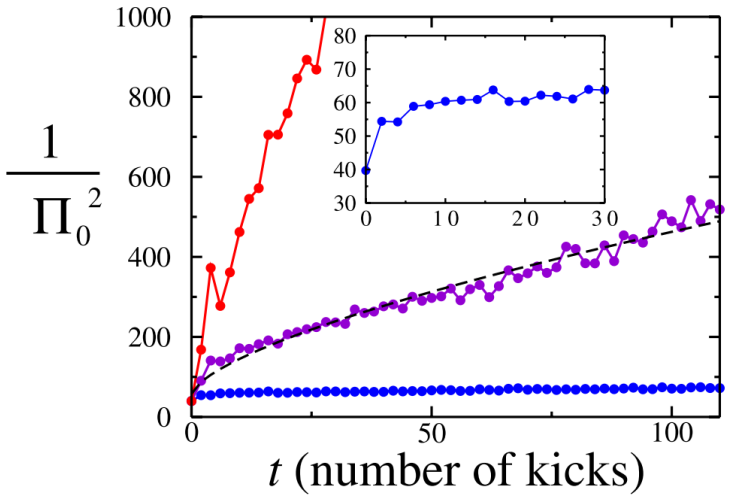

Figure 1.6. Experimental results presented in [33]. To study the mean square of momentum the population of zero-momentum $\Pi_0(t)$ was measured. The quantity $\Pi_0^{-2}(t)$ is proportional to $\langle p^2(t)\rangle$. In the localized regime it saturates (blue points), in the delocalized regime it grows linearly (red points). Near the metal-insulator transition it displays a anomalous diffusion (purple points). Figure from [33].

diffusive regime, during the application of kicks, the density broadens preserving its Gaussian shape. Experimentalists could study the behaviour of the mean squared momentum, $\langle p^2(t)\rangle$ by varying the kick strength. In the localized regime, the quantity saturates, whereas in the delocalized regime it growths linearly in time. Around the transition, it exhibits an anomalous diffusion $\langle p^2\rangle \propto t^{2/3}$, see Fig. 1.6. The transition between localized and diffusive regimes occurs at a critical kick strength, which value was precisely measured using finite-size scaling [41].

Since this experiment, the metal-insulator transition was also reported in a typical cold atomic experiments in [35, 36].

1.4.3 Observation of the quantum boomerang effect

Very recently, the first experimental observation of the quantum boomerang effect has been reported in [21]. Although the original idea presented in section 1.3 describes a return to the origin in configuration space, it is also possible to observe a similar behavior in momentum space using the kicked rotor setup. The experiment is based on a Bose-Einstein condensate of Lithium atoms without interactions. The atomic ensemble is prepared in a state centered at a nonzero position x_0, which, from the perspective of dynamical localization, is analogous to the nonzero initial momentum in the case of configuration space. The system is periodically kicked and the average momentum of the wave packet is measured. The number of kicks applied to the wave packet plays the role of time.

The main result is the observation of the return of the average momentum $\langle p\rangle$ to the origin, as shown in Fig. 1.7. As predicted by the theory, initially the average momentum increases (mimicking the ballistic motion of the wave packet). Then, after several kicks it is "reflected" and starts a slow return to the initial value.

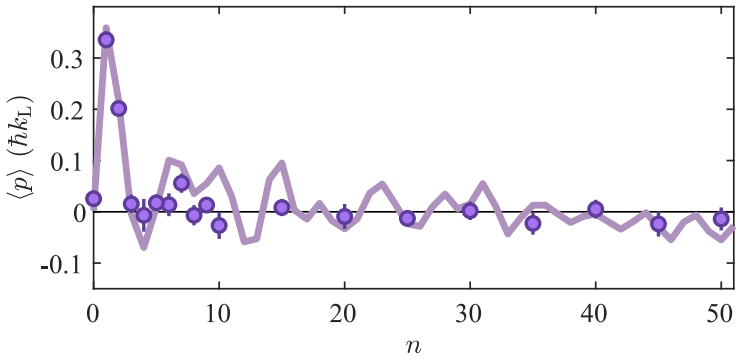

Figure 1.7. Experimental observation of the quantum boomerang effect [21]. In a kicked rotor system, the boomerang effect takes place in momentum space. Time evolution is expressed through the number of kicks n. The results clearly show that, after initial increase of $\langle p \rangle$, it returns to the initial value. Figure from [21].

1.5 Numerical methods

In this section, we briefly describe the numerical tools which have been used to obtain our results. They consist of home-made scripts using free, open source software and libraries. In principle, this approach guarantees the reproducibility of all presented results for anyone interested. This follows today's very popular idea that scientific methods should be open source, similarly to ideas coming from computer science.

We present also a short introduction to the two main numerical methods used in simulations: Chebyshev kernel method and exact diagonalization. Both of them allow for the calculation of the time evolution of quantum systems. Additionally, exact diagonalization gives access to energy spectra which also allows to analyze the localization features of the system.

1.5.1 Numerical tools and libraries

The majority of the tools used during the thesis were written in the Python language [42]. Its versatility and simplicity allows for fast prototyping and creating a clear, concise, and easy to understand code. The contemporary standard set of Python libraries allows for creating efficient scripts, which perform all necessary operations including reading of standardized input files, creation of the desired directory structure through shell utility tools, and even control of threading and multiprocessing. In our scripts, we use the whole SciPy ecosystem including NumPy [43], SciPy libraries [44], SymPy [45], Matplotlib [46] and IPython [47].

NumPy is a library introducing powerful arrays, which are ready for vectorization, broadcasting, and parallel operations. Alongside the arrays, the library includes an abundant choice of mathematical tools and functions created specially for NumPy types. The included methods allow for fast and reliable saving and reading data, using text files or memory efficient binary formats. One of the most important parts of the library is its integration with fast precompiled BLAS [48] and LAPACK routines [49], e.g. for linear algebra. All calculations can be easily parallelized – NumPy natively uses multithreading based on the OpenMP library [50].

The second most commonly used library is SciPy. The library includes ODE solvers, optimization

tools, interpolation algorithms, and numerical integrators. The library is also equipped with a rich collection of special functions for statistics. SciPy library, which is fully compatible with the NumPy array class, has its own selection of sparse matrix algebra types and functions.

SymPy is a Python library for symbolic calculations. It may be regarded as a full-featured computer algebra system, similar to Wolfram's Mathematica. Despite being free, it has a similar application range to fully paid alternatives. Additionally, it supports arbitrary precision numerical integration or ODE solvers based on many well established methods.

For graphical representation of data and theoretical results, we use Matplotlib, taking full advantage of the advanced graphical and typographical options available. The library allows for production of high quality 2D figures in a variety of hardcopy formats. It allows to use different fonts, including LaTeX mathematical fonts, which we believe helps in keeping all document's parts consistent. Last, but not least, is the development environment which helps enormously in the rapid design and prototyping of the scripts. For this purpose we use IPython together with Jupyter Notebooks [51].

Despite NumPy and SciPy being very well optimized for numerical calculations, sometimes we also used precompiled codes writen in C, C++, and Fortran languages. For small but fast routines written in external languages, Python is equipped with tools from libraries such as Cython [52], CFFI (*C Foreign Function Interface*) [53] or ctypes (python standard library, see [42]). Using these libraries, one can simply put the heaviest numerical work in highly optimized C routines.

1.5.2 The choice of numerical basis

All numerical simulations are performed using discretized systems. Because disorder is diagonal in configuration space, the discretization is applied to Hamiltonians in the configuration space representation: $x \to x_i = i\Delta x$, where Δx is the discretization constant. This approach is known as the finite element method. Assuming a one-dimensional Hamiltonian in the general form:

$$H = \frac{p^2}{2m} + V(x) = -\frac{\hbar^2}{2m}\frac{d^2}{dx^2} + V(x), \tag{1.81}$$

we replace the differential operator by the three-point stencil:

$$\frac{d^2}{dx^2}\phi(x) \to \frac{d^2}{dx^2}\phi(x_i) = \frac{\phi(x_{i+1}) - 2\phi(x_i) + \phi(x_{i-1})}{\Delta x^2}. \tag{1.82}$$

For short-hand notation $\phi(x_i) = \phi_i$ and $V(x_i) = V_i$. The Hamiltonian H is represented as the following tridiagonal matrix:

$$H = \begin{pmatrix} H_{11} & H_{12} & & \\ H_{21} & H_{22} & H_{23} & \\ & H_{32} & \ddots & \ddots \\ & & \ddots & \ddots \end{pmatrix}, \tag{1.83}$$

where $H_{ii} = \hbar^2/(m\Delta x^2) + V_i$, and $H_{i,i+1} = H_{i+1,i} = -\hbar^2/(2m\Delta x^2)$. We may use open boundary conditions (OBC) or periodic boundary conditions (PBC). When PBC are used, there are two additional nonzero matrix elements, $H_{1n} = H_{n1} = -\hbar^2/(2m\Delta x^2)$. The same idea is used when the Hamiltonian H describes a spinfull particle (for example, the Hamiltonian used in chapter 2 is mapped to a pentadiagonal matrix). In such a form, the Hamiltonian H is represented by a sparse

matrix. It means, for example, low computational cost of the matrix-vector multiplications, like $H|\psi\rangle$.

Because the disordered potential V is also discretized, its average correlation function is slightly modified. In the case of Gaussian uncorrelated disorder, which is used throughout the thesis, the δ-correlation function is replaced with a Kronecker delta $\delta_{i,j}$:

$$\overline{V_i V_j} = \frac{\gamma}{\Delta x}\delta_{i,j}. \tag{1.84}$$

The discretization rescales the disorder strength γ.

The discretization also changes the dispersion relation because the (discretized) Hamiltonian H describes a particle in a one-dimensional lattice. When we write down the equation for eigenfunctions in the disorder-free case:

$$H\phi_i = E\phi_i = -\frac{\hbar^2}{2m\Delta x^2}\left(\phi_{i-1} - 2\phi_i + \phi_{i+1}\right), \tag{1.85}$$

because the lattice is periodic (with period Δx), by using the Bloch theorem, we get:

$$E = \frac{\hbar^2}{m\Delta x^2}\left(1 - \cos(k\Delta x)\right). \tag{1.86}$$

This changes the group velocity

$$v = \frac{1}{\hbar}\frac{\mathrm{d}E}{\mathrm{d}k} = \frac{\hbar}{m\Delta x}\sin(k\Delta x). \tag{1.87}$$

The effect on the group velocity has to be taken into account, especially when one is interested in the calculation of, for example, $\langle p(t)\rangle$. When the discretization constant is large, the value of $p(t)$ should be substituted with $\hbar\sin(p(t)\Delta x/\hbar)/\Delta x$.

Equation (1.87) gives us an estimation of the discretization effects: we may neglect them as long as the velocity v (of the discrete system) does not differ from the true velocity (of the continuous system). In practice, this means $k\Delta x \ll 1$. The same condition may be obtained from a different perspective. The discretization has to be such that it allows to observe plane waves with momentum $\hbar k$, hence $k\Delta x \ll 1$. The same applies in the case of correlated disorders, the discretization constant Δx has to be much smaller than the correlation length. In general, Δx has to be the shortest length scale in the system.

1.5.3 Numerical methods

In numerical studies of the dynamics of quantum systems, we are interested in the solution of the time dependent Schrödinger equation. Assuming the initial state $|\psi_0\rangle$ we want to find the state after time t:

$$|\psi(t)\rangle = U(t)|\psi_0\rangle, \tag{1.88}$$

where $U(t)$ is the evolution operator, $U(t) = e^{-iHt/\hbar}$. For efficient use of computational resources, one needs to employ numerical methods which efficiently represent the evolution operator.

Chebyshev kernel method

Our first choice is to use the Chebyshev kernel method where the evolution operator is expressed in terms of Chebyshev polynomials of the Hamiltonian of order n, $T_n(x) = \cos(n \arccos(x))$. Their orthogonality relation is [54]:

$$\int_{-1}^{1} \mathrm{d}x \, \frac{T_n(x) T_m(x)}{\sqrt{1-x^2}} = \begin{cases} \frac{\pi}{2}\delta_{m,n} & \text{for } m \neq 0, n \neq 0, \\ \pi & \text{for } m = n = 0 \end{cases} \tag{1.89}$$

Moreover, Chebyshev polynomials can be generated iteratively

$$T_{n+1}(x) = 2xT_n(x) - T_{n-1}(x), \tag{1.90}$$

with $T_0(x) = 1$, $T_1(x) = x$. From our perspective, the most important feature of Chebyshev polynomials is that they span an orthogonal basis, such that piecewise smooth and continuous functions defined in the $[-1, 1]$ interval can be expressed using a series of Chebyshev polynomials:

$$f(x) = \sum_{n=0}^{\infty} a_n T_n(x), \tag{1.91}$$

where a_n coefficients can be easily calculated using the inner product. The series in Eq. (1.91) converges to the function $f(x)$ uniformly, see [55]. To express the evolution operator as a series of Chebyshev polynomials of the Hamiltonian, we have to normalize the Hamiltonian H, so that its spectrum lays in the interval $[-1, 1]$. Using $a = (E_{\max} - E_{\min})/2$ and $b = (E_{\max} + E_{\min})/2$, where $E_{\min}$ and $E_{\max}$ are the minimal and the maximal eigenvalues [5] of the Hamiltonian H, we introduce the normalized Hamiltonian $H_{\mathrm{norm}} = (H - b)/a$. The evolution operator may then be expressed as a series [56–59]:

$$U(\delta t) \approx e^{-ib\delta t}\Big(J_0(a\delta t) + 2\sum_{n=1}^{N}(-i)^n J_n(a\delta t) T_n(H_{\mathrm{norm}})\Big), \tag{1.92}$$

where $J_n(x)$ are the Bessel functions of the order n. In the practical implementation, we cannot sum an infinite number of terms. We introduce a cutoff of the series at order N. Value of N is estimated using δt and a see, for example [55, 60]. We keep only first N Bessel functions for which $|J_n(a\delta t)| > \epsilon$, with $\epsilon \ll 1$. Usually $N \sim a\delta t$.

The next step is to apply $T_n(H_{\mathrm{norm}})$ to the initial state $|\psi_0\rangle$. This can be done iteratively using Eq. (1.90):

$$T_{n+1}(H_{\mathrm{norm}})\,|\psi_0\rangle = 2H_{\mathrm{norm}} T_n(H_{\mathrm{norm}})\,|\psi_0\rangle - T_{n-1}(H_{\mathrm{norm}})\,|\psi_0\rangle\,, \tag{1.93}$$

with $T_0(H_{\mathrm{norm}})\,|\psi_0\rangle = |\psi_0\rangle$ and $T_1(H_{\mathrm{norm}})\,|\psi_0\rangle = H_{\mathrm{norm}}\,|\psi_0\rangle$. This way we reduce the problem of calculation of $T_{n+1}(H_{\mathrm{norm}})\,|\psi_0\rangle$ to simple applications of the operator H_{norm} on the vector $T_n(H_{\mathrm{norm}})\,|\psi_0\rangle$. When the total number of terms N is very large, it may be impractical to keep all vectors $T_n(H_{\mathrm{norm}})\,|\psi_0\rangle$ in the memory. Then, one can exploit the Clenshaw trick [61] to calculate the series in Eq. (1.92).

5. Note that in discretized, finite systems used in numerical simulations, the spectra of Hamiltonians are always bounded.

Exact diagonalization

Exact diagonalization is probably the most common tool used to investigate the quantum systems in discretized spaces. It allows to study both the statistical and dynamical characteristics of the system. Full diagonalization gives all eigenvalues and eigenvectors of the Hamiltonian H which we denote as $\{\epsilon_n, |\phi_n\rangle\}$. The main obstacle is the size of the Hilbert space. Usually, with this technique, it is only possible to study small systems (or with a small number of particles).

In contrast to iterative methods of time evolution, the time evolution of an initial state can be easily computed for an arbitrary time t:

$$|\psi(t)\rangle = \sum_n c_n \, e^{-i\epsilon_n t/\hbar} \, |\phi_n\rangle \,, \tag{1.94}$$

where $c_n = \langle\phi_n|\psi_0\rangle$. Knowing the eigenbasis extremely simplifies the calculation of the time evolution operator. Moreover, using the eigenbasis, we can directly calculate the infinite-time values of the observables in localized systems. Suppose we want to calculate the average infinite-time value of an operator $\hat{\mathcal{O}}$:

$$\hat{\mathcal{O}}(t) = \sum_{i,j} c_i^* c_j e^{-i(\epsilon_j - \epsilon_i)t/\hbar} \, \langle\phi_i| \, \hat{\mathcal{O}} \, |\phi_j\rangle \,. \tag{1.95}$$

When the eigenstates are localized, there exists a characteristic time called Heisenberg time τ_H beyond which off diagonal oscillatory terms in Eq. (1.95) vanish (diagonal approximation), and upon averaging over disorder realizations:

$$\overline{\hat{\mathcal{O}}} \xrightarrow{t \gg \tau_H} \sum_n \overline{|c_i|^2 \, \langle\phi_n| \, \hat{\mathcal{O}} \, |\phi_n\rangle}. \tag{1.96}$$

Thus, exact diagonalization allows us to calculate the infinite-time averages of interesting operators.

Studies of quantum systems using exact diagonalization give access to the spectrum structure. This can be used for the analysis of mean spacings or other statistical spectral quantities. A high number of energy levels eases the statistical analysis: the results converge quite fast to average values.

Exact diagonalization usually needs two preparatory steps: construction of the basis states (computational basis) and the calculation of the Hamiltonian matrix. Both processes allow to take advantage of system symmetries which may decrease the effective size of the Hilbert space. For spin systems, the most common technique [62] is to represent states as binary numbers (1 representing spin up, 0 representing spin down). Then, the elements of Hamiltonian matrix are calculated using binary `XOR` operation. An example of both steps of the implementation in the case of Bose-Hubbard model is presented in [63].

The main weaknesses of exact diagonalization are its memory consumption and the CPU-time for the diagonalization. The size of Hilbert space grows quickly with system size, and even quicker in many-body quantum systems with particle number. A rough estimate for the Hilbert space size in a Heisenberg model is $2^N/\sqrt{N}$ for a N spins in a chain, in the zero-spin sector. Putting $N = 18$ we obtain a practical limit for calculations using full exact diagonalization. Hamiltonian matrix for such a number of particles uses around 40GB of RAM. Full diagonalization using LAPACK routines uses of order $\mathcal{O}(D^3)$ floating point operations, where D is the Hilbert space size. This means, in practice, only systems with $D \sim 50000$ are fully diagonalizable.

Chapter 2

Quantum boomerang effect in systems without time reversal invariance

In chapter 1, we have introduced and described the quantum boomerang effect. Its existence has been shown using arguments based on time reversal invariance (TRI) symmetry of the system. The two main approaches proving the boomerang effect: the first based on the diagonal approximation (section 1.3.2), the second showing the long-time behavior (section 1.3.4), without TRI are no longer valid. In the present chapter, we study the boomerang effect in a system which breaks TRI to answer whether this symmetry is necessary for the presence of the phenomenon.

We begin with section 2.1, where we describe a system with spin-orbit coupling and explicitly show that time reversal symmetry is broken. In section 2.2, we study the classical dynamics and compare the classical solution with quantum numerical data in section 2.3. In section 2.4, we express the center of mass using the Green's functions, which are calculated in section 2.5. Finally, in section 2.6, we present the main theoretical result of the chapter: calculation of the center of mass temporal evolution in a system without time reversal invariance, using the Berezinskii diagrammatic technique. This section includes also a comparison of the theoretical solution with the numerical simulations. In section 2.7, we show that, even though TRI in the system is broken, the final density of the wave function is given by the famous Gogolin profile, similarly to the original boomerang study. The chapter is concluded in section 2.8.

2.1 Our model

In the present chapter, we study the existence of the quantum boomerang effect in systems without time reversal symmetry. In the introduction presented in section 1.3, TRI is used as an assumption in the proofs of the return to the origin. It means that TRI is a sufficient condition for the quantum boomerang effect. However, the necessity of TRI is not established. This is a question we answer in this chapter.

For this purpose, we study a single-particle disordered system with spin-orbit coupling, which is the minimum ingredient which breaks TRI and all anti-unitary symmetries. The spin-orbit coupling is ubiquitous in quantum mechanical systems. The interaction between the particle's spin and its motion is crucial in many currently studied phenomena like spin Hall effect [64, 65] observed in [66, 67]; or topological insulators, see [68–73]. In our study, we analyze an experimentally attainable

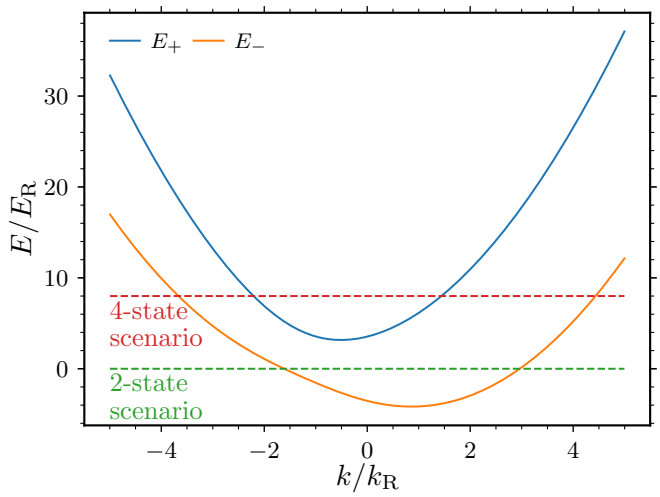

Figure 2.1. Spectrum of Hamiltonian (2.1) calculated for $\delta = \Omega = 5E_R/\hbar$. The energies are calculated from Eq. (2.3). Depending on the choice of parameters there are up to 4 possible eigenstates at a given energy with different velocities. Green dashed line represents an example of 2-state scenario, red dashed line represents an example of 4-state scenario.

cold atom one-dimensional system with an effective spin-orbit coupling.

Seemingly, for the spin-orbit interaction to occur, the particles must have appropriate intrinsic properties, like internal degrees of freedom. Such parameters are rarely controllable. However, in the ultra-cold matter experiments, there is a way to create an effective spin-orbit coupling. This may be achieved using a laser field, see [74]. The induced spin-orbit coupling may be of Dresselhaus [75] or Rashba [76] types. The first cold atom realizations of the spin-orbit coupling for Bose-Einstein condensates were presented in [77, 78] with the help of a momentum sensitive coupling created by Raman beams. The experiment presented in [77] realized the spin-orbit coupling with equal Dresselhaus and Rashba contributions resulting in the following one-dimensional Hamiltonian:

$$H_0 = \frac{\hbar^2 k^2}{2m} + \gamma\hbar k\sigma_z + \frac{\hbar\delta}{2}\sigma_z + \frac{\hbar\Omega}{2}\sigma_x, \tag{2.1}$$

where γ is the strength of the spin-orbit (SO) coupling, Ω is the Rabi frequency and δ the detuning. For the characteristic momentum and energy in the model, we choose $\hbar k_R = m\gamma$ and $E_R = m\gamma^2/2$. In the specific implementations of Hamiltonian (2.1) in the experimental setups of [77–79], this choice coincides with the recoil momentum and energy of the Raman photon, hence we use the subscript R. Matrices σ_i denote the standard Pauli matrices. The Hilbert space is spanned by 2-component spinors

$$\psi(x) = \begin{pmatrix} \psi_\uparrow(x) \\ \psi_\downarrow(x) \end{pmatrix}, \tag{2.2}$$

where $\psi_\uparrow(x)$ and $\psi_\downarrow(x)$ are complex valued functions. The spin-orbit coupling in the system described by Hamiltonian (2.1) breaks TRI. This reduces the applicability of the arguments for the quantum return to the origin presented in section 1.3.2.

In the absence of disorder, the Hamiltonian may be diagonalized yielding two energy bands

denoted by $\pm$ with energies $E_\pm$ and group velocities $v_\pm$:

$$\begin{aligned} E_\pm &= \frac{(\hbar k)^2}{2m} \pm \frac{\hbar}{2}\sqrt{(2\gamma k+\delta)^2+\Omega^2} \\ v_\pm &= \frac{1}{\hbar}\frac{\mathrm{d}E_\pm}{\mathrm{d}k} = \frac{\hbar k}{m} \pm \frac{\gamma(2\gamma k+\delta)}{\sqrt{(2\gamma k+\delta)^2+\Omega^2}} \end{aligned} \tag{2.3}$$

Example of the band structure calculated for $\delta = \Omega = 5E_\mathrm{R}/\hbar$ is presented in Fig. 2.1. From the structure of $E_\pm$ it is clear that depending on the parameter values, at a given energy, there may be up to four eigenstates with different velocities, see Fig. 2.1. Each eigenstate has its own spin state. The spin states with the same energy are not orthogonal to each other.

In our study, the Hamitlonian also includes a disordered potential, $H = H_0 + V(x)$, which we chose as a Gaussian uncorrelated disorder:

$$\overline{V(x)} = 0, \quad \overline{V(x)V(x')} = V_0^2\delta(x-x'). \tag{2.4}$$

The disorder is the same for both spin components. In this case, the disorder strength is denoted by V_0^2 in order to avoid a confusion with the SO coupling strength parameter γ.

The numerical simulations include both full exact diagonalization, which allows for the study of energy levels, and the Chebyshev kernel method for calculating the time evolution of a chosen initial state. The methods are briefly described in section 1.5, the extension to include the spin degree of freedom being straightforward. In both methods, we have simulated a system of finite size represented on a lattice with a small lattice constant, so that the discretization effects are negligible. The detailed parameters used in the numerical simulations are given in the following sections.

Time reversal symmetry breaking

The main aim of the study is to analyze the quantum boomerang effect in a system without time reversal symmetry. Hamiltonian (2.1) and the disordered Hamiltonian $H = H_0 + V(x)$ may break TRI. If $\gamma = 0$, then $\hbar\delta\sigma_z/2 + \hbar\Omega\sigma_x/2$ is a constant, and we are back to a spinless particle. If $\Omega = 0$, then σ_z is a good quantum number, and after a translation in k we are also back to a spinless particle. Hence, in the following, we assume that both γ and Ω are nonzero, i.e. there is finite spin-orbit coupling and coupling between the spin-up and spin-down states. The random potential $V(x)$ has no specific symmetry. It is not invariant under the parity transformation $x \to -x$. In general, the statistical distribution of $V(x)$ does not influence the symmetry properties of the system.

The disordered potential $V(x)$ breaks all possible spatial symmetries. This means also that any combinations of spin rotations with spatial symmetries are broken. Thus, the symmetries present in the system may be purely local. Additionally, because the Hamiltonian includes more than one spin component, i.e. σ_x and σ_z, there is no cylindrical symmetry – rotation around some axis – in the system. The only possible symmetries of the system may be connected with the time reversal operator.

For spinless particles, the standard time reversal operator T is the complex conjugation in configuration space, $T = K$, $T\psi(x) = \psi^*(x)$. In spin-1/2 systems, the standard time reversal symmetry operator has to be anti-unitary and generally takes the form of $T = UK$, there U is a suitable unitary operator, see [80]. Another important requirement for such an operator is that any wave

function should be obtained within a phase factor when T is applied twice:

$$T^2 = \pm 1. \tag{2.5}$$

The positive sign holds, in general, for spinless particles, whereas the negative sign for spin-1/2 quanta. The conventional time reversal operator for spin-1/2 particles results from requiring that

$$\begin{aligned} TxT^{-1} &= x, \\ T\sigma_x T^{-1} &= -\sigma_x, \\ T\sigma_y T^{-1} &= -\sigma_y, \\ T\sigma_z T^{-1} &= -\sigma_z, \\ TpT^{-1} &= -p, \\ TV(x)T^{-1} &= V(x). \end{aligned} \tag{2.6}$$

The operator reads:

$$T = e^{i\pi\sigma_y/2}K = i\sigma_y K, \tag{2.7}$$

such that

$$T\begin{pmatrix}\psi_\uparrow(x)\\ \psi_\downarrow(x)\end{pmatrix} = \begin{pmatrix}\psi^*_\downarrow(x)\\ -\psi^*_\uparrow(x)\end{pmatrix} \tag{2.8}$$

The operator defined by Eq. (2.7) has the following effect when applied to the Hamiltonian H:

$$THT^{-1} = \frac{p^2}{2m} + \gamma p\sigma_z - \frac{\hbar\delta}{2}\sigma_z - \frac{\hbar\Omega}{2}\sigma_x + V(x), \tag{2.9}$$

where $p = \hbar k$ is used for short-hand notation. This equation shows that $THT^{-1} \neq H$ which implies that the Hamiltonian H is not invariant under time reversal symmetry. However, this is not the end of the story. It is known that some systems are not invariant under the conventional time reversal T, but they are invariant under other anti-unitary unconventional time reversal operators. An important example of such a situation is the hydrogen atom in a constant magnetic field along z-axis, with included spin-orbit coupling, see [81, 82]. The Hamiltonian describing this system is not invariant under the symmetry represented by T. However, it shows invariance under the following anti-unitary symmetry:

$$T' = e^{i\pi J_x/\hbar}T, \tag{2.10}$$

where $\boldsymbol{J} = \boldsymbol{L} + \boldsymbol{S}$ is the total angular momentum. If the system has any anti-unitary symmetry, the TRI-based derivation of the quantum boomerang effect is likely to be extended to such a system. In other words, we must be sure that our system breaks all anti-unitary symmetries.

In our analysis for the unconventional or generalized time reversal operator, we will use the product of the rotation by $-\pi$ of the spin around the z-axis and the standard time reversal operator T:

$$\mathcal{T} = e^{i\pi\sigma_z/2}T = i\sigma_z T = i\sigma_x K. \tag{2.11}$$

The action of $\mathcal{T}$ on the standard operators is the following:

$$\begin{aligned} \mathcal{T}x\mathcal{T}^{-1} &= x, \\ \mathcal{T}\sigma_x\mathcal{T}^{-1} &= \sigma_x, \\ \mathcal{T}\sigma_y\mathcal{T}^{-1} &= \sigma_y, \\ \mathcal{T}\sigma_z\mathcal{T}^{-1} &= -\sigma_z, \\ \mathcal{T}p\mathcal{T}^{-1} &= -p, \\ \mathcal{T}V(x)\mathcal{T}^{-1} &= V(x), \end{aligned} \tag{2.12}$$

so that

$$\mathcal{T}H\mathcal{T}^{-1} = \frac{p^2}{2m} + \gamma p\sigma_z - \frac{\hbar\delta}{2}\sigma_z + \frac{\hbar\Omega}{2}\sigma_x + V(x). \tag{2.13}$$

This time, in comparison with Eq. (2.9), the only change in the Hamiltonian is present in the σ_z term, thus, for $\delta = 0$, the Hamiltonian is invariant under this anti-unitary symmetry.

If $\delta \neq 0$, there is the question whether there exists a symmetry transformation different from $\mathcal{T}$ obeyed by the Hamiltonian. Possible linear unitary operations should reverse σ_z (due to $\hbar\delta\sigma_z/2$ term) as well as reverse the momentum p (due to $\gamma p\sigma_z$ term). This could be achieved by the parity transformation, $x \to -x$. However, this symmetry is broken by the disordered potential $V(x)$. As a consequence, any generalized time reversal symmetry is broken for $\delta \neq 0$ and the Hamiltonian has to belong to the unitary symmetry class (see appendix 2.A).

After settling the question whether the studied system explicitly breaks TRI for $\delta \neq 0$, we also note that the generalized time reversal operator has an interesting feature, namely $\mathcal{T}^2 = +1$, which is atypical for spin-1/2 particles. Let ψ be an eigenstate to energy E for a Hamiltonian which is time reversal invariant, $[H, T] = 0$. When the time reversal operator squares to minus unity, $T^2 = -1$, it can be shown that if ψ is an eigenstate, then $T\psi$ is also an eigenstate with the same energy and the states are orthogonal:

$$\langle\psi|T\psi\rangle = \langle T\psi|T^2\psi\rangle^* = -\langle T\psi|\psi\rangle^* = -\langle\psi|T\psi\rangle = 0. \tag{2.14}$$

It means that all energy levels are doubly degenerate. The effect is called Kramers' degeneracy, see [83]. In our case, $\mathcal{T}^2 = +1$ and we do not expect any sign of degeneracy – this is fully supported by our numerical results (for $\delta = 0$). Moreover, the fact that $[H, \mathcal{T}] = 0$ for $\delta = 0$ with $\mathcal{T}$ squaring to unity, means that the Hamiltonian (for $\delta = 0$) may be constructed as a real symmetric matrix, see [80].

In appendix 2.A, we present an analysis of the symmetry properties of the Hamiltonian using statistical characteristics of the energy spectrum. This analysis fully confirms that, for nonzero γ, δ, and Ω, all generalized TRI are broken.

2.2 Classical solution to the boomerang problem (Boltzmann)

In the absence of disorder, k is a good quantum number and at a given value of k, we have two orthogonal spin states with different energies, cf. Fig. 2.1. Now, we study the disordered system and assume that disorder is weak. The effect of disorder is that the states with the same energy are coupled. The larger number of possible eigenstates at a chosen energy complicates the picture –

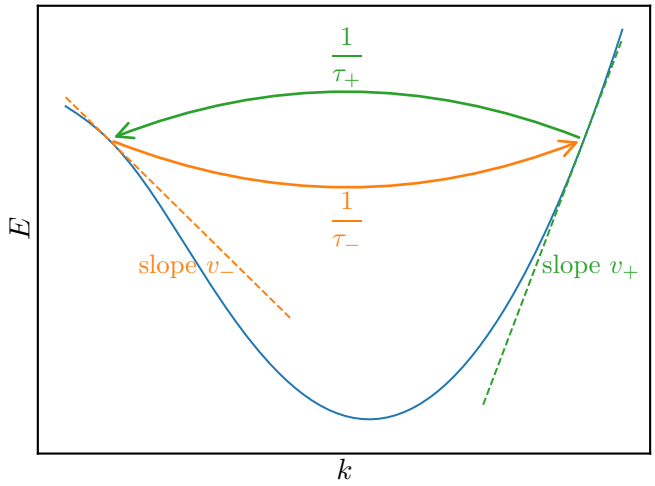

Figure 2.2. Graphical representation of the two-state scenario shown using the dispersion $E(k)$ of the lower band, Eq. (2.3). At a chosen energy there are two states: one with positive velocity v_+ and one with negative velocity v_-. Disorder couples the states, the rates of transitions between the populations are $1/\tau_\pm$, Eq. (2.15).

there are many possible scattering channels with different rates, which translate to more mean free times and paths.

2.2.1 Two-state scenario

When there are only two states at a chosen energy, the situation reassembles the TRI boomerang problem. With two possible states, one of them has negative velocity and the other one has positive velocity. We will denote the states by $\pm$ based on these velocities. The only complication is that there are in total four scattering events: $+ \to +$, $+ \to -$, $- \to -$, and $- \to +$ (arrows indicate the scattering process). The scatterings may be divided into forward/backward scatterings (e.g. $+ \to +$ is a forward scattering, $+ \to -$ is a backward scattering) or left/right scatterings (e.g. $+ \to +$ is a right scattering, $+ \to -$ is a left scattering). In the analysis of the center of mass dynamics, we use only two of them, corresponding to the scatterings where the direction of motion is changed. Let the $|\uparrow\rangle_\pm$ denote the spin states corresponding to a given velocity. We denote the scattering times between the states by $\tau_+ = \tau_{+\to-}$ and $\tau_- = \tau_{-\to+}$. The times are computed from the Fermi's golden rule, similarly to Eq. (1.32) in section 1.2. In the system, we have two contributions to the density of states: $1/(\hbar\pi v_+)$ for the $+$ states, and $1/(\hbar\pi v_-)$ for the $-$ states, where $v_\pm$ denote the absolute value of velocity. Taking this into account, we have:

$$\frac{1}{\tau_+} = \frac{2V_0^2 |\,{}_+\langle\uparrow \,|\, \uparrow\rangle_-|^2}{\hbar^2 v_-}, \quad \frac{1}{\tau_-} = \frac{2V_0^2 |\,{}_+\langle\uparrow \,|\, \uparrow\rangle_-|^2}{\hbar^2 v_+}, \tag{2.15}$$

The difference between the times comes due to the velocity. The two-state scattering is pictorially presented in Fig. 2.2. For short-hand notation, we will use $\kappa = |\,{}_+\langle\uparrow \,|\, \uparrow\rangle_-|^2$. The Boltzmann

equations for the populations $n_\pm(t)$ have the following form:

$$\begin{cases} \dfrac{\mathrm{d}n_+(t)}{\mathrm{d}t} &= \dfrac{n_-(t)}{2\tau_-} - \dfrac{n_+(t)}{2\tau_+}, \\ \dfrac{\mathrm{d}n_-(t)}{\mathrm{d}t} &= \dfrac{n_+(t)}{2\tau_+} - \dfrac{n_-(t)}{2\tau_-}. \end{cases} \tag{2.16}$$

The equations are very similar to the TRI case, cf. Eq. (1.57). Assuming the initial state $n_+(0) = 1$, $n_-(0) = 0$ the solution is given by:

$$\begin{aligned} n_+(t) &= \frac{1}{2}\left(\frac{\tau}{\tau_-} + \frac{\tau}{\tau_+}e^{-t/\tau}\right) \\ n_-(t) &= \frac{1}{2}\frac{\tau}{\tau_+}\big(1 - e^{-t/\tau}\big), \end{aligned} \tag{2.17}$$

where τ is defined as

$$\tau = \frac{2\tau_+\tau_-}{\tau_+ + \tau_-}. \tag{2.18}$$

Of course, the sum of populations is constant, $n_+(t) + n_-(t) = 1$. The infinite-time stationary populations are given by

$$n_+^\infty = \frac{\tau_+}{\tau_+ + \tau_-}, \quad n_-^\infty = \frac{\tau_-}{\tau_+ + \tau_-}. \tag{2.19}$$

In contrast to the TRI case, the stationary populations are no longer equal. This is a result of the difference between the velocities. The long-time average value of the velocity should be zero (even in the classical approach), hence the populations must be unequal. Simple calculation shows that the average velocity indeed vanishes $\langle v\rangle = v_+n_+^\infty - v_-n_-^\infty = 0$. The center of mass is calculated as a contribution of both components:

$$\langle x(t)\rangle = \int_0^t (v_+n_+(t') - v_-n_-(t'))\mathrm{d}t' = \tau v_+\big(1 - e^{-t/\tau}\big). \tag{2.20}$$

A similar result is obtained assuming that, initially, only the v_- state was populated. If we denote by $\langle x_\pm(t)\rangle$ the center of mass time dependence for a $\pm$ initial state, we have

$$\langle x_\pm(t)\rangle = \pm\tau v_\pm\big(1 - e^{-t/\tau}\big). \tag{2.21}$$

This result closely reassembles the TRI system, see Eq. (1.59), where the scattering mean free path is replaced by $\tau v_\pm$, $\ell \to v_\pm\tau$, and is hence asymmetric between the + and − directions of motion, but the relaxation time τ is the same in both directions.

Forward and backward scattered components of the center of mass

As we have shown in section 1.3.2, in the TRI case, the backscattered contribution to the center of mass is always zero, even at the classical level. In our system, we can study the forward and backward scattered components of the center of mass separately and compare the result to the TRI system.

In order to derive the equations for the forward- and backscattered contributions, denoted $\langle x(t)\rangle_+$

and $\langle x(t)\rangle_-$ respectively, we start from the Boltzmann equations for the densities $f_\pm(x,t)$ of the populations $n_\pm(t)$, i.e. $n_\pm(t) = \int f_\pm(x,t)\mathrm{d}x$. The Boltzmann equation reads:

$$\left(\frac{\partial f_\pm}{\partial t}\right)_{\text{coll}} = \frac{\partial f_\pm}{\partial t} \pm v_\pm \frac{\partial f_\pm}{\partial x}, \tag{2.22}$$

where $(\ldots)_{\text{coll}}$ denotes the total change due to scattering events. It means that the equations for the population densities are given by

$$\begin{cases} \dfrac{\partial f_+}{\partial t} &= -v_+ \dfrac{\partial f_+}{\partial x} - \dfrac{f_+}{2\tau_+} + \dfrac{f_-}{2\tau_-}, \\ \dfrac{\partial f_-}{\partial t} &= v_- \dfrac{\partial f_-}{\partial x} + \dfrac{f_+}{2\tau_+} - \dfrac{f_-}{2\tau_-}. \end{cases} \tag{2.23}$$

If we integrate the above equations over $\int \mathrm{d}x$, we will get nothing but Eq. (2.16). If we integrate them over $\int x\mathrm{d}x$ we will get the desired equations for the separated forward and backward scattered contributions:

$$\begin{cases} \dfrac{\partial \langle x(t)\rangle_+}{\partial t} &= v_+ n_+(t) - \dfrac{\langle x(t)\rangle_+}{2\tau_+} + \dfrac{\langle x(t)\rangle_-}{2\tau_-}, \\ \dfrac{\partial \langle x(t)\rangle_-}{\partial t} &= -v_- n_-(t) + \dfrac{\langle x(t)\rangle_+}{2\tau_+} - \dfrac{\langle x(t)\rangle_-}{2\tau_-}. \end{cases} \tag{2.24}$$

The change of the sign of the velocities results from the integration by parts. The densities $n_\pm(t)$ are given by Eq. (2.17). It is thus easy to solve the differential equations Eq. (2.24). As there are two possible initial states, we indicate them by an additional index inside $\langle\cdots\rangle$, i.e. $\langle x_\pm\rangle = \langle x_\pm\rangle_+ + \langle x_\pm\rangle_-$.
Solutions for the positive initial velocity:

$$\begin{aligned} \langle x_+(t)\rangle_+ =& \tau v_+ \left[\frac{2v_-}{v_+ + v_-}\left(1 - e^{-t/\tau}\right) + \frac{v_+ - v_-}{v_+ + v_-}\left(\frac{t}{\tau}\right)e^{-t/\tau}\right], \\ \langle x_+(t)\rangle_- =& \tau v_+ \left(\frac{v_+ - v_-}{v_+ + v_-}\right)\left(1 - e^{-t/\tau} - \left(\frac{t}{\tau}\right)e^{-t/\tau}\right). \end{aligned} \tag{2.25}$$

Solutions for the negative initial velocity:

$$\begin{aligned} \langle x_-(t)\rangle_+ =& \tau v_- \left(\frac{v_+ - v_-}{v_+ + v_-}\right)\left(1 - e^{-t/\tau} - \left(\frac{t}{\tau}\right)e^{-t/\tau}\right), \\ \langle x_-(t)\rangle_- =& -\tau v_- \left[\frac{2v_+}{v_+ + v_-}\left(1 - e^{-t/\tau}\right) - \frac{v_+ - v_-}{v_+ + v_-}\left(\frac{t}{\tau}\right)e^{-t/\tau}\right]. \end{aligned} \tag{2.26}$$

In both cases, the sum of contributions gives $\langle x_\pm\rangle = \pm\tau v_\pm(1 - e^{-t/\tau})$, as expected. The solutions of the Boltzmann equations are presented in Fig. 2.3. In contrast to the TRI case, when $v_- \neq v_+$, the backscattered contributions do not vanish. Moreover, the backscattered contributions are widely different from the forward scattered ones. In the short-time regime $\langle x_+(t)\rangle_-$ and $\langle x_-(t)\rangle_+$ scale as t^2, then they saturate at a finite value as $t \to \infty$.

The quadratic behavior of the backscattered center of mass may be explained easily. Without loss of generality, we can assume that the initial velocity is positive. At $t = 0$ the center of mass

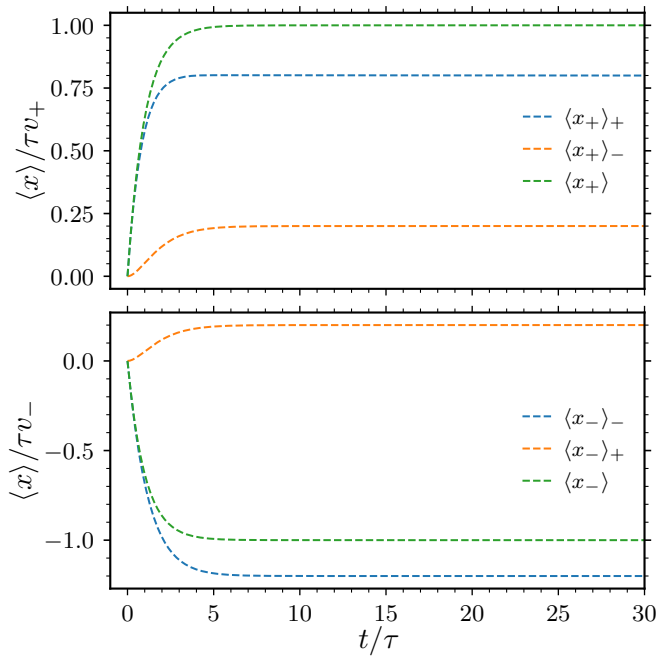

Figure 2.3. Temporal dynamics of the center of mass for both initial states with positive velocity v_+ (upper panel) and negative velocity v_- (lower panel) calculated using Eqs. (2.25), (2.26). The ratio of velocities is $v_+/v_- = 1.5$. The center of mass $\langle x_\pm\rangle$ is also divided into the forwardscattered ($\langle x_+\rangle_+$, $\langle x_-\rangle_-$) and backscattered ($\langle x_+\rangle_-$, $\langle x_-\rangle_+$) contributions. Similarly the to the TRI case, after the initial ballistic evolution the center of mass saturates at the finite value $\pm\tau v_\pm$.

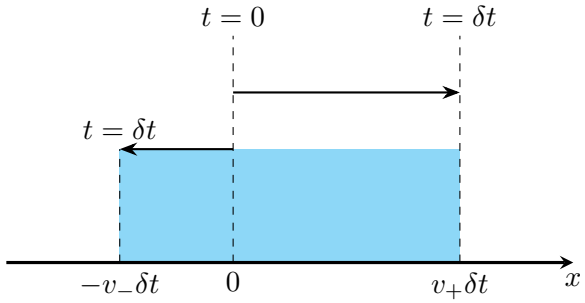

Figure 2.4. Time evolution of the wave packet for a very short time. Assuming an initial state with v_+, the majority of the packet moves forward but some parts may be immediately scattered backwards. After some short time δt, we may expect another backward scattering. Thus, the total backscattered part of the wave packet is located between $-v_-\delta t$ and $v_+\delta t$ (colored in blue). The whole backscattered population should be proportional to $\delta t/\tau_-$, hence the $\langle x_+\rangle_- \propto \delta t^2$. Analogous situation takes place for the initial state with the negative velocity.

position is at $x = 0$. Even for weak disorder, there is some small probability that the part of the wave packet is scattered backwards immediately at the beginning of the evolution. After some small but finite time δt, the leftmost backscattered part reaches position $x = -v_-\delta t$; on the other side, the rightmost backscattered part is at $x = v_+\delta t$ (assuming backscattering event at δt), see Fig. 2.4. Moreover, at time $t = \delta t$, the total population of the backscattered part should be proportional to $\delta t/\tau_-$. Altogether, this implies that the center of mass of the backscattered wave packet after $t = \delta t$ is proportional to $(v_+ + v_-)\delta t^2/\tau_-$, hence we expect a quadratic behavior for a short time.

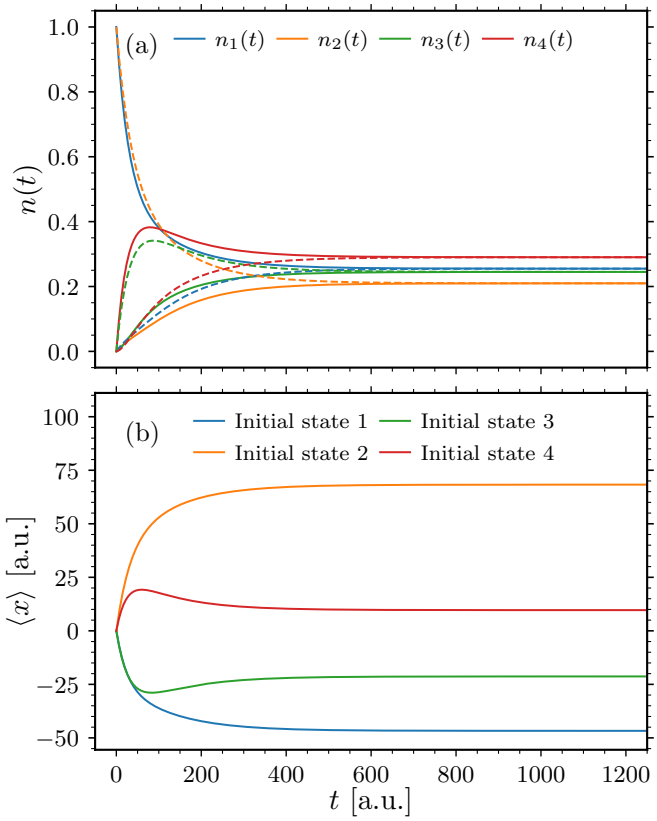

Figure 2.5. (a) Temporal evolution of the classical populations calculated from Eq. (2.33) for a system with $\delta = \Omega = 5E_{\mathrm{R}}/\hbar$, $V_0 = 1.875E_{\mathrm{R}}$ and initial state energy $E = 9.375E_{\mathrm{R}}$. The momenta at energy E are $k_1 = -3.9k_{\mathrm{R}}$, $k_2 = 4.62k_{\mathrm{R}}$, $k_3 = -2.44k_{\mathrm{R}}$, and $k_4 = 1.71k_{\mathrm{R}}$ (velocities are given in the main text). Solid lines show the results for an initially populated state with k_1. Dashed lines show results for the initial population only in the state with k_2. After short-time evolution, dashed and solid lines reach their stationary values independent of the initial state. (b) Calculation of total $\langle x \rangle$ in the same system for all possible initial states (indicated by the legend). As in the TRI case, after the short initial ballistic motion the center of mass saturates around a finite value and the evolution halts.

2.2.2 Four-state scenario: an example

While we will in the following analyze in detail the 2-state scenario, we would like to present an example with four states at a given energy. We will only analyze the classical evolution of populations and the total center of mass position.

We start by a simplification of the spin part of the Hamiltonian $H_0 = (\hbar k)^2/2m + H_s$:

$$H_s = \begin{pmatrix} \hbar\gamma k + \frac{\hbar\delta}{2} & \frac{\hbar\Omega}{2} \\ \frac{\hbar\Omega}{2} & -\hbar\gamma k - \frac{\hbar\delta}{2} \end{pmatrix} \tag{2.27}$$

Because the Hamiltonian H_s includes only σ_z and σ_x matrices we can employ an useful representation where the spin direction is determined by $\sigma_\theta = \boldsymbol{n} \cdot \boldsymbol{\sigma}$, where $\boldsymbol{n} = \cos\theta\hat{n}_z + \sin\theta\hat{n}_x$. Then:

$$\sigma_\theta = \begin{pmatrix} \cos\theta & \sin\theta \\ \sin\theta & -\cos\theta \end{pmatrix} \tag{2.28}$$

The matrix has eigenvalues ± 1 and its eigenvectors are

$$\phi_+ = \begin{pmatrix} \cos\theta/2 \\ \sin\theta/2 \end{pmatrix}, \quad \phi_- = \begin{pmatrix} -\sin\theta/2 \\ \cos\theta/2 \end{pmatrix}, \tag{2.29}$$

corresponding to the lower and upper bands. Using the matrix σ_θ we can rewrite the Hamiltonian H_s:

$$H_s = \sqrt{\left(\hbar\gamma k + \frac{\hbar\delta}{2}\right)^2 + \frac{\hbar^2\Omega^2}{4}}\sigma_\theta, \text{ with } \tan\theta = \frac{\Omega}{2\gamma k + \delta}. \tag{2.30}$$

Now, we can easily compute the transition amplitudes between the four possible states. Each state is characterized by a different value of the angle θ, and the amplitudes are simply given by

$$\begin{aligned} \langle\phi_+(\theta_i)|\phi_+(\theta_f)\rangle = \langle\phi_-(\theta_i)|\phi_-(\theta_f)\rangle = \cos\left(\frac{\theta_i - \theta_f}{2}\right), \\ \langle\phi_+(\theta_i)|\phi_-(\theta_f)\rangle = -\langle\phi_-(\theta_i)|\phi_+(\theta_f)\rangle = \sin\left(\frac{\theta_i - \theta_f}{2}\right). \end{aligned} \tag{2.31}$$

Using the Fermi's golden rule, the transition rates between the initial and the finial states are [1]:

$$\begin{aligned} r_{i,f} &\propto \frac{\cos^2((\theta_i - \theta_f)/2)}{v_f} \quad \text{between states of the same band} \\ r_{i,f} &\propto \frac{\sin^2((\theta_i - \theta_f)/2)}{v_f} \quad \text{between states of the different bands} \end{aligned} \tag{2.32}$$

where θ_i, θ_f denote the angles for the initial and final states, respectively, and v_f is the absolute value of the group velocity of the final state. The velocity shows up in the rate as a contribution to the density of states (cf. Eq. (2.15)). In this case, the evolution of the populations is characterized by:

$$\frac{\mathrm{d}\boldsymbol{n}}{\mathrm{d}t} = R\,\boldsymbol{n}, \tag{2.33}$$

where $\boldsymbol{n}$ is defined as $\boldsymbol{n} = (n_1(t), n_2(t), n_3(t), n_4(t))$, and R is a 4×4 scattering matrix. The total population is conserved, hence the eigenvalues of the scattering matrix have to be non-positive, $\lambda_i \leq 0$. From the general form of the matrix R:

$$R = \begin{pmatrix} -(r_{2,1} + r_{3,1} + r_{4,1}) & r_{1,2} & r_{1,3} & r_{1,4} \\ r_{2,1} & -(r_{1,2} + r_{3,2} + r_{4,2}) & r_{2,3} & r_{2,4} \\ r_{3,1} & r_{3,2} & -(r_{1,3} + r_{2,3} + r_{4,3}) & r_{3,4} \\ r_{4,1} & r_{4,2} & r_{4,3} & -(r_{1,4} + r_{2,4} + r_{3,4}) \end{pmatrix}, \tag{2.34}$$

it can be easily shown that there always exists a zero eigenvalue, which is directly connected with the infinite-time stationary populations.

For a given choice of parameters γ, δ and Ω, the solution of Eq. (2.33) can be easily calculated. However, the general solution is rather complex. It involves solving a fourth order polynomial, which in principle can be performed, but it means that the solutions are fairly complicated. Thus,

1. Equation (2.32) is noting but Eq. (2.15) for the two-state scenario, and κ is simply $\cos^2(\theta_i - \theta_f)/2$.

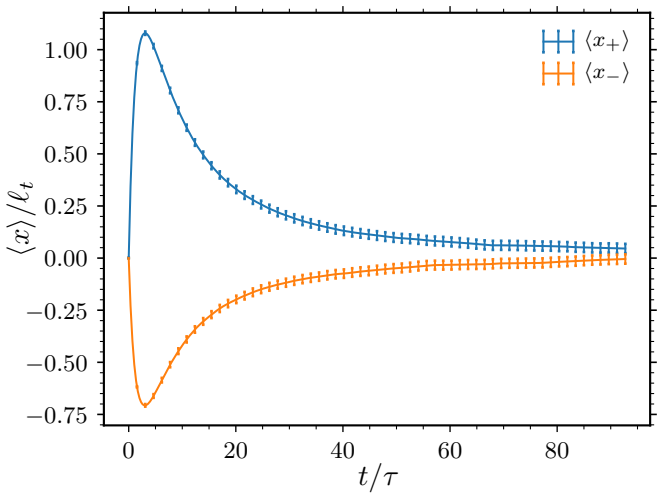

Figure 2.6. Quantum time evolution of a total center of mass Eq. (2.37) computed for both inital states, Eq. (2.36), as indicated by the legend. Although the spin-orbit system has no TRI we observe the full boomerang effect – the center of mass returns to the origin. This clearly shows that the quantum boomerang effect is present in systems without TRI. Results show that the characteristic time scale of the phenomenon is independent of the initial velocity. The length scale seems to depend on the initial velocity, as predicted by the classical approach, cf. Eqs. (2.25), (2.26). The results have been averaged over 40960 disorder realizations. Error bars represent statistical errors of the average.

in the following we restrict ourselves only to a short discussion of the classical results computed for a system with $\delta = \Omega = 5E_{\mathrm{R}}/\hbar$ for states at energy $E = 9.375E_{\mathrm{R}}$. The momenta corresponding to the energy E are $k_1 = -3.9k_{\mathrm{R}}$, $k_2 = 4.62k_{\mathrm{R}}$, $k_3 = -2.44k_{\mathrm{R}}$, and $k_4 = 1.71k_{\mathrm{R}}$. The corresponding absolute values of velocities: $v_1 = 3.0\gamma$, $v_2 = 3.65\gamma$, $v_3 = 3.12\gamma$, and $v_4 = 2.64\gamma$. The matrix R in dimensionless units reads:

$$\gamma R \approx \begin{pmatrix} -0.178 & 0.017 & 0.006 & 0.139 \\ 0.014 & -0.141 & 0.104 & 0.001 \\ 0.005 & 0.122 & -0.171 & 0.052 \\ 0.158 & 0.002 & 0.061 & -0.192 \end{pmatrix}. \tag{2.35}$$

The time evolution of the populations is shown in Fig. 2.5 (a) for two different initial states. As expected, the long-time values of $n_i(t)$ do not depend on the initial state and satisfy the condition of zero long-time average velocity.

Figure 2.5 (b) presents the time evolution of the total center of mass for all four possible initial states. It is clear that in this case $\langle x(t) \rangle$ cannot be described with a curve similar to $\ell(1 - e^{-t/\tau})$. Nonetheless, after the initial evolution, it stops and the center of mass saturates around some finite value. This behavior is very similar to the (classical) two-state description.

2.3 Quantum boomerang effect in the two-state scenario

In section 2.2, we have performed classical calculations for the center of mass in a disordered spin-orbit coupled system. Clearly, even for the case with only two possible states, the situation is

more complicated than in the TRI case. For this reason, we will now study this situation in detail. The simulations have been performed in a system with parameters $\delta = \Omega = 5E_{\mathrm{R}}/\hbar$. The system size is $L = 4000/k_{\mathrm{R}}$ with a discretization constant $\Delta x = 0.08/k_{\mathrm{R}}$. The initial energy of the state was chosen as $E_0 = 0$, so that the two states have momenta $k_- = -1.61k_{\mathrm{R}}$ and $k_+ = 2.96k_{\mathrm{R}}$ with the absolute values of velocities $v_- = 1.335\gamma$ and $v_+ = 2.003\gamma$. With $\kappa = 0.505$ and the disorder strength $V_0 = 0.875E_{\mathrm{R}}$, we have $\tau_- = 12.944\hbar/E_{\mathrm{R}}$, $\tau_+ = 8.626\hbar/E_{\mathrm{R}}$, and $\tau = 10.353\hbar/E_{\mathrm{R}}$. All presented results have been averaged over 40960 disorder realizations. The two initial states are labeled by $\pm$, as it is done in section 2.2.1.

To obtain meaningful results, the simulations have to be performed using the eigenstates of the Hamiltonian (2.1), not the spin-up and spin-down states used as the computational basis. This means that the initial states are combinations of the spin-up and spin-down components. For a given energy E_0, using Eq. (2.3), we can easily compute the appropriate values of momenta, denoted by the wave numbers k_+ and k_-. Using the eigenmomenta we define our initial states:

$$\Psi_0^+(x) = \mathcal{N}\exp(-x^2/2\sigma^2 + ik_+x)\,|\uparrow\rangle_+\,, \quad \Psi_0^-(x) = \mathcal{N}\exp(-x^2/2\sigma^2 + ik_-x)\,|\uparrow\rangle_-\,, \tag{2.36}$$

where the normalization constant is $\mathcal{N} = (\pi\sigma^2)^{-1/4}$, and $|\uparrow\rangle_\pm$ denote the (eigen) spin states for corresponding values of the wave numbers $k_\pm$. In our simulations, we have used $\sigma = 20/k_{\mathrm{R}}$. States $\Psi_0^\pm$ are not the exact eigenstates of the Hamiltonian H_0 – the finite value of σ means that they are only approximations to monochromatic waves. However, taking into account the results of [3], we can safely assume that as long as the initial states do not contain too many momentum components and disorder is weak, the results are essentially independent of σ. We assume also that the width of the wave packet σ is smaller than the mean free path [2].
The initial states have the $\mathcal{PT}$-symmetry, cf. section 1.3.3, hence in the following analysis we study directly the effect of the TRI breaking of the Hamiltonian on the quantum boomerang effect.

We compute the center of mass with the spin degrees of freedom averaged out:

$$\langle x(t)\rangle = \langle x(t)\rangle_\uparrow + \langle x(t)\rangle_\downarrow = \int x\overline{|\psi_\uparrow(x,t)|^2}\mathrm{d}x + \int x\overline{|\psi_\downarrow(x,t)|^2}\mathrm{d}x\,, \tag{2.37}$$

where $\psi_\uparrow(x,t)$ and $\psi_\downarrow(x,t)$ are the wave functions represented in the spin (computational) basis, and $\overline{|\psi(x,t)|^2}$ is the disorder averaged density. As we have pointed out in section 2.2.1, the two states have different mean free times, τ_+ and τ_-. However, the characteristic lengths associated with these time scales do not differ:

$$v_+\tau_+ = v_-\tau_- = \ell_t \tag{2.38}$$

We call this length scale transport mean free path ℓ_t. Figure 2.6 presents the result of simulations for the two initial states. Even though TRI is broken in the system, we observe the full boomerang effect.

Similarly to the TRI system, the center of mass returns to the origin. As in the TRI system, the ballistic part of the motion is followed by a reflection, after which the particle slowly returns to its initial position. The $\langle x\rangle$ curves for both initial states clearly indicate the existence of a single time scale independent of the initial velocity. This agrees with the classical result (cf. Eqs. (2.21),

2. This condition is for convenience of the calculation. It can be relaxed, as in the TRI case, where there is no needed inequality between σ and the mean free path [2].

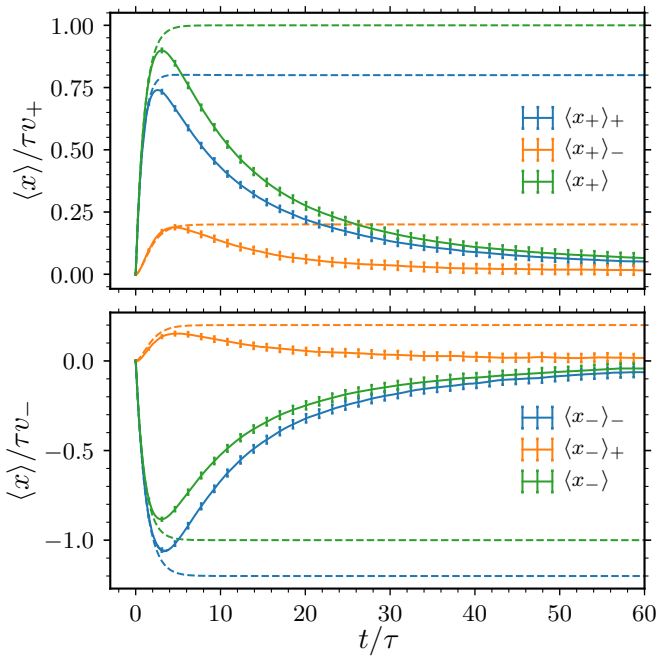

Figure 2.7. Center of mass $\langle x(t) \rangle$ calculated in simulations of the quantum system for both initial states, compared with the classical prediction, Eqs.(2.25), (2.26). Similarly to the TRI system, after agreement in the regime of the ballistic motion, the quantum particle starts a slow return to the origin. Agreement for short times supports the hypothesis that the quantum phenomenon is also characterized by a single time scale τ. The internal indices, $\langle x_\pm \rangle$, indicate the initial velocity, while external indices, $\langle x \rangle_\pm$, denote the forward/backward scattered component. Note that the $\langle x_- \rangle_+$ contribution of the negative initial state has opposite sign to $\langle x_- \rangle_-$ what is also predicted by the classical solution (because $v_+ > v_-$, see Eq. (2.26)).

(2.25), and (2.26)). The center of mass presented in Fig. 2.6 is rescaled using the transport mean free path ℓ_t different from τv_+ and τv_- which appear as the natural length scales in the solutions of Boltzmann equations (Eqs. (2.25), (2.26)).

The data displayed in Fig. 2.6 constitutes a major result of this study of the boomerang effect in systems where the TRI is broken, which is **completely unexpected**. Indeed, all previous studies of the boomerang [2, 3, 21, 84, 85] insisted on the importance of TRI (in addition to Anderson localization) for the boomerang effect. Here, we see that this point of view is clearly insufficient. We can now give a negative answer to the question asked in the first paragraph of this chapter, page 31; TRI is **not** necessary for the boomerang effect to exists. Moreover, as we have proved that all generalized TRI are broken (see section 2.1 and appendix 2.A), this excludes any explanation of the boomerang effect by symmetry considerations (as in section 1.3). Finally, we will show in section 2.6 how to perform a quasi-exact theoretical calculation of the boomerang effect in our system, which will not use any symmetry argument and agrees perfectly (see Fig. 2.21) with our numerical results. The short summary is: TRI is not needed for the quantum boomerang effect.

2.3.1 Backward and forward scattered wave functions

In the previous analysis, we average $\langle x(t) \rangle$ over the spin degree of freedom. It turns out that we can extract more information using a tailored analysis of the spin state.

If we assume weak disorder and that scattering happens only between the two states, then at any time of evolution, we can write that the total wave function, including spin, has the following form:

$$|\psi(x,t)\rangle = \psi_+(x,t)\,|\uparrow\rangle_+ + \psi_-(x,t)\,|\uparrow\rangle_- \,, \tag{2.39}$$

where $\psi_+(x,t)$ and $\psi_-(x,t)$ are the wave functions of the forward and backward scattered parts of the whole wave function [3] and $|\uparrow\rangle_\pm$ represent the *proper* spin eigenstates. The spin states are not orthogonal: ${}_-\langle\uparrow\,|\,\uparrow\rangle_+ \approx 0.71$. Thus, we define the orthogonal counterparts, denoted by $|\downarrow\rangle_\pm$. By projecting the total wave function onto the orthogonal spin states, we can extract $\psi_\pm(x,t)$:

$$\psi_+(x,t) = \frac{{}_-\langle\downarrow\,|\psi(x,t)\rangle}{{}_-\langle\downarrow\,|\,\uparrow\rangle_+}, \quad \psi_-(x,t) = \frac{{}_+\langle\downarrow\,|\psi(x,t)\rangle}{{}_+\langle\downarrow\,|\,\uparrow\rangle_-}. \tag{2.40}$$

Now we can easily define the center of mass positions for the forward and backward scattered parts of the wave function:

$$\langle x(t)\rangle_+ = \int x\overline{|\psi_+(x,t)|^2}\mathrm{d}x\,, \quad \langle x(t)\rangle_- = \int x\overline{|\psi_-(x,t)|^2}\mathrm{d}x\,. \tag{2.41}$$

Nevertheless, the wave functions $\psi_\pm(x,t)$ are not orthogonal. When we calculate the center of mass using Eq. (2.39), we find that $\langle x(t)\rangle_+$ and $\langle x(t)\rangle_-$ do not add up to a total $\langle x(t)\rangle$:

$$\langle\psi(x,t)|x|\psi(x,t)\rangle = \int x\Big[|\psi_+(x,t)|^2 + |\psi_-(x,t)|^2 + {}_+\langle\uparrow\,|\,\uparrow\rangle_-(\psi_+(x,t)\psi_-^*(x,t) + \text{c.c.})\Big]. \tag{2.42}$$

The cross-term proportional to ${}_+\langle\uparrow\,|\,\uparrow\rangle_-$ present in the integral is an oscillatory contribution $\sim e^{i(k_+-k_-)x}$, whose integral is around 1-2% of the total center of mass, thus almost negligible. The calculation of separate contributions: the forward and backward scattered parts of the wave function, enables us a direct comparison with the Boltzmann solutions, Eqs. (2.25), (2.26).

Figure 2.7 presents the comparison of the center of mass calculated in quantum simulations with the classical predictions for both initial states. The center of mass is divided into forward and backward scattered parts, allowing for a comparison of the separate components. The outcome of the comparison is very similar to the TRI system. For a very short time, the Boltzmann solution agrees with the quantum simulations. At longer times, all four contributions make an apparently similar U-turn and return to the origin. Additionally, we have a confirmation of our guess that the phenomenon is governed by a single time scale, τ. The center of mass for the initial state with negative velocity, similarly to the classical prediction, shows that the backscattered contribution has an opposite sign to the forward scattered one. The backscattered contribution moves in the direction of the maximum velocity, cf. Eqs. (2.26), (2.25).

3. Comparing with the densities $f_\pm(x,t)$ used in Sec. 2.2.1 we have $f_\pm(x,t) = |\psi_\pm(x,t)|^2$.

2.4 Center of mass in terms of Green's functions

To compute the center of mass theoretically, we express it using a product of the retarded and advanced Green's functions. We start from the general formula for the center of mass:

$$\langle x(t)\rangle = \int \mathrm{d}x\, x\overline{|\psi(x,t)|^2}. \tag{2.43}$$

To compute $\psi(x,t)$ we use the Green's functions:

$$\psi(x,t) = \int \mathrm{d}x'\, G^R(x,x',t)\Psi_0(x'), \quad \psi^*(x,t) = \int \mathrm{d}x''\, \left(G^R(x,x'',t)\right)^*\Psi_0^*(x''), \tag{2.44}$$

where $\Psi_0(x)$ is the initial state. To simplify the notation, we use the fact that $\left(G_0^R(x,x'',t)\right)^* = G_0^A(x'',x,-t)$, leading to:

$$\langle x(t)\rangle = \int \mathrm{d}x\,\mathrm{d}x'\,\mathrm{d}x''\, x\,\overline{G^R(x,x',t)G^A(x'',x,-t)}\Psi_0(x')\Psi_0^*(x''). \tag{2.45}$$

The average product of the Green's functions is usually much more complicated than the product of the average Green's functions. In this and the following sections, we focus on simplifications and application of the diagrammatic technique to compute this crucial object needed to calculate the desired observable, the center of mass.

The Green's functions have much simpler forms in the frequency representation. To simplify our calculations, we use the following identity:

$$\overline{G^R(x,x',t)G^A(x'',x,-t)} = \frac{1}{(2\pi\hbar)^2}\int \mathrm{d}\epsilon\,\mathrm{d}(\hbar\omega_1)\, e^{-i\omega_1 t}\overline{G^R(x,x',\epsilon)G^A(x'',x,\epsilon-\hbar\omega_1)}. \tag{2.46}$$

Now, if we put Eq. (2.46) into Eq. (2.45) we obtain:

$$\langle x(t)\rangle = \frac{1}{(2\pi\hbar)^2}\int \mathrm{d}x\,\mathrm{d}x'\,\mathrm{d}x''\,\mathrm{d}\epsilon\,\mathrm{d}(\hbar\omega_1)\, x e^{-i\omega_1 t}\overline{G^R(x,x',\epsilon)G^A(x'',x,\epsilon-\hbar\omega_1)}\Psi_0(x')\Psi_0^*(x''). \tag{2.47}$$

As a final step, we Fourier transform both sides of Eq. (2.47). The integral over time domain can be performed easily, yielding $2\pi\delta(\omega_1-\omega)$. Then, the integration over frequency ω_1 gives us the final result:

$$\langle x(\omega)\rangle = \frac{1}{2\pi\hbar}\int \mathrm{d}x\,\mathrm{d}x'\,\mathrm{d}x''\,\mathrm{d}\epsilon\, x\,\overline{G^R(x,x',\epsilon)G^A(x'',x,\epsilon-\hbar\omega)}\Psi_0(x')\Psi_0^*(x''). \tag{2.48}$$

Such an equation is not uncommon in many calculations. The temporal evolution, hence the dynamics of the system, is expressed using a product of Green's functions evaluated at different energies. Equation (2.48) is fully general and does not depend on the TRI breaking or other features of the system (for example spin).

2.5 Free Green's functions in the spin-orbit system

In order to calculate $\langle x(\omega)\rangle$ we need to find the expression for the product of the average Green's functions. We begin by expressing the disordered Green's function using the Born expansion (see

section 1.2, Eq. (1.13)) with the free Green's $G_0^{R/A}(x,x',\epsilon)$ and the disordered potential $V(x)$:

$$\begin{aligned} G^{R/A}(x,x',\epsilon) =& G_0^{R/A}(x,x',\epsilon) + \int \mathrm{d}x_1\, G_0^{R/A}(x,x_1,\epsilon)V(x_1)G_0^{R/A}(x_1,x',\epsilon) + \\ & \int \mathrm{d}x_1\,\mathrm{d}x_2\, G_0^{R/A}(x,x_1,\epsilon)V(x_1)G_0^{R/A}(x_1,x_2,\epsilon)V(x_2)G_0^{R/A}(x_2,x',\epsilon) + \dots \end{aligned} \tag{2.49}$$

To compute $G^{R/A}(x,x',\epsilon)$, we need to find the free Green's function in our model.

We study the system with an energy such that Hamiltonian (2.1) has only two solutions, which we call the 2-state approximation. It means that the available states are from the lower band, with energies:

$$\epsilon_k = \frac{\hbar^2 k^2}{2m} - \frac{\hbar}{2}\sqrt{(2\gamma k+\delta)^2+\Omega^2}, \tag{2.50}$$

and parameters γ, δ and Ω are such that there are only 2 solutions in the lower band at the given energy. The group velocity is defined as

$$v(k) = \frac{1}{\hbar}\frac{\mathrm{d}\epsilon_k}{\mathrm{d}k}. \tag{2.51}$$

To calculate the Green's functions, we use the standard approach, i.e. using the definition based on the Fourier transform between configuration and momentum spaces:

$$G_0^R(x,x',\epsilon) = \int \frac{\mathrm{d}k}{2\pi}\frac{e^{ik(x-x')}}{\epsilon-\epsilon_k+i0^+}. \tag{2.52}$$

In our system, for a given energy ϵ the integral has four poles such that $\epsilon-\epsilon_k=0$. Two of them are always real and two are fully complex. We denote the real poles as k_- and k_+, $k_- < k_+$.

2.5.1 Analysis of poles and branch cuts of Green's functions

For a moment, let us consider a more general scenario where $\epsilon-\epsilon_k = f(k)$ has some finite number of zeros. Let the zeros be denoted by k_j. We will argue that the main features of the Green's functions may be captured using only real (or close to being real) zeros of the function $f(k)$. The reason is that the imaginary part $\mathrm{Im}(k_j)$ results in an exponential decay of the Green's function:

$$G_0^R(x,x',\epsilon) = -i\sum_{k_j\in\Gamma}\frac{1}{\hbar v(k_j)}e^{i\,\mathrm{Re}(k_j)(x-x')}e^{-\,\mathrm{Im}(k_j)(x-x')}, \tag{2.53}$$

where Γ is an appropriate contour of integration such that $\mathrm{Im}(k_j)(x-x')>0$. It means that there exists some finite range (in configuration space) of the effect of the Green's function's complex poles.

To quantitatively approach this problem, we propose to use an arbitrary length scale ℓ_0 as a parameter. This creates a *strip* $1/\ell_0$ in the complex k space, see Fig. 2.8. In general, at distance $|x-x'|\gg\ell_0$, only the poles inside the strip give important contributions to the Green's function. If ℓ_0 is sufficiently large and all the complex poles k_j lay outside the strip, the Green's function may be approximated using only the real poles. Moreover, the same reasoning applies to branch cuts and other singularities of $f(k)$. If such objects are outside the relatively narrow, $1/\ell_0$, region in the complex k plane, we may discard their effect on the Green's function.

The only problem remains when one is interested in the values of the Green's function for

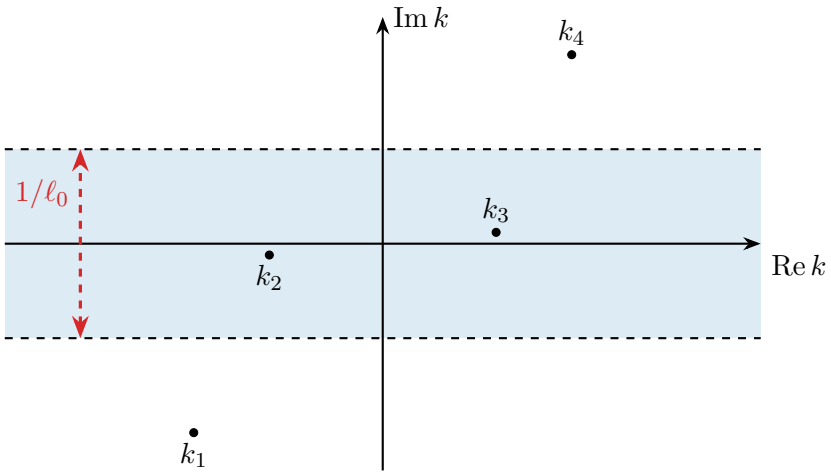

Figure 2.8. *Strip* defined by the length scale ℓ_0 in complex k space, where k_j represent roots of $\epsilon - \epsilon(k)$. k_2 and k_3 are near real axis, shifted only due to infinitesimal positive imaginary part of ϵ used in the calculation of the Green's function $G_0^R(x, x', \epsilon)$, Eq. (2.53), and k_1, k_4 are fully complex. If we are interested in distances $|x - x'| \gg \ell_0$ then we can safely discard contributions of k_1 and k_4 to the Green's function.

$x - x' < \ell_0$, e.g. $x = x'$. In such a situation, all poles of the Green's function contribute equally. For example, one could be interested in the density of states per unit volume, which is proportional to $\operatorname{Im} G_0^R(x', x', \epsilon)$. If one does not take into account the complex poles of G_0^R, the resulting Green's function will be discontinuous at $x = x'$ almost surely. Generally, the Green's function for $x = x'$ including all poles k_j is given by:

$$G_0^R(x, x', \epsilon) \propto \begin{cases} \sum_{\mathrm{Im}(k_j)>0} v(k_j)^{-1}, & x \to x' + 0^+ \\ -\sum_{\mathrm{Im}(k_j)<0} v(k_j)^{-1}, & x \to x' - 0^+ \end{cases} \tag{2.54}$$

Continuity requires that both expressions are equal on both sides of the limit $x \to x'$. Indeed, this is true when we include all zeros of $f(k)$. In general:

$$\sum_j \frac{1}{f'(k_j)} = 0 \tag{2.55}$$

for any analytic function $1/f(k)$ with simple poles at k_j. In our case, $f'(k_j)$ corresponds to the group velocity $v(k_j)$.

Sketch of a proof. Let $p = \deg f(k) > 2$, and γ_R be a great circle with radius R in the complex k plane. From Jordan's lemma:

$$\left| \int_{\gamma_R} \frac{\mathrm{d}k}{f(k)} \right| \leq C \frac{2\pi R}{R^p} \xrightarrow{R\to\infty} 0. \tag{2.56}$$

On the other hand, we can calculate the integral using the residue theorem inside the contour γ_R. If k_j are simple poles of the function $1/f(k)$, we can write that $f(k) = (k - k_j)g(k)$ around $k = k_j$, with $g(k_j)$ being analytic and $f'(k_j) = g(k_j)$.

Then, the integral can be easily evaluated:

$$\int_{\gamma_R} \frac{\mathrm{d}k}{f(k)} = 2\pi i \sum_k \frac{1}{f'(k_k)}. \tag{2.57}$$

This immediately shows that

$$\sum_j \frac{1}{f'(k_j)} = 0. \tag{2.58}$$

It means that if one includes all poles of Green's function, it will be continuous at $x - x' = 0$. □

Coming back to our original problem, we may have 2 real and 2 complex poles of the Green's function. However, due to the square root function, there are also 2 branch cuts in the complex k plane. It turns out that the branch cuts lay closer to the real axis than the 2 complex solutions (conjugates of each other). The branch cuts may be found in the same way as cuts of the function $\sqrt{z^2+1}$. In our case, due to the presence of γ, δ and Ω, the cuts are parallel to the imaginary axis, from points $(-\delta/2\gamma, \pm i\Omega/2\gamma)$ to $(-\delta/2\gamma, \pm i\infty)$, so that, if they lay outside the $1/\ell_0$ strip, their contributions can be neglected.

2.5.2 Green's functions

In disordered systems, the characteristic length scale is set by ℓ, i.e. the mean free path. If, in our calculations, we are interested only in distances of the order of ℓ, we can approximate the Green's function using only the real poles. Then, the Green's function can be easily calculated. For the retarded Green's function, the k_+ (resp. k_-) pole has a positive (resp. negative) velocity v_+ (resp. v_-). It means that, when $x > x'$, the integral in Eq. (2.52) is computed using the k_+ pole (upper contour) and if $x < x'$ the k_- pole is used (lower contour):

$$G_0^R(x, x', \epsilon) = \begin{cases} -\frac{i}{\hbar v_+} e^{ik^+(x-x')}, & x - x' > 0 \\ -\frac{i}{\hbar v_-} e^{ik^-(x-x')}, & x - x' < 0 \end{cases}, \tag{2.59}$$

where v_- and v_+ are absolute values of $v(k_\pm)$. The advanced Green's function is

$$G_0^A(x', x, \epsilon) = \begin{cases} \frac{i}{\hbar v_+} e^{-ik^+(x-x')}, & x - x' > 0 \\ \frac{i}{\hbar v_-} e^{-ik^-(x-x')}, & x - x' < 0 \end{cases}. \tag{2.60}$$

As expected for Green's functions, $G_0^A = (G_0^R)^\dagger$, which translates into $G_0^A(x, x', \epsilon) = \left(G_0^R(x', x, \epsilon)\right)^*$. Note, however, that in systems with TRI, the Green's functions also obey $G^{R/A}(k, \epsilon) = G^{R/A}(-k, \epsilon)$ which is **not** true in our system.

In the following, we will also use $G_0^A(x', x, \epsilon - \hbar\omega)$, with $\omega \ll \epsilon$. To calculate it, we change only the phase factor of the Green's functions Eq. (2.60):

$$\begin{aligned} k^-(\epsilon - \hbar\omega) &\approx k^- + \frac{\omega}{v_-}, \\ k^+(\epsilon - \hbar\omega) &\approx k^+ - \frac{\omega}{v_+}. \end{aligned} \tag{2.61}$$

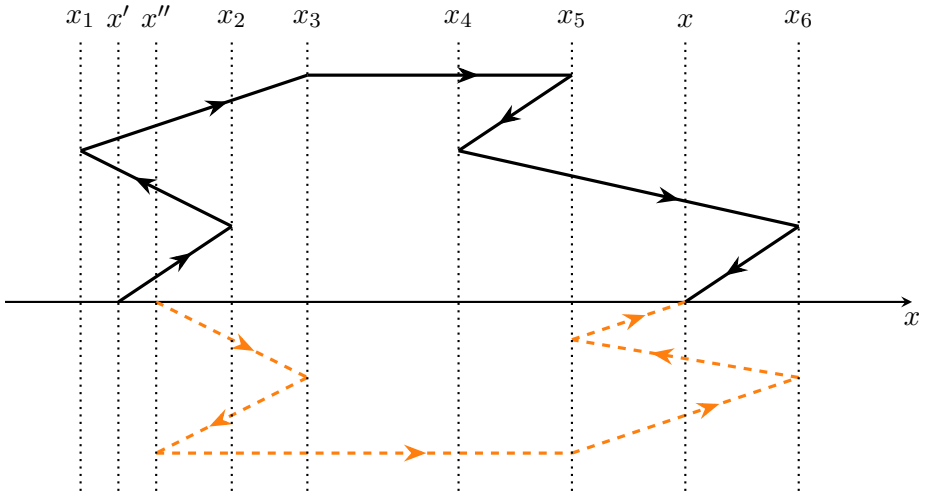

Figure 2.9. Example of a diagram contributing to $\overline{G^R(x,x',\epsilon)G^A(x'',x,\epsilon)}$. Solid lines represent G_0^R, dashed lines represent G_0^A, scattering events occur at points x_i. The vertical unfolding of the lines only allows for a convenient representation of the diagram, otherwise has no physical meaning.

so that

$$G_0^A(x',x,\epsilon-\hbar\omega)=\begin{cases}\frac{i}{\hbar v_+}e^{-i(k^+-\omega/v_+)(x-x')}, & x-x'>0\\ \frac{i}{\hbar v_-}e^{-i(k^-+\omega/v_-)(x-x')}, & x-x'<0\end{cases}. \tag{2.62}$$

The Green's functions clearly show that the evolution of a particle *from left to right* is controlled by the positive pole k_+ with the positive velocity, and *from right to left* by the negative one k_-. This introduces an asymmetry between the left and right directions of motion, what is expected in a system with broken TRI.

2.6 Berezinskii diagrammatic technique

Now, with explicit expressions for the free Green's functions, we can start the calculation of the average product of the retarded and advanced Green's functions. The studied problem is considered in a one-dimensional system and we can use a very powerful tool: the Berezinskii diagrammatic technique [4]. To evaluate the product $G^R(x,x',\epsilon)G^A(x'',x,\epsilon-\hbar\omega)$ we use the Born expansion Eq. (2.49) for both G^R and G^A, so that the G^RG^A involves only products of free Green's functions and potentials, that is multiply scattered paths.

The average product $\overline{G^R(x,x',\epsilon)G^A(x'',x,\epsilon-\hbar\omega)}$ includes all possible paths between points x' and x. In our approach, each contribution is represented as a diagram, see Fig. 2.9. Solid lines represent the free retarded Green's function and dashed lines depict the free advanced Green's functions. This way we can represent diagrammatically all terms appearing in the Born series, Eq. (2.49). The scattering events occur at the points x_i. For example, the top part of the diagram in Fig. 2.9 corresponds to a term with 6 scattering events and 7 free retarded Green's functions, whereas the bottom part to a term with 5 scattering events and 6 free advanced Green's functions.

However, we do not consider all possible diagrams. When disorder averaging is taken into account for the Gaussian δ-correlated potential, due to Wick's theorem, only diagrams whose scattering events are paired together contribute. An example of a diagram contributing to the averaged result

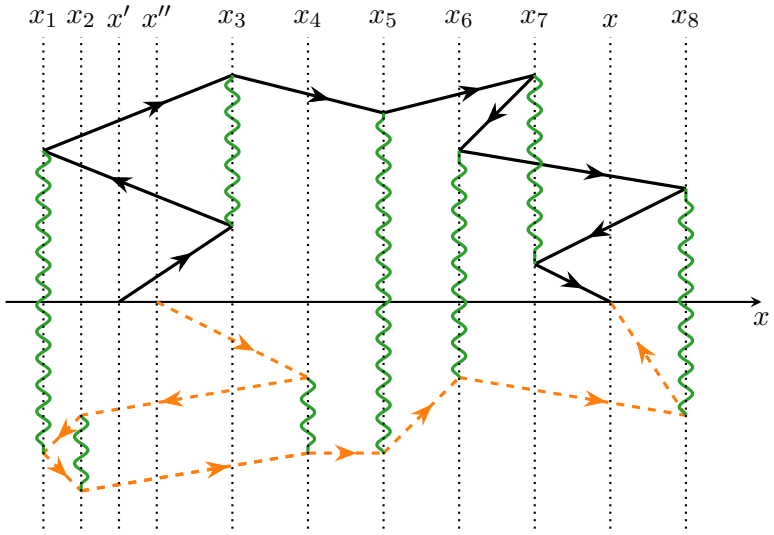

Figure 2.10. Diagram which contributes after disorder averaging, assuming δ-correlated Gaussian disorder. Solid lines represent G_0^R, dashed lines represent G_0^A, and the green lines are the correlation functions of the disordered potential.

is shown in Fig. 2.10. In the end, our aim is to sum all possible diagrams with nonzero contributions after the integration over x in Eq. (2.48).

In the diagrams, we assume that, for a given path connecting the initial point x' with the final point x, all scattering events happen at points x_i, $i = 1, \ldots, n$. Because we are in a one-dimensional system, these points can be ordered:

$$-\infty < x_1 \leq \ldots \leq x_i \leq x' \leq x_{i+1} \leq \ldots \leq x_j \leq x \leq x_{j+1} \leq \ldots \leq x_n < \infty. \tag{2.63}$$

Thanks to the ordering procedure, the signs of $x_i - x_j$ are fixed. The diagrams are built of the free propagators $G_0^{R/A}(x_j, x_i)$ and the correlation functions of the disorder at points x_i. The main idea of the Berezinskii diagrammatics is to transfer the factors from the lines to the scattering points, called *scattering vertices*. For example, if $x_i > x_j$, the free Green's function can be split:

$$G_0^R(x_i, x_j, \epsilon) = -\frac{i}{\hbar v_+} e^{ik_+(x_i - x_j)} = \sqrt{-\frac{i}{\hbar v_+}} e^{ik_+ x_i} \cdot \sqrt{-\frac{i}{\hbar v_+}} e^{-ik_+ x_j}, \tag{2.64}$$

where we formally associate the exponential factors to the vertices at points x_i and x_j. The difference between the TRI system and the unitary one is that the factors depend on the direction of movement. All possible situations are shown in Fig. 2.11. In the TRI system, the difference between propagation lines (a) and (b) reduces to a sign change of the phase factor. In our case, we have different velocities and phases. Nonetheless, the whole procedure is very similar, we have to analyze the initial and final points of the propagation lines, this time also taking into account their direction.

2.6.1 Initial vertices

To limit our analysis to the relevant diagrams, we start by selecting the appropriate initial vertices. In general, there are four possibilities presented in Fig. 2.12. The caption includes the

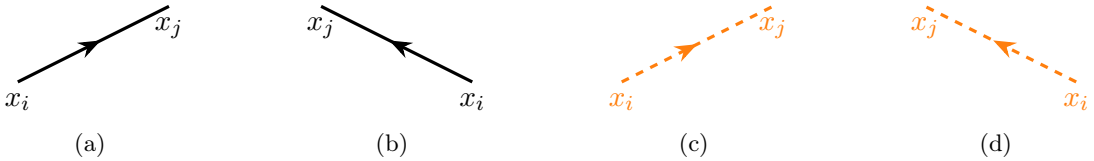

Figure 2.11. All possible propagation lines, where x_i is treated as the initial point in all situations. Expressions corresponding to the propagation lines: (a) $-\frac{i}{\hbar v_+}\exp(ik_+x_j)\exp(-ik_+x_i)$, (b) $-\frac{i}{\hbar v_-}\exp i(k_-x_j)\exp(-ik_-x_i)$, (c) $\frac{i}{\hbar v_+}\exp(-ik_+x_j)\exp(ik_+x_i)$, (d) $\frac{i}{\hbar v_-}\exp(-ik_-x_j)\exp(ik_-x_i)$

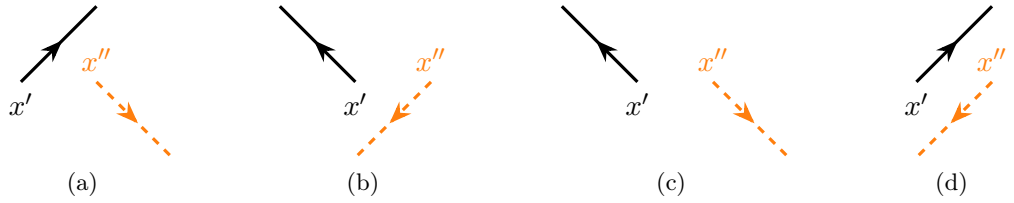

Figure 2.12. List of possible initial vertices. They correspond to factors:
(a) $(\hbar v^+)^{-1}\exp(ik^+(x''-x'))\exp(-i\omega x''/v^+)$, (b) $(\hbar v^-)^{-1}\exp(ik^-(x''-x'))\exp(i\omega x''/v^-)$,
(c) $(\hbar^2 v^- v^+)^{-1/2}\exp(i(k^+x''-k^-x'))\exp(-i\omega x''/v^+)$,
(d) $(\hbar^2 v^- v^+)^{-1/2}\exp(i(k^-x''-k^+x'))\exp(i\omega x''/v^-)$

factors corresponding to the vertices. Vertices (c) and (d) carry terms proportional to $\exp(i(k_\pm x''-k_\mp x'))$. Upon integration over the initial points (cf. Eq. (2.48)) and taking into account the initial states $\Psi_0(x')$, $\Psi_0^*(x'')$, they have a negligible contribution. Thanks to this, in the following, we consider only (a) and (b) as the possible initial vertices. They correspond to two different initial states of our system: the positive initial velocity (a) and the negative initial velocity (b). A similar analysis can be performed for the final vertices.

Further simplification is based on the assumption that no scattering happens between the initial points x' and x''. In the study of the TRI quantum boomerang effect [3], this assumption was justified by the fact that the initial state is much narrower than the mean free path. However, this assumption can be loosened and the same approach remains valid. There is no direct constraint on the relation between the wave packet width and the mean free path. Following the study of the TRI boomerang [2], we introduce $r = x' - x''$ and $\tilde{x} = (x' + x'')/2$. We see that the initial vertices Fig. 2.12 (a) and (b), in the limit $\omega \to 0$, can be approximated by similar vertices starting from a single point. This is visualized in Fig. 2.13. At the level of Green's functions this simplification

Figure 2.13. Graphical representation of simplification due to introduction of $r = x' - x''$ and $\tilde{x} = (x' + x'')/2$ in the limit of $\omega \to 0$.

takes the following form (cf. also [86]):

$$\overline{G^R(x,x',\epsilon)G^A(x'',x,\epsilon-\hbar\omega)} \approx e^{-ik_\pm r}\overline{G^R(x,\tilde{x},\epsilon)G^A(\tilde{x},x,\epsilon-\hbar\omega)}, \tag{2.65}$$

where k_+ is used for the vertex Fig. 2.12 (a) and k_- for Fig. 2.12 (b). We can plug this formula to Eq. (2.48):

$$\langle x(\omega)\rangle = \frac{1}{2\pi\hbar}\int \mathrm{d}x\,\mathrm{d}\tilde{x}\,\mathrm{d}r\,\mathrm{d}\epsilon\, x\, e^{-ik_\pm r}\overline{G^R(x,\tilde{x},\epsilon)G^A(\tilde{x},x,\epsilon-\hbar\omega)}\Psi_0(\tilde{x}+r/2)\Psi_0^*(\tilde{x}-r/2). \tag{2.66}$$

The r dependence can be integrated out using a prescription for the Wigner function (quasi-probability distribution) $W(\tilde{x},k)$:

$$\int_{-\infty}^{+\infty}\mathrm{d}r\, e^{-ik_\pm r}\Psi_0(\tilde{x}+r/2)\Psi_0^*(\tilde{x}-r/2) = 2\pi\hbar W(\tilde{x},k_\pm). \tag{2.67}$$

We end up with two Wigner's functions describing the two possible initial vertices associated with the different initial states:

$$\begin{aligned}\langle x_+(\omega)\rangle &= \int \mathrm{d}x\,\mathrm{d}\tilde{x}\,\mathrm{d}\epsilon\, x\underbrace{W(\tilde{x},k_+)}_{\text{vertex (a)}}\overline{G^R(x,\tilde{x},\epsilon)G^A(\tilde{x},x,\epsilon-\hbar\omega)}\\ \langle x_-(\omega)\rangle &= \int \mathrm{d}x\,\mathrm{d}\tilde{x}\,\mathrm{d}\epsilon\, x\underbrace{W(\tilde{x},k_-)}_{\text{vertex (b)}}\overline{G^R(x,\tilde{x},\epsilon)G^A(\tilde{x},x,\epsilon-\hbar\omega)}\end{aligned} \tag{2.68}$$

In the final simplification, we use a trick where we introduce the spectral function $A(\epsilon,k)$ [86]. In the weak disorder limit, we can safely use the free spectral function:

$$A(\epsilon,k) = \delta(\epsilon-\epsilon_k) = (\hbar v_+)^{-1}\delta(k-k_+) + (\hbar v_-)^{-1}\delta(k-k_-). \tag{2.69}$$

Then

$$W(\tilde{x},k_+) = \hbar v_+\int_\alpha^{+\infty}\mathrm{d}k\, W(\tilde{x},k)A(\epsilon,k), \quad W(\tilde{x},k_-) = \hbar v_-\int_{-\infty}^{\alpha}\mathrm{d}k\, W(\tilde{x},k)A(\epsilon,k), \tag{2.70}$$

where α is an arbitrary constant such that $k_- < \alpha < k_+$. It is used only to split the contributions of k_+ and k_- (e.g. if k_+ and k_- have opposite signs one may use $\alpha = 0$). This allows us to arrive at a formula very similar to the TRI case. If we use the initial state with positive velocity, i.e. $W(\tilde{x},k) = \hbar^{-1}\delta(\tilde{x})\delta(k-k_+)$ we end up with:

$$\langle x_+(\omega)\rangle = v_+\int \mathrm{d}x\, x\,\overline{G^R(x,0,\epsilon_0)G^A(0,x,\epsilon_0-\hbar\omega)}, \tag{2.71}$$

where ϵ_0 is the energy of the initial state. In this final formula, simplified by the analysis of relevant initial vertices, we are left with the average product of retarded and advanced Green's functions. Thanks to the statistical translational invariance, the integrand depends only on the relative position of the initial and final points. To simplify the next steps in the analysis, we will keep the initial

point $\tilde{x}$ in the the integral:

$$\langle x_+(\omega)\rangle = v_+ \int \mathrm{d}(x-\tilde{x})\,(x-\tilde{x})\,\overline{G^R(x,\tilde{x},\epsilon_0)G^A(\tilde{x},x,\epsilon_0-\hbar\omega)}, \tag{2.72}$$

and treat $(x-\tilde{x})$ as a single variable. In order to calculate this integral, we will now analyze the structure of the diagrams.

2.6.2 Calculation of the diagrams

Scattering vertices

In general, we would like to sum all significant diagrams to evaluate $\overline{G^R G^A}$. This task cannot be done directly. Let us reconsider the diagram presented in Fig. 2.10. The diagrams can be divided into intervals between consecutive scattering events, i.e. intervals between x_i and x_{i+1}. Each interval has a specific number of lines inside. There are in total 4 kinds of lines: retarded lines (in two directions) and advanced lines (also in two directions).

The numbers of lines are denoted as g_+, g_-, $(g_+)'$, and $(g_-)'$ respectively. For example, the interval between points x' and x_3 in Fig. 2.10 has the following set of lines $(2,1,2,1)$. The intervals are separated by scattering events which may change the number of lines. Each scattering vertex makes a definite change of respective lines, which we denote $\Delta g_\pm$ (retarded lines) and $(\Delta g_\pm)'$ (advanced lines).

The vertices with nonzero phases are negligible due to disorder averaging: different phases average to zero. Each incoming and outgoing G_0^R line from a vertex at point x carries a phase depending on the direction of the line and its type (in/out). Every incoming (outgoing) *positive* line, i.e. propagating to the right, carries a ik_+x ($-ik_+x$ respectively) phase. For the negative (i.e. propagating to the left) lines, the phases for incoming and outgoing lines are $-ik_-x$ and ik_-x respectively. For advanced lines, the phases are complex conjugates.

For single line vertices involving only retarded Green's functions, the phase of a scattering vertex is calculated from the total change of the number of lines, i.e. $\pm i(\Delta g_+ k_+ x - \Delta g_- k_- x)$. The condition for *phaselessness* of the vertex in the limit of $\omega \to 0$ is that the total numbers of incoming and outgoing lines (of each type) have to be equal, that is $\Delta g_\pm = 0$. This condition is very similar to the one found in [3, 4, 20, 22, 86]. However, in our system, k_+ and k_- do not cancel each other.

In the case of the mixed-line vertices, involving both G_0^R and G_0^A, the problem is slightly different: lines from G_0^R and G_0^A may cancel each other. The total phase of a vertex is

$$i\left((\Delta g_+ - (\Delta g_+)')k_+ - (\Delta g_- - (\Delta g_-)')k_-\right)x.$$

This means that the phaseless vertices are only if $\Delta g_\pm = (\Delta g_\pm)'$.

The scattering vertices also have to keep the solid and dashed lines continuous. The list of possible phaseless scattering vertices is shown in Fig. 2.14. Each vertex corresponds to a well defined factor

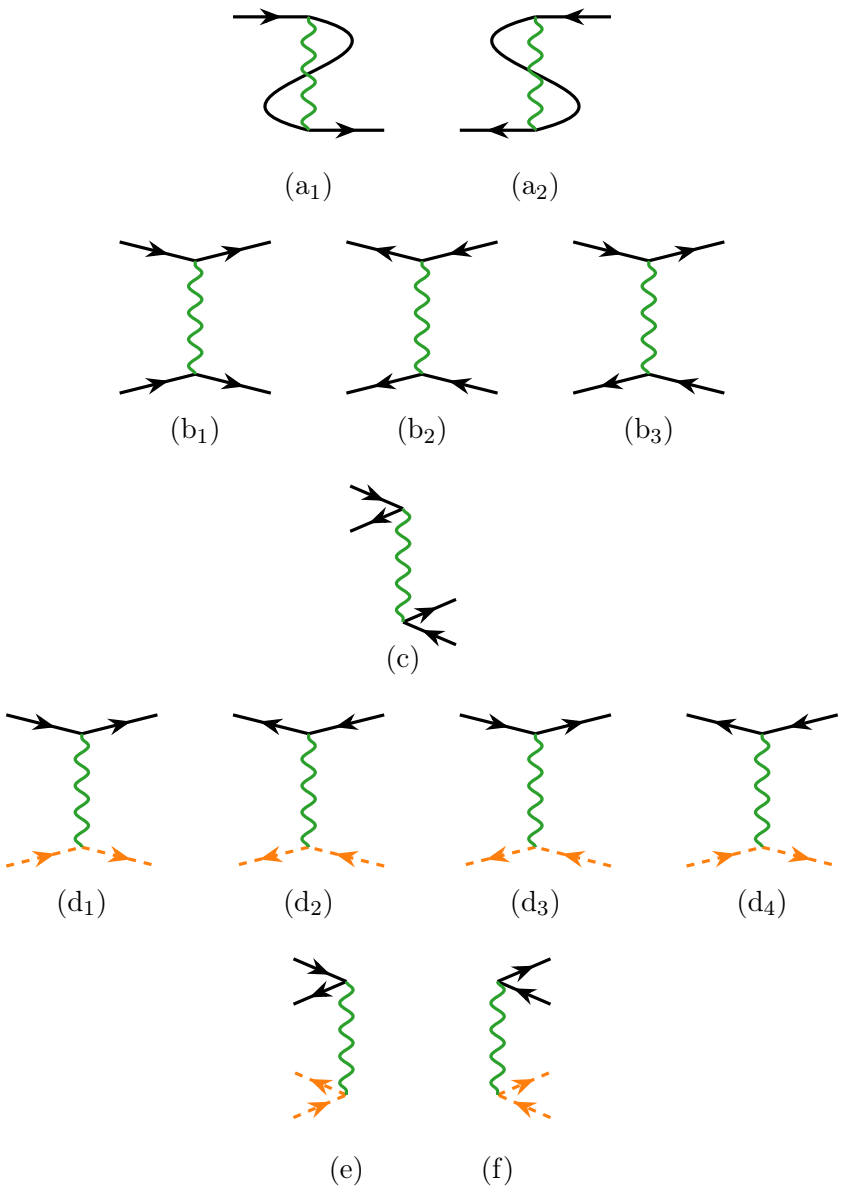

Figure 2.14. All possible phaseless scattering vertices. Vertices from (a), (b), and (c) families have also dashed-lines counterparts. The weights associated to the vertives are written in Eq. (2.73).

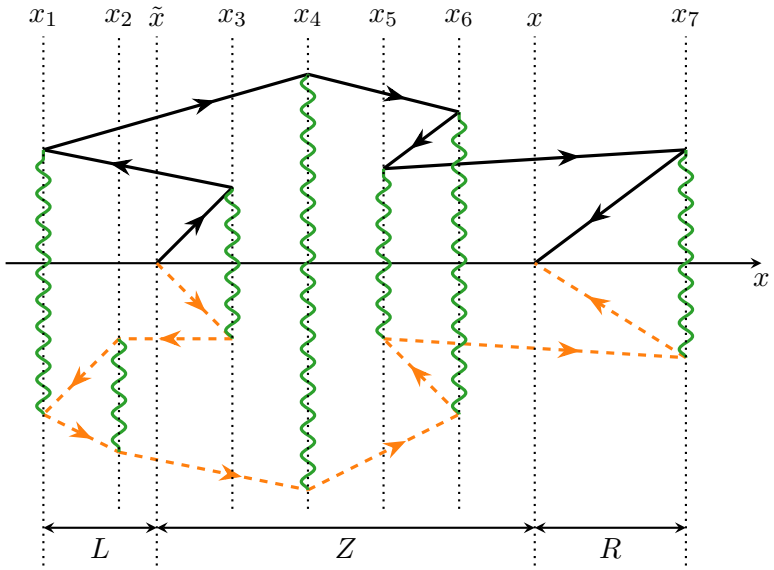

Figure 2.15. An example of a diagram contributing to $\overline{G^R G^A}$ built from the vertices presented in Fig. 2.14. The diagram is divided into L, Z, and R parts at points $\tilde{x}$ and x.

based on the scattering type. The weights are:

$$\mathrm{a}_1 : -\frac{V_0^2}{(\hbar v^+)^2}, \quad \mathrm{a}_2 : -\frac{V_0^2}{(\hbar v^-)^2},$$

$$\mathrm{b}_1 : -\frac{V_0^2}{(\hbar v^+)^2}, \quad \mathrm{b}_2 : -\frac{V_0^2}{(\hbar v^-)^2}, \quad \mathrm{b}_3 : -\frac{V_0^2}{(\hbar v^+)(\hbar v^-)}$$

$$\mathrm{c} : -\frac{V_0^2 |{}_-\langle\uparrow \mid \uparrow\rangle_+|^2}{(\hbar v^+)(\hbar v^-)},$$

$$\mathrm{d}_1 : \frac{V_0^2}{(\hbar v^+)^2}, \quad \mathrm{d}_2 : \frac{V_0^2}{(\hbar v^-)^2}, \quad \mathrm{d}_3 : \frac{V_0^2}{(\hbar v^+)(\hbar v^-)}, \quad \mathrm{d}_4 : \frac{V_0^2}{(\hbar v^+)(\hbar v^-)},$$

$$\mathrm{e} : \frac{V_0^2 |{}_-\langle\uparrow \mid \uparrow\rangle_+|^2}{(\hbar v^+)(\hbar v^-)} \exp\left(i\omega x \left(\frac{1}{v^+} + \frac{1}{v^-}\right)\right), \quad \mathrm{f} : \frac{V_0^2 |{}_-\langle\uparrow \mid \uparrow\rangle_+|^2}{(\hbar v^+)(\hbar v^-)} \exp\left(-i\omega x \left(\frac{1}{v^+} + \frac{1}{v^-}\right)\right). \tag{2.73}$$

Vertices (c), (e), and (f) have double backscattering events. It means that, in the spin system, the weights include a spin state overlap factor $|{}_-\langle\uparrow \mid \uparrow\rangle_+|^2 = \kappa$. Vertex (a) represents an *in place* scattering event, that is $G_0^{R/A}(x_i, x_{i-1}, \epsilon) V(x_i) G_0^{R/A}(x_i, x_i, \epsilon) V(x_i) G_0^{R/A}(x_{i+1}, x_i, \epsilon)$.

Equations

From this point, to lighten the notations, we put $\hbar = 1$.

Knowing all possible scattering vertices relevant for our problem, we can write down the equations describing the diagrams. For a moment, we will assume that $\tilde{x} < x$. Each diagram contributing to the final sum may be divided into L, Z, and R parts, like it is done in Fig. 2.15. The parts of the diagram are characterized by the total number of incoming and outgoing solid and dashed lines. Because the scattering vertices change the number of lines by at most 2, we know that the L and R parts always have $g_\pm = (g_\pm)' = m$ lines attached . Thus, we denote $g = g_+ + g_-$ and

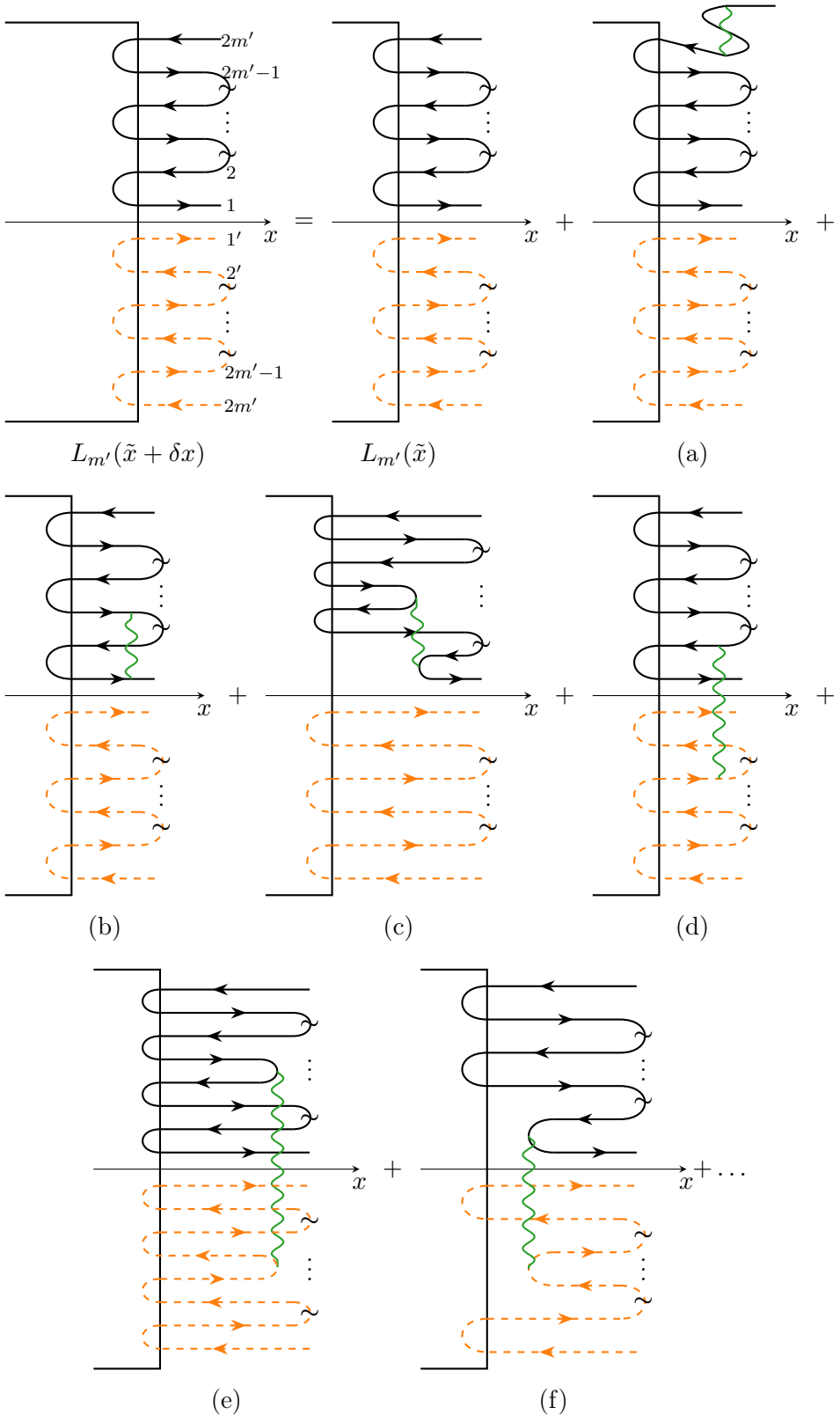

Figure 2.16. Schematic representation of Eq. (2.74). $L_{m'}(\tilde{x}+\delta x)$ can be constructed with $L_{m'}(\tilde{x})$ and all possible combinations of the scattering vertices. The figure shows one example for each scattering vertex.

$(g)' = (g_+)' + (g_-)'$ and for the left and right parts $g = (g)' = 2m$. For example, for L in Fig. 2.15 we have $g = (g)' = 2$.

The central block Z has one additional line which "connects" points x' and x, so its direction depends on the sign of $x - x'$. In total, Z has $g = (g)' = 2m + 1$ lines at each boundary. However, these numbers may differ between the boundaries, for example, the Z block from Fig. 2.15 has $g = (g)' = 3$ at the left boundary, while $g = (g)' = 1$ at the right boundary.

As the next step in the calculation, we denote by $L_{m'}(\tilde{x})$ the sum of contributions from all left-hand L parts that have the right boundary at the point $\tilde{x}$ with $g = 2m'$ lines. Analogously, by $R_m(x)$ we denote the sum of right-hand contributions R which have the left boundary at point x with $g = 2m$ lines. The central part contributions are gathered under $Z_{m',m}(\tilde{x}, x)$ where the left boundary has $g = 2m' + 1$ lines and the right one has $g = 2m + 1$.

Now, to calculate $L_{m'}(\tilde{x})$, we consider how it changes with an infinitesimal change of the boundary position, say $\tilde{x} \to \tilde{x} + \delta x$ by adding all possible contributions from different scattering vertices. For this purpose, we number the lines on the boundary by assigning consecutive numbers to the outgoing and incoming lines, as presented in Fig. 2.16. The figure also shows a schematic way of adding new vertices to the diagram. Then, we count all possibilities of adding new vertices to $L_{m'}(\tilde{x})$, bearing in mind that the lines cannot create loops nor cross each other. Finally, we get the following equation:

$$\begin{aligned}
L_{m'}(\tilde{x} + \delta x) &= L_{m'}(\tilde{x}) + V_0^2 \delta x L_{m'}(\tilde{x}) \left[-\frac{2m'}{v_+^2} - \frac{2m'}{v_-^2} \right] \\
&+ V_0^2 \delta x L_{m'}(\tilde{x}) \left[-\frac{m'(m'-1)}{v_+^2} - \frac{m'(m'-1)}{v_-^2} - \frac{2m'^2}{v_+ v_-} - \frac{2\kappa m'(m'-1)}{v_+ v_-} + \frac{m'^2}{v_+^2} + \frac{m'^2}{v_-^2} + \frac{2m'^2}{v_+ v_-} \right] \\
&+ \frac{\delta x V_0^2 \kappa}{v_+ v_-} \left[m'^2 L_{m'+1}(\tilde{x}) e^{i\omega\tilde{x}(\frac{1}{v_+} + \frac{1}{v_-})} + m'^2 L_{m'-1}(\tilde{x}) e^{-i\omega\tilde{x}(\frac{1}{v_+} + \frac{1}{v_-})} \right].
\end{aligned} \tag{2.74}$$

After taking the limit $\delta x \to 0$ and some simplifications:

$$\begin{aligned}
\frac{\mathrm{d}L_{m'}(\tilde{x})}{\mathrm{d}x'} = &- V_0^2 L_{m'}(\tilde{x}) \left[\frac{m'}{v_+^2} + \frac{m'}{v_-^2} + \frac{2\kappa m'(m'-1)}{v_+ v_-} \right] + \\
&\frac{V_0^2 \kappa m'^2}{v_+ v_-} \left[L_{m'+1}(\tilde{x}) e^{i\omega\tilde{x}(\frac{1}{v_+} + \frac{1}{v_-})} + L_{m'-1}(\tilde{x}) e^{-i\omega\tilde{x}(\frac{1}{v_+} + \frac{1}{v_-})} \right].
\end{aligned} \tag{2.75}$$

This equation can be solved under the form of $L_{m'}(\tilde{x}) = e^{-i\omega m'\tilde{x}(\frac{1}{v_+} + \frac{1}{v_-})} L_{m'}$, where $L_{m'}$ does not depend on $\tilde{x}$. We find the algebraic equation for $L_{m'}$:

$$\left(-\frac{v_+^2 + v_-^2 - 2\kappa v_+ v_-}{\kappa v_+ v_-} + \frac{i\omega(v_+ + v_-)}{\kappa V_0^2} \right) L_{m'} + m' \Big(L_{m'+1} + L_{m'-1} - 2L_{m'} \Big) = 0. \tag{2.76}$$

In other words, L_m satisfies:

$$sL_m + m(L_{m+1} + L_{m-1} - 2L_m) = 0, \tag{2.77}$$

(a) $\Gamma_{+,\cdot}$ (b) $\Gamma_{-,\cdot}$ (c) $\Gamma_{\cdot,+}$ (d) $\Gamma_{\cdot,-}$

Figure 2.17. Possible initial and final vertices, after all simplifications. Their weights are as follows: (a) $\Gamma_{+,\cdot} = (\hbar v_+)^{-1}\exp(-i\omega\tilde{x}/v_+)$; (b) $\Gamma_{-,\cdot} = (\hbar v_-)^{-1}\exp(i\omega\tilde{x}/v_-)$; (c) $\Gamma_{\cdot,+} = (\hbar v_+)^{-1}\exp(i\omega x/v_+)$; (d) $\Gamma_{\cdot,-} = (\hbar v_-)^{-1}\exp(-i\omega x/v_-)$

where

$$s = -\frac{v_+^2 + v_-^2 - 2\kappa v_+ v_-}{\kappa v_+ v_-} + \frac{i\omega(v_+ + v_-)}{\kappa V_0^2}. \tag{2.78}$$

The equation for L_m is the same as in the TRI case [3], and the full solution is given in [22]:

$$L_m(s) = -s\,\Gamma(m+1)\Psi(m+1, 2; -s), \tag{2.79}$$

where $\Psi(a, b; z)$ is the confluent hypergeometric function of the second kind. The right blocks $R_m(x)$ are found to obey $R_m(x) = L_m(-x)$ with the same $R_m = L_m$.

In the TRI system, L_m satisfies Eq. (2.77) but with $s_{\mathrm{TRI}} = 2i\omega v_0/V_0^2$, where v_0 is the velocity of the state with the energy ϵ_0 in the TRI system. The main difference is that the s_{TRI} is fully imaginary, while in our case s has a finite real part. However, when $\omega \gg 1$, the real part of s can be neglected and does not influence the final result.

The equation for $Z_{m',m}$ is a little more involving. For the outer parts L and R the numbers of left and right lines are equal. This has to be true simply because if the particle line goes into R_m it must also go out (and vice versa). On the other hand, the central part $Z_{m',m}$ has in total $2m'+1$ and $2m+1$ lines, the one extra line has a direction determined by the sign of $x - \tilde{x}$. It introduces a kind of asymmetry because our vertices differentiate left and right lines. Here, we use the assumption that $\tilde{x} < x$, so the additional line is going from left to right (see Fig. 2.15). Furthermore, the total derivative of $Z_{\cdot,m}(x)$ with respect to x has to include also the ending vertex (or initial vertex for $Z_{m',\cdot}(\tilde{x})$). Formally

$$\frac{\mathrm{d}Z_{\cdot,m}(x)}{\mathrm{d}x} = \frac{\mathrm{d}Z_{\cdot,m}(x)}{\mathrm{d}x}\bigg|_{\text{"vertex"}} \cdot Z_{\cdot,m}(x)\Big|_{\text{"body"}} + Z_{\cdot,m}(x)\Big|_{\text{"vertex"}} \cdot \frac{\mathrm{d}Z_{\cdot,m}(x)}{\mathrm{d}x}\bigg|_{\text{"body"}}. \tag{2.80}$$

The "vertex" derivative depends on the type of the vertex: final or initial and the velocity associated. The list of all possible initial and final vertices is shown in Fig. 2.17. The "body" derivative is calculated in the same manner as the derivative for $L_m(x)$, by counting all scattering vertex contributions.

For example, the derivative calculated at the right border, assuming that $\tilde{x} < x$, and taking the

vertex to be $\Gamma_{\cdot,\pm}$:

$$\begin{aligned}\frac{\mathrm{d}Z_{\cdot,m}(x)}{\mathrm{d}x} =& \pm\frac{i\omega}{v_\pm}Z_{\cdot,m}(x) - \gamma Z_{\cdot,m}(x)\left[\frac{m+1}{v_+^2}+\frac{m}{v_-^2}+\frac{2m^2\kappa}{v_+v_-}\right]\\ &+\frac{\gamma\kappa}{v_+v_-}\left[m^2 Z_{\cdot,m-1}e^{-i\omega x(\frac{1}{v_+}+\frac{1}{v_-})}+(m+1)^2 Z_{\cdot,m+1}e^{i\omega x(\frac{1}{v_+}+\frac{1}{v_-})}\right].\end{aligned} \tag{2.81}$$

If $\tilde{x} > x$, which means that there are more lines going to the left, only the expression in the first bracket changes:

$$\begin{aligned}\frac{\mathrm{d}Z_{\cdot,m}(x)}{\mathrm{d}x} =& \pm\frac{i\omega}{v_\pm}Z_{\cdot,m}(x) - \gamma Z_{\cdot,m}(x)\left[\frac{m}{v_+^2}+\frac{m+1}{v_-^2}+\frac{2m^2\kappa}{v_+v_-}\right]\\ &+\frac{\gamma\kappa}{v_+v_-}\left[m^2 Z_{\cdot,m-1}e^{-i\omega x(\frac{1}{v_+}+\frac{1}{v_-})}+(m+1)^2 Z_{\cdot,m+1}e^{i\omega x(\frac{1}{v_+}+\frac{1}{v_-})}\right].\end{aligned} \tag{2.82}$$

Of course, in such a case with $\tilde{x} > x$, we may also need to adjust the vertex derivative, depending on its type. When $v_- = v_+$ and $\kappa = 1$, all these equations reduce to the TRI solution, reproducing the results found in [3].

Unfortunately, we are not aware of any analytic solution for the recursion relation Eq. (2.82). This is, however, not a major obstacle, a quasi-analytic calculation of the quantum boomerang effect being possible, as shown in the next section.

2.6.3 How to compute $\langle x(t)\rangle$?

We can now compute $\langle x(\omega)\rangle$ using Eq. (2.71) and the weights of diagrams computed in section 2.6.2. To gather all possible diagrams, we divide them into 4 families, $\Gamma_{\pm,\pm}(x,\tilde{x})$, where $\pm$ denote the initial/final vertices $\Gamma_{\pm,\pm}$ (see Fig. 2.17). The connection between $\Gamma_{\pm,\pm}(x,\tilde{x})$ and L, Z and R is not completely trivial – it depends on the sign of $x-\tilde{x}$. To distinguish different objects, we introduce another index: $\Gamma^{\tilde{x}<x}_{\pm,\pm} = \Gamma_{\pm,\pm}(\tilde{x},x)$ and $\Gamma^{\tilde{x}>x}_{\pm,\pm} = \Gamma_{\pm,\pm}(x,\tilde{x})$. Here we will focus on $\Gamma^{\tilde{x}<x}_{+,+}$, which is a contribution of diagrams with the initial and the final positive velocities and $\tilde{x} < x$:

$$\Gamma^{\tilde{x}<x}_{+,+} = \sum_{\substack{m=0,\\ m'=0}}^{\infty} L_{m'}(\tilde{x})Z_{m',m}(\tilde{x},x)R_m(x). \tag{2.83}$$

A simple analysis shows that the similar contribution for $\tilde{x} > x$ is slightly different:

$$\Gamma^{\tilde{x}>x}_{+,+} = \sum_{\substack{m=0,\\ m'=0}}^{\infty} L_{m'+1}(x)Z_{m',m}(x,\tilde{x})R_{m+1}(\tilde{x}). \tag{2.84}$$

Now, we are ready to compute the $\langle x_+\rangle^{\tilde{x}<x}_+$ contribution. Because the weights of the initial and final vertices are not included into L, Z or R, we also have to take into account the weight of the $\Gamma_{+,+} = v_+^{-2}$:

$$\langle x_+(\omega)\rangle^{\tilde{x}<x}_+ = \frac{v_+}{v_+^2}\int_0^\infty \mathrm{d}(x-\tilde{x})\,(x-\tilde{x})\Gamma^{\tilde{x}<x}_{+,+} = \frac{2\ell_t}{v_+}\sum_{m'} L_{m'}S^0_{m'}, \tag{2.85}$$

where to get $S^0_{m'}$ we use the definition of $\Gamma^{\tilde{x}<x}_{+,+}$:

$$\sum_{m'} L_{m'} S^0_{m'} = \frac{1}{2\ell_t}\int_0^\infty \mathrm{d}(x-\tilde{x})\,(x-\tilde{x}) \sum_{m,m'} L_{m'}(\tilde{x}) Z_{m',m}(\tilde{x},x) R_m(x), \tag{2.86}$$

from which we infer that

$$S^0_{m'} = \frac{1}{2\ell_t}\sum_m \int_0^\infty \mathrm{d}(x-\tilde{x})\,(x-\tilde{x}) e^{-i\omega m'\tilde{x}\left(\frac{1}{v_-}+\frac{1}{v_+}\right)} Z_{m',m}(\tilde{x},x) R_m(x) \tag{2.87}$$

To simplify the integral, we introduce [4]

$$\nu = \omega \frac{v_+ + v_-}{\kappa V_0^2} \tag{2.88}$$

such that

$$S^0_{m'} = \frac{1}{2\ell_t}\sum_m \int_{-\infty}^x \mathrm{d}\tilde{x}\,(x-\tilde{x}) e^{-i\nu m'\tilde{x}/2\ell_t} Z_{m',m}(\tilde{x},x) e^{i\nu m x/2\ell_t} R_m, \tag{2.89}$$

and we have changed the variables of the integration. We will not calculate this integral directly. Instead, using the derivative of $Z_{m',m}(\tilde{x},x)$ we want to find an iterative equation for $S^0_{m'}$. We briefly sketch the idea behind the calculation of the equation for $S^0_{m'}$.

Here, we start by expanding the integral from Eq. (2.89) using integration by parts:

$$\int f\mathrm{d}g\, h\mathrm{d}\tilde{x} = (fgh) - \int \mathrm{d}f\, gh\mathrm{d}\tilde{x} - \int fg\mathrm{d}h\,\mathrm{d}\tilde{x}\,, \tag{2.90}$$

where we take

$$f = x-\tilde{x}, \quad g = \frac{2\ell_t}{-i\nu m'} e^{-i\nu m'\tilde{x}/2\ell_t}, \quad h = Z_{m',m}(\tilde{x},x) e^{i\nu m x/2\ell_t} R_m. \tag{2.91}$$

After performing the expansion, it suffices to sum both sides over $1/2\ell_t \sum_m$ to get the desired iterative relation:

$$2\ell_t Q^0_{m'} + i\nu\left(m' + \frac{v_-}{v_+ + v_-}\right) S^0_{m'} - 2\ell_t V_0^2 \beta^+_{m'} S^0_{m'} + (m')^2 S^0_{m'-1} + (m'+1)^2 S^0_{m'+1} = 0, \tag{2.92}$$

where $Q^0_{m'}$ is defined in the following way:

$$Q^0_{m'} = \frac{1}{2\ell_t}\sum_m \int_{-\infty}^x \mathrm{d}\tilde{x}\, e^{-i\nu m'\tilde{x}/2\ell_t} Z_{m',m}(\tilde{x},x) e^{i\nu m x/2\ell_t} R_m, \tag{2.93}$$

and it obeys its own iterative equation (calculated in a similar way to Eq. (2.92)):

$$R_{m'} + i\nu\left(m' + \frac{v_-}{v_+ + v_-}\right) Q^0_{m'} - 2\ell_t V_0^2 \beta^+_{m'} Q^0_{m'} + (m')^2 Q^0_{m'-1} + (m'+1)^2 Q^0_{m'+1} = 0. \tag{2.94}$$

The same concept can be applied to $\langle x_+(\omega)\rangle^{\tilde{x}>x}_+$, where we denote the S^0 and Q^0 counterparts by

4. Note when $\omega \gg 1$, $i\nu$ is equal to s from Eq. (2.77).

S^1 and Q^1. Their equations are found:

$$\begin{aligned} -2\ell_t Q^1_m + i\nu\Big(m + \frac{v_+}{v_- + v_+}\Big) S^1_m - 2\ell_t V_0^2 \beta^-_m S^1_m + m^2 S^1_{m-1} + (m+1)^2 S^1_{m+1} = 0, \\ R_{m+1} + i\nu\Big(m + \frac{v_+}{v_- + v_+}\Big) Q^1_m - 2\ell_t V_0^2 \beta^-_m Q^1_m + m^2 Q^1_{m-1} + (m+1)^2 Q^1_{m+1} = 0, \end{aligned} \tag{2.95}$$

The m-dependent factors $\beta^\pm_m$ come from the derivatives of $Z_{m',m}(\tilde{x}, x)$:

$$\begin{aligned} \beta^+_m &= \frac{m+1}{v_+^2} + \frac{m}{v_-^2} + \frac{2\kappa m^2}{v_- v_+} \\ \beta^-_m &= \frac{m}{v_+^2} + \frac{m+1}{v_-^2} + \frac{2\kappa m^2}{v_- v_+} \end{aligned} \tag{2.96}$$

Similar equations can be calculated for $\Gamma^{\tilde{x}<x}_{+-}$ and $\Gamma^{\tilde{x}>x}_{+-}$. This time:

$$\Gamma^{\tilde{x}<x}_{+-} = \sum_{\substack{m=0,\\ m'=0}}^{\infty} L_{m'}(\tilde{x}) Z_{m',m}(\tilde{x}, x) R_{m+1}(x), \quad \Gamma^{\tilde{x}>x}_{+-} = \sum_{\substack{m=0,\\ m'=0}}^{\infty} L_{m'}(x) Z_{m',m}(x, \tilde{x}) R_{m+1}(\tilde{x}) \tag{2.97}$$

The variables connected with $\langle x_+(\omega)\rangle_-$ are called S^2, Q^2 and S^3 and Q^3. Because all equations are akin to Eqs. (2.92), (2.94), we do not write all of them in the main text of the thesis.
In total, we can write that the complete solution is given by:

$$\begin{aligned} \langle x_+(\omega)\rangle_+ &= \frac{2\ell_t}{v_+} \sum_m \left(L_m S^0_m + L_{m+1} S^1_m\right), \\ \langle x_+(\omega)\rangle_- &= \frac{2\ell_t}{v_-} \sum_m \left(L_m S^2_m + L_m S^3_m\right). \end{aligned} \tag{2.98}$$

The problem is reduced to finding a solution of the equations for the families of S and Q. Up to our best knowledge, there are no known fully analytic solutions for these quantities. However, we can take advantage of the fact that both S and Q can be expanded in powers of $1/\nu$ and compute $\langle x(t)\rangle$ as a time series. The details of this calculation and a comment on $\beta^\pm_m$ are presented in appendix 2.B.

In the calculation of $\langle x(t)\rangle$ in the TRI system [2, 3] the final result depends only on L_m and Q_m. Our equations have an extra quantity, S_m. Additionally, Q_m and S_m consist of four families (denoted by the upper index) instead of two. There are two main reasons for this difference. The first is due to the fact that we calculate the center of mass directly, see Eq. (2.45), instead of using the Ehrenfest theorem. This step means that we have an additional term, $(x - \tilde{x})$, in the integral, see for example Eq. (2.89). If this term was absent, there would be only Q_m in the final formula. The second difference comes from the fact, that in the TRI system, there are connections between the families of diagrams $\Gamma_{\pm\pm}(x, \tilde{x})$. They reduce the total number of different quantities needed for the final formula.

2.6.4 Center of mass $\langle x(t)\rangle$

Finally, we have the desired result: the time evolution of both components of the total center of mass in the form of a time series. Without any loss of generality, we focus on the solutions for the

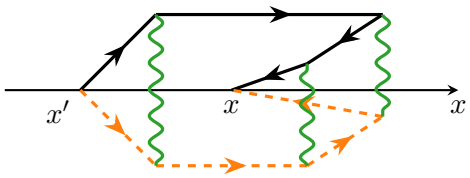

Figure 2.18. Diagram constructed using scattering vertices (d), (e), and (f). With three or more scattering vertices, it is possible to construct diagrams which are not included in the Boltzmann approximation.

positive initial velocity. To simplify the notation, we use $v_+ = v$ and $v_- = \Delta \cdot v$, so that the time series is expressed only in the terms of Δ

$$\Delta = \frac{v_-}{v_+}, \tag{2.99}$$

and the characteristic time and length scales. The results are given by:

$$\begin{aligned}
\frac{\langle x_+(t)\rangle_+}{v\tau} &= \frac{t}{\tau} - \frac{1}{1+\Delta}\left(\frac{t}{\tau}\right)^2 + \frac{3-\Delta}{6(1+\Delta)}\left(\frac{t}{\tau}\right)^3 + \frac{\Delta(\Delta+1)\left(\Delta\left(\Delta^2+\Delta-3\right)-7\right)-2}{12(\Delta+1)^5}\left(\frac{t}{\tau}\right)^4 + \mathcal{O}\left(t^5\right) \\
\frac{\langle x_+(t)\rangle_-}{v\tau} &= \frac{1-\Delta}{2(1+\Delta)}\left(\frac{t}{\tau}\right)^2 - \frac{1-\Delta}{3(1+\Delta)}\left(\frac{t}{\tau}\right)^3 + \frac{\Delta(9-\Delta(\Delta(3\Delta(\Delta+3)+8)-8))+3}{24(\Delta+1)^5}\left(\frac{t}{\tau}\right)^4 + \mathcal{O}\left(t^5\right)
\end{aligned} \tag{2.100}$$

The solutions agree up to third order with the Boltzmann predictions, Eqs. (2.25):

$$\begin{aligned}
\frac{\langle x_+(t)\rangle_+^{\text{Boltz.}}}{v\tau} &= \frac{t}{\tau} - \frac{1}{1+\Delta}\left(\frac{t}{\tau}\right)^2 + \frac{3-\Delta}{6(1+\Delta)}\left(\frac{t}{\tau}\right)^3 + \frac{\Delta-2}{12(1+\Delta)}\left(\frac{t}{\tau}\right)^4 + \mathcal{O}(t^5) \\
\frac{\langle x_+(t)\rangle_-^{\text{Boltz.}}}{v\tau} &= \frac{1-\Delta}{2(1+\Delta)}\left(\frac{t}{\tau}\right)^2 - \frac{1-\Delta}{3(1+\Delta)}\left(\frac{t}{\tau}\right)^3 + \frac{1-\Delta}{8(1+\Delta)}\left(\frac{t}{\tau}\right)^4 + \mathcal{O}(t^5)
\end{aligned} \tag{2.101}$$

The same behavior was observed in the calculation of $\langle x(t)\rangle$ in the TRI case [3]. The reason is the following: the whole set of scattering vertices, shown in Fig. 2.14, allows for a construction of diagrams which are not included into the classical solution obtained with the ladder diagrams [7]. All Boltzmann-type diagrams can be obtained using vertices (d), (e), and (f). However, even this restricted set of scattering vertices allows for the construction of diagrams not included in the Boltzmann approximation. To build such a diagram, there have to be at least three scattering events, meaning that the quantum correction should appear at fourth order in the time series. A diagram built of the vertices (d) and (e), contributing to the quantum correction, is presented in Fig. 2.18.

Similarly to the TRI boomerang study [3], the time series has a finite radius of convergence. In the TRI case, the radius was numerically found to be $t_{\text{conv.}} = 4\tau$, where τ is the scattering mean free time. In our study, we do not analyze the convergence in detail. Nonetheless, from our results it seems that the radius slightly depends on the value of Δ, i.e the ratio of the velocities. Figure 2.19 shows the comparison of the numerical data, the Boltzmann, and the quantum solution (calculated up to $(t/\tau)^{11}$ order). Similarly to the TRI results, all curves agree very well for very short times. Then the quantum solution deviates due to the finite radius of convergence. Nevertheless, we note

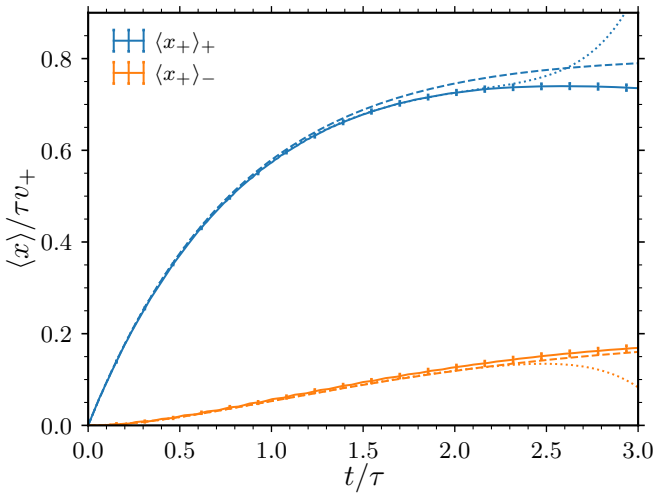

Figure 2.19. Comparison of the numerical results (solid lines with error bars), Boltzmann solutions (dashed lines), Eq. (2.25) and the short-time quantum solution $\Delta = 2/3$ (dotted lines), Eq. (2.100) for $\langle x_+(t)\rangle_+$ and $\langle x_+(t)\rangle_-$, plotted for very short times. In this time regime, the classical and quantum solutions almost do not differ and agree very well with the numerical data.

that the classical solution is an excellent approximation at very short times.

There is an important question: is there, similarly to the TRI system, universality for the center of mass time dependence? From the classical solution in our system, cf. Eq. (2.21), we have seen that the $\langle x\rangle$ curve does not depend on the ratio of velocities[5]. The quantum solution, $\langle x_+\rangle = \langle x_+\rangle_+ + \langle x_+\rangle_-$, agrees with the classical solution up to the third order, similarly to the TRI case:

$$\begin{aligned}\frac{\langle x_+(t)\rangle}{v\tau} &= \frac{t}{\tau} - \frac{1}{2}\left(\frac{t}{\tau}\right)^2 + \frac{1}{6}\left(\frac{t}{\tau}\right)^3 - \frac{\Delta(\Delta(\Delta(\Delta+4)+8)+4)+1}{24(\Delta+1)^4}\left(\frac{t}{\tau}\right)^4 + \mathcal{O}(t^5)\\ \frac{\langle x_+(t)\rangle^{\text{Boltz.}}}{v\tau} &= \frac{t}{\tau} - \frac{1}{2}\left(\frac{t}{\tau}\right)^2 + \frac{1}{6}\left(\frac{t}{\tau}\right)^3 - \frac{1}{24}\left(\frac{t}{\tau}\right)^4 + \mathcal{O}(t^5)\end{aligned} \tag{2.102}$$

However, all terms starting from fourth order depend on Δ. This breaks the universality of the $\langle x\rangle$ curve in the quantum solution. In other words, the dependence of $\langle x_+(t)\rangle/v\tau$ versus t/τ, which is universal in the TRI system, here depends on the additional parameter $\Delta = v_-/v_+$. The TRI time series is fully recovered when $\Delta = 1$ is used.

We should also note that the time series has the same form when $\Delta \to \Delta^{-1}$ (up to a constant factor). In the numerical data, we have seen that the sum of contributions does not depend on the choice of the initial state (up to the total sign). This bevahior is expected and proven by the theory.

To describe the center of mass time evolution beyond the short-time regime, following the same idea as in [3], we use a Padé approximant. It is clear that the long-time scaling should be the same as in the TRI system, that is, $\langle x(t \gg \tau)\rangle \sim t^{-2}$ with some unknown constants. This is also supported

5. In fact τ depends on the velocities, however here we are considering an explicit dependence on the ratio of the velocities.

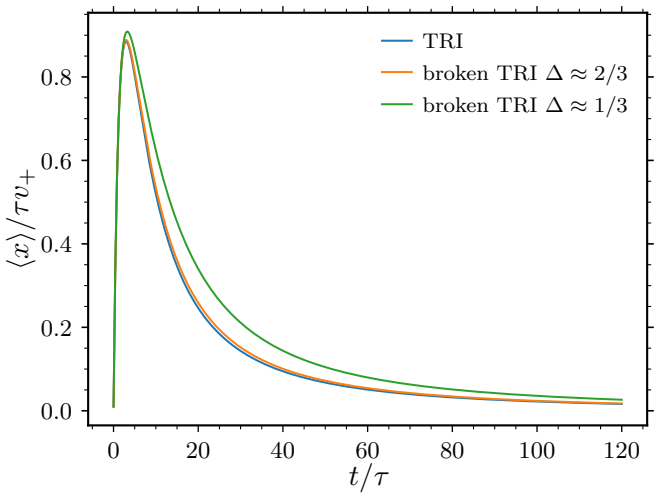

Figure 2.20. Comparison of the Padé approximated quantum results for the TRI system (blue line) and broken TRI systems with different values of velocities ratio $\Delta = v_-/v_+$ ($\Delta = 2/3$ orange line, $\Delta = 1/3$ green line).

by the numerical evidence. In our approach, we compute the center of mass as:

$$\frac{\langle x(t)\rangle}{\tau v_\pm} = \left(\frac{\tau}{t}\right)^2 \lim_{n\to\infty} R_n(t), \tag{2.103}$$

where $R_n(t)$ is a diagonal Padé approximant, whose coefficients are calculated from the short-time Taylor series. To obtain high accuracy of the approximation, we use $n = 30$, but there is no visible difference between results obtained with lower n, for example $n = 20$. For practical purposes, the calculation of $R_n(t)$ is done for each studied value of Δ separately – full symbolic calculations are cumbersome and do not bring any added value.

Figure 2.20 shows resulting curves of $\langle x(t)\rangle$ for the TRI system and the spin-orbit system for two different values of Δ. One can immediately see that the difference between the TRI result and our result for $\Delta = 2/3$, which approximately describes our system investigated numerically, is extremely small. Due to the finite size of statistical errors, such curves may not be distinguishable using numerical data. A bigger difference between the spin-orbit and TRI systems is visible for a much higher (or lower) ratio of the velocities, showing that in fact the quantum solution is not universal.

We finish the section with a comparison of the theoretical solution with the numerical data. Figure 2.21 presents the results for both initial states. In this case, we performed a slight refitting of the theoretical prediction to the data. From previous works [3, 84], it is known that the *boomerang curves* need a very high number of disorder realizations to have small statistical error bars. Moreover, the theoretical approach is valid in the weak disorder limit, $k\ell \gg 1$, where the mean free path is rather large, requiring large system sizes. This makes the numerical simulations difficult and extremely time consuming. However, to see the agreement between the data and the theoretical predictions, we do not have to make such simulations.

The net difference in the results appears as a difference between the exact mean free time and length (present in the simulations) and their values calculated with the Born approximation (used in the theoretical calculations). It means that the difference can be captured using a simple adjustment

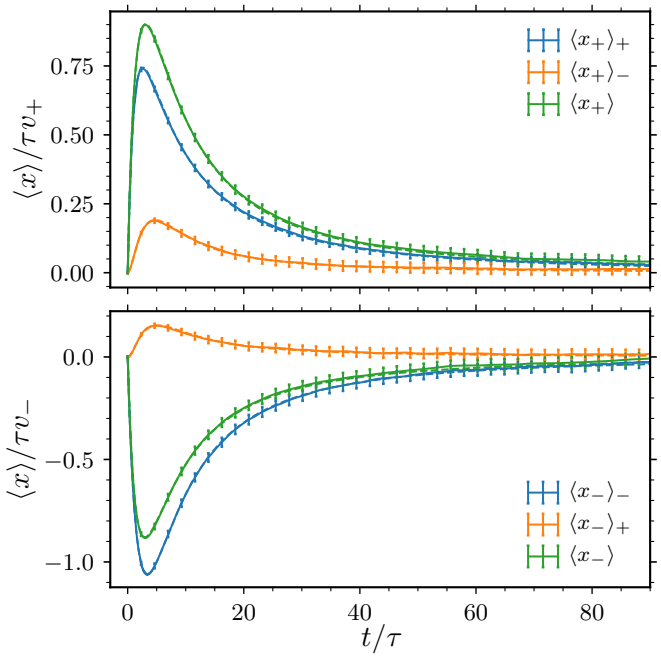

Figure 2.21. Comparison of the quantum solutions (dashed lines) with the numerical data (solid lines with error bars) for both possible initial states. Theoretical curves are subjected to a small adjustment procedure to account for differences between the exact scattering mean free time and its value computed with the Born approximation (details in the main text). The theoretical and numerical results overlap almost perfectly. The result shows that the boomerang effect is fully present in a system without time reversal invariance, and that we have a quasi-exact theoretical prediction which **works extremely well**.

of the time and length scales. We use this approach in Fig. 2.21. The rescaling is done using a fitting procedure, which also includes weights based on the statistical errors. The fitted parameters differ from the values computed with the Born approximation on the order of few %. For the positive velocity, where $k_+(\tau v_+) \approx 120$:

$$\begin{aligned} \langle x_+ \rangle : &\qquad \tau_{\text{fit}} = 1.03\tau, \quad \ell_{\text{fit}} = 1.015\tau v_+ \\ \langle x_+ \rangle_+ : &\qquad \tau_{\text{fit}} = 1.04\tau, \quad \ell_{\text{fit}} = 1.01\tau v_+ \\ \langle x_+ \rangle_- : &\qquad \tau_{\text{fit}} = 1.03\tau, \quad \ell_{\text{fit}} = 1.07\tau v_+ \end{aligned} \tag{2.104}$$

For the negative velocity, $k_-(\tau v_-) \approx 45$:

$$\begin{aligned} \langle x_- \rangle : &\qquad \tau_{\text{fit}} = 0.99\tau, \quad \ell_{\text{fit}} = 0.99\tau v_+ \\ \langle x_- \rangle_+ : &\qquad \tau_{\text{fit}} = 1.13\tau, \quad \ell_{\text{fit}} = 0.87\tau v_+ \\ \langle x_- \rangle_- : &\qquad \tau_{\text{fit}} = 1.01\tau, \quad \ell_{\text{fit}} = 1.00\tau v_+ \end{aligned} \tag{2.105}$$

The corrections performed for the backscattered contributions are slightly higher than for the forward scattered contributions. The backscattered components are intrinsically of higher order than the forward components, hence the larger difference between the exact and Born parameters is expected. After these small corrections, the agreement between the theory and the numerical data is almost perfect. The final result shows that the boomerang effect not only survives the breaking of TRI, but also the time evolution of the center of mass can be captured theoretically, using similar, albeit somewhat generalized, tools.

Discussion of broad wave packets

Initially, in the theoretical calculations, we have assumed that the initial size of the wave packet is smaller than the scattering mean free path. In the TRI system, it is known that the initial width of the wave packet may be larger than the scattering mean free path [2]. In our numerical simulations, anticipating that this could be true also in the spin-orbit system, we have used an initial width σ only slightly smaller than τv_+ and τv_-. Indeed, the same idea as in the TRI system can be used to relax the assumption on the initial width of the wave packet.

We follow here the same reasoning as in [2]. If we assume that the average density profile is given by the average density propagator $P(x,t)$ and the initial state density $|\Psi_0(x)|^2$:

$$\overline{|\psi(x,t)|^2} = \int \mathrm{d}\tilde{x}\, P(x-\tilde{x},t)|\Psi_0(\tilde{x})|^2. \tag{2.106}$$

The propagator $P(x-\tilde{x},t)$ represents the average probability of particle initially at point $\tilde{x}$ reaching x at time t. The density $|\psi(x,t)|^2$ is then used to compute the center of mass position. The change of variables $x' = \tilde{x} - x$ shows that the width of the initial density does not play any role in the calculation of the center of mass.

2.6.5 The four-state scenario – return to the origin.

In our study of the quantum boomerang effect in the system without TRI, we do not analyze in detail the case with more than 2 possible momentum states. Even though, our preliminary numerical

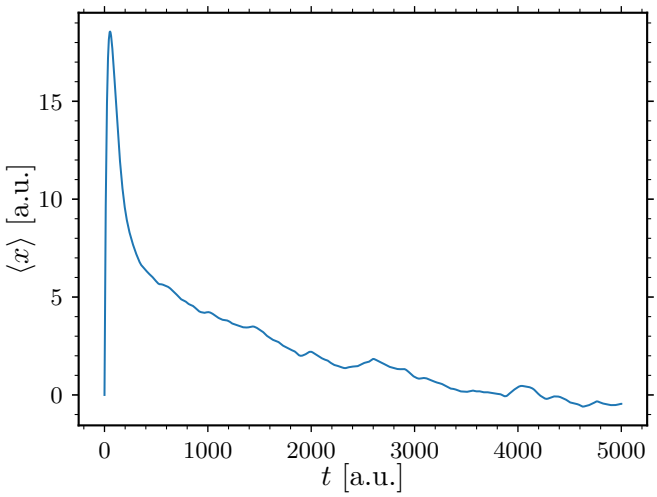

Figure 2.22. Preliminary results for temporal evolution of the center of mass computed for a 4-state scenario. The values of parameters $\delta = \Omega = 5E_{\mathrm{R}}/\hbar$ are the same as in the 2-state analysis. The energy is $E = 9.375E_{\mathrm{R}}$ and $V_0 = 1.875E_{\mathrm{R}}$ (the same as in Fig. 2.5) and there are two eigenstates from the lower band and two eigenstates from the upper band. The initial state is constructed similarly to the two component case. Here, we chose the initial momentum $k_4 = 1.71k_{\mathrm{R}}$ with velocity $v_4 = 2.64\gamma$ (corresponding to red curve in Fig. 2.5 (b)). The center of mass undergoes more complicated dynamics, nonetheless the preliminary result suggests a full return to the origin.

results indicate that the return to the origin is still present. This hints the possibility of studying the boomerang effect in even more complicated systems. A preliminary result is shown in Fig. 2.22.

Nonetheless, the presence of more momentum states at a given energy introduces many difficulties. The higher number of scattering channels makes the analysis of mean free times, and Green's functions much more complicated. For sure, the diagrammatic approach should consist of many new vertices making the Berezinskii technique additionally complex.

We have observed that, with states from the lower and upper bands involved, even a rather weak disorder mixes additional states, making numerical simulations more difficult.

2.7 The final density

The last part of our study of the TRI broken system is the analysis of the localization length and the final state spatial density. Although the mean free path can be estimated from the spectral function, we calculate the localization length directly. This way we avoid the errors related to the Born approximation and may check if the localization length is given by $\xi_{\mathrm{loc}} = 2\ell_t$ in the spin-orbit system. This is a prediction of DMPK equation [87, 88] for a single scattering channel situation, i.e. two-state approximation, for details see [89].

2.7.1 Recursive Green's function method

To compute numerically the localization length ξ_{loc}, we use the recursive Green's function method proposed by MacKinnon and Kramer [90–92]. The method was successfully used in many theoretical works, see, for example [93–95]. We briefly explain the method and compare its prediction with the

result of our study. Let us consider a one-dimensional tight-binding nearest neighbor Hamiltonian

$$\mathcal{H} = \sum_{i,j} H_{i,j} \left|i\right\rangle \left\langle j\right| = \begin{pmatrix} H_{1,1} & V_1 & & \\ V_1^* & H_{2,2} & V_2 & \\ & V_2^* & H_{3,3} & \ddots \\ & & \ddots & \ddots \end{pmatrix} \tag{2.107}$$

where $|i\rangle$ represents the state on a regular lattice at site i. The system may be divided into two parts: for sites $1, \ldots, N$ and for site $N+1$. This way we can construct the Green's function describing the whole system and the Green's function for the site $N+1$. The Green's function of the central region is such that [92]:

$$(E + i0^+ - H_{i,j})G_{i,j} - H_{i,j+1}G_{i+1,j} - H_{i,i-1}G_{i-1,j} = \delta_{i,j}, \tag{2.108}$$

where E is the energy. Now, consider a lattice with the total length N. If we add another site, then the *new* Hamiltonian will consist of three parts:

$$\mathcal{H} = H_{i,j} + (V_N + V_N^*) + H_{N+1,N+1} \tag{2.109}$$

where $V_N = H_{N,N+1}$ is the off-diagonal part coupling the Nth site to $(N+1)$th site. Here we assume that the coupling between the sites is the same for all sites, $V_N = V$. To calculate the Green's function for the $(N+1)$ site system, we start with the Dyson's equation:

$$G_{i,j}^{(N+1)} = G_{i,j}^{(N)} + G_{i,N}^{(N)} \, V \, G_{N+1,j}^{(N+1)}. \tag{2.110}$$

The upper index denotes the total number of sites in the system. This equation simply means that if we know the Green's function for a system of length N, and we know the coupling between the system and the newly added site, we can compute the Green's function for the larger system. In particular, for $j = N+1$ we get:

$$G_{i,N+1}^{(N+1)} = G_{i,N+1}^{(N)} + G_{i,N}^{(N)} \, V \, G_{N+1,N+1}^{(N+1)} = G_{i,N}^{(N)} \, V \, G_{N+1,N+1}^{(N+1)}. \tag{2.111}$$

The first term vanishes because it represents a connection between sites i and $N+1$ in a N site system. Now, if we consider Eq. (2.108) for $i = j = N+1$ we get

$$\left(E + i0^+ - H_{N+1,N+1}^{(N+1)}\right) G_{N+1,N+1}^{(N+1)} - V^* \, G_{N,N+1}^{(N+1)} = 1. \tag{2.112}$$

The final simplification comes from Eq. (2.111) with $i = N$. Together with Eq. (2.111), but this time for $i = 1$, we end up with two equations allowing an iterative calculation of the Green's functions:

$$\begin{aligned} G_{1,N+1}^{(N+1)} &= G_{1,N}^{(N)} \, V \, G_{N+1,N+1}^{(N+1)}, \\ G_{N+1,N+1}^{(N+1)} &= \left(E + i0^+ - H_{N+1,N+1}^{(N+1)} - V^* \, G_{N,N}^{(N)} V\right)^{-1}. \end{aligned} \tag{2.113}$$

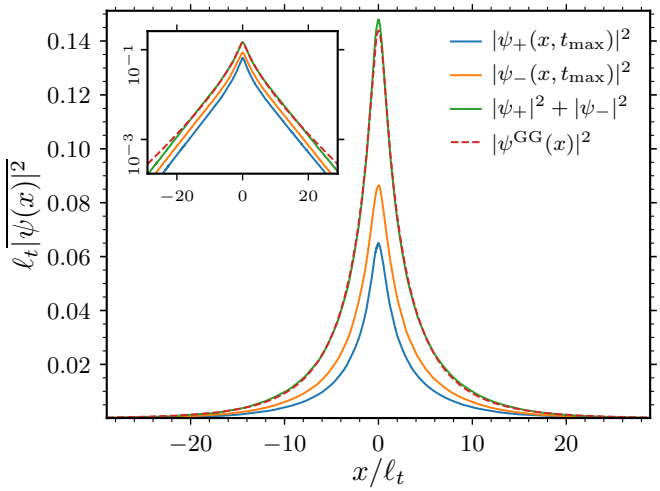

Figure 2.23. Comparison of the final density profile ($t_{\max} = 90\tau$) of the initial state with positive velocity, and the Gauss-Gogolin profile given by Eq. (2.116). The inset shows the same quantities plotted in a logarithmic scale. The agreement is excellent, the tiny difference in the wings will disappear at longer time.

To calculate the localization length, we start with the observation that the transmission of the system is $|G_{1,N}|^2$. The inverse localization length is given by:

$$\xi_{\mathrm{loc}}^{-1} = -\lim_{L\to\infty} \frac{\ln|G_{1,N}(L)|^2}{L}, \tag{2.114}$$

where L is the length of the system. Within this approach, the typical transmission is proportional to $\exp(-L/\xi_{\mathrm{loc}})$. Thanks to the theorems by Furstenberg and Oseledets [96, 97], this quantity is self-averaging, meaning that the propagation of the Green's function over very large systems has a similar result to averaging over different disorder realizations.

In practice, the iterative procedure used in the calculations can be implemented very efficiently. The method may be easily generalized to quasi-one-dimensional systems, see, for example [98]. In the spin-orbit case, the objects used in the calculations are 2×2 matrices. The length of the system can be easily extended even up to 10^9 sites giving very precise results.

In a weakly disordered TRI one-dimensional system, the localization length is simply given by 2 transport mean free paths, $\xi_{\mathrm{loc}} = 2\ell$ [14]. In our simulation scenario, the transport mean free path is $\ell_t = v_+\tau_+ = v_-\tau_-$ is $\ell_t = 34.57/k_{\mathrm{R}}$. The localization length calculated from the recursive Green's function method is $\xi_{\mathrm{loc}} = (69.72 \pm 0,008)/k_{\mathrm{R}}$. This result confirms that in our system, in the 2-state scenario, the localization length is given by 2 transport mean free paths [6], $\xi_{\mathrm{loc}} = 2\ell_t$. The small difference between the numerical values is caused by higher order corrections.

2.7.2 Wave packet density at long time

The full return of the wave packet to its initial position in TRI systems also means that its infinite-time density profile is symmetric around $x = 0$. In the case of an initially well localized wave

6. In the one-dimensional TRI system with isotropic scattering the transport mean free path and scattering mean free path are equal.

packet, this infinite-time density is the Gogolin profile [20], parametrized by the mean free path ℓ:

$$\overline{|\psi_\ell^{\text{Gogolin}}(x, t=\infty)|^2} = \int_0^\infty \frac{\mathrm{d}\eta\, \pi^2}{32\ell} \frac{\eta(1+\eta^2)^2 \sinh(\pi\eta) e^{-(1+\eta^2)|x|/8\ell}}{(1+\cosh(\pi\eta))^2}, \tag{2.115}$$

Our numerical simulations extend up to $t_{\max} = 90\tau$. Naturally, this value is far from the infinite-time limit, but the maximal time should be sufficient to observe that the final density converges to the infinite-time profile. For the reason that our initial state is a Gaussian wave packet, the final density profile is not the Gogolin profile, but a convolution of the Gogolin profile with a Gaussian, which we call Gauss-Gogolin profile:

$$\overline{|\psi^{\text{GG}}(x)|^2} = \frac{1}{\sqrt{\pi\sigma^2}} \int_{-\infty}^{+\infty} \mathrm{d}x'\, e^{-(x-x')^2/\sigma^2} \overline{|\psi_\ell^{\text{Gogolin}}(x')|^2}. \tag{2.116}$$

The Gauss-Gogolin profile is parametrized both by the mean free path and the initial width of the Gaussian wave packet σ. Figure 2.23 shows the final density for the forward and backward scattered components of the wave function, as well as their sum together with the Gauss-Gogolin profile calculated for $\sigma = 20/k_{\text{R}}$ and $\ell_t = 34.57/k_{\text{R}}$. The agreement between the data and the theoretical profile is excellent. The inset shows the same plot on a logarithmic scale where tiny deviations can be seen – we attribute them to the finite time of the simulation. The figure presents data for the initial positive velocity, but the results for the negative velocity initial state are exactly the same. Once again, we observe a similar behavior as in the TRI case. Independently of the initial velocity, the final wave function density is symmetric around $x = 0$. We should note that the original Gogolin profile was calculated in the TRI system with the help of the Berezinskii technique [20]. This indicates that the same result could be obtained using our diagrams.

2.8 Conclusion

In this chapter, we have studied the quantum boomerang effect in a system where TRI and all anti-unitary symmetries are broken. We have analyzed the problem both in the classical and quantum approaches. The classical solution is very alike the classical one in the TRI system: after the initial ballistic motion, the wave packet localizes at a finite distance. The simulations of the quantum system with broken TRI and all anti-unitary symmetries have shown that the quantum boomerang effect is present in the system. In the simulation, we have used a $\mathcal{PT}$-symmetric initial state, so that our analysis has directly probed the influence of TRI of the Hamiltonian on the quantum boomerang effect.

By generalizing the Berezinskii diagrammatic technique to a system without TRI, we have computed the time evolution of the center of mass in a quasi-analytic way. The result predicts a full boomerang effect, that is, the return of the wave packet to its origin. The analytical and numerical results show an excellent agreement. Even though the original diagrammatics have been modified to some extent, similar concepts in the solutions have been used. Finally, we have also shown that the final density profile almost perfectly agrees with our theoretical prediction.

The lack of time reversal symmetry plays no role in the existence of the quantum boomerang effect. Even in a truly unitary system, the wave packet with nonzero initial velocity returns to the initial point. Our result shows that as long as the initial state has $\mathcal{PT}$ symmetry (cf. sec-

tion 1.3.3), time reversal symmetry is not necessary for the phenomenon to occur, which generalizes and somewhat contradicts the conclusions of [21].

Our analysis showing that the boomerang exists in systems without TRI means also that the quantum boomerang effect is not fully understood. Originally, TRI was used to prove the boomerang effect existence. This means that we are lacking a simple explanation why just the Anderson localization is needed for the quantum boomerang effect. This should be the primary perspective for future work.

Another interesting direction for future studies would be to study higher-dimensional systems, where it is known that, above some energy, the states are no longer localized. It would be very interesting to use the presence of the boomerang as a tool for pinpointing the transition position (similarly to TRI three-dimensional system [3]). Our study is mainly focused on the single scattering channel system, so it could be desired to extend the diagrammatic approach to systems with more scattering channels.

Appendix 2.A *Discussion:* energy spacings, mean gap ratio, and symmetry classes

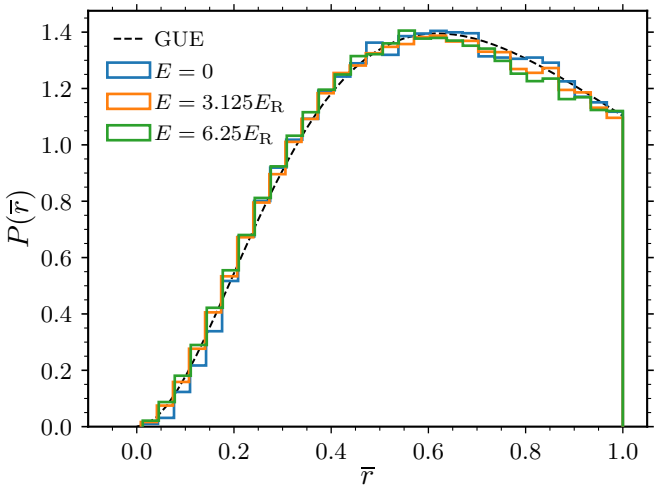

Figure 2.24. Numerically calculated distributions $P(\overline{r})$ of gap ratio, Eq. (2.118) computed in the spin-orbit system with $\delta = \Omega = 5E_R/\hbar$, around different energies: $E = 0$, $E = 3.125E_R$ and $E = 6.25E_R$. Black dashed line shows the theoretical distribution for the GUE symmetry class, Eq. (2.119). Independently of energy, the numerical distributions are in very good agreement with the theoretical curve.

Symmetry properties of quantum systems can be analyzed using the spectral properties of the Hamiltonian [99–101]. Level spacing distributions may fall into one of several classes of Gaussian matrix ensembles. This may give a hint about the symmetries. In our case, we know that the system breaks TRI, hence one would expect the statistics to follow the Gaussian Unitary Ensemble (GUE). It means that the spacing distribution should be given approximately by (for details, see [80, 102, 103]):

$$P(s) = \frac{32}{\pi^2} s^2 e^{-4s^2/\pi}, \tag{2.117}$$

where s are spacings normalized to unity $s = (E_{i+1} - E_i)/\Delta$, with Δ the mean spacing. Direct comparison between numerical spacings and theoretical prediction is not an easy task because the normalization of the spacings is obtained through a procedure called unfolding. It is possible to avoid the unfolding by computing the gap ratio $\overline{r}_n$ as defined in [104, 105]:

$$\overline{r}_n = \min\left(r_n, \frac{1}{r_n}\right), \quad r_n = \frac{\delta_n}{\delta_{n-1}}, \tag{2.118}$$

where δ_n is the spacing between neighbouring energy levels. This may be also used to calculate the mean gap ratio $\langle\overline{r}\rangle$, i.e. the average value around a chosen energy in the spectrum. The full analysis of $\langle\overline{r}\rangle$ for our system is beyond the scope of the present appendix [7].

Still, we would like to show that, even if the complete analysis may be very complicated, it is possible to support our prediction about the symmetry class of the system. Taking into account our

7. The detailed study of the mean gap ration for one- and two-dimensional Anderson model was presented in [106]. Recently, the problem was revisited in [107, 108] where one-dimensional Anderson and Aubry-André models were considered.

theoretical investigation of symmetries, one could expect that the distribution of the gap ratio will reproduce the GUE prediction (see [105]):

$$P_{\mathrm{GUE}}(\overline{r}) = \frac{81\sqrt{3}}{2\pi}\frac{(r+r^2)^2}{(1+r+r^2)^4}. \tag{2.119}$$

We calculate numerically distributions of $\overline{r}$ in the spin-orbit system with $\delta = \Omega = 5E_{\mathrm{R}}/\hbar$ (the same values as used to study the dynamics of the center of mass) and disorder strength $V_0 = 3.125E_{\mathrm{R}}$, where an uncorrelated uniform distribution of the disorder has been used. The results have been averaged over 5000 disorder realizations. Figure 2.24 presents the distributions obtained around three different energies, $E = 0$, $E = 3.125E_{\mathrm{R}}$ and $E = 6.25E_{\mathrm{R}}$, and a comparison with the theoretical GUE distribution, Eq. (2.119). Clearly, the numerical distributions agree with the theoretical curve. All of them show a characteristic quadratic bevahior for small values of $\overline{r}$.

The very good agreement between the numerical distributions and the theoretical GUE distribution supports our claim that the studied Hamiltonian belongs to the unitary symmetry class.

Appendix 2.B Calculation of the time series $\langle x(t)\rangle$

2.B.1 Equations for different types of diagrams

In section 2.6.3 we give the full equations for the $\Gamma^{\tilde{x}<x}_{+,+}$ and $\Gamma^{\tilde{x}>x}_{+,+}$ contributions to the center of mass. Below we also add the equations used to calculate $\langle x_+\rangle_-$. Equations for $\Gamma^{\tilde{x}<x}_{+-}$:

$$\begin{aligned} 2\ell_t Q_m^2 + i\nu\Big(m+\frac{v_-}{v_-+v_+}\Big)S_m^2 - 2\ell_t\gamma\beta_m^+ S_m^2 + m^2 S_{m-1}^2 + (m+1)^2 S_{m+1}^2 = 0 \\ R_{m+1} + i\nu\Big(m+\frac{v_-}{v_-+v_+}\Big)Q_m^2 - 2\ell_t\gamma\beta_m^+ Q_m^2 + m^2 Q_{m-1}^2 + (m+1)^2 Q_{m+1}^2 = 0 \end{aligned} \tag{2.120}$$

Equations for $\Gamma^{\tilde{x}>x}_{+-}$:

$$\begin{aligned} -2\ell_t Q_m^3 + i\nu\Big(m+\frac{v_+}{v_-+v_+}\Big)S_m^3 - 2\ell_t\gamma\beta_m^- S_m^3 + m^2 S_{m-1}^3 + (m+1)^2 S_{m+1}^3 = 0 \\ R_{m+1} + i\nu\Big(m+\frac{v_+}{v_-+v_+}\Big)Q_m^3 - 2\ell_t\gamma\beta_m^- Q_m^3 + m^2 Q_{m-1}^3 + (m+1)^2 Q_{m+1}^3 = 0 \end{aligned} \tag{2.121}$$

where $\nu = (v_- + v_+)\omega/\kappa V_0^2$, and

$$\begin{aligned} \beta_m^+ &= \frac{m+1}{v_+^2} + \frac{m}{v_-^2} + \frac{2\kappa m^2}{v_- v_+} \\ \beta_m^- &= \frac{m}{v_+^2} + \frac{m+1}{v_-^2} + \frac{2\kappa m^2}{v_- v_+} \end{aligned} \tag{2.122}$$

2.B.2 Solution for short time: large ω expansion

The full center of mass position $\langle x(t)\rangle$ can be written as a time series with coefficients χ_n:

$$\langle x(t)\rangle = \sum_{n=1}^{\infty}(-1)^{n+1}\chi_n\left(\frac{t}{\tau}\right)^n. \tag{2.123}$$

The first term should represent the initial ballistic motion. Using Fourier transform of t^n, $\mathscr{F}(t^n) = (i\omega)^{-(n+1)}\Gamma(n+1)$, and using also $\omega = \kappa V_0^2\nu/(v_- + v_+)$:

$$\langle x(\nu)\rangle = \sum_n (-1)^{n+1}\chi_n \frac{\Gamma(n+1)(v_-+v_+)^{n+1}}{(i\nu)^{n+1}\tau^n(\kappa V_0^2)^{n+1}} \tag{2.124}$$

We can also expand Eq. (2.98) in a series in $1/\nu$.

$$\langle x_+(\omega)\rangle_+ = \frac{2\ell_t}{v_+}\sum_m (L_m S_m^0 + L_{m+1}S_m^1) = \sum_n \frac{\zeta_n}{(i\nu)^n}, \tag{2.125}$$

where ζ_n are calculated from the expansion of L_m and S_m in powers of $1/\nu$. Then, we can easily calculate the time components χ_n:

$$\chi_n = (-1)^{n+1}\frac{\tau^n\zeta_{n+1}}{\Gamma(n+1)(v_-+v_+)^{n+1}}. \tag{2.126}$$

For the purpose of calculation of ζ_n we start with an assumption that L_m, $R_m = L_m$, Q_m, and

S_m have expansions in powers of $1/\nu$:

$$L_m(\nu) = \sum_{n=0}^{\infty} \frac{l_{m,n}}{(i\nu)^n}, \quad Q_m(\nu) = \sum_{n=0}^{\infty} \frac{q_{m,n}}{(i\nu)^n}, \quad S_m(\nu) = \sum_{n=0}^{\infty} \frac{s_{m,n}}{(i\nu)^n}. \tag{2.127}$$

Values of $l_{m,n}$ can be calculated directly because for very large ω (which also means ν):

$$L_m = -i\nu\Gamma(m+1)\Psi(m+1,2;-i\nu), \tag{2.128}$$

and the series expansion of the confluent hypergeometric function of the second kind is known analytically, see [54] and appendix A.

The only difficulty lays in the calculation of $q_{m,n}$ and $s_{m,n}$. To find the expansions, we can use the iterative structure of the equations for Q_m^i and S_m^i. In general, these equations have the following form:

$$\left[i\nu a_m + b_m\right] Q_m + m^2 Q_{m-1} + c_m Q_{m+1} + d_m = 0, \tag{2.129}$$

where, for example, $d_m = R_m$ for the equation for Q_m^0, and d_m series coefficients are denoted by $d_{m,n}$. To solve this equation, the strategy is the following. We start with $m = 0$ and find the solution for the lowest order of $(i\nu)^{-1}$. It can be easily found that $q_{0,0} = 0$. Then, we move to $m = 1$ and find that $q_{0,1} = q_{1,1} = 0$. In general:

$$q_{m,n} = 0 \text{ for } n \leq m, \tag{2.130}$$

thus we can write that

$$Q_m(\nu) = \sum_{n>m}^{\infty} \frac{q_{m,n}}{(i\nu)^n}. \tag{2.131}$$

By scanning m and solving the equations for the (next) lowest order in $(i\nu)^{-1}$ we end up with a set of equations, which can be solved iteratively:

$$\begin{aligned}
q_{m,m+1} &= -\frac{1}{a_m}(d_{m,m} + m^2 q_{m-1,m}), \\
q_{m,m+2} &= -\frac{1}{a_m}(d_{m,m+1} + b_m q_{m,m+1} + m^2 q_{m-1,m}), \\
q_{m,m+i} &= -\frac{1}{a_m}(d_{m,m+i-1} + b_m q_{m,m+i-1} + m^2 q_{m-1,m+i-1} + c_m q_{m+1,m+i-1}) \text{ for } i \geq 3.
\end{aligned} \tag{2.132}$$

The strategy for finding $s_{m,n}$ is exactly the same. As the equations for S_m^i include Q_m^i the series expansions of Q_m^i have to be found in the first step. Due to the fact that for all types of Q_m^i we have $q_{m,n\leq m} = 0$ the series for S_m is shifted:

$$s_{m,n} = 0 \text{ for } n \leq m+1. \tag{2.133}$$

Then $s_{m,n}$ are calculated using very similar iterative equations to Eqs. (2.132) (with a shift of m by 1), where for example $d_{m,n} = 2\ell_t q_{m,n}$ for S_m^0.

Knowing the series expansions of S_m and L_m the coefficients χ_n can be calculated easily, giving the whole time series Eq. (2.123).

2.B.3 Comment on the choice of β

To calculate the center of mass, we use the set of equations for S and Q. They include β_m^+ (used in Eqs. (2.94), (2.92) and (2.120)) and β_m^- (used in Eqs. (2.95) and (2.121)). From the discussion presented in section 2.6.4 we know that the quantum short-time solutions have to agree with the classical Boltzmann solutions. This is not the case when $\beta_m^\pm$ are used. We have empirically found that using β_m^0:

$$\beta_m^0 = \frac{2\kappa m^2 + 2m + 1}{v_- v_+} \tag{2.134}$$

gives the correct results for the first three χ_n terms. Moreover, we have also found an excellent agreement of predictions using β_m^0 with the numerics at all times.

We suppose the reason of this empirical rule lies in the contribution of the vertices (a) in Fig. 2.14, which involves $G_0^{R/A}(x,x)$. This factor is not correctly computed, see the discussion in section 2.5. The work on this problem is still in progress at the time of writing the thesis.

Chapter 3

Quantum boomerang effect for interacting particles in the mean-field approximation

After the introduction of the quantum boomerang effect in chapter 1 and the study of time reversal symmetry breaking in chapter 2, we analyze the effect of interactions on the phenomenon. In this chapter, we discuss the effects of interactions under the form of nonlinearity included into the Schrödinger equation, i.e. in the mean-field approximation for a bosonic gas.

The chapter begins with a short introduction to weakly interacting bosonic gases in section 3.1, where we introduce the Gross-Pitaevskii equation. In section 3.2, we briefly explain the model and the numerical implementation of the nonlinearity. Section 3.3 presents the main numerical results: the destruction of the boomerang effect due to interactions and its dependence on the initial state. In section 3.4 we introduce a method allowing for the analysis of the "plane wave boomerang". The main result of the chapter: an effective description of the boomerang effect in the interacting system using a single parameter, is presented in section 3.5. Then, in section 3.6, we show that this parameter is related to the self-energy in the interacting system. The parameter also describes the changes of the scattering mean free time and scattering mean free path, what we discuss in section 3.7. Finally, section 3.8 concludes the chapter.

3.1 Weakly interacting bosonic gases

In a cold atomic gas, atoms are not independent particles, but do interact. Even under a high level of control over systems' properties, one should analyze the effect of inter-particle interactions. In our case, we analyze the interactions in cold bosonic gases. The situation described in the chapter is probably the most common experimental scenario, where an initially trapped Bose-Einstein condensate is allowed to evolve in a disorder potential [15, 109].

For dilute bosonic gases, the following condition holds: the range of interactions r_0 is much smaller than the average distance between particles $q = n^{-1/d}$, where n is the average gas density and d is the dimensionality of the system. This scenario means that we can focus only on two-body interactions, because diluteness ensures that simultaneous interactions of three or more particles are much less frequent. If the momenta relevant for the scattering process satisfy $p \ll \hbar/r_0$, the

scattering amplitude may be reduced to a single low-energy quantity describing the scattering in the s-wave channel: the scattering length a. In such systems, we may use this length as the only parameter characterizing interactions. We define the regime of weak interactions by $|a| \ll q$. In our scenario, the particles repel each other, so $a > 0$. Note however, that we study weak interactions, so that most conclusions apply also for weakly attractive interactions, $a < 0$.

Let us start by analyzing the two-body bosonic Hamiltonian

$$\hat{H} = \int \hat{\Psi}^\dagger(\boldsymbol{r})\Big(-\frac{\hbar^2}{2m}\Delta + V_{\text{ext}}(\boldsymbol{r})\Big)\hat{\Psi}(\boldsymbol{r})\mathrm{d}\boldsymbol{r} + \frac{1}{2}\int \hat{\Psi}^\dagger(\boldsymbol{r}')\hat{\Psi}^\dagger(\boldsymbol{r})V(\boldsymbol{r}'-\boldsymbol{r})\hat{\Psi}(\boldsymbol{r})\hat{\Psi}(\boldsymbol{r}')\mathrm{d}\boldsymbol{r}\,\mathrm{d}\boldsymbol{r}', \tag{3.1}$$

where $V(\boldsymbol{r}-\boldsymbol{r}')$ is the two-body potential and $\hat{\Psi}^{(\dagger)}(\boldsymbol{r})$ are bosonic field operators fulfilling the standard commutation relations:

$$\big[\hat{\Psi}(\boldsymbol{r}), \hat{\Psi}^\dagger(\boldsymbol{r}')\big] = \delta(\boldsymbol{r}-\boldsymbol{r}'). \tag{3.2}$$

$V_{\text{ext}}(\boldsymbol{r})$ represents any external single-particle potential, for example, disorder. The time-dependent equation for the field operator is obtained in the Heisenberg picture

$$i\hbar\partial_t\hat{\Psi}(\boldsymbol{r}) = \big[\hat{\Psi}(\boldsymbol{r}), \hat{H}\big]. \tag{3.3}$$

Now, if we now assume that we are in a dilute gas with weak interactions, we can use the approximation called Bogoliubov prescription [110]:

$$\hat{\Psi}(\boldsymbol{r}) = \hat{a}_0\psi(\boldsymbol{r}) + \delta\hat{\Psi}(\boldsymbol{r}), \tag{3.4}$$

where $\hat{a}_0$ is the operator annihilating a particle in the $\psi(\boldsymbol{r})$ state, $\psi(\boldsymbol{r})$ is a *classical field* and $\delta\hat{\Psi}(\boldsymbol{r})$ is a small quantum correction. The first term describes the condensate fraction, while the correction includes all non-condensed particles. In a system dominated by the condensate, we may put $\delta\hat{\Psi}(\boldsymbol{r}) = 0$, and replace $\hat{a}_0$ by $\sqrt{N}$. These steps greatly simplify Eqs. (3.1), (3.3) which, in such a situation, describe a single-particle wave function $\psi(\boldsymbol{r})$. The wave function is normalized to unity, whereas the total number of particles calculated from the field operator is N.

Until now, we have not used any assumption about the interaction potential. It can be replaced by an effective potential which has the same scattering length in the s-wave channel, for example, the contact interaction potential:

$$V(\boldsymbol{r}-\boldsymbol{r}') = V_0\delta(\boldsymbol{r}-\boldsymbol{r}'). \tag{3.5}$$

At first order, i.e. Born approximation, the scattering length is:

$$a = \frac{\mu}{2\pi\hbar^2}\int V(\boldsymbol{r})\mathrm{d}\boldsymbol{r} = \frac{\mu}{2\pi\hbar^2}V_0, \tag{3.6}$$

where μ is the reduced mass of the two-body system. For systems where particles have the same mass, such as in Bose-Einstein condensates, $\mu = m/2$ and we can write [111]:

$$V_0 = \frac{4\pi\hbar^2 a}{m}. \tag{3.7}$$

As expected, the result depends only on one parameter, the scattering length a. For low energy collisions, this approach can be used extensively as long as one studies scales larger than a. The simplification of the real interaction potential may lead to a breakdown of the approximation when analyzing microscopic phenomena. Although we will study one-dimensional systems, we should note that the effective delta-potential requires a proper regularization in higher-dimensional systems.

3.1.1 Gross-Pitaevskii equation

We can now focus on the equation governing the evolution of a weakly interacting Bose-Einstein condensate in a disordered potential $V_{\mathrm{dis}}(\boldsymbol{r})$. Starting from Eq. (3.3) and Eq. (3.4), and neglectig the quantum correction $\delta\hat{\Psi}(\boldsymbol{r})$, we obtain the time dependent Schrödinger equation for $\psi(\boldsymbol{r})$:

$$i\hbar\partial_t\psi(\boldsymbol{r},t) = \left(-\frac{\hbar^2}{2m}\Delta + V_{\mathrm{dis}}(\boldsymbol{r}) + N\int \mathrm{d}\boldsymbol{r}'\, V(\boldsymbol{r}')|\psi(\boldsymbol{r}',t)|^2\right)\psi(\boldsymbol{r},t), \tag{3.8}$$

where we also substituted $\hat{a}_0^\dagger\hat{a}_0$ by the total number of particles N. The last step involves using the effective contact potential $V(\boldsymbol{r}') = V_0\delta(\boldsymbol{r}')$:

$$i\hbar\psi(\boldsymbol{r},t) = \left(-\frac{\hbar^2}{2m}\Delta + V_{\mathrm{dis}}(\boldsymbol{r}) + g|\psi(\boldsymbol{r},t)|^2\right)\psi(\boldsymbol{r},t), \tag{3.9}$$

where we have introduced the interaction strength $g = NV_0$. The wave function $\psi(\boldsymbol{r},t)$ is normalized to unity:

$$\int \mathrm{d}\boldsymbol{r}\,|\psi(\boldsymbol{r},t)|^2 = 1. \tag{3.10}$$

Equation (3.9) is called Gross-Pitaevskii equation (GPE) named after Eugene Paul Gross [112] and Lev Petrovich Pitaevskii [113]. The equation was derived to study non-uniform Bose gases at low temperature. It has the form of a single-particle Schrödinger equation with an additional nonlinear time-dependent potential $g|\psi(\boldsymbol{r},t)|^2$ which describes the interaction between particles.

The energy functional can be calculated starting from Eq. (3.1). Following all simplifying steps described above, we arrive at

$$E = \int\left(\frac{\hbar^2}{2m}|\nabla\psi(\boldsymbol{r})|^2 + V_{\mathrm{dis}}(\boldsymbol{r})|\psi(\boldsymbol{r})|^2\right)\mathrm{d}\boldsymbol{r} + \frac{g}{2}\int|\psi(\boldsymbol{r})|^4\mathrm{d}\boldsymbol{r}\,. \tag{3.11}$$

Here, the energy is calculated from the single-particle wave function $\psi(\boldsymbol{r})$, hence if one is interested in the total energy, it is given by $E_{\mathrm{tot}} = NE$. The first term in Eq. (3.11) is a typical sum of the kinetic and potential single-particle energies. The second one is the interaction energy.

The applicability of the GPE is somewhat restricted. Firstly, the total number of particles N has to be large. The second approximation is the use of an effective potential, so by using the GPE we can only investigate phenomena which take place on distances larger than the interaction range. Lastly, the derivation assumes that the interactions are only in the s-wave channel, and the interaction strength (directly connected to the scattering length) is small. Finally, in our study we are interested in the dynamics of such systems. In such a situation, someone could question the validity of approximations leading to the GPE. However, the GPE is more than merely a description of the single-particle wave function, the authors of [114, 115] rigorously prove that indeed the GPE preserves the underlying many-body correlations. The GPE was successfully used in many experi-

ments involving cold bosonic gases, see [116]. More details about the cold atomic dilute gases may be found in [117, 118].

In the following sections, we analyze the effect of interactions treated in the mean-field approximation on the quantum boomerang effect. We should also comment on the possibility of using higher-order approximations, i.e. Bogoliubov excitations. Disordered systems including quantum corrections were successfully studied in many works, for example see [119–125]. The main obstacle for the application of the GPE to describe the boomerang effect may be the depletion of the condensate fraction. This effect could be grasped using the quantum corrections. However, it is known that even the mean-field nonlinearity strongly affects localization effects. Hence, we stay at the simplest level, restricting the study to the GPE.

3.2 The model

To study the boomerang effect in the presence of interactions, we use the one-dimensional GPE:

$$i\hbar\frac{\partial\psi(x,t)}{\partial t} = \Big(\frac{p^2}{2m} + V(x) + g|\psi(x,t)|^2\Big)\psi(x,t), \tag{3.12}$$

where g is, as defined above, the interaction strength, and $V(x)$ is the disordered potential which is a representation of a Gaussian uncorrelated process:

$$\overline{V(x)} = 0, \quad \overline{V(x)V(x')} = \gamma\delta(x-x'). \tag{3.13}$$

The parameter γ measures the disorder strength and determines the characteristic scattering mean free time τ_0 and the scattering mean free path ℓ_0, which are given in the Born approximation by (cf. section 1.2, Eqs. (1.36) and (1.40)):

$$\tau_0 = \frac{\hbar^3 k_0}{2m\gamma}, \quad \ell_0 = v_0\tau_0 = \frac{\hbar^4 k_0^2}{2m^2\gamma}. \tag{3.14}$$

Similarly to chapter 2, we can use the uncorrelated disorder because it is sufficient to capture the main features of the boomerang effect. Following [3], we take a Gaussian wave packet with mean velocity $\hbar k_0/m$ as the initial state:

$$\psi(x, t=0) = \Big(\frac{1}{\pi\sigma^2}\Big)^{1/4}\exp(-x^2/2\sigma^2 + ik_0x), \tag{3.15}$$

where σ and k_0 as chosen such that the initial wave function is sharply peaked around $\hbar k_0$ in momentum space. This is satisfied when $\sigma k_0 \gg 1$. This initial state resembles an experimental scenario, where the BEC is prepared in a harmonic trap, e.g. [32]. Although, the Gaussian state with $k_0 = 0$ is not a true ground state of a harmonic trap in the presence of interactions, for small values of interaction strength, Gaussians (with $k_0 = 0$) may be seen as a good approximation. This detail does not influence the results presented below. We work in the weak disorder regime, where the mean free path is much longer than the particle de Broglie wavelength. This is fulfilled as long as $k_0\ell_0 \gg 1$. Finally, the center of mass position (CMP) is calculated in a similar way to section 2.4:

$$\langle x(t)\rangle = \int x\overline{|\psi(x,t)|^2}\mathrm{d}x\,. \tag{3.16}$$

Two assumptions: about the width of the initial wave packet $k_0\sigma \gg 1$ and about weak disorder, $k_0\ell_0 \gg 1$, allow to have a well-known non-interacting limit. There is, however, no constraint relating the wave packet width σ and the mean free path ℓ_0, for example, the wave packet may be very broad compared to ℓ_0. If the assumptions about the wave packet width σ and the disorder strength γ are not valid, the initial wave packet will consist of many momentum components, and hence instead of one mean free time, one will deal with a whole distribution of mean free times. This unnecessarily complicates the studied phenomenon, most probably without any change of the final conclusions.

3.2.1 Numerical experiments

For all numerical works, there is an important question about the method used to simulate the quantum system. In this problem we are interested only in the time evolution of the system and for this purpose we use the Chebyshev kernel method (see section 1.5.3). However, the expansion of the evolution operator includes only the linear part,

$$H = p^2/2m + V(x), \tag{3.17}$$

and cannot be used for the the nonlinear part $g|\psi(x,t)|^2$, which is time-dependent.

The Chebyshev method is a typical iterative method, where the evolution is calculated using small time steps Δt. The advantage of the method is that its complexity, i.e. the total number of terms in the Chebyshev series, also depends on the size of the time step Δt. For large time steps one has to calculate many terms in the series, while for fairly small steps, the same results can be obtained with a much smaller number of terms in the expansion.

The nonlinear part of the Hamiltonian can be applied to the wave function simply in the form of a phase factor $\exp(-ig|\psi(x,t)|^2\Delta t/\hbar)$.

$$\psi(x,t+\Delta t) \approx \underbrace{\exp\left(-\frac{iH\Delta t}{\hbar}\right)}_{\text{Chebyshev}} \underbrace{\exp\left(-\frac{ig|\psi(x,t)|^2\Delta t}{\hbar}\right)}_{\text{diagonal in position space}} \psi(x,t) \tag{3.18}$$

Using a small time step Δt we can control the size of this phase factor, keeping it reasonably small in order to avoid errors in the evolution. This approximation is efficient only when g is also sufficiently small. Typically, we should keep $g|\psi(x,t)|^2\Delta t$ of the order of 10^{-2}. This, of course, is the simplest possible solution of the problem. It is possible to use a more elaborate method as, for example, the symmetric Trotter expansion, see [126, 127], which decreases the total error accumulated during the time evolution. As long as g is small (the situation we are interested in), using Eq. (3.18) is sufficient and computationally efficient.

In our simulations, we chose $1/k_0$ to be the unit of length. The total length of the system simulated was $L = 4000/k_0$, divided into 20000 points, so that the discretization effects are negligible. The disorder strength used is $\gamma = 0.1\hbar^4 k_0^3/m^2$ meaning that we may assume disorder to be weak:

$$\begin{aligned} k_0\ell_0 &= 5 \\ k_0\Delta x &= 0.2 \end{aligned} \tag{3.19}$$

Naturally, $1/k_0\ell_0$ corrections to the Born approximation may be expected, however they do not

influence our results, because the boomerang effect is robust and does not depend on the Born approximation. Maximal time in the simulations is $t_{\max} = 2500\tau_0$.

The interaction strength is expressed in units of $\hbar^2 k_0/m$, energy is expressed via $E_0 = \hbar^2 k_0^2/2m$ (in units of $\hbar^2 k_0^2/m$), and time by τ_0 (in units of $m/\hbar k_0^2$). This may be regarded as a basis for geometric parameter scaling. For an arbitrary real number λ, we can rescale the problem $x \to \lambda x$, $k_0 \to k_0/\lambda$, $t \to \lambda^2 t$, $\gamma \to \gamma/\lambda^3$, and $g \to g/\lambda^3$ yielding the same results. The idea of the geometric scaling is valid only in the case of Gaussian uncorrelated disorder. For correlated potentials, the correlation length of the potential introduces and additional scale which breaks this scaling. A consequence is that the connection between τ_0 and ℓ_0 is more complex [128].
In all numerical results presented in this chapter, we put $k_0 = 1$, $m = 1$ and $\hbar = 1$. The results have been averaged over 5×10^5 disorder realizations (unless otherwise stated).

3.3 Effect of the nonlinearity on the boomerang effect

3.3.1 Nonlinearity and Anderson localization

The effects of nonlinearities on Anderson localization were analyzed in many previous theoretical works, often controversial, see [129–139]. The main conclusion is that the nonlinearity acts as a decoherence mechanism which leads to the destruction of full localization and revival of the transport. The nonlinear part of the Hamiltonian (3.9), $g|\psi(x,t)|^2$, may be considered as a time-dependent random potential. It means that each scattering path carries a small fluctuating phase. In total, this breaks the interference between multiple scattering paths and destroys the coherence needed for Anderson localization. The effect depends both on the interaction strength and the local density in configuration space. It can be viewed as a competition between localization and decoherence effects leading to subdiffusion of the wave packets in time, see [140]. Subdiffusion dilutes the wave packet, weakening the effect of nonlinearity which consequently allows for some *revival of localization*. It is the competition between decoherence and dilution which governs the long-time dynamics.

Subdiffustion is described by a power law, $\langle x^2 \rangle \propto t^\alpha$ with $\alpha < 1$, see [141]. Interaction induced subdiffusion in a disordered system was successfully observed in a cold atomic experiment based on Potassium atoms [142]. The experimental data suggests that $\alpha < 1/2$, which is consistent with the theoretical works. However, the theoretical predictions do not agree on the specific value of α, which ranges from $\alpha = 1/3$ [132], to $\alpha = 2/5$, for example, in [129, 135]. One of the latest numerical works strongly supports that, for a very long-time evolution, the exponent is $\alpha = 1/3$ [139]. The cited results consider only one-dimensional systems, the value of α should depend on the dimension of the system.

We are not focused on the subdiffusion process. Aforementioned numerical and theoretical works analyze initial states with zero average velocity, which is not our case. Nevertheless, using the initial state defined in Eq. (3.15) with the initial width $\sigma = 10/k_0$, we numerically investigate the time evolution of $\langle x^2(t) \rangle$. The result is presented in Fig. 3.1. The numerical data clearly shows a power-like time dependence, however, we restrain ourselves from further analysis of this phenomenon, which is not the main point of the boomerang study. From the boomerang effect perspective, the presence of the subdiffusion may be an indication of its destruction. The time reversal symmetry argument for the existence of the full boomerang effect presented in section 1.3 (see also [2, 3]) used

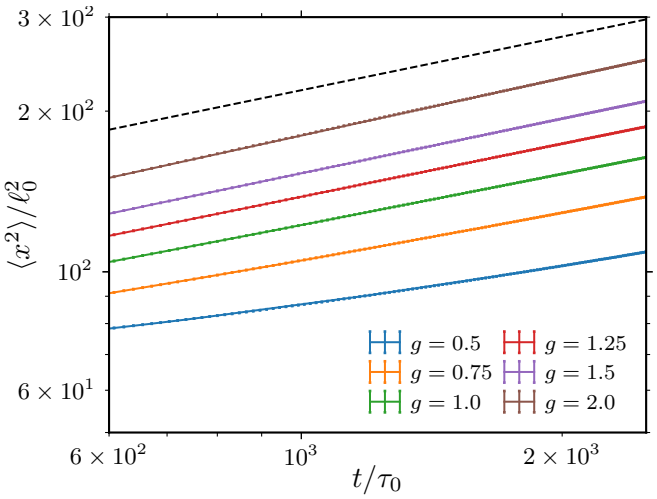

Figure 3.1. Average value of the mean squared displacement $\langle x^2 \rangle$ versus time for the state with initial width $\sigma = 10/k_0$, for different values of interaction strength. Numerical data clearly shows a power-like behavior. The black dashed line represents power law $\langle x^2 \rangle \propto t^\alpha$ with $\alpha = 1/3$. Numerical results are compatible with the exponent $\alpha \approx 1/3$ within 5%. The size of the error bars is of order of the line width.

a connection between the center of mass $\langle x \rangle$ and the mean squared displacement $\langle x^2 \rangle$:

$$\partial_t \langle x^2 \rangle = 2 v_0 \langle x \rangle. \tag{3.20}$$

In the non-interacting system, the left hand side of this equation vanishes due to Anderson localization. If subdiffusion is present, we may expect $\langle x(t = \infty) \rangle \neq 0$. Naturally, Eq. (3.20) may not be valid in nonlinear systems. However, this still may constitute a first indication that the boomerang effect is destroyed or weakened by interactions.

3.3.2 Destruction of the boomerang effect

We start the numerical study with the initial state, Eq. (3.15), with $\sigma = 40/k_0$, much broader than the mean free path, $\ell_0 = 5/k_0$. Results for various interaction strengths g are presented in Fig. 3.2. The initial evolution is very similar to the non-interacting case: the center of mass initially moves ballistically. The next phase of the evolution is also analogous, we observe that the CMP is reflected towards the origin. However, the long-time behavior is affected by the interactions. For all nonzero values of g, the center of mass does not fully return to its origin, saturating at some finite value. A preliminary observation of the partial destruction of the boomerang effect can be found in the arXiv preprint [143] and [2]. However, these results are not part of the published work [3].

When $g = 0$, disorder induces Anderson localization causing the wave packet to return to its origin: the boomerang effect. With nonzero g, the nonlinear part of the GPE (3.9) is a time-dependent source of dephasing. The dephasing partially destroys the quantum interference effects between multiple scattering paths, affecting the boomerang effect. The impact of the interactions is not immediate and the interactions do not destroy the localization completely. If this were the case, we would observe a classical motion of the CMP (see section 1.3).

Center of mass temporal evolutions among different disorder realizations are normally dis-

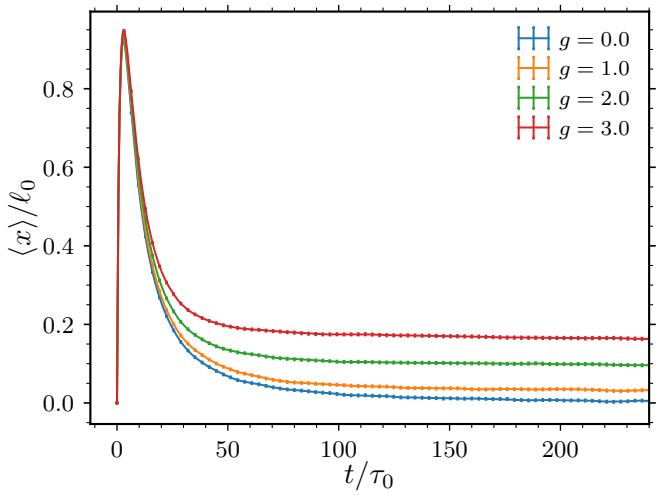

Figure 3.2. Center of mass position time evolution for an initial wave packet with $\sigma = 40/k_0$ for different values of the interaction strength g. The short-time bevahior remains almost unchanged, whereas the long-time evolution clearly depends on the interaction strength. The error bars represent statistical average errors.

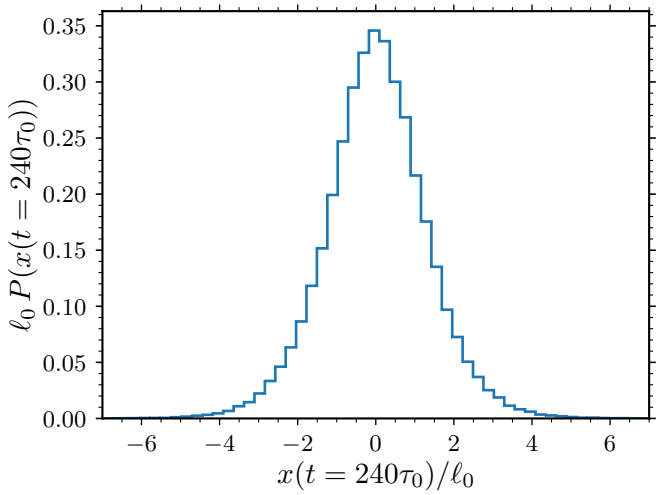

Figure 3.3. Distribution of $x(t = 240\tau_0)$ among various realizations of disorder (10^5 disorder realizations), calculated for $g = 0$. Very similar results are obtained for nonzero g.

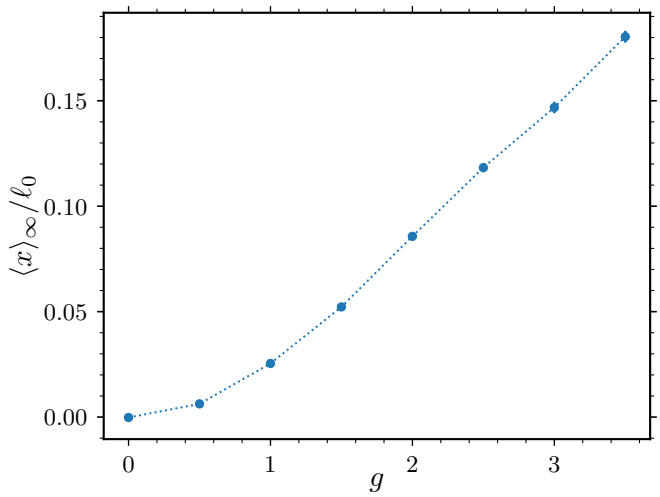

Figure 3.4. Long-time average $\langle x\rangle_\infty$ versus interaction strength g for the wave packet with initial width $\sigma = 40/k_0$. Data includes error bars calculated as the standard deviation of the points used in the average, Eq. (3.21).

.

tributed [1] what is shown in Fig 3.3, such that we use the standard error of the mean as the estimator of the errors for $\langle x(t)\rangle$.

To study in detail the long-time evolution, we calculate the long-time average of the CMP, $\langle x\rangle_\infty$, defined in the following way:

$$\langle x\rangle_\infty = \frac{1}{t_2 - t_1}\int_{t_1}^{t_2} \langle x(t)\rangle \mathrm{d}t\,, \tag{3.21}$$

where we choose $t_1 \approx 1250\tau_0$ and $t_2 \approx 2500\tau_0$. The results are essentially independent of these bounds, provided they are very much longer than the scattering mean free time τ_0. This way we calculate a very good estimate of the infinite-time value of the saturated CMP. The results are shown in Fig. 3.4. For small values of the interaction strength g, the dependence is quadratic and becomes approximately linear for larger values of g. Data points also include error bars representing the standard deviation. For the long time $t \gg \tau_0$, when the CMP is saturated, the values of $\langle x(t)\rangle$ at various t are strongly correlated. Due to this effect, there is no guarantee that the points are normally distributed, and, for the error estimate, we use only the standard deviation.

Before moving to a more detailed analysis of $\langle x\rangle_\infty$ for various initial widths we restrict the analysis to the weak interaction regime, where the long-time CMP $\langle x\rangle_\infty \ll \ell_0$.

3.3.3 Dependence on the initial density

Because the interaction depends on $|\psi(x,t)|^2$, the initial width of the wave packet σ is an important parameter of our system. Although the calculations showing the existence of the boomerang effect assume that the initial wave packet is narrow, this assumption can be loosened almost completely without any change in the proof (see [2] for details). Independently of the wave packet's width, the non-interacting CMP follows the same analytically known time evolution. For interacting systems, this is no longer true and their long-time behavior depends on the initial width σ. The

1. As discussed in section 1.3.3, the expectation value $\langle x(t\to\infty)\rangle$ is in general nonzero for a single realization of disorder. It is only after averaging over disorder realizations that is vanishes.

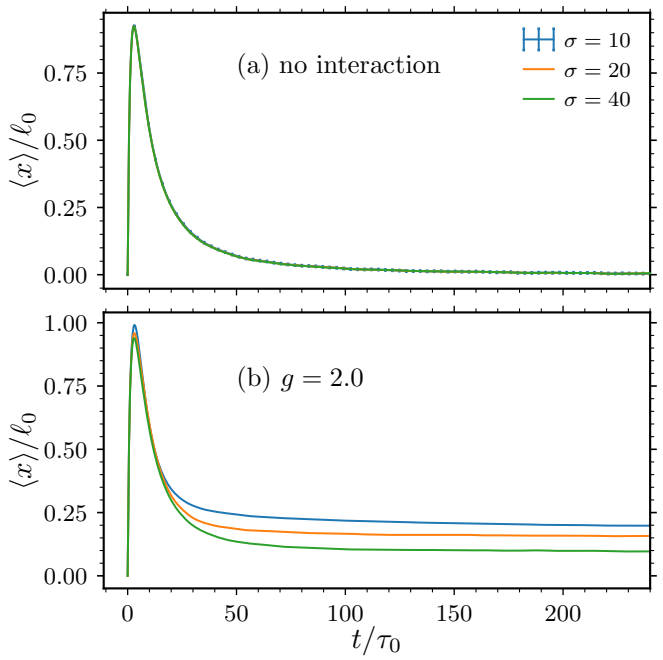

Figure 3.5. (a) Comparison of the non-interacting center of mass $\langle x(t)\rangle$ for wave packets of widths $\sigma k_0 = 10, 20$ and 40. All three curves overlap, indicating that $\langle x(t)\rangle$ is independent of σ in the non-interacting limit. (b) Same as panel (a) but for nonzero interaction strength $g = 2.0$. Here, the saturation point of $\langle x(t)\rangle$ is higher for initially narrower, i.e. denser, wave packets. Error bars indicating statistical erros are shown only in panel (a) for $\sigma = 10$ to indicate their order of magnitude.

nonlinearity is initially larger for spatially narrow wave packets due to the higher average density. Thus, the effect of the interactions on the boomerang effect is expected to be stronger. This is precisely depicted in Fig. 3.5, where we show CMP time evolutions for wave packets with initial widths $\sigma k_0 = 10, 20, 40$ for the non-interacting case $g = 0$ and for $g = 2.0$. In the first case, there is no difference between the results. For nonzero interactions, their effect is the weakest for the widest wave packet, and the largest for the narrowest one. This clearly shows that $\langle x\rangle_\infty$ does not depend only on the interaction strength, but also on the wavepacket size.

The final CMP is evidently a function of σ and g, however it is not a function of these two independent variables. A closer investigation reveals that the same values of $\langle x\rangle_\infty$ can be obtained by different combinations of σ and g. As an example, in Fig. 3.6 we show $\langle x(t)\rangle$ for $\sigma k_0 = 5$, 10, 20 and 40 with different values of g. The curves are very similar, with approximately the same $\langle x\rangle_\infty$. This result suggests that there exists a different parameter, a combination of g and σ, describing the observed destruction of the boomerang effect.

3.4 Plane wave boomerang

In section 3.3.3, we have shown that the final CMP depends on both the interaction strength g and the initial wave packet size σ. In principle, we could analyze a broader and broader wave packet with increasing σ but there is a well defined formal limit $\sigma = \infty$, i.e. plane wave. Plane waves, $\psi_0(x) = \sqrt{\rho_0}\exp(ik_0x)$ correspond to a definite initial momentum $\hbar k_0$ and we can treat them as infinitely broad wave packets. They are extensively used in other studies of disordered systems and

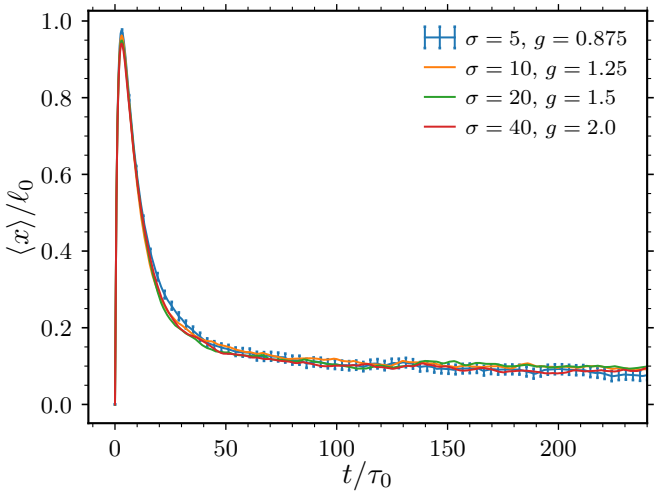

Figure 3.6. Center of mass $\langle x(t)\rangle$ versus time for different initial states chosen such that $\langle x\rangle_\infty/\ell_0 \approx 0.08$. All the curves overlap within statistical errors. Results have been averaged over 16000 disorder realizations, the error bars are shown only for $\sigma = 5/k_0$.

serve as generic states used in theoretical works.

Plane waves have a flat density profile, which implies that the $|\psi(x,t)|^2$ is also uniform at any time, and thus, from Eq. (3.16) $\langle x(t)\rangle = 0$ at all times. Nonetheless, there exists a possibility of measuring an effective center of mass time evolution for plane waves. Using the Ehrenfest theorem [144, 145] we can connect the center of mass to the average momentum. In the non-interacting system we can write:

$$\frac{\mathrm{d}\langle x\rangle}{\mathrm{d}t} = \frac{1}{m}\langle p(t)\rangle \Longleftrightarrow \langle x(t)\rangle = x_0 + \frac{1}{m}\int_0^{t'}\langle p(t')\rangle \mathrm{d}t' \,, \tag{3.22}$$

where, for our problem, the initial position is $x_0 = 0$. We should, however, note that the Ehrenfest theorem is valid only for infinite systems, or if we restate the condition, for wave functions which do not touch the system boundaries [2]. Plane waves do touch the system boundaries and the first equality in Eq (3.22) is not valid. However, the integral in Eq. (3.22) is well defined. Thus, to study CMP for plane waves, $\sigma = \infty$, we propose the following observable, which is an extension of the usual center of mass position:

$$\langle x(t)\rangle_{\text{p.w.}} \coloneqq \frac{1}{m}\int_0^{t}\langle p(t')\rangle \mathrm{d}t' \,. \tag{3.23}$$

The above approach is valid for *any* wave packet, even in more complicated systems, like the spin system studied in chapter 2. For any initial state, it is possible to calculate the average momentum, and then *extract* the CMP out of it. When employing the Ehrenfest theorem, one can use the periodic boundary condition. The method may be practical for small systems, where a direct calculation of $\langle x(t)\rangle$ may be strongly influenced by the boundary effect. Then, the CMP calculated from Eq. (3.23) includes the total distance traveled by the center of mass.

As a first step, we have compared the evolutions of $\langle x(t)\rangle$ and $\langle x(t)\rangle_{\text{p.w.}}$ for a wave packet. The

2. The Ehrenfest theorem uses the commutator $[x, H] = [x, p^2]/2m$ which is not only $i\hbar p/m$ but also contains boundary terms in a finite system. When the wave function $\psi(x)$ does not touch the boundary, these terms can be neglected.

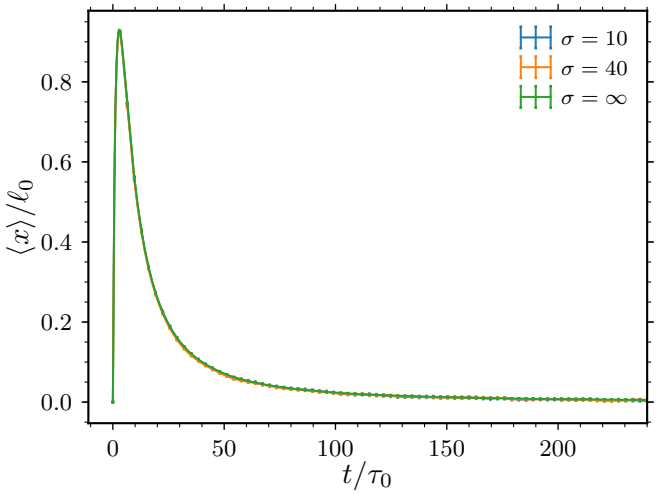

Figure 3.7. Comparison of non-interacting $\langle x(t) \rangle$ for wave packets with widths $\sigma k_0 = 10, 40$ and $\langle x(t) \rangle_{\text{p.w.}}$ calculated using Eq. (3.23). All three curves are in excellent agreement.

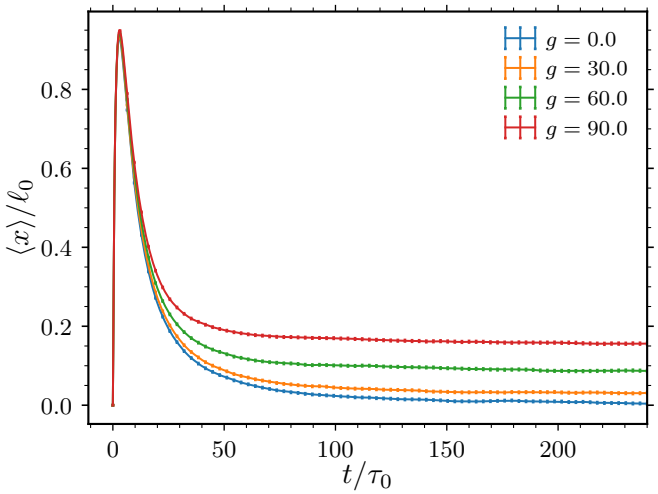

Figure 3.8. Temporal evolution of the center of mass for plane waves calculated using Eq. (3.23) for different values of interaction g. All curves have been averaged over 16000 disorder realizations. The plane wave density is $\rho_0 = 1/L = 2.5 \times 10^{-4} k_0$.

excellent agreement validated our idea that $\langle x(t) \rangle_{\text{p.w.}}$ is really a meaningful extension of $\langle x(t) \rangle$ for the quantum boomerang effect. As a next step, we present $\langle x(t) \rangle_{\text{p.w.}}$ calculated for plane waves as well as $\langle x(t) \rangle$ computed for finite width wave packets in Fig. 3.7. The result for plane wave is in excellent agreement with curves for wave packets with finite σ. Therefore, CMP for plane waves agrees with the theoretical prediction of the quantum boomerang effect. This result goes beyond the original boomerang effect where only finite width wave packets were studied [3].

We now turn to interacting systems. The presence of interactions should not change the correspondence between $\langle x(t) \rangle$ and $\langle x(t) \rangle_{\text{p.w.}}$. Such a test is very simple, hence for this purpose we analyzed the numerical simulation of the CMP for interacting, finite width wave packet with $\sigma = 10/k_0$. Then we compared the $\langle x(t) \rangle$ with $\langle x(t) \rangle_{\text{p.w.}}$. Both methods give the same results.

The density of plane wave $\rho_0 = 1/L$ may be treated as a parameter in place of the wave packet width σ. As a consequence, the same $\langle x(t) \rangle_{\text{p.w.}}$ curves are obtained for different systems sizes,

provided g is scaled such that $g/L = g\rho_0$ is constant. Accordingly, from now, we identify $\langle x(t)\rangle_{\text{p.w.}}$ with $\langle x(t)\rangle$ introduced for wave packets and omit the subscripted label onwards.

For plane waves with nonzero values of g, our main observation remains the same as for the wave packets. After the initial ballistic evolution and reflection towards the origin, the boomerang effect is partially destroyed. This result is presented in Fig. 3.8. The interactions strengths used are, as expected, much larger than those used for wave packets. This agrees with our intuition that the final value of the CMP depends both on the interaction strength and the spatial density $|\psi|^2$. A closer look at Fig. 3.8 shows another interesting feature of plane waves. Even though the simulations are averaged only over 16000 realizations (versus 5×10^5 for the wave packets), the statistical error bars are comparable to the errors for wave packets. This is because plane waves explore a much larger space (i.e. the whole system), thus average faster over a smaller number of disorder configurations. In the next sections, for the final CMP, we use 5×10^5 disorder realizations also for the plane waves.

3.5 Universal scaling of the boomerang effect in interacting systems

From the results presented in sections 3.3 and 3.4, it is natural to wonder whether the observed phenomenon – the destruction of the boomerang effect, studied through $\langle x\rangle_\infty$ – can be described using a single parameter. This can be viewed similarly to scaling approaches well known from single-particle Anderson localization, see [17, 18, 146–148].

3.5.1 Break time and break energy

Before we attempt to rescale the final CMP, we introduce a parameter, which will be very useful in the following. The long-time behavior in the non-interacting case is known (see section 1.3, Eq. (1.77)):

$$\langle x(t)\rangle \approx 64\ell_0 \frac{\ln(t/4\tau_0)\tau_0^2}{t^2}, \tag{3.24}$$

for $t \gg \tau_0$. If we neglect the logarithmic part, $\langle x(t)\rangle$ decays as t^{-2}. For small values of g, the behavior of $\langle x\rangle_\infty$ is clearly quadratic with g, see Fig. 3.4. It suggests that one may define a characteristic time scale associated with weak interactions inversely proportional to the interaction g. We call this time scale *brak time* t_b and define it by the relation

$$\langle x(t_b)\rangle_{g=0} = \langle x\rangle_\infty(g), \tag{3.25}$$

where for the left hand side we use the prediction of the non-interacting theory, Eq. (3.24), and, for the right-hand side, we use the numerically obtained values of the final CMP $\langle x\rangle_\infty$. For any time scale in quantum mechanics, one can associate an energy scale. Here, we introduce the *break energy*:

$$E_b = \frac{2\pi\hbar}{t_b}. \tag{3.26}$$

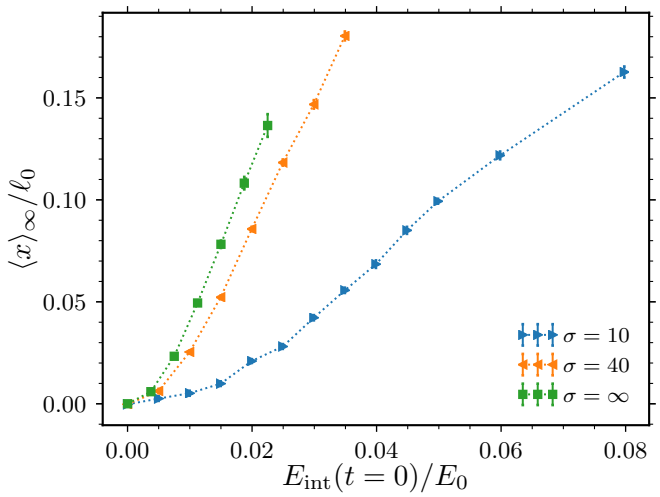

Figure 3.9. Dependence of the long-time average $\langle x\rangle_\infty$, Eq. (3.21), on the initial interaction energy. For wave packets $E_{\rm int}(t=0) = g/(2\sqrt{2\pi}\sigma)$, while $E_{\rm int}(t=0) = g\rho_0/2$ for plane waves. Error bars represent standard deviation of the averaged points.

3.5.2 Interaction energy

A natural candidate for a parameter depending both on g and the wave packet size σ is the average interaction energy:

$$E_{\rm int}(t) = \frac{g}{2}\int \overline{|\psi(x,t)|^4}\mathrm{d}x\,. \tag{3.27}$$

We also recall that the total energy is conserved by the GPE, and is the sum of the non-interacting part (kinetic and potential) and the interacting part:

$$E_{\rm tot} = \frac{\langle p^2\rangle}{2m} + \langle V\rangle + E_{\rm int}. \tag{3.28}$$

The simplest approach to the interaction energy is to study its initial value. For $t=0$, the interaction energy is given by

$$E_{\rm int}(t=0) = \frac{g}{2\sqrt{2\pi}\sigma} \text{ for wave packets,} \quad E_{\rm int}(t=0) = \frac{g\rho_0}{2} \text{ for plane waves.} \tag{3.29}$$

For example, the curves presented in Fig. 3.6 show similar values of $\langle x\rangle_\infty$ having widely different pairs of σ and g; however, their initial values of the interaction energy are comparable.

Figure 3.9 presents the values of long-time averages $\langle x\rangle_\infty$ versus the initial interaction energy $E_{\rm int}(t=0)$ for wave packets $\sigma k_0 = 10, 40$ and plane waves. While the values of σ and g are very different across the initial states, the curves shown in Fig. 3.9 are qualitatively similar. This suggests that indeed the interaction energy is an important parameter. The behavior of the final CMP is quadratic for small values of the initial interaction energy. From the previous section, we know that there is another quantity derived from the long-time averages $\langle x\rangle_\infty$ – the break energy E_b.

Using this observation, we turn to the study of the break energy versus the initial interaction energy. We show this dependence in Fig. 3.10. First of all, we immediately see that the break energy is comparable to the initial interaction energy (within a factor 4). In particular, because $E_{\rm int}(t=0)$ is proportional to the interaction strength g, we find the sought linear dependence of the

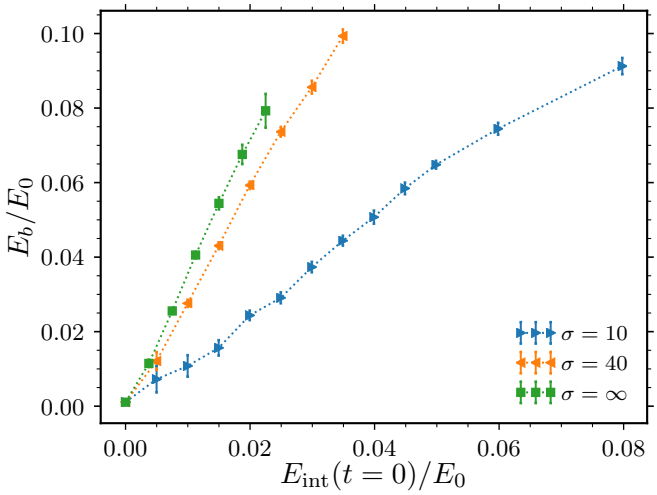

Figure 3.10. Break energy E_b versus initial interaction energy $E_{\rm int}(t=0)$. The break energy is defined by $E_b = 2\pi\hbar/t_b$, where the break time t_b is calculated using Eq. (3.25) and is a characteristic time beyond which the boomerang effect disappears. Error bars on the break energy are due to the error bar on the break time calculated from the long-time average of CMP, and ultimately to the statistical error bars on $\langle x(t)\rangle$.

break energy E_b on the interaction energy $E_{\rm int}(t=0)$. For small values of the interaction energy, the curves seem to be linear and their slope increases with the width of the initial state. Moreover, the curve for $\sigma = 40/k_0$ does not deviate much from the limiting case $\sigma = \infty$ for plane waves.

3.5.3 Randomization of the interaction energy

It is clear that the initial interaction energy is not the best parameter describing the breaking of the quantum boomerang effect by interactions. Results shown in Figs. 3.9, 3.10 do not fall on the same universal curve. The main reason comes from the fact that $E_{\rm int}(t)$ varies significantly from $t = 0$ onwards. Examples for different initial states and interaction strengths are presented in Fig. 3.11. It shows that the time evolution of the interaction energy may be divided into two main stages. In the first stage, at short time, $E_{\rm int}(t)$ rapidly increases, while in the second stage, $E_{\rm int}(t)$ slowly decays in the case of wave packets, whereas for plane waves its value remains stationary. Figure 3.11 shows only 3 examples, but the situation is generic for all initial states and all interaction strengths considered.

The first stage may be explained by analyzing the initial part of the time evolution. By definition, Eq. (3.27), the interaction energy, depends on the fourth moment of the field, $|\psi(x,t)|^4$, which obeys:

$$\overline{|\psi(x,t)|^4} = \overline{|\psi(x,t)|^2}^2 + \mathrm{Var}\Big(|\psi(x,t)|^2\Big). \tag{3.30}$$

For plane waves, whose initial profile $|\psi(x, t=0)|^2$ is completely flat, the variance at $t = 0$ is zero. However, at a short time, on the scale of the scattering mean free time, the density develops fluctuations due to scattering on the disordered potential. This increases the variance and the interaction energy. In the case of plane waves, we observe a doubling of the initial interaction energy. The factor 2 enhancement can be explained by assuming that, after a few scattering mean free times, $\psi(x,t)$ becomes a complex Gaussian variable. This can be easily verified in numerical

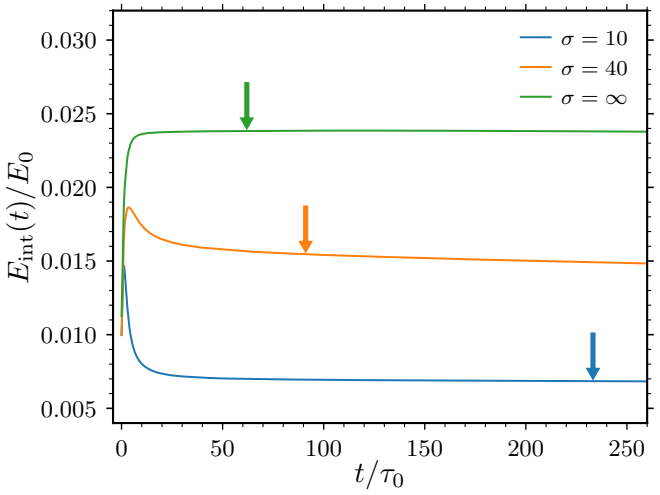

Figure 3.11. Temporal evolution of the average interaction energy for different initial states and interaction strengths. The plot shows data for wave packets with $[\sigma = 10, g = 0.25]$, $[\sigma = 40, g = 1.0]$ and $[\sigma = \infty, g = 45, \rho_0 = 0.00025]$. In the plane wave limit, specklization doubles $E_{\rm int}(t = 0)$ over a short-time scale comparable to the scattering mean free time τ_0, which then remains stationary at long time. For finite σ, randomization is also visible, but followed by a slow decay at long times due to wave packet spreading. From $t = t_b$ onwards, however, the decay is very slow. The location of the break time t_b is indicated by arrows for each curve.

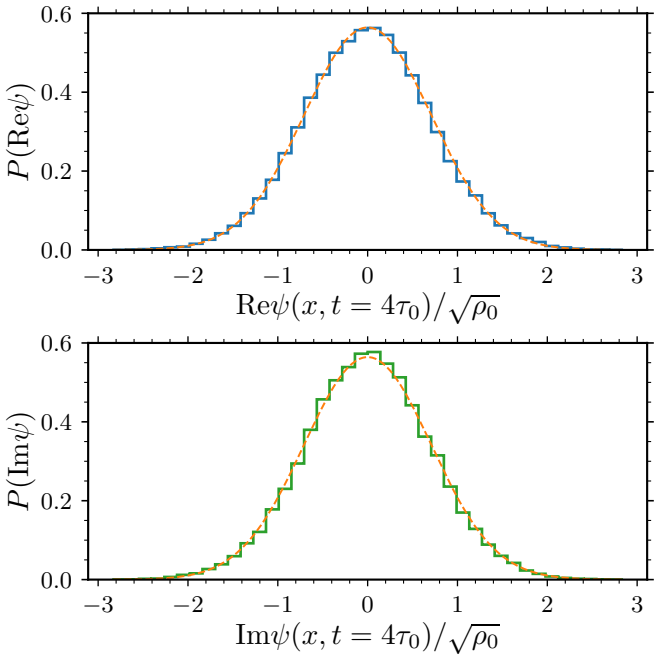

Figure 3.12. Histograms of the real (blue) and imaginary (green) parts of the wave function $\psi(x, t)$ at time $t = 4\tau_0$ for an initial plane wave state without interactions. The orange dashed line plotted in both histograms represents the distribution given by Eq. (3.31). This proves that, after few scattering events, the wave function $\psi(x, t)$ is a Gaussian distributed complex random variable.

simulations.

Figure 3.12 shows histograms of the real and imaginary parts of $\psi(x,t)$ after $t = 4\tau_0$, for a single disorder realization, for a plane wave in the non-interacting case (similar histogram is obtained in the interacting case $g \neq 0$). At such time, the components of the wave function are fully randomized. Both histograms of the real and imaginary parts are almost perfect Gaussian distributions whose variance is given by the state's initial density $\rho_0 = 1/L$:

$$P\big(\mathrm{Re}\,\psi(x,t)\big) = P\big(\mathrm{Im}\,\psi(x,t)\big) = \mathcal{N}(0,\rho_0/2), \tag{3.31}$$

where $\mathcal{N}(\mu,\sigma^2)$ denotes the Gaussian normal distribution:

$$\mathcal{N}(\mu,\sigma^2) = \frac{1}{\sqrt{2\pi\sigma^2}} e^{-\frac{(x-\mu)^2}{2\sigma^2}}. \tag{3.32}$$

This fully agrees with the expected distributions for a *(circular)* complex Gaussian variable, $P(\psi(x,t)) = \mathcal{CN}(0,\rho_0)$ [149, 150]. Hence, after the randomization, the variance in Eq. (3.30) is $\overline{|\psi(x,t)|^2}^2$, effectively doubling $\overline{|\psi(x,t)|^4}$. Because the randomization takes place at a very short time, of the order of τ_0, the interactions do not change this reasoning and it is also valid for interacting systems. The randomization is very similar to the appearance of optical speckles in scattering media, see, for example [13], thus we call this phenomenon *specklization* of the wave function.

The specklization implies that, for plane waves $E_{\mathrm{int}}(t \gg \tau_0) = 2E_{\mathrm{int}}(t=0)$. For wave packets with finite widths, the effect is also present, albeit slightly smaller. The reason is the following: the infinitely wide plane waves are randomized very efficiently by the disordered potential. A similar enhancement is observed for wave packets, as long as they cover many speckle grains, that is, for $k_0\sigma \gg 1$.

The second stage of the time evolution of the interaction energy is much less complicated. For the finite width wave packets, we observe a decay due to broadening and dilution of the wave packet. The decay slows down quickly, together with a decrease of the spreading, due to the dilution and localization effects which slow down the overall dynamics of the system, see section 3.3.1. The interaction energy of plane waves remains almost constant, without any visible decline, as expected.

3.5.4 Nonlinear energy

The complicated time evolution of $E_{\mathrm{int}}(t)$ makes a detailed rescaling analysis of the boomerang effect rather complex. Figure 3.11 shows that after the break time t_b, Eq. (3.25), the values of $E_{\mathrm{int}}(t)$ approximately do not change in time [3]. This suggests to use the value of the interaction energy at the break time t_b, instead of the initial one. Although, for the finite σ wave packets, the interaction energy still slowly evolves, we show below that this approach provides us with very satisfactory results.

Before probing such a rescaling, we make a final adjustment. The matter of our interest, the boomerang effect, is a dynamical phenomenon governed by the GPE, see Eq. (3.9). The structure of the GPE shows that the dynamical evolution is governed by a quantity twice as large as the interaction energy, whose density is proportional to $g|\psi(x,t)|^4/2$. On this basis, we introduce the

3. At very long time, $t \gg t_b$ the system may display a subdiffusive behavior with a very slow decrease of the interaction energy, see section 3.3.1. This regime, however, is out of the scope of our study.

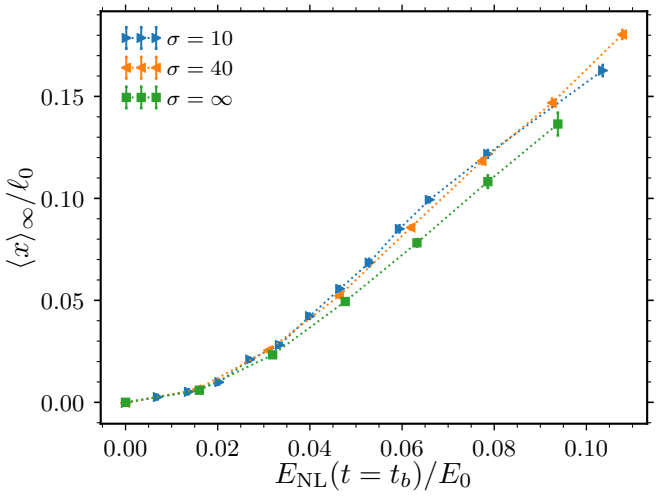

Figure 3.13. Infinite-time position of the center of mass $\langle x \rangle_\infty$ for different initial states (wave packets of various sizes, plane wave) and various interaction strengths g, plotted versus the nonlinear energy at the break time $E_{\rm NL}(t = t_b)$, see Eqs. (3.33), (3.25). The fact that all numerical data collapse on a single curve proves that the quantum boomerang effect for interacting particles is universal and is governed by a single parameter.

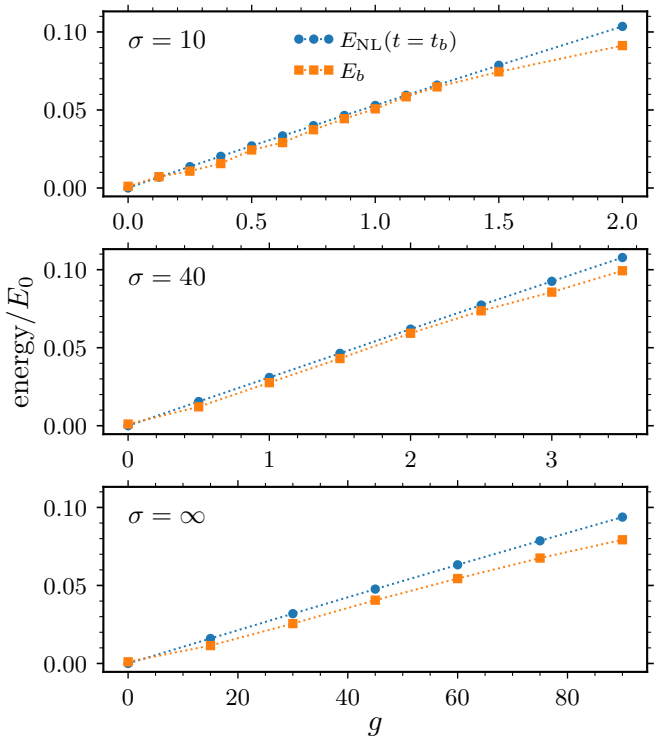

Figure 3.14. Comparison of the break energy, E_b, and the nonlinear energy at the break time $E_{\rm NL}(t = t_b)$ (see Eqs. (3.33), (3.25)), for increasing values of the interaction strength. Each panel presents results for a different initial state. The excellent agreement shows that $E_{\rm NL}(t = t_b)$ is the proper parameter controlling the quantum boomerang effect for interacting particles.

nonlinear energy, defined as

$$E_{\mathrm{NL}}(t) = 2E_{\mathrm{int}}(t) = g \int \overline{|\psi(x,t)|^4} \mathrm{d}x \,. \tag{3.33}$$

In section 3.6 we will show that the nonlinear energy is closely related to the nonlinear self-energy of the system.

We can now re-analyze the boomerang effect using the nonlinear energy at the break time, $E_{\mathrm{NL}}(t = t_b)$, as the control parameter of the interaction strengths and wave packet widths. We show in Fig. 3.13 the final CMP $\langle x \rangle_\infty$ as a function of the nonlinear energy calculated at the break time. In contrast with Fig. 3.9, now all points collapse on a single universal curve. As initially expected, in the regime of small nonlinear energy, $\langle x \rangle_\infty$ shows a quadratic dependence (and later a linear dependence). This means that the nonlinear energy is the desired parameter governing the destruction of the quantum boomerang effect.

Finally, in Fig. 3.14 we compare the values of the break energy $E_b = 2\pi\hbar/t_b$ which characterize the breaking of the quantum boomerang effect and the nonlinear energy at the break time, $E_{\mathrm{NL}}(t = t_b)$, for wave packets with $\sigma = 10/k_0$, $40/k_0$ and plane waves, $\sigma = \infty$, and for various values of the interaction strength g. It shows a compelling evidence that these quantities are very similar. A small difference is visible for plane waves. We suspect this discrepancy to be related to an early thermalization, which leads to a slow residual decay of $\langle x \rangle$. This, in turn, results in an underestimation of the break energy.

Such a good agreement shows that, even for a complex phenomenon like the boomerang effect, it is possible to establish a simple model able to capture the main features of the phenomenon. Our parameter, the nonlinear energy at the break time, successfully characterizes the essential features of the quantum boomerang effect for interacting particles.

3.5.5 Comment on the weak interaction and the weak disorder limits

Weak interaction regime

Until now, we have not specified what we exactly understand by the regime of weak interactions, stating only that we will focus on the regime of interactions for which $\langle x \rangle_\infty \ll \ell_0$. The observed final values of CMP $\langle x \rangle_\infty$ depend both on the initial width σ and interaction strength g. As we have shown, this dependence may be captured by a single parameter, the nonlinear energy E_{NL} at the break time. However, to quantitatively establish some bounds for the weak interaction, it is simpler to analyze the matter from the perspective of the break time. The regime of $\langle x \rangle_\infty \ll \ell_0$ may be restated using the time domain: the break time has to be much larger than the mean free time, i.e. $t_b \gg \tau_0$. This is the case in our study, where the shortest break times are larger than $25\tau_0$.

The break time may be viewed as a function of the nonlinear energy, which explicitly depends on the interaction strength. In most cases, the time evolution of the nonlinear energy is highly nontrivial and it is difficult to estimate the values of g for which one remains in the regime $\langle x \rangle_\infty \ll \ell_0$. However, using plane waves, we can make an estimation for the break time, because we know the value of the nonlinear energy for time much larger than τ_0, $E_{\mathrm{NL}}(t \gg \tau_0) = 2g\rho_0$. This gives an estimate for the break time in the case of plane waves:

$$t_b = \frac{\pi\hbar}{g\rho_0}. \tag{3.34}$$

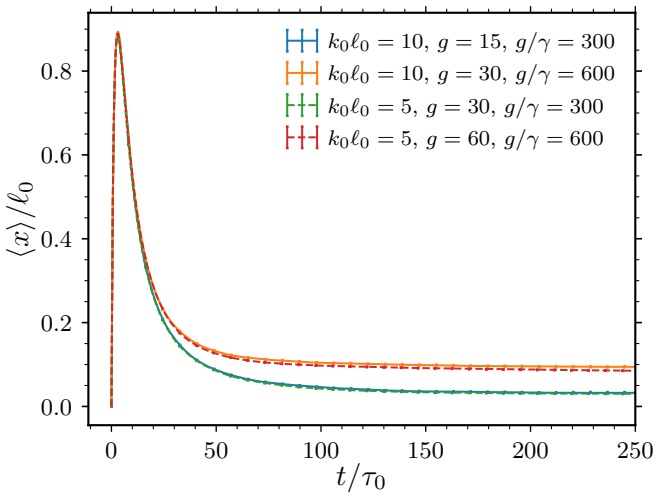

Figure 3.15. Comparison of data for plane waves, $\rho_0 = 2.5 \times 10^{-4}$, for two different values of the disorder strength γ such that $k_0\ell_0 = 5$ and $k_0\ell_0 = 10$ with $k_0 = 1$. When the interaction strength g is scaled proportionally to γ, the same curves are obtained, proving the validity of the scaling of the break time t_b with g, and the universality governing the breaking of the quantum boomerang effect by interactions.

The numerically calculated values of the break time agree with this prediction within a 10–15% margin. The condition $t_b \gg \tau_0$ now translates into

$$g \ll \frac{\pi\hbar}{\rho_0\tau_0}, \tag{3.35}$$

which, for our choice of system parameters, gives an estimate $g \ll 2500$. The highest value of the interaction strength used in our numerical simulations is $g = 90$, i.e. largely in the weak interaction regime. Yet, we suspect that the small discrepancies visible in the right part of Fig. 3.14 for $\sigma = \infty$ are the precursors of the breaking of the weak interaction regime.

In the case of wave packets, the evolution of the nonlinear energy is more complicated. Nonetheless, we may give a rough estimate for the interaction strength based on Eq. (3.35). Replacing ρ_0 by $1/\sigma$, we get

$$g \ll \frac{\pi\hbar\sigma}{\tau_0}, \tag{3.36}$$

what is also true for all values used in our study.

Disorder strength

We have studied only one value of the disorder strength γ. How does the change of γ influence the values of $\langle x\rangle_\infty$? In the non-interacting case, the whole boomerang dynamics is completely determined by values of the scattering mean free time τ_0 and the scattering mean free path ℓ_0, which explicitly depend on the disorder strength, see Eq (3.14). In the interacting system, another quantity comes into the game, the interaction strength g. The important parameter for the rescaling of the boomerang is, however, the ratio of the break time t_b and the mean scattering time τ_0. As an

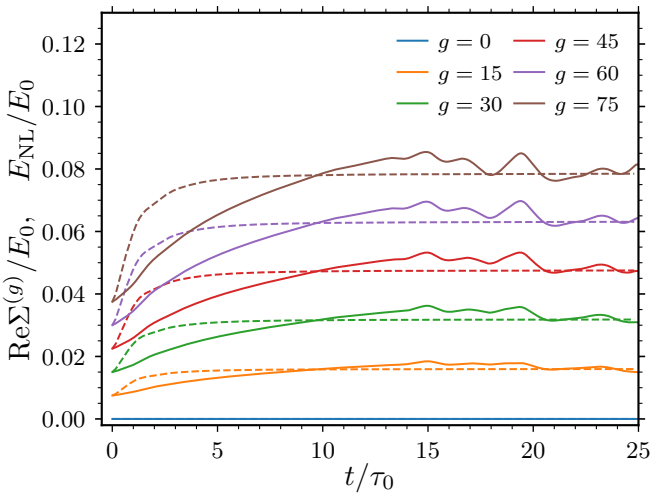

Figure 3.16. Numerically calculated real parts of the self energy $\Sigma^{(g)}$ (solid lines) versus time, for several values of the interaction strength. In the plot we additionally show the evolution of nonlinear energies $E_{\mathrm{NL}}(t)$ (dashed lines). The legend indicates the curves from bottom to top.

example, if we consider the plane waves, we obtain:

$$\frac{t_b}{\tau_0} = \frac{2\pi m}{\hbar^2 \rho_0 k_0} \frac{\gamma}{g}. \tag{3.37}$$

From this, it is completely clear that, if we rescale both the disorder strength γ and the interaction strength g by the same factor, we will obtain equivalent results when the $\langle x \rangle / \ell_0$ is plotted versus t/τ_0. This is shown in Fig. 3.15, where we compare two pairs of curves computed for plane waves with different values of γ and g. Curves with the same γ/g ratio overlap confirming our prediction. Additionally, the agreement between different pairs γ and g also confirms the scaling of t_b with the interaction strength g. Of course, this simple approach is expected to work only in the regime of weak interactions and weak disorder.

3.6 Self-energy in interacting systems

In the previous sections, we have seen that the interactions modify the long-time dynamics. These changes, depending both on the interaction g and the initial state (through σ), may be encompassed by the use of the nonlinear energy E_{NL}. In this section, we also show that the same nonlinear energy is relevant for the short-time dynamics. Let us consider first the non-interacting case.

The self-energy is a key concept in the analysis of disordered systems. It is a complex valued function of the state energy E and its momentum $\hbar k_0$, responsible for the change of the dispersion relation and the exponential decay of the average Green's function in configuration space, for details see section 1.2. In the following, we will denote it by $\Sigma_E(k_0)$. The self-energy is connected with the average Green's function through

$$\overline{G}^R_E(k_0) = \frac{1}{E - E_0 - \Sigma_E(k_0)}, \tag{3.38}$$

where $\overline{G}^R_E(k_0)$ is the average retarded Green's function. The energy E_0 is just the energy of states

in a disorder-free system, e.g. $E_0 = \hbar^2 k_0^2/2m$. The self-energy vanishes in a disorder-free system and, in the weak disorder limit, it is much smaller than E_0.

Therefore, if the self-energy is that important, how can we determine it? It cannot be done in a direct way, like the center of mass position, $\langle x \rangle$. We will use a different approach. Consider the evolution operator – it is the temporal Fourier transform of the Green's function. Assuming that the self-energy is a smooth function of E, we may calculate the average autocorrelation function for plane waves:

$$\overline{\langle \psi_0 | \psi(t) \rangle} = e^{-i(E_0 + \Sigma_E(k_0))t/\hbar} = e^{-i(E_0 + \mathrm{Re}\,\Sigma_E(k_0))t/\hbar} e^{\mathrm{Im}\,\Sigma_E(k_0)t/\hbar}, \tag{3.39}$$

$|\psi_0\rangle$ being a plane wave with wave vector k_0. From this, it is clear that $\mathrm{Re}\,\Sigma_E$ is an energy shift and $-\mathrm{Im}\,\Sigma_E$ is the decay rate of the autocorrelation $\overline{\langle \psi_0 | \psi(t) \rangle}$ as a result of the presence of disorder. Equation (3.39) allows us to extract the self-energy. Numerical calculations have to be done carefully because we have to compute the complex logarithm of the quickly decreasing average autocorrelation $\overline{\langle \psi_0 | \psi(t) \rangle}$. Nonetheless, this gives us access to the self-energy $\Sigma_E(k_0)$. For a non-interacting system, the imaginary part of the self-energy is

$$\mathrm{Im}\,\Sigma_E^{(0)}(k_0) = -\frac{\hbar}{2\tau_0}, \tag{3.40}$$

where the superscript (0) denotes the zero interaction.

In the case of interacting systems, for example, described by the GPE, the situation is in general much more complicated. The nonlinearity in the GPE, see Eq. (3.9), causes the whole notion of a linear time evolution operator not to be valid any more. In addition, the notion of self-energy is not well defined, because the autocorrelation $\overline{\langle \psi_0 | \psi(t) \rangle}$ has no reason to have an exponential form as in Eq. (3.39). However, we can still extract an effective self-energy using this equation from the numerical simulations performed for plane waves. In fact, there are two possible approaches: the static one, where the self-energy is calculated directly from Eq. (3.39) and the dynamical one, where the self-energy could be computed from the following equality:

$$\log \overline{\langle \psi_0 | \psi(t) \rangle} = -iE_0 t - i \int_0^t \Sigma_E(k_0, t') \mathrm{d}t' \,. \tag{3.41}$$

The self-energy extracted both ways is time-dependent. The dynamical method should be preferred over the static one [4]. Despite this, in our work, we use the static method, because the results obtained with the dynamical method were too noisy to get meaningful results. In some sense, it is a phenomenological attempt to quantify the effect of disorder in an interacting system.

To study the impact of the interactions on the self-energy, we define the nonlinear part of the self-energy, $\Sigma^{(g)}$ in the following way:

$$\Sigma^{(g)} = \Sigma_E^{(g)}(k_0) - \Sigma_E^{(0)}(k_0), \tag{3.42}$$

where both $\Sigma_E^{(g)}(k_0)$ and $\Sigma_E^{(0)}(k_0)$ are calculated numerically using the average autocorrelation, Eq. (3.39). The results of numerical simulations are shown in Fig. 3.16, where we observe that the nonlinear self-energy increases during several τ_0 and then saturates approximately around twice

4. The static self-energy depends on the whole evolution up to time t. This retardation effect is visible in our results, see Fig. 3.16. The expected saturation of the nonlinear self-energy $\Sigma^{(g)}$ (see the main text and Eq. (3.45)) takes longer than for the nonlinear energy E_{NL}.

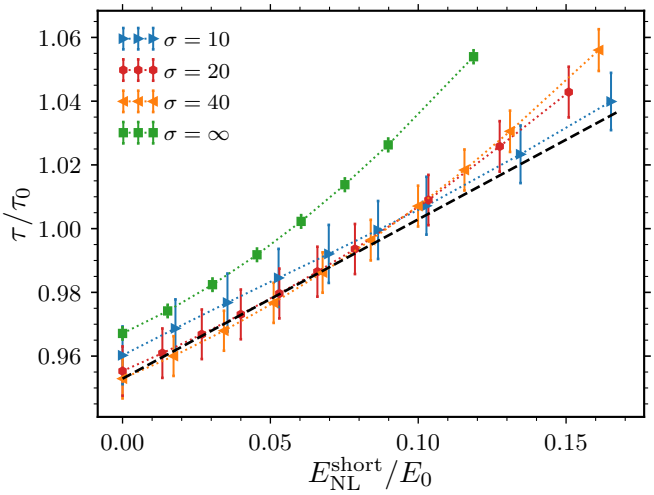

Figure 3.17. Fitted values of the scattering mean free time τ for wave packets of different initial widths versus the nonlinear energy average over the fit window $E_{\mathrm{NL}}^{\mathrm{short}}$. The black dashed line shows the prediction of Eq. (3.46)

its initial value.

It is easy to compute exactly $\Sigma^{(g)}$ at short time:

$$\overline{\langle\psi_0|\psi(t)\rangle} \approx e^{-i(E_0+\Sigma^{(0)}_{E_0}+g\rho_0)t/\hbar}, \tag{3.43}$$

from which we have the result:

$$\Sigma^{(g)}(t=0) = E_{\mathrm{NL}}(t=0) = g\rho_0. \tag{3.44}$$

The first equality is valid for any initial state $\psi_0(x)$. The second equality holds only for plane waves. From section 3.5.3, we know that due to disorder, after a few scattering mean free times, the specklization of the wave function leads to an enhancement of the nonlinear energy by a factor 2. It is thus very natural, and fully confirmed by our numerical results, shown in Fig. 3.16, that the nonlinear self-energy also doubles in time, and, for long time, we have:

$$\Sigma^{(g)}(t \gg \tau_0) = E_{NL}(t \gg \tau_0) = 2g\rho_0. \tag{3.45}$$

This can be shown using theoretical tools [151] and discussed in appendix 3.A. Our numerical data presented in Fig. 3.16 confirm the relation between the nonlinear self-energy and the nonlinear energy at intermediate time. After the initial growth, both quantities saturate around $2g\rho_0$ and follow a close evolution. Altogether, our observations strongly suggest that $\Sigma^{(g)}$ and E_{NL} govern the dynamics of interacting disordered systems. This also justifies the conclusion of section 3.5, since the self-energy is typically involved in calculations of observables, in particular of the center-of-mass position.

3.7 Modification of the observed mean scattering time

One of our first observations made in section 3.3 is that the initial evolution of the CMP is not affected by interactions. Closer investigations of Fig. 3.2 confirm that, in the short-time regime, i.e. $t < 20 - 30\tau_0$, all CMP curves are almost unaffected by the nonlinearity. The only visible effect is that both the mean free time and mean free path are slightly increased. The non-interacting theoretical prediction for $\langle x(t)\rangle$ depends on τ and ℓ, see section 1.3. By fitting this prediction to our interacting data restricted to a short time, we can extract the values of the effective scattering mean free time τ and scattering mean free path ℓ.

Fits have been performed for a time window $t \in [0, t_{\rm fit}]$, with $t_{\rm fit} = 20\tau_0$. We have also included weights to the data points inversely proportional to the statistical errors of the points. The size of the time window $t_{\rm fit}$ is chosen to include the whole ballistic part of the evolution and the beginning of the reflection. Change of $t_{\rm fit}$ does not significantly modify the results.

From τ and ℓ, we calculate the mean velocity $v = \ell/\tau$. We observe that v remains almost unchanged by the interactions. It is, however, a little bit higher than the value $\hbar k_0/m$ predicted by the Born approximation. This apparent discrepancy is caused by corrections to the Born approximation, which are of higher order in $1/k_0\ell_0 \ll 1$. Given this, we can restrict ourselves to the analysis of the mean scattering time τ only.

The fitted values of τ are presented in Fig. 3.17 as a function of the nonlinear energy averaged over the fitting time window $E_{\rm NL}^{\rm short}$. We chose such an averaging because, at short time, the nonlinear energy undergoes a rapid increase due to the specklization of the wave function. The increase of τ, especially at small values of $E_{\rm NL}^{\rm short}$, is linear for all initial states. To explain this behavior we expand the scattering mean free time at the Born approximation $\tau(E \simeq E_0 + E_{\rm NL})$ to the leading order in $E_{\rm NL} \ll E_0$, which yields:

$$\tau \simeq \tau(g = 0) + \frac{\hbar}{2k_0\gamma} E_{\rm NL}, \tag{3.46}$$

where $\tau(g = 0)$ is the true value of the scattering mean free path. In our system $\tau(g = 0) \approx 0.95\tau_0$. The predictions of equation Eq. (3.46) are presented in Fig. 3.17 as a dashed black line, where for $\tau(g = 0)$ we use a point computed for $\sigma = 40/k_0$. The agreement between the numerical data and Eq. (3.46) is very good. The values of τ increase with the rate predicted by the equation. The fact that the curves for different initial widths are shifted is due to a small dependence of $\tau(g = 0)$, which is interaction independent, on the width σ, which is beyond the Born approximation. At larger values of $E_{\rm NL}^{\rm short}$, all curves deviate from the linear behavior and start bending upwards. This effect is smaller with decreasing the wave packet's initial width. This alteration happens in a regime of a relatively strong boomerang breakdown, hence the application of a fit based on the non-interacting prediction is less reliable.

3.8 Conclusion

In this chapter, we have studied the quantum boomerang effect in the presence of interactions on the basis of the one-dimensional Gross-Pitaevskii equation. The interactions are introduced through a nonlinear term in the Schrödinger equation, hence in a mean-field approach. We found that the interactions do not destroy completely the quantum boomerang effect, that is, the center of mass a wave packet launched with a finite velocity is still retro-reflected after several scattering events.

Nevertheless, the effect is only partial: the interactions inhibit the full return to the origin, stopping the center of mass at some finite position on its way back.

Our interpretation of the phenomenon is the following: the interactions, which have the form of a time-dependent random potential, destroy the coherence between multiple scattering paths. To characterize this phenomenon, we have introduced a break time – the characteristic time scale beyond which the destruction of interference prevents the wave packet to return to its initial position. Finally, using this break time, we have shown that it is possible to universally describe the phenomenon for all initial states and interaction strengths using a single parameter, the nonlinear energy calculated at the break time. Additionally, we have shown that the nonlinear energy is closely connected with a part of the self-energy originating from the interactions, and may be also used to explain the modification of the scattering mean free time and path.

The analysis presented in this chapter is limited to the regime of weak disorder and weak interactions. For stronger disorder, the quantitative description of the phenomenon becomes more complicated, but the overall conclusions are expected to be the same, at least for weak interactions. For a stronger disorder scenario, the wave function contains many energy components, each being characterized by different mean free scattering time and mean free path. In such a case (but without interactions), each component will undergo the boomerang effect, and the final result will contain a superposition of various scattering times and lengths. This will surely complicate the analysis of the center of mass time evolution. With the interactions included, we expect that each energy component will display a partial destruction of the boomerang, i.e. nonzero value of the final position $\langle x \rangle_\infty$.

In the regime of weak disorder and strong interactions, we may expect the break time to decrease to the order of the mean scattering time. This may also change qualitatively the phenomenon introducing a much stronger competition between interaction and disorder effects, which is not present in the weak disorder and weak interaction limit.

The last important question is to know whether the observed destruction of the boomerang effect due to interactions remains valid beyond the mean-field description. This may be an interesting problem for possible ultra-cold atom experiments, and is the subject of chapter 4.

Appendix 3.A Nonlinear self-energy corrections

Here we briefly sketch the calculation of the self-energy for interacting systems based on the approach presented in [151]. To lighten the notation we put $\hbar = 1$. At lowest order in g and disorder strength γ, here represented by $(k_0\ell_0)^{-1}$, the two first diagrams contributing to the self-energy are:

$\Sigma =$ 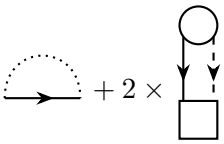 $+ 2 \times$ (3.47)

The first one represents the self-energy at the Born approximation in a non-interacting system, cf. section 1.2:

$$\Sigma^{(0)}_\epsilon(k) = \frac{1}{2\pi}\int \mathrm{d}k'\, P(k-k')G^R_0(\epsilon,k'), \tag{3.48}$$

where $G^R_0(\epsilon,k) = (\epsilon - k^2/2m + i0^+)^{-1}$ is the disorder-free Green's function (assuming a one-dimensional system), and $P(k-k')$ is the disorder correlation function in momentum representation. The second diagram shows the *nonlinearity event*, where the propagating Green's function is scattered on an density $|\psi|^2$. To better understand this diagram, we show it with more details in Fig. 3.18. Solid lines with arrows depict the free Green's functions in the energy-momentum representation $G^R_0(\epsilon,k)$, the square is a *nonlinearity* event – a scattering event on the density (thus proportional to g), while the circle represents the average intensity $I_{\epsilon,\omega}(k)$ defined as a diagonal part of

$$I_{\epsilon,\omega}(k,q) = \overline{\psi_{\epsilon+\frac{\omega}{2}}\Big(k+\frac{q}{2}\Big)\psi^*_{\epsilon-\frac{\omega}{2}}\Big(k-\frac{q}{2}\Big)}, \quad I_{\epsilon,\omega}(k,q) = (2\pi)\delta(q)I_{\epsilon,\omega}(k), \tag{3.49}$$

where $\psi_\epsilon(k)$ is the wave function in the energy-momentum representation. This also means that the average intensity is given by:

$$I_{\epsilon,\omega}(k) = \overline{\psi_{\epsilon+\frac{\omega}{2}}(k)\psi^*_{\epsilon-\frac{\omega}{2}}(k)} \tag{3.50}$$

The factor 2 before the second diagram in Eq. (3.47) comes from two possibilities of pairing one of the incoming solid lines as a partner for the dashed line (see Fig. 3.18). To compute the first-order nonlinear contribution to the self-energy, we have to evaluate the diagram shown in Fig. (3.18). To calculate the outgoing Green's function with energy ϵ and momentum k, we have to integrate over

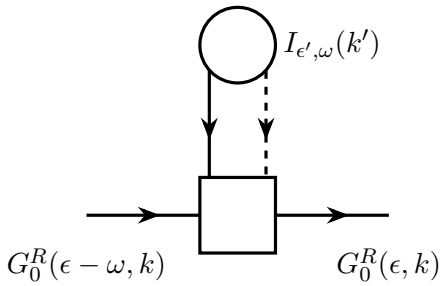

Figure 3.18. Diagram representing a nonlinear average Green's function generated by the second diagram from Eq. (3.47). The solid lines represent free Green's functions $G^R_0(\epsilon,k)$, the circle depicts the average intensity defined in Eq. (3.49), and the square represents the scattering of the Green's function on the intensity, called a nonlinearity event. The factor 2 in Eq. (3.47) comes from two possibilities of pairing the incoming solid lines (vertical or horizontal one) with the dashed line.

all possible incoming energies and momenta:

$$G^{(g)}(\epsilon,k) = 2g\int_{-\infty}^{+\infty}\frac{\mathrm{d}\epsilon'}{2\pi}\int_{-\infty}^{+\infty}\frac{\mathrm{d}\omega}{2\pi}\int\frac{\mathrm{d}k'}{2\pi}G_0^R(\epsilon-\omega,k)I_{\epsilon',\omega}(k')G_0^R(\epsilon,k). \tag{3.51}$$

At first sight, the equation suggests that the nonlinearity induces a shift in the energy, that is, a redistribution of the energy because of nonlinear scattering events. This is true in general. However, if we start from a plane wave, that is a uniform density, the situation is much simpler, and the calculation can be performed at first order in g.

To compute this integral, we start by using the normalization condition for the wave functions:

$$\overline{\psi(x,t)\psi^*(x,t)} = \rho_0\theta(t), \tag{3.52}$$

where $\theta(t)$ is the Heaviside step function. We can express the density using the diagonal intensity $I_{\epsilon,\omega}(k)$:

$$\begin{aligned}&\overline{\psi(x,t)\psi^*(x,t)} = \\ &\int\frac{\mathrm{d}k}{2\pi}\frac{\mathrm{d}q}{2\pi}\frac{\mathrm{d}\epsilon}{2\pi}\frac{\mathrm{d}\omega_1}{2\pi}e^{-ixq}e^{-i\omega_1 t}\overline{\psi_{\epsilon+\frac{\omega_1}{2}}\Big(k+\frac{q}{2}\Big)\psi^*_{\epsilon-\frac{\omega_1}{2}}\Big(k-\frac{q}{2}\Big)} = \int\frac{\mathrm{d}k}{2\pi}\frac{\mathrm{d}\epsilon}{2\pi}\frac{\mathrm{d}\omega_1}{2\pi}e^{-i\omega_1 t}I_{\epsilon,\omega_1}(k),\end{aligned} \tag{3.53}$$

where we have used the definitions of the average intensity and its diagonal part. This yields:

$$\rho_0\theta(t) = \int\frac{\mathrm{d}k}{2\pi}\frac{\mathrm{d}\epsilon}{2\pi}\frac{\mathrm{d}\omega_1}{2\pi}e^{-i\omega_1 t}I_{\epsilon,\omega_1}(k). \tag{3.54}$$

Finally, we multiply both sides by $e^{i\omega t}$ and integrate over the time domain. Then, the left-hand side of the equation is Fourier transformed into frequency domain and the right-hand side can be simplified thanks to a Dirac-delta function in frequency:

$$\frac{\rho_0}{-i\omega+0^+} = \int\frac{\mathrm{d}k}{2\pi}\frac{\mathrm{d}\epsilon}{2\pi}I_{\epsilon,\omega}(k). \tag{3.55}$$

This identity allows us to finally calculate the integral from Eq. (3.51).

$$G^{(g)}(\epsilon,k) = 2g\rho G_0^R(\epsilon,k)\int\frac{\mathrm{d}\omega}{2\pi}\frac{G_0^R(\epsilon-\omega,k)}{-i\omega+0^+} = 2g\rho_0\Big(G_0^R(\epsilon,k)\Big)^2. \tag{3.56}$$

The last integral is performed thanks to the fact that the $G_0^R(\epsilon-\omega,k)$ as a function of ω has poles only in the upper complex half-plane (cf. section 1.2). From this equation, we conclude that the nonlinear self-energy (center of the diagram Fig. 3.18) is just a multiplication by the factor $2\rho_0 g$. Thus, the full self-energy in the nonlinear system is given by:

$$\Sigma_\epsilon^{(g)}(k) = 2g\rho_0 + \frac{1}{2\pi}\int\mathrm{d}k'\,P(k-k')G_0^R(\epsilon,k'), \tag{3.57}$$

where the integral in the right-hand side of the equation is the self-energy of the linear part of the problem at the Born approximation, Eq. (3.48). Here, the interactions and disorder are decoupled: the self-energy has two independent contributions, one depending solely on disorder and the second depending only on the interactions. As we will show in the following section, there is also another

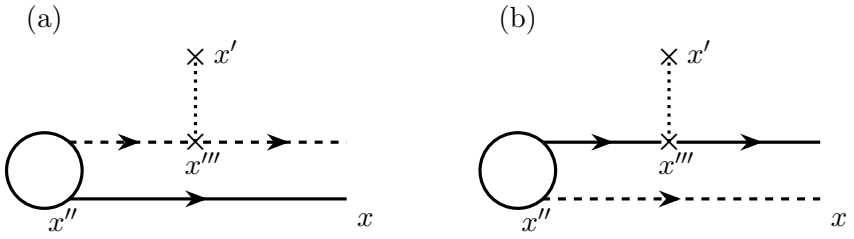

Figure 3.19. Two types of diagrams contributing to the hybrid correlator $\overline{|\psi(x,t)|^2 V(x')}$. The circle denotes the average intensity, solid and dashed lines are the propagators, cf. Fig. 3.18, while the cross represents scattering on the disordered potential.

contribution which emerges from the interplay between the interactions and disorder.

The physical interpretation of Eq. (3.57) is rather clear. As the average density is spatially uniform, it results in a spatially uniform average interaction energy. Upon a shift of the total energy by this interaction energy, one is back to the non-interacting case.

If the average density is not uniform, e.g. an initial wave packet, one can infer that, in a local density approximation, one can replace ρ_0 in Eq. (3.57) by a local, space-dependent density. This will result in a self-energy depending both on time and space, that is a more complicated situation. The local fluctuations of the density give a contribution which is smaller, discussed in section 3.A.1.

3.A.1 Hybrid correlator

At first order of the interaction strength g, there exists another diagram where the disorder potential $V(r)$ is correlated with the effective nonlinear time dependent potential $g|\psi(x,t)|^2$. Diagrams representing this kind of scattering are shown in Fig. 3.19. We call such an object a *hybrid correlator*. Using the hybrid correlator, we can calculate the self-energy, similarly to the self-energy at the Born approximation in a linear system:

$$\Sigma_\epsilon^{(\mathrm{hybrid})}(k) = \frac{1}{2\pi}\int \mathrm{d}k'\, P^{\mathrm{NL}}(k-k') G_\epsilon^{(0)}(k'), \tag{3.58}$$

where the power spectrum is defined as

$$P^{\mathrm{NL}}(k) = 4g \int \mathrm{d}(x-x')\, e^{-ik(x-x')} \overline{|\psi(x,t)|^2 V(x')}, \tag{3.59}$$

where $4g$ comes from two contributions: factor $2g$ from two possibilities of pairing the lines (as in the nonlinear self energy) and a factor 2 because we have to include also diagrams for $\overline{|\psi(x',t)|^2 V(x)}$. To calculate the contribution of the diagram, we use Eq. (3.53) and explicitly write the propagators:

$$\begin{aligned}
&\overline{|\psi(x',t)|^2 V(x)} = \\
&\gamma \int \frac{\mathrm{d}\epsilon}{2\pi}\frac{\mathrm{d}\omega}{2\pi}\frac{\mathrm{d}k}{2\pi} e^{-i\omega t} I_{\epsilon,\omega}(k) \int \mathrm{d}x''\,\mathrm{d}x'''\, \overline{V(x')V(x''')} \times \\
&\Big[G_\epsilon^R(x,x'') G_\epsilon^A(x'',x''') G_\epsilon^A(x''',x'') + G_\epsilon^A(x'',x) G_\epsilon^R(x''',x'') G_\epsilon^R(x,x''') \Big].
\end{aligned} \tag{3.60}$$

To simplify the equation, we use the fact that $\overline{V(x)V(x')} = \gamma\delta(x-x')$ and also introduce the average energy distribution $f_\epsilon(t)$:

$$f_\epsilon(t) = \frac{1}{2\pi\nu_\epsilon}\int \frac{\mathrm{d}\omega}{2\pi}\frac{\mathrm{d}k}{2\pi} e^{-i\omega t} I_{\epsilon,\omega}(k), \tag{3.61}$$

where ν_ϵ is the average density of states. Then, the hybrid correlator may be written as

$$\begin{aligned}&\overline{|\psi(x',t)|^2 V(x)} = \\ &\gamma^2 \int \mathrm{d}\epsilon\, \nu_\epsilon f_\epsilon(t) \int \mathrm{d}x'' \left[G^R_\epsilon(x,x'')G^A_\epsilon(x'',x')G^A_\epsilon(x',x'') + G^A_\epsilon(x'',x)G^R_\epsilon(x',x'')G^R_\epsilon(x,x')\right].\end{aligned} \tag{3.62}$$

The final simplification uses the following identity:

$$\gamma \int \mathrm{d}x'\, G^R_\epsilon(x')G^A_\epsilon(x'-x) = i/(2\pi\nu_\epsilon)(G^R_\epsilon(x) - G^A_\epsilon(x)), \tag{3.63}$$

yielding:

$$\overline{|\psi(x',t)|^2 V(x)} = \frac{i\gamma}{2\pi}\int \mathrm{d}\epsilon\, f_\epsilon(t)\Big[\big(G^R_\epsilon(x',x)\big)^2 - \big(G^A_\epsilon(x,x')\big)^2\Big]. \tag{3.64}$$

In the weak disorder limit and for short time, the energy distribution remains sharply peaked at $\epsilon = \epsilon_0 = k_0^2/2m$ and we can easily perform the integral obtaining the final result:

$$\overline{|\psi(x',t)|^2 V(x)} = \frac{i\gamma}{2\pi\nu_{\epsilon_0}}\Big[\big(G^R_\epsilon(x',x)\big)^2 - \big(G^A_\epsilon(x,x')\big)^2\Big] \propto e^{-|x-x'|/2\ell_0}\sin(2k_0|x-x'|). \tag{3.65}$$

Comparison between the predictions of Eq. (3.65) and numerical data, unfortunately, has shown rather large discrepancies. For short time, we have observed that the exponential decay of the correlation function is faster than predicted by the theoretical approach. Only the oscillatory part was confirmed, however this is an obvious fact – the change of momentum during the scattering is always $2k_0$ in the weak disorder limit in one-dimensional systems. The probable reason of this difference lays in the theoretical assumptions used to derive this equation. The theory presented in this section was proposed to describe three- and two-dimensional systems in the diffusive regime, where a perturbative diagrammatic expansion is meaningful. On the contrary, the one-dimensional disordered systems are always localized, i.e. the diffusive approach and approximations are not valid in such systems. Nevertheless, the numerically observed $\overline{|\psi(x',t)|^2 V(x)}$ correlator is not widely different from the predictions of Eq. (3.65). We have calculated the values of the self-energy defined in Eq. (3.58) using the numerically calculated function $P^{\mathrm{NL}}(k)$. The results clearly show that this correction is much smaller than $g\rho_0$. This is to be expected: the self-energy correction originating from the hybrid correlator is $k_0\ell_0$ times smaller than first order correction.

A correct calculation of the hybrid correlator in one-dimensional system could possibly be obtained using the phase formalism introduced by H. Prüfer in [152]. The formalism initially founded to study Sturm-Liouville problems, see for example [153], was successfully applied to one-dimensional disordered quantum systems, e.g. [154–157]. Similar ideas were also successfully applied to *quasi*-two-dimensional systems, e.g. [158].

Altogether, it remains that the effect of the $\overline{|\psi(x',t)|^2 V(x)}$ correlator is much smaller than the dominant contribution computed in Eq. (3.57).

Chapter 4

Many-body quantum boomerang effect

After a detailed study of the boomerang effect in systems with mean-field interactions in chapter 3, here we attempt the quasi-exact approach. Apart from the study of weakly interacting bosons and fermions, we analyze the quantum boomerang effect in the Tonks-Girardeau gas, where impenetrable bosons are known to be fully Anderson localized.

The chapter starts with an introduction of the methods used to simulate many-body systems in section 4.1. In section 4.2 we also introduce the matrix product states, and the time evolving block decimation algorithm used in our simulations. Weakly interacting bosons are analyzed in section 4.3, where we make a comparison with the the mean-field approximation. In section 4.4 we compute the break times for weakly interacting bosons and show their connection with the interaction strength. Section 4.5 relates the observed results to the phenomenon of many-body localization. Simulations of the Tonks-Girardeau gas together with the numerical evidence for the presence of the full boomerang effect are the subject of section 4.6. In section 4.7, we analyze the impact of interactions for strongly interacting bosons, which map onto weakly interacting fermions. Finally, we show that the case of strongly interacting bosons can also be described by break times in section 4.8. In this section, we also show that this characteristic time scale may be related to other time scales present in the system. The chapter is concluded in section 4.9.

4.1 Simulations of the many-body system

4.1.1 Mapping to Bose-Hubbard model

Let us start, as before (cf. section 3.1) with a one-dimensional many-body bosonic Hamiltonian:

$$\hat{H} = \int \hat{\Psi}^\dagger(x)\Big(-\frac{\hbar^2}{2m}\Delta + V_{\text{ext}}(x) + \frac{U}{2}\hat{\Psi}^\dagger(x)\hat{\Psi}(x)\Big)\hat{\Psi}(x)\mathrm{d}x\,, \tag{4.1}$$

where $V_{\text{ext}}(x)$ represents the disorder, and U is the strength of the two-body contact potential. In the thermodynamic limit, in the absence of $V_{\text{ext}}(x)$, the Hamiltonian is integrable, and its ground state can be found exactly [159], using the famous Bethe ansatz. For nonzero external potential, the integrability is lost and different numerical methods have to be employed to study such systems.

In the following, we adopt the method introduced in [160] and map the Hamiltonian (4.1) to a model on a equidistant grid, where the position is given by $x_j = \Delta x j$, $j \in \mathbb{Z}$, and Δx is called a grid

(lattice) spacing. We start by expressing the field operators by

$$\hat{\Psi}(x) = \sum_j \psi_j(x)\hat{a}_j, \tag{4.2}$$

where $\hat{a}_j$ are bosonic annihilation operators with commutation relation $[\hat{a}_i, \hat{a}_j^\dagger] = \delta_{i,j}$, and the single-particle wave functions $\psi_j(x)$ are defined in the following way:

$$\psi_j(x) = \begin{cases} (\Delta x)^{-1/2} & \text{for } x \in \left[(j-\frac{1}{2})\Delta x, (j+\frac{1}{2})\Delta x\right], \\ 0 & \text{elsewhere} \end{cases} \tag{4.3}$$

so that $\psi_j(x)$ is a rectangular function centered around $x = x_j$. The lattice constant has to obey two conditions. The first is natural – the lattice spacing has to be much smaller than the average distance between the particles ρ^{-1}. The second comes from the interactions. In the model, we replace the true interaction potential by the short-range effective contact potential described by the scattering length denoted by a. It means that the lattice constant Δx should be much larger that the scattering length a. Both things considered, Δx has to fulfill:

$$a \ll \Delta x \ll \rho^{-1}. \tag{4.4}$$

In the discretization procedure, the integrals are replaced by sums and the derivative is expressed as the three-point stencil:

$$\frac{\partial^2 \hat{\Psi}(x_j)}{\partial x^2} \to \frac{\hat{\Psi}(x_{j-1}) - 2\hat{\Psi}(x_j) + \hat{\Psi}(x_{j+1})}{\Delta x^2}. \tag{4.5}$$

The resulting Hamiltonian has the form of a Bose-Hubbard Hamiltonian [161]:

$$\hat{H} = -J_0 \sum_j \left(\hat{a}_j^\dagger \hat{a}_{j+1} + \text{c.c.}\right) + V_j \sum_j \hat{n}_j + \frac{U_0}{2} \sum_j \hat{n}_j(\hat{n}_j - 1), \tag{4.6}$$

where the parameters J_0, U_0 and V_i are directly connected with the lattice constant and the parameters of Hamiltonian [1] (4.1):

$$J_0 = \frac{\hbar^2}{2m\Delta x^2}, \quad U_0 = \frac{U}{\Delta x}, \quad V_j = V_{\text{ext}}(x_j). \tag{4.7}$$

In (4.6) we have neglected the term $1/\Delta x^2 \sum_j \hat{n}_j$, which is nothing else than a constant energy shift $N/\Delta x^2$ since the number of particles in conserved. The mapping allows one to use a method developed for simulations of lattice models to study many-body bosonic systems.

We have mapped the continuous system to the Bose-Hubbard model. Let us mention that the model features a transition between Mott insulator and superfluid phases [162, 163] which was successfully observed in a cold atomic experiment [164], using an optical lattice (for more details see [165, 166]). However, in the $\Delta x \to 0$ limit, the parameter J_0/U_0 tends to infinity, like $1/\Delta x$. Then,

1. The final form of the Hamiltonian depends on the discretization scheme used for the derivative in Hamiltonian (4.1). We could have used a different stencil, e.g. a five point one. Besides improving the convergence of the derivative, it also changes the final form.

the average occupation number goes to zero, so that our model is always in the superfluid phase.

4.2 The model

4.2.1 Time-evolving block decimation algorithm

Bose-Hubbard model is not tractable analytically and is quite difficult for numerical studies. The dimension of the Hilbert space D_b grows exponentially both in the system size M (number of sites) and the particle number N, $D_b = (N+M-1)!/(N!(M+1)!)$. It implies that the simulations of large systems, where we discretize a continuous space fulfilling assumption given in Eq. (4.4), may be extremely difficult. On these grounds, we turn toward one of the most effective methods for simulations of quantum one-dimensional systems: the time-evolving block decimation (TEBD) approach. The method and algorithm were proposed by G. Vidal in [5, 6], and utilize matrix product state techniques.

Consider N identical bosons on M lattice sites. The full basis can be built using Fock states $|i_1, i_2, \ldots, i_M\rangle$, where, at each site, we may have up to N particles with the constraint that their sum is constant, i.e. $\sum_l i_l = N$. Then, any many-body state can be written in the following form:

$$|\Psi\rangle = \sum_{i_1,\ldots,i_N} c_{i_1,\ldots,i_M} |i_1, i_2, \ldots, i_N\rangle , \tag{4.8}$$

where $c_{i_1,\ldots,i_M}$ are complex coefficients. This form is not very convenient for numerical simulations. Instead, it is possible to express states using matrix product states (MPS, for reviews see [167–169]), in the form proposed by G. Vidal in [5]:

$$|\Psi\rangle = \sum_{\substack{\alpha_1,\ldots,\alpha_M \\ i_1,\ldots,i_M}} \Gamma^{i_1}_{1,\alpha_1} \lambda^{[1]}_{\alpha_1} \Gamma^{i_2}_{\alpha_1,\alpha_2}, \ldots, \Gamma^{i_M}_{\alpha_M,1} |i_1, i_2, \ldots, i_M\rangle . \tag{4.9}$$

At each site l, we introduce a set of matrices Γ^{i_l} and, at bonds between sites l and $l+1$ (lth bond), vectors $\lambda^{[l]}$. The indices i_l run from 0 to the maximal occupation $i_{\max}$; the indices α_l run from 1 to χ, which is an important MPS parameter called bond dimension. For sufficiently large χ (e.g. $\chi \geq D_b$) the representation of state $|\Psi\rangle$ is exact. However, for many interesting states an excellent approximation is obtained for a much smaller value of χ [2]. Using this state representation, the Schmidt decomposition of the state $|\Psi\rangle$ into subsystems A (containing sites 1 to l) and B (containing sites $l+1$ to M), simply reads:

$$|\Psi\rangle = \sum_{\alpha_l} \lambda^{[l]}_{\alpha_l} |A^{[1\cdots l]}_{\alpha_l}\rangle |B^{[(l+1)\cdots M]}_{\alpha_l}\rangle , \tag{4.10}$$

2. Note that G. Vidal considered spin-1/2 chains, so that $i_{\max} = 1$. For bosons, the proper choice of $i_{\max}$ is an additional degree of freedom in the approximation. Usually, the maximal occupation $i_{\max}$ is chosen so that the results are converged.

where the subsystems' states are expressed using the matrices Γ^{i_l} and vectors $\lambda^{[l]}$:

$$\begin{aligned} |A^{[1\cdots l]}_{\alpha_l}\rangle &= \sum_{\alpha_1,\ldots,\alpha_{l-1}} \Gamma^{i_1}_{1,\alpha_1}\lambda^{[1]}_{\alpha_1},\ldots,\Gamma^{i_l}_{\alpha_{l-1},\alpha_l}\,|i_1,\ldots,i_l\rangle \\ |B^{[(l+1)\cdots M]}_{\alpha_l}\rangle &= \sum_{\alpha_{l+1},\ldots,\alpha_M} \Gamma^{i_{l+1}}_{\alpha_l,\alpha_{l+1}},\ldots,\lambda^{[M-1]}_{\alpha_{M-1}}\Gamma^{i_M}_{\alpha_M,1}\,|i_{l+1},\ldots,i_M\rangle \end{aligned} \tag{4.11}$$

If the states are only slightly entangled, the $\lambda^{[l]}$ decay fast and the bond dimension can be low, while keeping an excellent approximation to the state. The key problem lays in calculating the matrices and vectors from the coefficients $c_{i_1,\ldots,i_M}$. This task can be done by performing a series of Schmidt decompositions of the state $|\Psi\rangle$ using SVDs [5]. The first SVD gives:

$$|\Psi\rangle = \sum_{i_1,\alpha_1} \Gamma^{i_1}_{1,\alpha_1}\lambda^{[1]}_{\alpha_1}\,|i_1\rangle\,|\Phi^{[2\ldots M]}_{\alpha_1}\rangle\,, \tag{4.12}$$

where $|\Phi^{[2\ldots M]}\rangle$ is the state describing sites 2 to M. The next SVD is applied to the state $|\Phi^{[2\ldots M]}\rangle$, which allows for the calculation of $\lambda^{[2]}$ and Γ^{i_2}. This way one can obtain the whole state $|\Psi\rangle$ in the MPS representation, Eq. (4.9). For simple states, e.g. Fock states, the decomposition is not needed, the vectors $\lambda^{[l]}$ and matrices Γ^{i_l} may be written explicitly.

The dimension of matrices Γ^{i_l} determines the amount of computational resources needed to perform numerical simulations. The effectiveness of the MPS representation decreases with the growth of states' entropy because of the growing χ needed for faithful state's approximation. Thus, only slightly entangled states can be simulated effectively.

The algorithm

When acting with the evolution operator on the state $|\Psi\rangle$, matrices Γ^{i_l} and vectors $\lambda^{[l]}$ change. In the following, we assume that the Hamiltonian describing the system consists only of single-site operators, for example, site particle number $\hat{n}_j$, and two-site operators, e.g. $\hat{a}^\dagger_j\hat{a}_{j+1}$. In the description of the algorithm, we focus on the more involving two-site operators. To simplify the presentation of the algorithm, we will explicitly write the dimensions of the various tensors, using the local Hilbert space dimension $d = i_{\max} + 1$ and the bond dimension χ.

Let us consider a two-site operator $\hat{O}$. Suppose we want to compute the result of its action on the state $|\Psi\rangle$ at sites $l+1, l+2$. The operator can be expressed in the local basis as a $d^2 \times d^2$ matrix:

$$O^{(i_{l+1}i_{l+2}),(i'_{l+1}i'_{l+2})} = \langle i_{l+1}, i_{l+2}|\,\hat{O}\,|i'_{l+1}, i'_{l+2}\rangle\,. \tag{4.13}$$

Because the operator acts on sites $l+1, l+2$, we need only to consider the vectors and matrices associated with these sites. If we introduce a 4-dimensional tensor ($d \times d \times \chi \times \chi$):

$$\Psi^{i_{l+1}i_{l+2}} = \lambda^{[l]}\Gamma^{i_{l+1}}\lambda^{[l+1]}\Gamma^{i_{l+2}}\lambda^{[l+2]}, \tag{4.14}$$

where the vectors λ have dimension χ, and Γ are 3-dimensional tensors with ($d \times \chi \times \chi$). We can

easily write down the action of the operator $\hat{O}$ on $\Psi^{i_l i_{l+1}}$:

$$\Phi^{i_{l+1}i_{l+2}}_{\alpha_l,\alpha_{l+2}} = \sum_{i'_{l+1},i'_{l+2}} O^{(i_{l+1}i_{l+2}),(i'_{l+1}i'_{l+2})} \Psi^{i'_{l+1}i'_{l+2}}_{\alpha_l,\alpha_{l+2}}. \tag{4.15}$$

The resulting 4-dimensional tensor $\Phi^{i_{l+1}i_{l+2}}$ has dimensions $(d \times d \times \chi \times \chi)$. The state after the action of $\hat{O}$ has to be re-expressed as a MPS, thus the structure of the matrices and vectors has to be restored. We group the 4 indices of $\Phi^{i_{l+1}i_{l+2}}$ into two composite indices $(\alpha_l i_{l+1})$, $(i_{l+2}\alpha_{l+2})$ of dimension $d\chi$, and perform SVD of the $d\chi \times d\chi$ matrix:

$$\Phi_{(\alpha_l i_{l+1}),(i_{l+2}\alpha_{l+2})} = \sum_{\alpha_{l+1}} U_{(\alpha_l i_{l+1}),\alpha_{l+1}} \tilde{\lambda}^{[l+1]}_{\alpha_{l+1}} (V^\dagger)_{\alpha_{l+1},(i_{l+2}\alpha_{l+2})}. \tag{4.16}$$

After the decomposition, the new $\tilde{\lambda}^{[l+1]}$ may contain $d\chi$ singular values. To keep the dimensions of the matrices and vectors constant, a truncation is used, and only χ the highest singular values are kept. The truncation is the main source of error in the algorithm. To restore the original form of the MPS, we define:

$$\tilde{\Gamma}^{i_{l+1}}_{\alpha_l,\alpha_{l+1}} = \left(\lambda^{[l]}\right)^{-1}_{\alpha_l} U^{i_{l+1}}_{\alpha_l,\alpha_{l+1}}, \quad \tilde{\Gamma}^{i_{l+2}}_{\alpha_{l+1},\alpha_{l+2}} = V^{i_{l+2}\dagger}_{\alpha_{l+1},\alpha_{l+2}} \left(\lambda^{[l+2]}\right)^{-1}_{\alpha_{l+2}}, \tag{4.17}$$

so that the Φ has the form (cf. the from of Ψ before applying $\hat{O}$, Eq. (4.14)):

$$\Phi^{i_{l+1},i_{l+2}} = \lambda^{[l]} \tilde{\Gamma}^{i_{l+1}} \tilde{\lambda}^{[l+1]} \tilde{\Gamma}^{i_{l+1}} \lambda^{[l+2]} \tag{4.18}$$

The action of the single-site operators is much simpler because they change only the matrices Γ^{i_l}. In practice one-site operators can be included into two-site operators.

To perform the time evolution of $|\Psi\rangle$, we act with the evolution operator e^{-iHt} on the whole state. We assume now that the Hamiltonian consists of only two-site operators,

$$\hat{\mathcal{H}} = \sum_l \hat{h}_l, \tag{4.19}$$

where $\hat{h}_l$ acts only on sites $l, l+1$. We can see that the whole set of $\hat{h}_l$ can be split into two families, acting on odd and even links:

$$\hat{\mathcal{H}} = \hat{\mathcal{H}}_o + \hat{\mathcal{H}}_e, \quad \hat{\mathcal{H}}_o = \sum_{\text{odd } l} \hat{h}_l \quad \hat{\mathcal{H}}_e = \sum_{\text{even } l} \hat{h}_l. \tag{4.20}$$

All operators from a given family commute with each other, i.e. $[\hat{h}_j, \hat{h}_{j+2}] = 0$. We can use this fact in the evolution procedure. If we denote by δt the small time step, the evolution operator can be expressed using a Suzuki-Trotter decomposition [126, 170]. For example, second order decomposition reads:

$$e^{-i\hat{\mathcal{H}}\delta t} = e^{-i\hat{\mathcal{H}}_o \delta t/2} e^{-i\hat{\mathcal{H}}_e \delta t} e^{-i\hat{\mathcal{H}}_o \delta t/2} + \mathcal{O}(\delta t^3). \tag{4.21}$$

As the operators from a given family (odd/even) commute, their action on a state can be calculated in parallel. Furthermore, higher order evolution operator decompositions can also be used, see [127, 170]. In our numerical scheme, we use the standard symmetric Trotter decomposition, as well

as the recently proposed fourth order expansions using 10 exponentials [171].

4.2.2 Matrix Product State and momentum kick

In this thesis, we concentrate on the dynamics of wave packets having nonzero initial velocities. For the single-particle wave functions, it means that we multiply a wave function with zero average velocity by a phase factor including the velocity e^{ik_0x}. When the state is in the MPS form, the procedure is quite different, we cannot multiply all matrices (or vectors) by the phase factor.

The kick acts on the state in configuration space, whereas the MPS is represented in a space which is a mixture of configuration space and Fock basis. Moreover, in our approach we want all of the particles to have the same initial velocity – we do not differentiate them. Fortunately, this can be achieved in a straightforward way.

The total phase imprinting the initial velocity should include factors for all particles:

$$\prod_{n=1}^{N} \exp(ik_0x_n) = \exp\left(ik_0 \sum_{n}^{N} x_n\right), \tag{4.22}$$

where n numbers the particles and k_0 represents the velocity by $v_0 = \hbar k_0/m$ with m being the particle mass. The sum inside the exponent may be rewritten using particle occupations at each site

$$\sum_{n}^{N} x_n = \sum_{l} i_l x_l. \tag{4.23}$$

This allows us to use the MPS representation. To kick the MPS, we modify the matrices Γ^{i_l} as:

$$\Gamma^{i_l} \to \Gamma^{i_l} \cdot e^{ik_0 i_l l \Delta x}. \tag{4.24}$$

The vectors $\lambda^{[l]}$ are not changed because the kick does not change the properties of the MPS links. Moreover, the proposed idea does not change the form of the MPS. In general, however, if one would want to kick only part of the particles, the situation would be much more difficult. The only solution then would be to split the particles into two separate groups which changes the MPS form as well as the forms of matrix product operators in the Hamiltonian.

4.2.3 Numerical simulations

The dynamics of a disordered many-body system were successfully studied using this approach. In [172], the many-body Anderson localization of solitons was analyzed. We follow the same ideas and use similar tools in the analysis. The disorder, as in the previous chapters, is a Gaussian uncorrelated disorder:

$$\overline{V(x)} = 0, \quad \overline{V(x)V(x')} = \gamma\delta(x - x'), \tag{4.25}$$

where γ is the disorder strength. Together with the state's energy, determined by the value of k_0, it gives the values of the mean free time and mean free path at the Born approximation (cf. section 1.2, Eqs. (1.36), (1.40)):

$$\tau_0 = \frac{\hbar^3 k_0}{2m\gamma}, \quad \ell_0 = \frac{\hbar^4 k_0^2}{2m^2\gamma}. \tag{4.26}$$

For the initial state, we have chosen a non-interacting Gaussian wave packet, similarly to section 3.2. To prepare the state in the MPS form, we have computed the ground state of N non-interacting bosons in a harmonic potential using imaginary time evolution. The frequency of the potential was chosen to match the desired initial wave packet width [3] . The resulting particle density $n_0(x)$

$$n_0(x) = \frac{N}{\sqrt{\sigma^2\pi}} e^{-x^2/\sigma^2}, \tag{4.27}$$

corresponds to the superposition of N single-particle wave functions (cf. section 3.2):

$$\psi_0(x, t=0) = \left(\frac{1}{\pi\sigma^2}\right)^{1/4} \exp(-x^2/2\sigma^2). \tag{4.28}$$

As the last step of preparation, the state was kicked, as described in section 4.2.2. As before, the parameters of the initial state σ and k_0 are chosen in such a way, that the single-particle wave function does not contain many momentum components, i.e. $\sigma k_0 \gg 1$.

The center of mass time evolution is studied through the particle density $n(x,t)$:

$$\langle x(t)\rangle = \sum_l x_l \, \overline{n(x_l, t)}, \tag{4.29}$$

where $\overline{(\cdots)}$ denotes the average over disorder realizations. The density $n(x_l,t) = \langle\Psi(t)|\hat{n}_l|\Psi(t)\rangle$ can be conveniently calculated using the MPS form of the state $|\Psi\rangle$. Because $\hat{n}_l$ acts only on a single site we split the state $|\Psi\rangle$ into three components: the subsystem containing sites $1,\ldots,l-1$, denoted $|\Phi^{[1,\ldots,l-1]}\rangle$, the subsystem containing sites $l+1,\ldots,M$, $|\Phi^{[l+1,\ldots,M]}\rangle$, and the state containing only site l, $|\Phi^{[l]}\rangle$, similarly to Eqs. (4.10), (4.11):

$$|\Psi\rangle = |\Phi^{[l+1,\ldots,M]}\rangle \, |\Phi^{[l]}\rangle \, |\Phi^{[l+1,\ldots,M]}\rangle \, . \tag{4.30}$$

In the calculation of the particle number, the states $|\Phi^{[1,\ldots,l-1]}\rangle$ and $|\Phi^{[l+1,\ldots,M]}\rangle$ factor out, because they do not contain any information about the site l. We are left only with the contribution of site l:

$$\langle\Psi|\hat{n}_l|\Psi\rangle = \sum_{\alpha_{l-1},\alpha_l,i_l} i_l \left(\lambda^{[l-1]}_{\alpha_{l-1}}\right)^2 \left(\lambda^{[l]}_{\alpha_l}\right)^2 \left|\Gamma^{i_l}_{\alpha_{l-1},\alpha_l}\right|^2 . \tag{4.31}$$

Even with MPS and TEBD approaches, the numerical calculations are extensive. Bearing in mind that the boomerang effect needs many disorder realizations to average properly, we have restricted ourselves to a rather small system, with short maximal time and weak interactions. The interactions lead to a fast increase of the entropy of entanglement [4], requiring an increasing value of χ to represent the many-body state faithfully.

The maximal time of the simulations has a similar effect. While, in a crude approximation, interactions decide on the rate of entanglement increase, the total simulation time sets the maximum value of the entropy. Hence, to perform longer simulations, higher values of χ are needed. Finally, the system size also plays a role, albeit it is less important than the value of MPS dimension χ.

3. Similarly to section 3.2 a Gaussian wave packet is not the ground state of the interacting system in a harmonic trap. Because the studied values of interaction strengths are small, we assume that this does not change significantly the results. Additionally, in the present section, we want to be consistent with the approach from section 3.2.

4. See Fig. 4.6 in section 4.5, where the entropy growth is discussed.

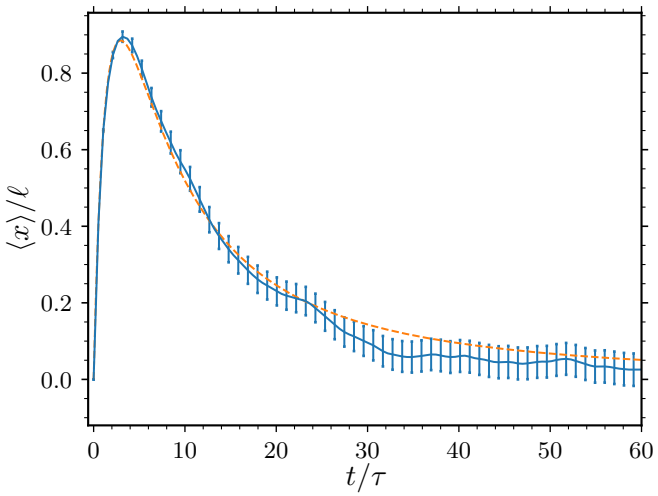

Figure 4.1. Comparison of simulations calculated for non-interacting bosons (solid line with error bars) and the theoretical single-particle prediction Eq. (1.80) (dashed line) using the same parameters of the system. The many-body simulations have been averaged over 1000 disorder realizations. The agreement between the curves is quite good (within the error bars) indicating that the TEBD simulations well reproduce the exact dynamics, in the absence of interactions.

We have to underline that the simulations are only quasi-exact, meaning that we can control the error by a proper choice of the parameters. Even though the simulations have been performed using a large computer grid structure, PL-Grid [5], converged results are obtained for low N only.

Similarly to the Gross-Pitaevskii study, we chose $1/k_0$ as the unit of length. The system size is $L_{\text{size}} = 400/k_0$, and the system is divided into $L = 2000$ lattice sites, so that the discretization $\Delta x = 0.2/k_0$ is the same as in the mean-field calculation, described in section 3.2. The disorder strength is chosen to be $\gamma = 0.1\hbar^4 k_0^3/m^2$ meaning that $k_0\ell_0 = 5$ so that the disorder is weak. In this study, we use only one width of the wave packet, $\sigma = 10/k_0$. This value allows for a modest size of the system, while, in the mean-field calculations, we have seen that $\sigma = 2\ell_0$ gives results which do not much differ from the results obtained for broader wave packets, see section 3.5.

The maximal time of simulations is, unfortunately, much shorter, $t_{\max} = 60\tau_0$ than in the GPE study. Nonetheless, this value allows us to observe the desired phenomenon. In our simulations, we have to keep the total number of particles quite low, $N = 5$. In this numerical scheme, higher values seem to be completely unattainable. In all numerical results, we assume that $k_0 = 1$, $m = 1$, and $\hbar = 1$. The many-body simulations have been averaged over 500 disorder realizations (unless otherwise stated). In the following section, we also present numerical results for the mean-field system, where the same parameters have been used, apart from the number of disorder configurations, which is 10^5.

4.3 Weakly interacting bosons

4.3.1 Non-interacting system

We start our study with a very simple but important check – observation of the boomerang for non-interacting bosons simulated using the TEBD algorithm. In Fig. 4.1 a comparison of the many-body (but without interactions) and the theoretical single-particle prediction Eq. (1.80) is shown. The results agree very well – as expected. For the numerical data, we compute the statistical errors, which are estimated by the errors of the average. To account for differences between the exact scattering mean free time τ (scattering mean free path ℓ) and the mean free time τ_0 (mean free path ℓ_0), we perform a fitting of the theoretical $\langle x(t)\rangle$, which yields $\tau = 0.94\tau_0$ and $\ell = 1.07\ell_0$. Figure 4.1 shows also that the statistical errors are quite large, of the order of 0.1ℓ. This shows how important is the total number of disorder configurations used in the simulations.

4.3.2 Comparison with the Gross-Pitaevskii equation

Similarly to the mean-field study, we expect that the interactions will destroy the full boomerang effect. The center of mass should be reflected and, during the return to the origin, it should saturate at some finite value of $\langle x\rangle$. This time, however, due to large values of the statistical errors, we focus on the comparison of many-body and mean-field results. The latter can be easily calculated with a much larger number of disorder realizations, so that the statistical errors are almost negligible.

Before we make an accurate comparison between the many-body and the mean-field results, we have to make an adjustment to the Gross-Pitaevskii equation. Usually, when the Gross-Pitaevskii equation is derived, it is assumed that the number of particles is very large, $N \gg 1$. When the equation is inferred from the energy functional, it takes the following form [117, 173]:

$$i\hbar\partial_t\psi(x,t) = \left(-\frac{\hbar^2}{2m}\Delta + V_{\text{ext}}(x) + U(N-1)|\psi(x,t)|^2\right)\psi(x,t). \tag{4.32}$$

If we put $g = U(N-1)$ we are back to the Gross-Pitaevskii equation, Eq. (3.9) from section 3.1.1. When $N \gg 1$ we can safely replace $N-1$ by N in the interaction term. However, when the number of particles is $N = 5$, we cannot make such a replacement.

In the analysis of the mean-field boomerang effect, one of our main conclusions is that the infinite-time position of the center of mass depends on the nonlinear energy, directly connected to the g factor. This means that to get a meaningful comparison of many-body and mean-field results, the GPE has to include the correct factor, i.e. in our case $g = U(N-1)$.
Note that when we simulate only one particle, $N = 1$, using such an approach, the many-body Hamiltonian and the GPE reduce (properly) to a non-interacting description.

In Fig. 4.2, we show comparisons of the results for many-body and mean-field systems for different interaction strengths. Unsurprisingly, we observe that, for nonzero interactions, the boomerang effect is only partial. After the initial evolution, typical for the boomerang effect, the center of mass does not return to the origin but saturates at some finite position. This closely resembles the behavior observed in the mean-field approach.

5. The processors used are Intel Xeon E5-2680v3 12C 2.5 GHz, with 24 threads available. The calculations were run in parallel (depending on the problem using either 6, 12 or 24 threads).

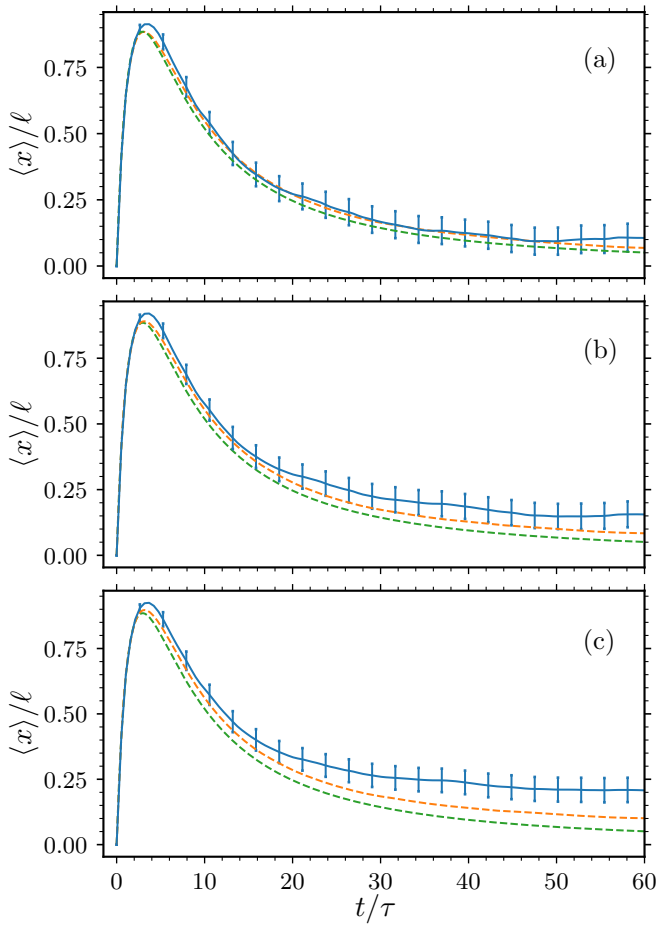

Figure 4.2. Comparison of results obtained in the many-body simulations (solid lines with error bars), the mean-field simulations (orange dashed lines), and the single-particle theoretical prediction, Eq. (1.80) (green dashed line). Panels correspond to (a) $U = 0.1$, (b) $U = 0.15$, and (c) $U = 0.2$. While for the lowest interaction between particles the curves seem to agree qualitatively (panel (a)), with the increase of the interactions the many-body result saturates at a significantly higher value. Many-body results are averaged over 500 disorder realizations.

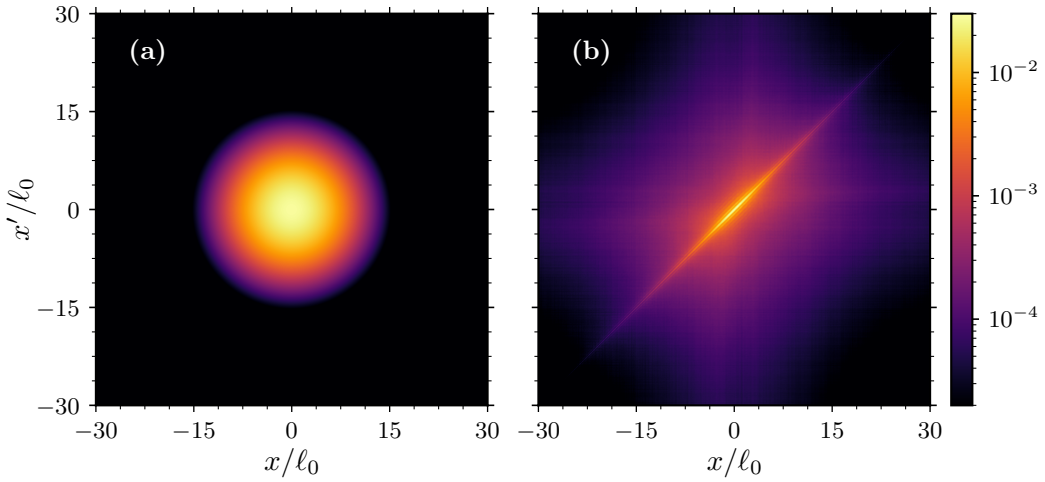

Figure 4.3. (a) The absolute value of the initial one-body density matrix $|\rho_0(x, x')|$, Eq. (4.37). (b) Average of the absolute value of the one-body density matrix $\overline{|\rho(x, x')|}$ of the final state for the interaction strength $U = 0.2$. During the time evolution, disorder destroys the initial correlation. The final average density matrix is correlated only around $x = x'$.

From the numerical side, in the case of $U = 0.05$ (not shown in Fig.4.2) and $U = 0.1$, we have used the bond dimension $\chi = 250$ and $i_{\max} = 5$, and the average CPU-time needed for simulation of a single disorder realization has been $t_{\text{CPU}} \approx 500$ CPUh. For $U = 0.15$ and $U = 0.2$ we have used $\chi = 350$ and $i_{\max} = 4$ (similar results have been obtained with $i_{\max} = 5$), with the total time $t_{\text{CPU}} \approx 850$ CPUh for a single disorder realization. Altogether, generating Fig. 4.2 thus requires $\sim 10^6$ CPUh.

As in the non-interacting case, the statistical errors of the many-body results are much higher. On the one side, it can be seen that, for the lowest presented value of interaction $U = 0.1$, the many-body and mean-field solutions are in agreement (within error bars). On the other side, when the interaction strength is higher, for example, in panels (b) and (c), the curves seem to separate and the many-body $\langle x(t)\rangle$ saturates significantly higher than the mean-field one.

The interactions present in the system may be understood as a source of dephasing mechanism which destroys Anderson localization, hence the boomerang. From this perspective, it should be natural that, when we treat the interactions without approximation, their impact should be larger, meaning that the final center of mass position could be higher. This would explain the increase in the positions of the saturation level. However, the simulations include only few particles (barely exceeding the regime of few body quantum mechanics). We cannot exclude that, in the limit of a very large number of particles, this difference vanishes.

Another fact that should also be taken into account is that the maximal time of the many-body simulations is much shorter than in our study of the mean-field system. Although there are no reasons to claim that, in the infinite-time limit, the many-body and mean-field results agree, it may be that the many-body $\langle x(t)\rangle$ is subject to some slow residual dynamics which decrease the final center of mass position.

4.3.3 One-body reduced density matrix

In order to study the difference between the many-body and the mean-field results, we analyze the one-body reduced density matrix. It is defined in the following way:

$$\rho(x,x') = \langle \hat{\Psi}^\dagger(x')\hat{\Psi}(x)\rangle, \tag{4.33}$$

and is frequently used to study correlations in many-body systems, see [117]. For a pure state $\Psi(x_1, x_2, \ldots, x_N)$ it is calculated as

$$\rho(x,x') = N \int \mathrm{d}x_2\, \mathrm{d}x_3\, \ldots \mathrm{d}x_N\, \Psi^*(x', x_2, \ldots, x_N)\Psi(x, x_2, \ldots, x_N). \tag{4.34}$$

The diagonal part of the density matrix is the particle density $\rho(x,x) = n(x)$, and it is normalized according to:

$$\int \rho(x,x)\mathrm{d}x\, = N. \tag{4.35}$$

We want to compare the average features of the one-body density matrix to a true condensate (described by the GPE). If the system is entirely in the condensate, i.e.

$$\Psi(x_1, \ldots, x_N) = \phi(x_1)\phi(x_2)\ldots\phi(x_N),$$

where $\phi(x)$ denotes the one-particle condensate wave function, the density matrix is simply given by:

$$\rho(x,x') = N\phi(x)\phi^*(x'). \tag{4.36}$$

For example, in our case, the initial density matrix is given by

$$\rho_0(x,x') = \frac{N}{\sqrt{\sigma^2\pi}} e^{-(x^2+x'^2)/2\sigma^2 + ik_0(x-x')}, \tag{4.37}$$

because we use a non-interacting initial state.

To study numerically the one-body density matrix, we have slightly changed the parameters of the system – we have increased the disorder strength, so that $k_0\ell_0 = 2.5$. We have checked that, in this situation, the many-body simulations also reproduce the results presented earlier in the section – the boomerang effect is only partial. To simulate the problem more efficiently, every single disorder realization simulation has been divided into temporal intervals where the bond dimension χ is progressively increased. The maximal bond dimension used $\chi_{\max} = 500$, with maximal occupation $i_{\max} = 4$, resulting in $t_{\mathrm{CPU}} \approx 1150$ CPUh.

Such parameters allow us to calculate the final state at $t_{\max} = 120\tau_0$, which should be a better approximation of the infinite-time limit. Figure 4.3 shows the initial density matrix, Eq. (4.37), and the average absolute value of the one-body density matrix, $\overline{|\rho_f(x,x')|}$ at the final time calculated for $U = 0.2$. Contrary to the initial density matrix, the final one is strongly correlated only around the diagonal, $x = x'$. This effect is caused by disorder, which destroys the initial correlation [6].

To quantitatively check the amount of the condensate fraction in the final density matrix, we have to compute the eigenvalues of $\rho(x,x')$, the largest one being the condensate fraction [174, 175].

6. Due to localization, using a single-particle approach, we expect the correlation to decay over one scattering mean free path ℓ, $\langle\psi^*(x')\psi(x)\rangle \sim \exp(-|x-x'|/\ell)$.

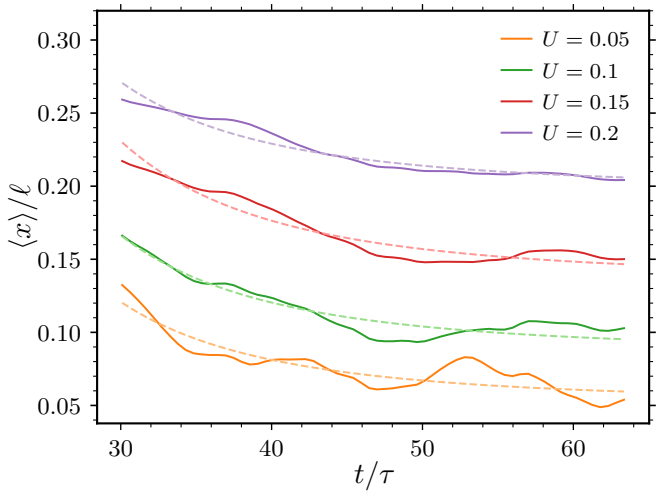

Figure 4.4. Time evolution of the center of mass (solid lines) in the interval $[30\tau, 64\tau]$ where a fitting of the algebraic decay (dashed lines), Eq. (4.42), is performed. When the exponent $\alpha = 3$ is used, the resulting fits yield very good results.

We diagonalize $\rho(x, x')$ as:

$$\rho(x, x') = \sum_j \lambda_j \chi_j(x) \chi_j^*(x'), \tag{4.38}$$

where λ_j are eigenvalues and $\chi_j(x)$ span an orthonormal basis. In non-interacting systems, the functions $\chi_j(x)$ correspond to single-particle wave functions and the eigenvalues are their occupations. When such a system is fully condensed, as, e.g. in the initial state Eq. (4.37), there is only one major eigenvalue, $\lambda_0 = N$ and $\chi_0(x)$ is the condensate wave function. When interactions are present, this approach may be generalized. The interactions decrease the value of λ_0, however

$$\sum_j \lambda_j = N. \tag{4.39}$$

The state is considered a condensate as long as $\lambda_0 \sim N$.

In our case, we calculate the average values of the four highest λ_j. It turns out that:

$$\overline{\frac{\lambda_0}{N}} \approx 0.15, \quad \overline{\frac{\lambda_1}{N}} \approx 0.11, \quad \overline{\frac{\lambda_2}{N}} \approx 0.09, \quad \overline{\frac{\lambda_3}{N}} \approx 0.06. \tag{4.40}$$

This shows that the final state of the system is very far from a true condensate. The Gross-Pitaevskii equation describes only the condensate fraction of the system, while our system mainly consists of particles outside the condensate, hence its dynamics cannot be accurately described by means of the Gross-Pitaevskii equation. This reinforces the conclusion that the difference between the numerical results of the many-body and mean-field systems comes from truly many-body effects.

4.4 Break time for weakly interacting bosons

Knowing that the boomerang effect for weakly interacting bosons is similar to the mean-field approximation, following the ideas of section 3.3, we try to extract the break time, a time scale after which the boomerang effect vanishes.

In the case of the mean-field approximation, to study the long-time center of mass position, we used the long-time average, calculated in the following way:

$$\langle x\rangle_\infty = \frac{1}{t_2 - t_1}\int_{t_1}^{t_2}\langle x(t)\rangle \mathrm{d}t\,. \tag{4.41}$$

For the weakly interacting bosons, the maximal time of simulation $t_{\max} \approx 64\tau$ is much shorter than in section 3.3, where the maximal evolution time extended over $2500\tau_0$. For example, in our simulations, even for the non-interacting case, the final CMP is nonzero. Because of this, we cannot trust the results computed using the average, Eq. (4.41). To overcome this problem, we fit an algebraic decay to the data:

$$\langle x(t)\rangle = \langle x\rangle_\infty + \frac{\beta}{t^\alpha}, \tag{4.42}$$

where $\langle x\rangle_\infty$ and β are fitting parameters. The fit is performed in the time interval $[30\tau, t_{\max} \approx 64\tau]$, where τ denotes the true mean free time extracted by fitting the theoretical boomerang effect prediction (see section 1.3.5, Eq. (1.80)) to the non-interacting results. We remind that for the non-interacting system the long time evolution of the center of mass reads (section 1.3.4, Eq. (1.77)):

$$\langle x(t \gg \tau)\rangle \approx 64\ell\frac{\ln(t/4\tau)\tau^2}{t^2}, \tag{4.43}$$

where τ and ℓ are the mean free time and mean free path. When $U = 0$, the exponent $\alpha = 2$ in Eq. (4.42) results in $\langle x\rangle_\infty = 0$. For nonzero interactions, we find that the decay is slightly faster and we put $\alpha = 3$. Figure 4.4 shows a comparison of the numerical data with fitted functions. The fits show very good agreement with the data. It also turns out that the overall fitting results, i.e. the values of $\langle x\rangle_\infty$, only slightly depend on the exponent value α in Eq. (4.42) and the time interval.

The next step is to calculate the break time t_b – characteristic time which has proven extremely useful in the study of the mean-field approximation, see section 3.5. It can be computed using the following relation (cf. Eq. (3.25)):

$$\langle x(t_b)\rangle_{\text{non-int.}} = \langle x\rangle_\infty(U), \tag{4.44}$$

where the left-hand side is the non-interacting theoretical prediction, Eq (1.80), and for the right-hand side we use the final CMP $\langle x\rangle_\infty$ from the fit of the algebraic decay, Eq. (4.42). Fitting errors on the $\langle x\rangle_\infty$ values allow us to compute the error bars on the break times.

In analogy to the mean-field study, we expect $1/t_b$ to be proportional to the counterpart of the nonlinear energy introduced in section 3.5.4. We use the interaction strength U, as a measure of the interaction energy in the system. The dependence of $1/t_b$ versus U is shown in Fig. 4.5, where we present the many-body results as well as the mean-field results (where $\langle x\rangle_\infty$ is calculated from the long-time average, Eq. (4.41)). While for the mean-field results the dependence is obviously linear, the meany-body result also suggests a linear behavior, with a small deviation of the point with $U = 0.05$. This point, the lowest value of the interaction, requires the longest time of evolution to saturate around the true $\langle x\rangle_\infty$ value. It means that the long-time CMP value may be overestimated, which leads to an underestimation of the break time. On the opposite side, for stronger interactions the linearity is better. This is also related to the fact that the final CMP values are higher, hence, to compute the break time, a shorter time evolution is needed.

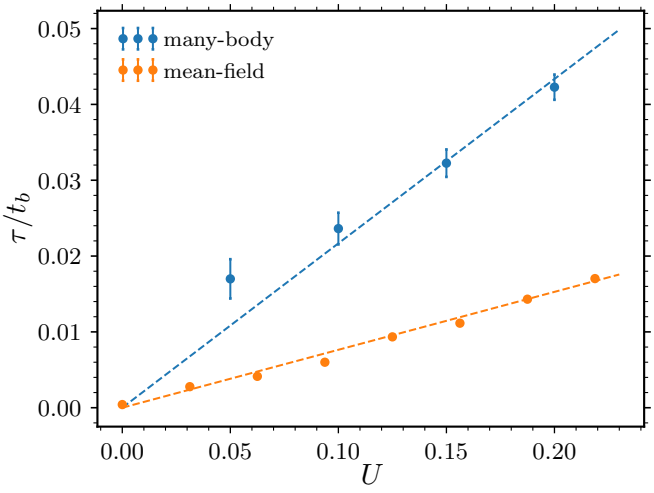

Figure 4.5. Inverse of the break time t_b computed for the many-body simulations (blue points with error bars, computed from the fits of the algebraic decay, Eq. (4.42)) and the mean-field simulations (orange points, calculated using long-time averaging, Eq. (4.41)) versus the interaction strength U. Dashed lines present the best linear fits $\tau/t_b = aU$, with slope coefficients $a_{\text{many-body}} = 0.22$ and $a_{\text{mean-field}} = 0.076$. The mean-field data is clearly linear, as expected. For the many-body results, with a small deviation of the point for $U = 0.05$, the points strongly suggest linear dependence. The error bars represent the error of the estimation of the break time based on the errors on the final CMP value.

Figure 4.5 clearly shows that the break times in many-body simulations are significantly shorter than in the mean-field approximation, what is also visible in Fig. 4.2. From the fitted linear functions (dashed lines in Fig. 4.5) we estimate that

$$\frac{t_b^{\text{many-body}}}{t_b^{\text{mean-field}}} \approx 0.35. \tag{4.45}$$

The fact that the break time is shorter for the full many-body calculation than in the mean-field approximation, emphasizes the importance of quantum fluctuations. This is also supported by the analysis of the average one-body density matrix in section 4.3.3.

4.5 Comment on many-body localization

Anderson localization describes non-interacting particles. For many years, the question of its fate in interacting systems was puzzling physicists. The field was revitalized by the seminal works of Gornyi, Mirlin and Polyakov [176], and Basko, Aleiner and Altshuler [177], where a perturbative approach led to the discovery of a new phenomenon called many-body localization (MBL). The works predict the existence of an insulating phase in disordered interacting many-body systems. In recent years, many-body localization has been intensively studied in numerous theoretical works (for reviews see [178, 179]) and observed using different experimental platforms [180–184].

Although we do not investigate many-body localization in detail, we cannot escape from making a comment on MBL and we make an attempt to relate the results obtained in our work to the known properties of the many-body localized systems.

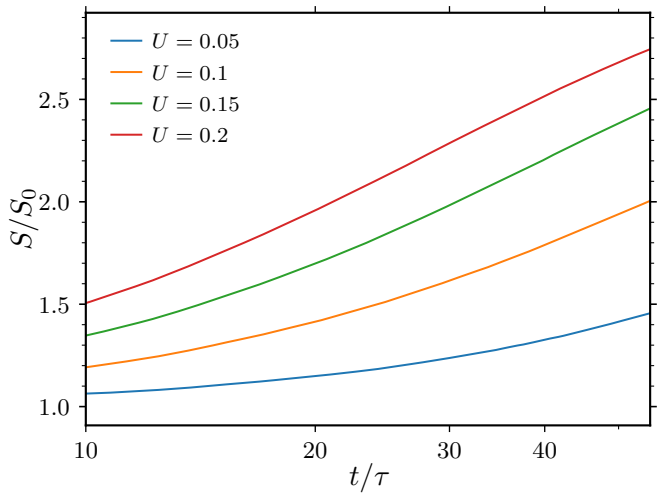

Figure 4.6. Time evolution of bipartite entanglement entropy $S(t)$ defined in Eq. (4.46), S_0 denotes the average long-time value of the entropy in the non-interacting system (approximately constant). The results show a hint of logarithmic growth for times $t > 30\tau$.

Our numerical method allows us to calculate the time dependence of the supremum of the entanglement entropy [172] over all possible bipartitions of the system:

$$S = \sup_{l} \left(-\sum_{\alpha_l} \left(\lambda_{\alpha_l}^{[l]}\right)^2 \ln\left(\lambda_{\alpha_l}^{[l]}\right)^2 \right), \tag{4.46}$$

where l runs over all links between sites. In a single realization of disorder, typically, the entropy is maximal at a single link around the center of the system. In generic many-body localized systems, the entanglement entropy is expected to grow logarithmically with time, $S \sim \ln(t)$, what was firstly observed numerically in [185, 186] and then proved theoretically in [187, 188].

The time evolution of the entanglement entropy defined by Eq. (4.46) is presented in Fig. 4.6. This result shows that the entropy in our system may indeed grow logarithmically. However, this should not be treated as a sign of many-body localization for several reasons. Typically, MBL is studied in systems with much higher interaction strengths (for example, see [189, 190]) than considered in our work, where $U_0/J_0 \ll 1$ (translating Δx, and U to Bose-Hubbard model parameters). The other ingredient are particles – in our system the average filling, taking into account only the sites occupied by the initial density profile, is also very low, $n \approx 0.1$. Together with the small number of particles considered, this cannot be compared to other studies of interacting bosons localized on a lattice.

Moreover, the maximal time of the evolution is probably too short to say whether the observed entropy growth is logarithmic. Lastly, the disorder strength used in our work corresponds to the Anderson localization weak disorder regime, which should not be sufficient to induce the many-body localization effect.

4.6 Strongly interacting bosons – Tonks-Girardeau limit

After the analysis of weakly interacting bosons, we now turn to the other extreme case – strong interactions. From the perspective of the earlier GPE analysis, this regime of interactions is new and may lead to phenomena absent in weakly interacting systems.

A one-dimensional system of bosons with repulsive contact interactions may be described by the Lieb-Liniger model, [159]:

$$H = \sum_{j=1}^{N} \left(-\frac{\hbar^2}{2m} \frac{\partial^2}{\partial x_j^2} + V_{\text{ext}}(x_j) \right) + U \sum_{1 \leq j < k \leq N} \delta(x_j - x_k), \tag{4.47}$$

where $U > 0$ is the coupling constant and m denotes the atom mass. The model is frequently characterized by a dimensionless parameter $\zeta = mU/\hbar^2 n$, where $n = N/L$ being the average density of bosons, and L is the system length. When $\zeta = 0$, the model corresponds to free bosons while $\zeta \to \infty$ is called the Tonks-Girardeau limit.

The Tonks-Girardeau gas describes impenetrable (or *hard-core*) bosons, which can be mapped to non-interacting spinless [7] fermions, [191, 192]. The model can be solved exactly in the free case $V_{\text{ext}} = 0$ (for details see [193]). Reference [194] proved that the Tonks-Girardeau gas can be obtained in cold atomic experiments, and the experimental observations of hard-core Rubidium bosons were reported shortly after in [195, 196].

The Tonks-Girardeau gas is highly correlated. However, it does not mean that the interactions destroy Anderson localization. Because the bosons are mapped to non-interacting fermions, Anderson localization is expected to be fully present in the system. The disordered non-interacting fermions are localized in a one-dimensional disordered system. Anderson localization of the Tonks-Girardeau gas is discussed in [197].

If Anderson localization is present, we expect that, for a wave packet with some initial velocity, we should observe the return to origin. To answer whether it still looks like the boomerang effect, we performed numerical simulations using the same approach as in the case of weakly interacting bosons.

The MPS representation has a parameter which describes the local Hilbert space. For simulations of N bosons, it is natural to set the maximal site occupation around the value of the total particle number, $i_{\max} \approx N$. This parameter can be also used in the other way – we can restrict the maximal occupation to be $i_{\max} = 1$, so that no more than one particle can reside at the same lattice site. This realizes the concept of impenetrability of the Tonks particles.

On the numerical side, our results have been simulated in a similar way to the weakly interacting bosons. The main difference is that, in the Tonks-Girardeau gas, we enlarged the discretization constant, so that $\Delta x k_0 = 1$. By using larger Δx, we can decrease the number of lattice sites in the simulations and scale down CPU-time. The main effect of larger Δx is its influence on the dispersion relation. As we show in the next sections, apart from the change of velocity due to worse discretization, the quantum return to the origin still can be analyzed.

7. In literature also: spin-polarized.

4.6.1 Initial state

In all previously studied cases, the initial state was given by a Gaussian wave packet. The Gaussian wave packet is the single-particle ground state of a harmonic trap. In the boomerang studies, we are always interested in initially localized states and the harmonic trap potential gives us a control over the initial width of the wave packet. However, for Tonks particles ($i_{\max} = 1$), a Gaussian wave packet cannot be considered as a proper ground state of the Tonks-Girardeau gas. Since hard-core bosons are mapped to non-interacting fermions, the ground state of the Tonks-Girardeau gas can be calculated exactly in the absence of the disordered potential.

Let $\psi_n(x)$ denote a single-particle eigenstate in the harmonic potential. In the case of non-interacting bosons, we assume that all of them are described by the eigenstate of the lowest energy, $\psi_0(x)$. When the particles are fermionic, they cannot occupy the same eigenstate, hence the state with the lowest energy has the following form in the Fock basis (ordered by increasing energy):

$$|\mathrm{GS}\rangle = |\underbrace{1\ldots1}_{N}0\ldots\rangle\,. \tag{4.48}$$

The occupation density can be calculated through $n_{\mathrm{GS}}(x) = \langle\hat{\Psi}^\dagger(x)\hat{\Psi}(x)\rangle_{\mathrm{GS}}$, where $\hat{\Psi}(x)$ and $\hat{\Psi}^\dagger(x)$ are field operators. Action of the field operator $\hat{\Psi}(x)$ on $|\mathrm{GS}\rangle$ produces a sum with single-particle eigenstates as weights:

$$\hat{\Psi}(x)\,|\mathrm{GS}\rangle = \sum_{n=0}^{N-1} \psi_n(x)\,|\mathrm{GS}\rangle_n\,, \tag{4.49}$$

where $|\mathrm{GS}\rangle_n$ denotes a Fock state with zero at the n-th position. Then the occupation density can be calculated easily, yielding

$$n_{\mathrm{GS}}(x) = \sum_{n=0}^{N-1} |\psi_n(x)|^2. \tag{4.50}$$

The resulting density is much broader than the ground state of the harmonic oscillator of the single-particle. It has N maxima, see Fig. 4.8. They can be viewed as the positions of classical particles repelling each other, residing in a confined space.

For practical purposes, the ground state of the Tonks-Girardeau gas in a harmonic trap is calculated using the imaginary time evolution. Application of this method guarantees that the state has a proper MPS structure and, after a kick as described in section 4.2.2, it is directly applicable to the real time evolution. The resulting numerical density can be compared with the theoretical one – indeed the agreement is excellent.

4.6.2 Boomerang effect in Tonks-Girardeau gas

Figure 4.7 presents the time evolution of the center of mass $\langle x(t)\rangle$ for the Tonks-Girardeau gas. The center of mass time evolution follows the single-particle boomerang effect. To show the agreement between the numerical data and the theoretical prediction (see section 1.3.5, Eq. (1.80)) we perform a refitting procedure which accounts for the difference between the exact mean free time τ (mean free path ℓ) and the mean free time τ_0 (mean free path ℓ_0) computed using the Born approximation. The simulations of the Tonks-Girardeau gas are fairly simple, in our case for $N = 5$ particles, bond dimension $\chi = 35$ was enough to approximate the system with the MPS efficiently,

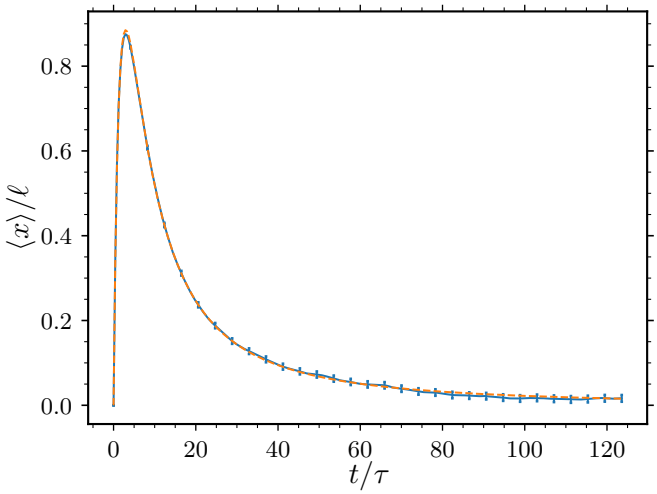

Figure 4.7. Time evolution of center of mass $\langle x \rangle$ for Tonks-Girardeau gas (solid blue line with error bars) compared with single-particle theoretical prediction (orange dashed line) section 1.3.5, Eq. (1.80). Result is fitted using theoretical boomerang prediction to rescale the mean scattering time τ and length ℓ. After rescaling the numerical data perfectly agrees with the theoretical curve. The results have been averaged over 10000 disorder realizations. Error bars represent statistical average uncertainties.

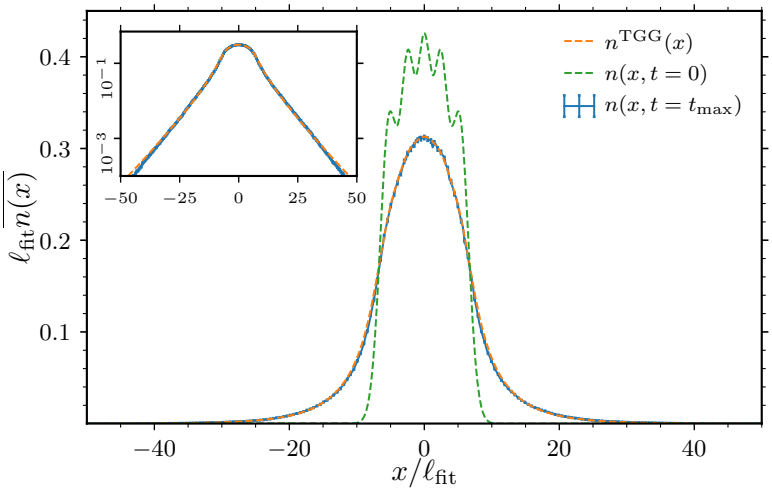

Figure 4.8. Final density profile for kicked hard core bosons (blue solid line with error bars), compared with the Tonks-Girardeau-Gogolin profile (dashed orange line) and the initial particle density (dashed green line), Eq. (4.50). The numerical data agrees fully with the theoretical Tonks-Girardeau-Gogolin profile $n^{\rm TGG}(x)$, Eq. (4.52). The inset shows the theoretical and numerical final profiles to show agreement even in the exponentially decaying tails.

yielding $t_{\mathrm{CPU}} \approx 0.15$ CPUh per disorder realization.

After refitting, the agreement between the Tonks-Girardeau gas and the theoretical prediction is excellent. The disorder strength used should result in $k_0\ell_0 = 5$. The fitted exact values of mean free time and path are $\tau = 0.97\tau_0$ and $\ell = 0.9\ell_0$, which means that the values are consistent with the Born approximation. There is, however, a slight complication. The particles of the Tonks-Girardeau gas have slightly different energies, because they are different eigenstates of the harmonic potential. This should mean that each particle has a different mean free time, hence $\langle x(t)\rangle$ should be a superposition of the boomerang curves with different τ.

The energy of the n-th eigenstate of the harmonic potential is $(n+\frac{1}{2})\hbar\omega$, where ω is the frequency of the potential. In our analysis we use kicked states, and the kick adds $\hbar^2k_0^2/2m$ to the total energy. If $\hbar^2k_0^2/2m \gg (n+\frac{1}{2})\hbar\omega$, we may assume that all states have roughly the same scattering mean free time and path. This is the case in our simulations, where $\omega = 0.01$. The small dispersion of energies does not influence the final $\langle x(t)\rangle$, and we observe the universal boomerang curve.

We also study the final particle density. It is symmetric and has exponentially decaying tails. Although [197] used a slightly different initial state (ground state of the trap including the disorder), a similar behavior of the tails in their simulations was reported. After our observation that the boomerang effect is described by a single-particle theoretical result, we construct an infinite-time density profile based on the (single-particle) Gogolin profile:

$$\overline{|\psi_\ell^{\mathrm{Gogolin}}(x, t=\infty)|^2} = \int_0^\infty \frac{\mathrm{d}\eta\,\pi^2}{32\ell} \frac{\eta(1+\eta^2)^2 \sinh(\pi\eta) e^{-(1+\eta^2)|x|/8\ell}}{(1+\cosh(\pi\eta))^2}, \tag{4.51}$$

which depends on the mean free path. Analogously to section 2.7.2, the final density should be given by the convolution of the Gogolin profile with the initial particle density $n_{\mathrm{GS}}(x)$:

$$\overline{n^{\mathrm{TGG}}(x)} = \int_{-\infty}^{+\infty} \mathrm{d}x'\, n_{\mathrm{GS}}(x-x') \overline{|\psi_\ell^{\mathrm{Gogolin}}(x')|^2}, \tag{4.52}$$

The initial density is a sum of separated densities of consecutive harmonic oscillator eigenstates.

In the analysis of the final density profile, we also fit $\overline{n^{\mathrm{TGG}}(x)}$ to numerical data. The numerical calculation of the Tonks-Girardeau-Gogolin profile for $x/\ell \gg 1$ is laborious, thus we fit the profile only around $x = 0$ for several points. The value of the fitted mean free path is $\ell_{\mathrm{fit}} \approx 4.025/k_0$. The mean free path extracted from the center of mass $\langle x(t)\rangle$ is $\ell = 4.5/k_0$. Taking into account the fact that $\ell_0 k_0 = 5$, so that corrections to the Born approximation may be visible, the agreement between ℓ_{fit} and ℓ is good.

Figure 4.8 shows both the numerical and fitted final densities as well as the initial density profile. Even this very crude fitting method gives us very good results – the numerical and theoretical infinite-time densities agree very well. The inset presenting the densities in a logarithmic scale shows almost no difference far from the region of fit. Similarly to the center of mass, we could expect to observe a superposition of Tonks-Girardeau-Gogolin profiles with different values of ℓ. However, because the differences between the energies of the component states are small, the final result can be fitted with a single curve. The initial maxima in the profile are completely lost in the final density. The final density is symmetric around the origin, hence we observe the full return to the origin.

4.7 Strongly interacting bosons – mapping to weakly interacting fermions

For an arbitrary interaction strength in Hamiltonian (4.47), the bosonic model can be mapped to interacting fermions [198–200]. The interaction is much more complicated, it maps to a momentum-dependent attractive interaction [201]. The fermions are governed by the following Hamiltonian:

$$H_F = \sum_{j=1}^{N} \left(-\frac{\hbar^2}{2m} \frac{\partial}{\partial x_j} + V_{\text{ext}}(x_j) \right) + V_F, \tag{4.53}$$

where V_F denotes the fermionic interaction term:

$$V_F = \frac{\hbar^4}{m^2 U} \sum_{1 \le j < k \le N} \left(\frac{\partial}{\partial x_j} - \frac{\partial}{\partial x_k} \right) \delta(x_j - x_k) \left(\frac{\partial}{\partial x_j} - \frac{\partial}{\partial x_k} \right). \tag{4.54}$$

The eigenfunctions of the Lieb-Liniger Hamiltonian Eq. (4.47) coincide with the eigenstates of Hamiltonian (4.53) when particle coordinates x_j are ordered and their sign is changed upon exchange of the particle coordinates. The models have the same eigenspectra.

Strongly repulsive bosons map to weakly attractive fermions with, assuming no disorder and no traping potential, Fermi momentum $k_F = n\pi$, with the Fermi energy $E_F = n^2\pi^2\hbar^2/2m$, where n is the average density [200]. The mapping can be used to study systems in different potentials including disordered ones, e.g. [202] studies the fluid-insulator transition for strongly interacting bosons.

In section 4.2.3, we argued that the simulations of disordered many-body systems are very difficult and require large amounts of computational resources. To compute simulations of strongly interacting bosons (mapping to weakly interacting fermions), we allow only two particles at one site, $i_{\max} = 2$. In the case of weak interactions, such constraint would for sure change the results and simulations would not be faithful. On the other hand, when the interactions are strong, the probability of having more than two particles at one site is small [8]. This trick greatly reduces the cost of simulations. We note that the fermionic interaction strength is proportional to U^{-1}, see Eq. (4.54). In order to simplify the notation, in the following sections we use $U_F = U^{-1}$ to represent the interaction strength between the fermions.

In the study of weakly interacting bosons, the anticipations about the possible outcome were based on the mean-field treatment. Now, with weakly interacting fermions, we do not have such help, hence our simulations are more expensive. This is the reason why we increase Δx from $\Delta x k_0 = 0.2$ to $\Delta x k_0 = 1$. This move allows us to save the computational resources and calculate the time evolution for longer times than for weakly interacting bosons.

4.7.1 Destruction of the boomerang effect

At the qualitative level, the effect of interactions on the boomerang effect should not depend on their details. For strongly interacting bosons, mapping to weakly interacting fermions, we also expect that interactions will weaken Anderson localization. The interactions, which are considered

8. Remember that also the total number of particles is rather low, $N = 5$ and that the interaction energy in the Bose-Hubbard model for n particles at the same site is $Un(n-1)/2 = 3U$ for $n = 3$.

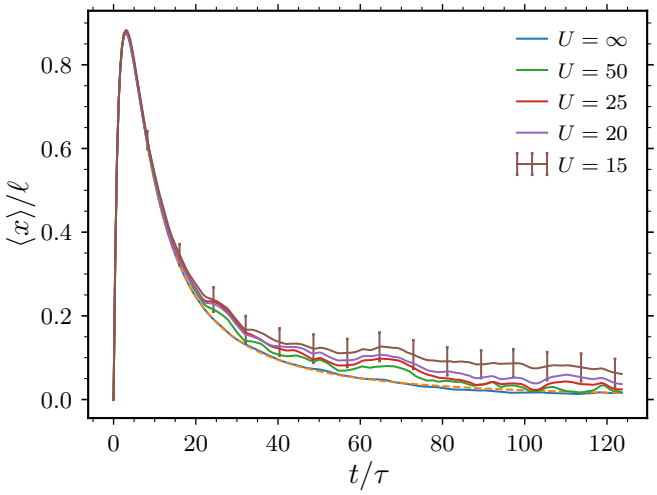

Figure 4.9. Center of mass time evolution for different values of interactions U. Similarly to mean-field and weakly interacting bosons, the short time evolution is almost unaffected by interactions. At longer times, the center of mass saturates are some finite values. Error bars indicate statistical average errors and are shown only for one curve to indicate their magnitude.

as an effective dephasing mechanism, lead to the destruction of coherence between scattering paths, and finally to destruction of the full boomerang effect.

Figure 4.9 presents the result of the center of mass time evolution. Similarly to the non-interacting case, after the initial ballistic evolution, the center of mass is reflected towards the origin. Analogously to the mean-field and weakly interacting bosonic cases, the destruction of the boomerang effect is visible in the long time regime. For all situations with non-infinite U (nonzero effective interaction between fermions U_F), we observe that the return is not complete: the CMP saturates at some nonzero value. The figure shows also the statistical error bars. Because the number of disorder realizations is small, the errors are relatively large. Nonetheless, the effect of interactions is clearly visible and can be analyzed taking into account the uncertainties. The limited maximal time of evolution does not allow us to study in detail the mean square displacement of the particle density.

The numerical simulations have been divided into temporal intervals with growing bond dimension. In all simulations $i_{\max} = 2$, and the following maximal bond dimensions have been used:

$$\begin{aligned} U = 50: &\quad \chi_{\max} = 820, \quad t_{\mathrm{CPU}} \approx 720 \text{ CPUh}, \\ U = 25: &\quad \chi_{\max} = 680, \quad t_{\mathrm{CPU}} \approx 330 \text{ CPUh}, \\ U = 20: &\quad \chi_{\max} = 530, \quad t_{\mathrm{CPU}} \approx 140 \text{ CPUh}, \\ U = 15: &\quad \chi_{\max} = 390, \quad t_{\mathrm{CPU}} \approx 55 \text{ CPUh}. \end{aligned} \tag{4.55}$$

The computation times denote the time used for a single disorder configuration.

The main observation is that the boomerang effect is only partial, even though the effective interactions between fermions are attractive and fairly complicated. There is no qualitative difference between the results of the mean-field approximation, weakly interacting bosons and weakly interacting fermions. Interactions weaken the quantum boomerang effect.

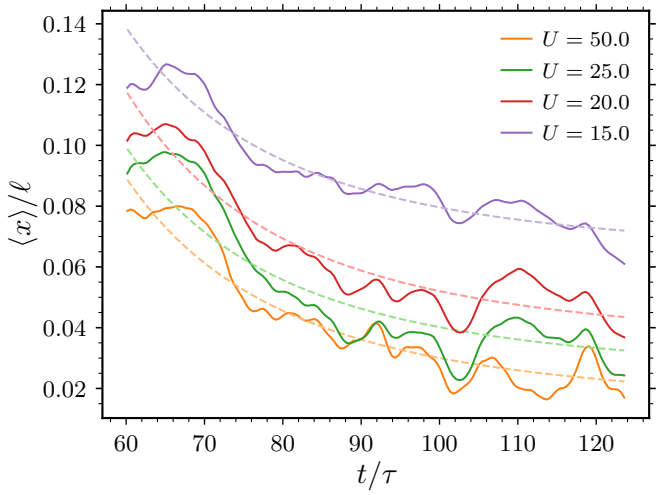

Figure 4.10. Time evolution of the center of mass in the interval $[60\tau, 120\tau]$ (solid lines) and fits of the algebraic decay, Eq. (4.56) (dashed lines). Similarly to Fig. 4.4, with the exponent $\alpha = 3$, the resulting fits yield satisfactory results.

4.7.2 Final center of mass position

Similarly to the study of the boomerang effect in the mean-field approximation in section 3.3 and the weakly interacting bosons in section 4.4, we analyze the final center of mass position. Even though the calculations for strongly interacting bosons have larger maximal time, the observed destruction of the boomerang is smaller – saturation levels are much closer to the non-interacting curve. Moreover, similarly to the weakly interacting bosons, the non-interacting CMP is significantly above zero, even near the final time of the simulation.

Once again, instead of calculating the long-time average Eq. (4.41), we use the algebraic fit in the time interval $[60\tau, 120\tau]$:

$$\langle x(t) \rangle = \langle x \rangle_\infty + \frac{\beta}{t^\alpha}, \tag{4.56}$$

where $\langle x \rangle_\infty$ and β are fitting parameters. Analogously to the weakly interacting bosons, we expect that for the exponent $\alpha = 2$, the fit for the non-interacting will return $\langle x \rangle_\infty = 0$. This is the case. Moreover, for the nonzero values of $U_F = U^{-1}$ we take $\alpha = 3$ (as in section 4.4). Figure 4.10 shows a comparison of the numerical data with fitted functions. The data shows high correlation between different interaction strengths because we use the same disorder realizations. Also in this case, we have checked that the overall fitting result is almost independent of the exponent value α in Eq. (4.56).

In Fig. 4.11, we present the dependence of the final CMP on the effective interaction strength U_F between fermions. Likewise, in the case of the mean-field approximation, section 3.3.2, for the smallest values of the interaction strength, the dependence seems to be quadratic. This confirms that the observed breakdown of the full boomerang effect does not depend on the details of the interactions present in the system.

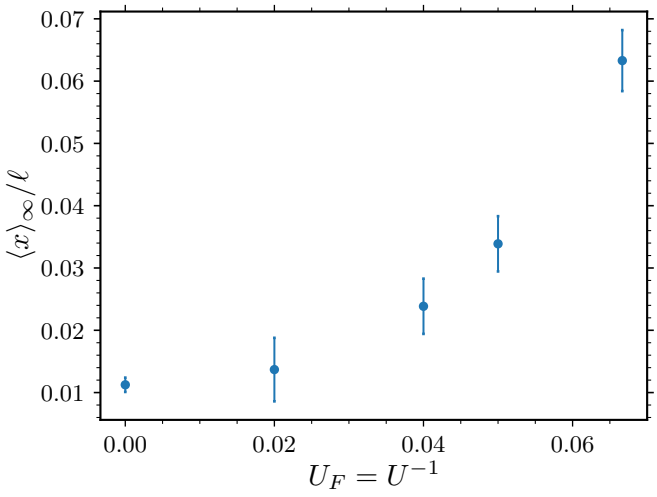

Figure 4.11. Final center of mass position $\langle x \rangle_\infty$ versus $U_F = U^{-1}$. The errors for the points result from the fitting of the decay Eq. (4.56). Alike in the mean-field study, the dependence of the final CMP on the effective interaction strength between fermions $U_F = U^{-1}$ is quadratic.

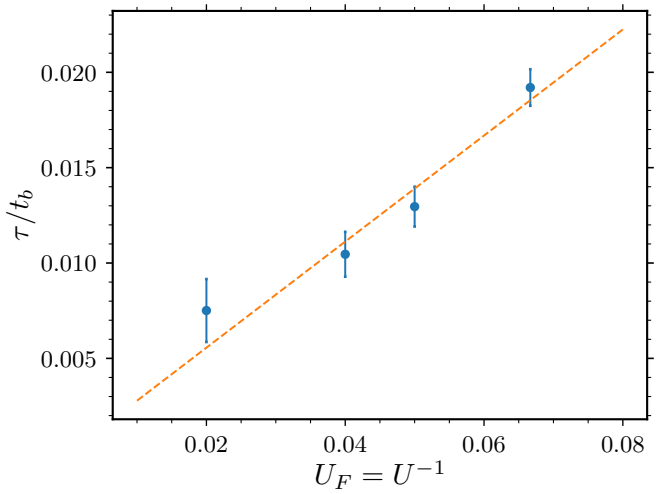

Figure 4.12. Inverse of the break times t_b versus $U_F = U^{-1}$ calculated for the final center of mass $\langle x \rangle_\infty$ by fitting an algebraic decay, Eq. (4.56). The errors are calculated using the errors of $\langle x \rangle_\infty$. The data strongly suggests linear dependence. The dashed line presents the best linear fit $\tau / t_b = 0.28 U_F = 0.28/U$.

4.8 Break time for strongly interacting bosons

Given the results presented in the previous section, we may ask whether the destruction of the boomerang effect for strongly interacting bosons can be effectively described using the break time, a universal parameter introduced in section 3.5 (see Eq. (3.25) and Eq. (3.26)).

4.8.1 Break time – boomerang effect

For the weakly interacting bosons, the use of break time was a natural extension of the mean-field approximation. In the case of strongly interacting bosons (mapping to weakly interacting fermions), this has to be analyzed in detail. Figure 4.11 shows the approximately quadratic dependence of $\langle x\rangle_\infty$ on the effective interaction strength between fermions U_F. We, once again, remind the long time evolution of the center of mass

$$\langle x(t \gg \tau)\rangle \approx 64\ell \frac{\ln(t/4\tau)\tau^2}{t^2}, \tag{4.57}$$

which, if we neglect the logarithmic part, supports the idea of calculating the break time based on the t^{-2} decay. Analogously to the case of weakly interacting bosons, the break time is computed from (cf. Eq. (4.44))

$$\langle x(t_b)\rangle_{\text{non-int.}} = \langle x\rangle_\infty(U), \tag{4.58}$$

where the left hand side is the non-interacting theoretical prediction. For the right-hand side, we use $\langle x\rangle_\infty$ extracted from the fits.

This time, we expect $1/t_b$ to be proportional to the fermionic counterpart of the nonlinear (interaction) energy introduced for the mean-field analysis (cf. section 3.5.4). From the form of the fermionic interaction term, Eq. (4.54), we see that $U_F = U^{-1}$ is a measure of the interaction energy.

Figure 4.12 shows the dependence of $1/t_b$ on the effective interaction $U_F = U^{-1}$ suggesting a linear behavior. Similarly to the weakly interacting bosons case, the point for the weakest interactions slightly deviates from the linear dependence. When the boomerang effect is only moderately affected by the interactions, the time evolution has to be very long to extract the exact value of the final CMP. When $\langle x\rangle_\infty$ are overestimated, the corresponding t_b are smaller than the exact break times.

Nonetheless, the results are very similar to the ones obtained for the mean-field approximation, see section 3.5, and for the weakly interacting bosons, see Fig. 4.5. It means that the underlying mechanism of the destruction of the boomerang effect is similar, independently of the type of interaction. The destruction of the boomerang may be fully characterized by a single parameter, the break time t_b, proportional to the interaction strength between the particles.

4.8.2 Break time for the entropy of entanglement

In the simulations, we can also observe another interaction-driven phenomenon, which can be characterized by its own time scale. Due to the interactions, we observe a growth of the entropy of entanglement in the system. Does it increase on the same time scale t_b?

Figure 4.13 shows the time evolution of the entropy of entanglement averaged over the possible bipartitions. For the Tonks-Girardeau gas case, apart from the initial growth, the entropy saturates, what is also confirmed by the analysis of the supremum of the entropy. We denote the final value of

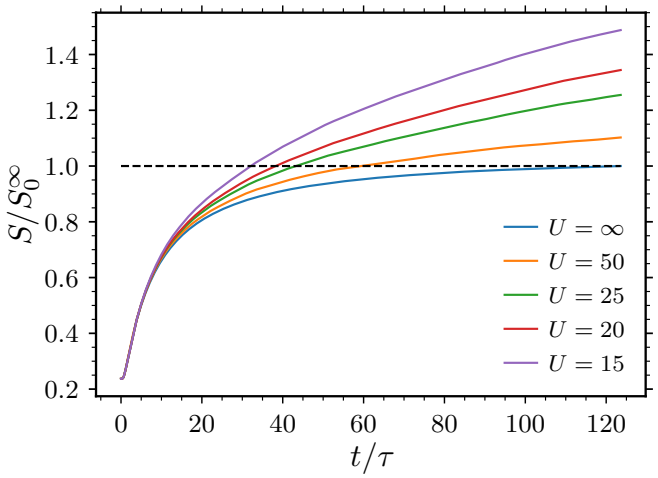

Figure 4.13. Time evolution of the entropy of entanglement (average over all possible bipartitions) for different values of the interaction strength U. S_0^∞ denotes the final value of the entropy in the Tonks-Girardeau gas.

the entropy for the Tonks-Girardeau gas by S_0^∞. When the interactions are not infinite, the entropy grows further.

We can define a characteristic time scale called entropy break time, denoted by t_b^S, for which the entropy between the interacting particles exceeds the final value of the Tonks-Girardeau gas entropy S_0^∞. We calculate its value from the following relation:

$$S(t_b^S)(U) = S_0^\infty, \tag{4.59}$$

where for the left-hand side, we use the data for nonzero interactions. Figure 4.14 presents a comparison of the boomerang break times and entropy break times. The relation between the break times is approximately linear. The ratio between the break times is similar for all points, approximately equal to $t_b^S/t_b \approx 0.5$.

There is yet another time scale that we can compare with our results. Bose-Hubbard model, Eq. (4.6), for strong repulsion $U_0 \gg J_0$ can be effectively described by the Heisenberg XXZ spin chain where doubly occupied lattices are mapped to spin-up states and empty sites to spin-down states [203–205]. The characteristic time scale of the spin system is given by U_0/J_0^2. It turns out that the boomerang break times (expressed in units of the scattering mean free time) agree within several percent with the characteristic times coming from the spin chain:

$$\begin{aligned}
U_0 = 50 \quad & \frac{U_0}{J_0^2} = 200 \qquad t_b = 133.2\tau, \\
U_0 = 25 \quad & \frac{U_0}{J_0^2} = 100 \qquad t_b = 95.6\tau, \\
U_0 = 20 \quad & \frac{U_0}{J_0^2} = 80 \qquad t_b = 77.2\tau, \\
U_0 = 15 \quad & \frac{U_0}{J_0^2} = 60 \qquad t_b = 52.1\tau.
\end{aligned} \tag{4.60}$$

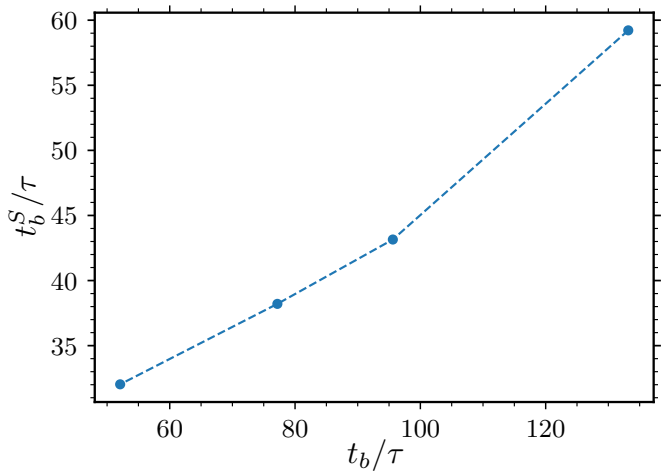

Figure 4.14. Entropy based break times t_b^S plotted versus boomerang break times t_b. The values of break times are comparable within a factor 2. The dependence is more or less linear, the slight deviation for the point around $t_b \approx 130\tau$ originates probably in the overestimation of the $\langle x \rangle_\infty$ due to too short time evolution.

As explained above, the break time for the highest interaction strength U_0 is underestimated.

The last observation together with the fact that $t_b^S \approx 0.5 t_b$ strongly suggests that the destruction of the quantum boomerang effect can be characterized by the same time scale as other many-body phenomena existing in the system. Such observation goes far beyond the mean-field analysis and shows that the destruction of Anderson localization in many-body systems may be grasped using the same tools which allow to exhibit the effects of interactions in many-body systems.

4.9 Conclusion

In this chapter we have discussed the effect of interactions on the quantum boomerang effect using quasi-exact many-body approach. On the numerical side, the simulations have been performed using the time evolving block decimation algorithm based on matrix product states. This has allowed us to study the weakly interacting bosons, the Tonks-Girardeau gas, and strongly interacting bosons, which can be mapped to weakly interacting fermions.

The first part of our study has shown that the effect of weak interactions between the bosons is qualitatively similar to the behavior in the mean-field approximation. This time, however, the interactions are not approximated, which strengthens their effect on the destruction of the boomerang effect: the final center of mass positions are higher than in the mean-field approximation. This translates to shorter break times of the many-body system. In the simulations, the total number of particles is not very high, so, to support this conclusion, we have also analyzed the features of the average one-body density matrix which have clearly shown that the condensate fraction in our system is very low. Hence, the observed phenomena are necessarily exceeding the mean-field analysis.

In the second part of the chapter, we have shown that the particles of the Tonks-Girardeau gas undergo the full boomerang effect. Apart from agreement between the numerical and theoretical

results for the center of mass evolution, we have shown that the final particle density is given by a convolution of the Gogolin profile and the initial particle density. In the presence of non-infinite interactions between bosons (that is, effective weak interactions between fermions), the boomerang effect is only partial. To study the destruction of the boomerang effect in detail, we have calculated the break time and shown that is proportional to the interaction strength between bosons, i.e. inversely proportional to the effective interaction strength between the fermions. Moreover, from the analysis of the entropy of entanglement, we have computed another characteristic time and shown that this time is comparable and proportional to the break time.

To understand better the presented results, simulations with a larger number of particles should be performed as a continuation of this work, e.g. for $N = 10$ particles. In [172], many-body Anderson localization of a bright soliton was studied from the perspective of the composite particle. It would be very interesting to check whether such a composite object undergoes the quantum boomerang effect. Another perspective could be an investigation of the boomerang effect in systems with different interaction models. Furthermore, a very interesting study of the boomerang effect could be performed in the regime of higher interactions and disorder strengths. This might allow for making more connections with the many-body localization phenomenon, although it may require huge computer resources.

Conclusion

In this thesis, we have investigated various aspects of the quantum boomerang effect, a newly discovered phenomenon present in Anderson localized disordered systems. We have studied the influence of time reversal symmetry breaking on the existence of the phenomenon and analyzed the impact of interactions using the mean-field approximation and a quasi-exact approach.

Summary of the results

In chapter 2, we have studied a one-dimensional system with spin-orbit coupling, which breaks time reversal invariance and all anti-unitary symmetries. Until now, the fate of the boomerang effect in systems without time reversal invariance was not known. We have directly shown that time reversal invariance of the system is not a necessary condition for the quantum boomerang effect. The classical picture is very similar to the one in systems with time reversal invariance: after the initial ballistic evolution, particles localize at a finite distance. Using a generalization of the Berezinskii diagrammatic technique, we have calculated, in a quasi-analytic form, the quantum prediction for the temporal evolution of the center of mass which agrees perfectly with the quantum numerical simulation. The result confirms that the particle returns to its origin at very long time. In contrast to the time reversal invariant system, the theoretical solution is not universal. It depends on an additional parameter. Furthermore, we have shown that the final wave packet density is described by the Gogolin profile.

The analysis of the impact of the interactions on the quantum boomerang effect consists of two parts. In chapter 3, we have thoroughly investigated the problem using the mean-field approximation. For nonzero interactions, we have observed a partial destruction of the boomerang effect. After the initial evolution and reflection of the center of mass, it saturates at a finite position. The interactions are viewed as a time-dependent fluctuating potential which weakens Anderson localization, hence the boomerang effect. In addition to wave packets, we have performed the analysis of the boomerang effect for plane waves. The numerical results have led us to an important parameter that universally characterizes the destruction of the boomerang effect: the nonlinear energy. This parameter captures all features of the destruction of the boomerang effect.

The second part of the study of interactions has used a quasi-exact approach to many-body systems. Chapter 4 includes the analysis of weakly interacting bosons, the Tonks-Girardeau gas, and strongly interacting bosons. The numerical simulations have been based on the time-evolving block decimation algorithm employing matrix product states. For weakly interacting bosons, we have observed the destruction of the boomerang, similar to the mean-field study. In this case, however, the effect of the interactions is stronger. Analyzing the average one body density matrix, we have shown that the final state is far from a Bose-Einstein condensate. It shows that quantum corrections,

absent in the mean-field approximation, have a strong effect on the destruction of the boomerang effect. Break times, i.e. time scales at which the boomerang effect is destroyed, calculated from the many-body simulations are significantly shorter than in the mean-field approach.

For the Tonks-Girardeau gas, we have observed the full quantum boomerang. The particles in a disordered Tonks-Girardeau gas are Anderson localized. Hence, the boomerang effect is expected. Moreover, we have shown that the final density agrees with a theoretical infinite-time profile based on the Gogolin profile.

The last part of the study has focused on strongly interacting bosons, which map to weakly interacting fermions. Likewise, the interactions weaken the boomerang effect. We have shown that for strongly interacting bosons, the observed phenomenon may also be captured using the same approach as in the mean-field approximation. Taken together, these findings demonstrate that the destruction of the boomerang effect due to interactions is universal. Additionally, we compared break times to other interaction-driven time scales, showing many similarities.

Outlook

To complete the thesis' conclusion, we would like to propose possible directions for future studies. The results presented in the thesis extend the knowledge of the quantum boomerang effect and can serve as starting points for future research.

We have to underline once more the importance of the results of chapter 2. Initially, the proof of the existence of the quantum boomerang effect was based on two pillars: Anderson localization and time reversal symmetry. We now know that the phenomenon does not need this symmetry. However, we have only a technical proof for the two-state scenario and preliminary results showing that the boomerang effect is present in the four-state scenario. It reveals that the quantum boomerang effect is more general than initially assumed. This sets the most important direction for future research. We are lacking a simple explanation that only Anderson localization is needed for the quantum boomerang effect. This perspective is, probably, the most important, intriguing, as well as desired.

The existence of the boomerang effect without time reversal invariance leads to another interesting perspective: a study of the boomerang effect in higher-dimensional systems. We revealed that time reversal symmetry is not needed for the phenomenon in one-dimensional systems, but we do not have any evidence that it is true in higher dimensions. Answering this question may also help in understanding why time reversal invariance is not a necessary condition for the quantum boomerang effect.

In the thesis, we slightly generalized the Berezinskii technique. In our opinion, it is a little bit forgotten. We believe that the diagrammatic approach may be adopted also to other one-dimensional systems and used in theoretical calculations.

Future research should also address interacting systems. Interactions are an indispensable part of experiments, the results of which, as theorists, we would like to see. The analysis of the mean-field approximation could be reinvestigated by including Bogoliubov excitations or using a novel hydrodynamic approach [206]. This is probably a tractable problem which could shed light on the difference between the mean-field and many-body results.

Studies should not restrict only to approximate treatments of interactions. For example, we are curious if a solitonic boomerang may be observed. Alike the Tonks-Girardeau gas, bright solitons in disordered systems display Anderson localization. Hence, we could expect the full boomerang effect

in such a system. The quantum return to the origin of a composite object would be a new unseen phenomenon.

Lastly, also from the perspective of many-body interactions, an investigation of many-body localized systems could be very intriguing. Whether a many-body localized system displays a quantum boomerang effect – either partial, total, or zero – is a challenging question left for future studies.

Appendix A

Formulary

Useful formulas with all necessary constants

A.1 Fourier transforms

Transforms between position x and wave number k domains, assuming d dimensions:

$$f(x) = \frac{1}{(2\pi)^d} \int \mathrm{d}k^d \, e^{ik\cdot x} \hat{f}(k), \tag{A.1}$$

$$\hat{f}(k) = \int \mathrm{d}x^d \, e^{-ik\cdot x} f(x). \tag{A.2}$$

Dirac delta function normalization:

$$\int \mathrm{d}k^d \, e^{ik\cdot x} = (2\pi)^d \delta(x), \quad \int \mathrm{d}x^d \, e^{-ik\cdot x} = (2\pi)^d \delta(k). \tag{A.3}$$

Transforms between time t and frequency ω domains:

$$f(t) = \frac{1}{2\pi} \int \mathrm{d}\omega \, e^{-i\omega t} \tilde{f}(\omega), \tag{A.4}$$

$$\tilde{f}(\omega) = \int \mathrm{d}t \, e^{i\omega t} f(t). \tag{A.5}$$

Dirac delta function normalization:

$$\int \mathrm{d}\omega \, e^{i\omega t} = 2\pi\delta(t), \quad \int \mathrm{d}t \, e^{-i\omega t} = 2\pi\delta(\omega). \tag{A.6}$$

Transforms between time t and energy ϵ domains:

$$f(t) = \frac{1}{2\pi\hbar} \int \mathrm{d}\epsilon \, e^{-i\epsilon t/\hbar} \tilde{f}(\epsilon), \tag{A.7}$$

$$\tilde{f}(\epsilon) = \int \mathrm{d}t \, e^{i\epsilon t/\hbar} f(t). \tag{A.8}$$

Dirac delta function normalization:

$$\int \mathrm{d}\epsilon\, e^{i\epsilon t/\hbar} = 2\pi\hbar\delta(t), \quad \int \mathrm{d}t\, e^{-i\epsilon t/\hbar} = 2\pi\hbar\delta(\epsilon). \tag{A.9}$$

A.2 Density of states

For a spectrum $\epsilon = \hbar^2 k_\epsilon^2/2m$:

$$\text{1D:} \quad \nu_\epsilon = \frac{m}{\pi k_\epsilon \hbar^2} \tag{A.10}$$

$$\text{2D:} \quad \nu_\epsilon = \frac{m}{2\pi\hbar^2} \tag{A.11}$$

$$\text{3D:} \quad \nu_\epsilon = \frac{m k_\epsilon}{2\pi^2\hbar^2} \tag{A.12}$$

In general:

$$\nu_\epsilon = \frac{dA_d}{(2\pi)^d}\frac{m k_\epsilon^{d-2}}{\hbar^2}, \tag{A.13}$$

where A_d is the volume of the unit sphere in d dimensional space:

$$A_d = \frac{\pi^{d/2}}{\Gamma(1+d/2)}, \quad A_1 = 2, \quad A_2 = \pi, \quad A_3 = \frac{4\pi}{3}. \tag{A.14}$$

A.3 Green's functions for a free particle

Energy-momentum representation:

$$G_0^{R,A}(\epsilon, k) = \frac{1}{\epsilon - \epsilon_k \pm i0^+} \tag{A.15}$$

Energy-configuration space representation:

$$\text{1D:} \quad G_0^{R,A}(\epsilon, r) = \mp i\pi\nu_\epsilon e^{\pm i k_\epsilon |r|}, \tag{A.16}$$

$$\text{2D:} \quad G_0^{R,A}(\epsilon, r) = \mp i\pi\nu_\epsilon H_0^{(1,2)}\left(k_\epsilon |r|\right), \tag{A.17}$$

$$\text{3D:} \quad G_0^{R,A}(\epsilon, r) = -\pi\nu_\epsilon \frac{e^{\pm i k_\epsilon |r|}}{k|r|}, \tag{A.18}$$

where $H_0^{(1,2)}(x)$ is the Hankel function of the first or second kind: $H_0^{(1,2)} = J_0(x) \pm i Y_0(x)$ and $J_0(x)$, $Y_0(x)$ are the Bessel functions of the first and second kind.

A.4 Averaged Green's functions

Energy-momentum representation:

$$\overline{G}^{R,A}(\epsilon, k) = \frac{1}{\epsilon - \epsilon_k \pm i\frac{\hbar}{2\tau}}, \tag{A.19}$$

where no real part of self energy is assumed and $1/\tau = -2\,\mathrm{Im}\,\Sigma(\epsilon, k)/\hbar$.

Energy-configuration space:

$$\text{(in any dimension)} \quad \overline{G}^{R,A}(\epsilon, r) = G_0^{R,A} e^{-|r|/2\ell}, \tag{A.20}$$

where ℓ is defined as $\ell = \frac{\hbar k}{m}\tau$, and the weak disorder limit, $k\ell \gg 1$, is assumed:

$$\sqrt{k^2 \pm im/\hbar\tau} \approx k \pm i/2\ell.$$

In the above equations the momentum $\hbar k$ is a representation of the energy, not a variable.

A.5 Disorder strength γ

In any dimension:

$$\gamma = \frac{\hbar}{2\pi\nu_\epsilon \tau}. \tag{A.21}$$

For particular dimensions:

$$\text{1D:} \quad \gamma = \frac{\hbar^4 k^2}{2m^2\ell} \tag{A.22}$$

$$\text{2D:} \quad \gamma = \frac{\hbar^4 k}{m^2\ell} \tag{A.23}$$

$$\text{3D:} \quad \gamma = \frac{\pi\hbar^4}{m^2\ell} \tag{A.24}$$

A.6 Generally useful mathematical formulas

Simple pole residue calculation using de l'Hôpital rule. Assume that function $f(z)$ has a simple pole at $z = c$, additionally assume that $f(z) = g(z)/h(z)$, where $g(z)$ and $h(z)$ are holomorphic, and such that $h(c) = 0$ and $h'(c) \neq 0$. Then we can show that:

$$\mathrm{Res}_{z\to c} f(z) = \lim_{z\to c} \frac{(z-c)g(z)}{h(c)} \overset{\text{de l'Hôpital}}{=} \lim_{z\to c} \frac{g(z) + zg'(z) - cg'(z)}{h'(z)} = \frac{g(c)}{h'(c)}. \tag{A.25}$$

Sokhotski-Plemelj theorem (sometimes called *Cauchy formula*). Assume that we want to evaluate a Cauchy type integral over an interval $a < 0 < b$ on a real axis. Let $f(z)$ be complex function continuous on the real axis (inside desired interval). Then

$$\lim_{\varepsilon\to 0^+} \int_a^b \frac{f(x)}{x \pm \varepsilon} \mathrm{d}x = \mp i\pi f(0) + \mathcal{P}\int_a^b \frac{f(x)}{x} \mathrm{d}x\,, \tag{A.26}$$

where $\mathcal{P}$ denotes Cauchy principal value.

Sign of imaginary part of a simple pole. Assume that we are interested in calculating integral of a function $(\epsilon - H(k))^{-1}$ over a real k axis. Let $k_i(\epsilon)$ be one of solutions to equation $\epsilon - H(k) = 0$. Then, usually, for integration we use residue theorem which facilitates the integral. We have to determine what are the poles that we include into the contour of the integration, depending on the

sign of their imaginary part. For this we may use following:

$$k_i(\epsilon + i\eta) \approx k_i(\epsilon) + i\eta \frac{\mathrm{d}k_i(\epsilon)}{\mathrm{d}\epsilon}, \tag{A.27}$$

so that the sign of the imaginary part is determined by the derivative of k_i with respect to ϵ. If we know the inverse relation, i.e. dispersion relation $\epsilon(k)$, the sign is determined by the sign of the group velocity $v_g(k)$.

Asymptotic expansion of the confluent hypergeometric function of the second kind. This function appears in the solution of Berezinskii equations for the center of mass time evolution. In our analysis we are interested in a series expansion for short times, which translates to large frequencies $\omega \gg 1$. The analytic expansion is known, it can be found in Abramovitz and Stegun (p. 508) [54]:

$$\Psi(a,b;z) = z^{-a}\left(\sum_{n=0}^{R-1} \frac{(a)_n(1+a-b)_n}{n!} z^{-n} + \mathcal{O}(|z|^{-R})\right), \quad \text{for } |z| \gg 1, \text{ and } -\frac{3\pi}{2} < \arg z < \frac{3\pi}{2}, \tag{A.28}$$

where $(a)_n$ is the Pochhammer symbol:

$$(a)_n = a(a+1)(a+2)\dots(a+n-1), \quad (a)_0 = 1. \tag{A.29}$$

Bibliography

[1] P. W. Anderson, Phys. Rev. **109**, 1492 (1958).

[2] T. Prat, *Anderson localization with cold atoms : dynamics in disorder and prospects from chaos*, Ph.D. thesis, Université Pierre et Marie Curie (2017).

[3] T. Prat, D. Delande, and N. Cherroret, Phys. Rev. A **99**, 023629 (2019).

[4] V. L. Berezinskiĭ, Zhurnal Eksp. i Teor. Fiz. **65**, 1251 (1973).

[5] G. Vidal, Phys. Rev. Lett. **91**, 147902 (2003).

[6] G. Vidal, Phys. Rev. Lett. **93**, 040502 (2004).

[7] E. Akkermans and G. Montambaux, *Mesoscopic Phys. Electrons Photons* (Cambridge University Press, 2007).

[8] C. A. Müller and D. Delande, in *Ultracold Gases Quantum Inf.* (Oxford University Press, 2011) pp. 441–533.

[9] B. A. Lippmann and J. Schwinger, Phys. Rev. **79**, 469 (1950).

[10] C. Gardiner, *Stochastic Methods: A Handbook for the Natural and Social Sciences* (Springer Berlin, 2009).

[11] G. C. Wick, Phys. Rev. **80**, 268 (1950).

[12] D. Clément, A. F. Varón, J. A. Retter, L. Sanchez-Palencia, A. Aspect, and P. Bouyer, New J. Phys. **8**, 165 (2006).

[13] J. W. Goodman, *Speckle Phenomena in Optics: Theory and Applications, Second Edition* (SPIE, Bellingham, Washington, 2020).

[14] D. J. Thouless, J. Phys. C Solid State Phys. **6**, L49 (1973).

[15] B. Shapiro, J. Phys. A Math. Theor. **45**, 143001 (2012).

[16] V. V. Volchkov, M. Pasek, V. Denechaud, M. Mukhtar, A. Aspect, D. Delande, and V. Josse, Phys. Rev. Lett. **120**, 060404 (2018).

[17] E. Abrahams, P. W. Anderson, D. C. Licciardello, and T. V. Ramakrishnan, Phys. Rev. Lett. **42**, 673 (1979).

[18] F. J. Wegner, Zeitschrift fur Phys. B Condens. Matter Quanta **25**, 327 (1976).

[19] H. Arodz and L. Hadasz, *Lectures on Classical and Quantum Theory of Fields*, Graduate Texts in Physics (Springer International Publishing, Cham, 2017).

[20] A. Gogolin, Sov. J. Exp. Theor. Phys. **44**, 1003 (1976).

[21] R. Sajjad, J. L. Tanlimco, H. Mas, A. Cao, E. Nolasco-Martinez, E. Q. Simmons, F. L. N. Santos, P. Vignolo, T. Macrì, and D. M. Weld, arXiv Prepr. (2021), arXiv:2109.00696 .

[22] E. Nakhmedov, V. Prigodin, and Y. Firsov, Zhurnal Eksp. i Teor. Fiz. **92**, 2133 (1987).

[23] G. A. G. A. Baker, *Essentials of Padé approximants* (Academic Press, 1975).

[24] N. F. Mott, *Electronic Process in Non-crystalline Materials* (Oxford : Clarendon Press, 1979).

[25] P. A. Lee, Phys. Today **41**, 36 (1988).

[26] P. E. Wolf and G. Maret, Phys. Rev. Lett. **55**, 2696 (1985).

[27] M. P. Albada and A. Lagendijk, Phys. Rev. Lett. **55**, 2692 (1985).

[28] C. C. Bradley, C. A. Sackett, J. J. Tollett, and R. G. Hulet, Phys. Rev. Lett. **75**, 1687 (1995).

[29] M. H. Anderson, J. R. Ensher, M. R. Matthews, C. E. Wieman, and E. A. Cornell, Science **269**, 198 (1995).

[30] T. Schulte, S. Drenkelforth, J. Kruse, W. Ertmer, J. Arlt, K. Sacha, J. Zakrzewski, and M. Lewenstein, Phys. Rev. Lett. **95**, 170411 (2005).

[31] L. Fallani, J. E. Lye, V. Guarrera, C. Fort, and M. Inguscio, Phys. Rev. Lett. **98**, 130404 (2007).

[32] J. Billy, V. Josse, Z. Zuo, A. Bernard, B. Hambrecht, P. Lugan, D. Clément, L. Sanchez-Palencia, P. Bouyer, and A. Aspect, Nature **453**, 891 (2008).

[33] J. Chabé, G. Lemarié, B. Grémaud, D. Delande, P. Szriftgiser, and J. C. Garreau, Phys. Rev. Lett. **101**, 255702 (2008).

[34] S. S. Kondov, W. R. McGehee, J. J. Zirbel, and B. DeMarco, Science **334**, 66 (2011).

[35] F. Jendrzejewski, A. Bernard, K. Müller, P. Cheinet, V. Josse, M. Piraud, L. Pezzé, L. Sanchez-Palencia, A. Aspect, and P. Bouyer, Nat. Phys. **8**, 398 (2012).

[36] G. Semeghini, M. Landini, P. Castilho, S. Roy, G. Spagnolli, A. Trenkwalder, M. Fattori, M. Inguscio, and G. Modugno, Nat. Phys. **11**, 554 (2015).

[37] M. Pasek, G. Orso, and D. Delande, Phys. Rev. Lett. **118**, 170403 (2017).

[38] S. Katsumoto, F. Komori, N. Sano, and S.-i. Kobayashi, J. Phys. Soc. Japan **56**, 2259 (1987).

[39] S. Waffenschmidt, C. Pfleiderer, and H. v. Löhneysen, Phys. Rev. Lett. **83**, 3005 (1999).

[40] F. L. Moore, J. C. Robinson, C. F. Bharucha, B. Sundaram, and M. G. Raizen, Phys. Rev. Lett. **75**, 4598 (1995).

[41] B. Kramer and A. Mackinnon, Rep. Prog. Phys **56**, 1469 (1993).

[42] Python Software Foundation, "Python programming language," (1991-2021).

[43] C. R. Harris, K. J. Millman, S. J. van der Walt, R. Gommers, P. Virtanen, D. Cournapeau, E. Wieser, J. Taylor, S. Berg, N. J. Smith, R. Kern, M. Picus, S. Hoyer, M. H. van Kerkwijk, M. Brett, A. Haldane, J. F. del Río, M. Wiebe, P. Peterson, P. Gérard-Marchant, K. Sheppard, T. Reddy, W. Weckesser, H. Abbasi, C. Gohlke, and T. E. Oliphant, Nature **585**, 357 (2020).

[44] P. Virtanen, R. Gommers, T. E. Oliphant, M. Haberland, T. Reddy, D. Cournapeau, E. Burovski, P. Peterson, W. Weckesser, J. Bright, S. J. van der Walt, M. Brett, J. Wilson, K. J. Millman, N. Mayorov, A. R. J. Nelson, E. Jones, R. Kern, E. Larson, C. J. Carey, I. Polat, Y. Feng, E. W. Moore, J. VanderPlas, D. Laxalde, J. Perktold, R. Cimrman, I. Henriksen, E. A. Quintero, C. R. Harris, A. M. Archibald, A. H. Ribeiro, F. Pedregosa, and P. van Mulbregt, Nat. Methods **17**, 261 (2020).

[45] A. Meurer, C. P. Smith, M. Paprocki, O. Čertík, S. B. Kirpichev, M. Rocklin, A. T. Kumar, S. Ivanov, J. K. Moore, S. Singh, T. Rathnayake, S. Vig, B. E. Granger, R. P. Muller, F. Bonazzi, H. Gupta, S. Vats, F. Johansson, F. Pedregosa, M. J. Curry, A. R. Terrel,

Š. Roučka, A. Saboo, I. Fernando, S. Kulal, R. Cimrman, and A. Scopatz, PeerJ Comput. Sci. **2017** (2017), 10.7717/peerj-cs.103.

[46] J. D. Hunter, Comput. Sci. Eng. **9**, 90 (2007).

[47] F. Pérez and B. E. Granger, Comput. Sci. Eng. **9**, 21 (2007).

[48] L. S. Blackford, A. Petitet, R. Pozo, K. Remington, R. C. Whaley, J. Demmel, J. Dongarra, I. Duff, S. Hammarling, G. Henry, *et al.*, ACM Transactions on Mathematical Software **28**, 135 (2002).

[49] E. Anderson, Z. Bai, C. Bischof, S. Blackford, J. Demmel, J. Dongarra, J. Du Croz, A. Greenbaum, S. Hammarling, A. McKenney, and D. Sorensen, *LAPACK Users' Guide*, 3rd ed. (Society for Industrial and Applied Mathematics, Philadelphia, PA, 1999).

[50] L. Dagum and R. Menon, IEEE Comput. Sci. Eng. **5**, 46 (1998).

[51] *Jupyter Book* (Executable Notebooks Community, 2020).

[52] S. Behnel, R. Bradshaw, C. Citro, L. Dalcin, D. S. Seljebotn, and K. Smith, Comput. Sci. Eng. **13**, 31 (2011).

[53] A. Rigo and M. Fijałkowski, "C Foreign Function Interface," (2012).

[54] M. Abramowitz and I. A. Stegun, *Handbook of Mathematical Functions* (National Bureau of Standards, 1966).

[55] J. P. Boyd, *Chebyshev & Fourier spectral methods* (Springer-Verlag, 1989).

[56] C. Leforestier, R. Bisseling, C. Cerjan, M. Feit, R. Friesner, A. Guldberg, A. Hammerich, G. Jolicard, W. Karrlein, H.-D. Meyer, N. Lipkin, O. Roncero, and R. Kosloff, J. Comput. Phys. **94**, 59 (1991).

[57] S. Roche and D. Mayou, Phys. Rev. Lett. **79**, 2518 (1997).

[58] A. Weiße, G. Wellein, A. Alvermann, and H. Fehske, Rev. Mod. Phys. **78**, 275 (2006).

[59] H. Fehske, J. Schleede, G. Schubert, G. Wellein, V. S. Filinov, and A. R. Bishop, Phys. Lett. A **373**, 2182 (2009).

[60] H. Fehske, R. Schneider, and A. Weisse, *Computational many-particle physics* (Springer, 2008).

[61] C. W. Clenshaw, Math. Comput. **9**, 118 (1955).

[62] A. Läuchli, *New states quantum matter* (Proceedings of the Les Houches Summer School "Modern theories of correlated electron systems", 2009).

[63] J. M. Zhang and R. X. Dong, Eur. J. Phys. **31**, 591 (2010).

[64] M. Dyakonov and V. Perel, J. Exp. Theor. Phys. Lett. **13**, 467 (1971).

[65] M. Dyakonov and V. Perel, Phys. Lett. A **35**, 459 (1971).

[66] Y. K. Kato, Science **306**, 1910 (2004).

[67] M. Konig, S. Wiedmann, C. Brune, A. Roth, H. Buhmann, L. W. Molenkamp, X.-L. Qi, and S.-C. Zhang, Science **318**, 766 (2007).

[68] C. L. Kane and E. J. Mele, Phys. Rev. Lett. **95**, 146802 (2005).

[69] B. A. Bernevig, T. L. Hughes, and S.-C. Zhang, Science **314**, 1757 (2006).

[70] C. L. Kane and E. J. Mele, Science **314**, 1692 (2006).

[71] D. Hsieh, D. Qian, L. Wray, Y. Xia, Y. S. Hor, R. J. Cava, and M. Z. Hasan, Nature **452**, 970 (2008).

[72] J. E. Moore, Nature **464**, 194 (2010).

[73] M. Z. Hasan and J. E. Moore, Annu. Rev. Condens. Matter Phys. **2**, 55 (2011).

[74] X.-J. Liu, M. F. Borunda, X. Liu, and J. Sinova, Phys. Rev. Lett. **102**, 046402 (2009).

[75] G. Dresselhaus, Phys. Rev. **100**, 580 (1955).

[76] Y. A. Bychkov and E. I. Rashba, J. Phys. C Solid State Phys. **17**, 6039 (1984).

[77] Y.-J. Lin, K. Jiménez-García, and I. B. Spielman, Nature **471**, 83 (2011).

[78] C. Hamner, Y. Zhang, M. A. Khamehchi, M. J. Davis, and P. Engels, Phys. Rev. Lett. **114**, 070401 (2015).

[79] Y. Yue, C. A. R. Sá de Melo, and I. B. Spielman, Phys. Rev. A **102**, 033325 (2020).

[80] F. Haake, S. Gnutzmann, and M. Kuś, *Quantum Signatures of Chaos*, Springer Series in Synergetics (Springer International Publishing, Cham, 2018).

[81] D. Delande and J. C. Gay, Phys. Rev. Lett. **57**, 2877 (1986).

[82] G. Wunner, U. Woelk, I. Zech, G. Zeller, T. Ertl, F. Geyer, W. Schweitzer, and H. Ruder, Phys. Rev. Lett. **57**, 3261 (1986).

[83] H. A. Kramers, Proc. R. Netherlands Acad. Arts Sci. **33**, 959 (1930).

[84] J. Janarek, D. Delande, N. Cherroret, and J. Zakrzewski, Phys. Rev. A **102**, 1 (2020).

[85] L. Tessieri, Z. Akdeniz, N. Cherroret, D. Delande, and P. Vignolo, Phys. Rev. A **103**, 063316 (2021).

[86] J. P. R. Valdes and T. Wellens, Phys. Rev. A **93**, 063634 (2016).

[87] O. N. Dorokhov, Dorokhov, and O. N., JETPL **36**, 318 (1982).

[88] P. Mello, P. Pereyra, and N. Kumar, Ann. Phys. (N. Y). **181**, 290 (1988).

[89] C. W. J. Beenakker, Rev. Mod. Phys. **69**, 731 (1997).

[90] A. MacKinnon and B. Kramer, Phys. Rev. Lett. **47**, 1546 (1981).

[91] A. MacKinnon and B. Kramer, Zeitschrift für Phys. B Condens. Matter **53**, 1 (1983).

[92] A. MacKinnon, Zeitschrift fur Phys. B Condens. Matter **59**, 385 (1985).

[93] K. Nikolić and A. MacKinnon, Phys. Rev. B **50**, 11008 (1994).

[94] F. Sols, in *Quantum Transp. Ultrasmall Devices* (Springer, Boston, MA, 1995) pp. 329–338.

[95] C. H. Lewenkopf and E. R. Mucciolo, J. Comput. Electron. **12**, 203 (2013).

[96] H. Furstenberg and H. Kesten, Ann. Math. Stat. **31**, 457 (1960).

[97] V. I. Oseledets, Tr. Mosk. Mat. Obs. **19**, 179 (1968).

[98] K. L. Lee, B. Grémaud, C. Miniatura, and D. Delande, Phys. Rev. B **87**, 144202 (2013).

[99] O. Bohigas, M. J. Giannoni, and C. Schmit, Phys. Rev. Lett. **52**, 1 (1984).

[100] O. Bohigas, M.-J. Giannoni, and C. Schmit (Springer, Boston, MA, 1985) pp. 103–111.

[101] O. Bohigas, M.-J. Giannoni, and C. Schmit, in *Stoch. Process. Class. Quantum Syst.* (Springer Berlin Heidelberg, Berlin, Heidelberg, 1986) pp. 118–138.

[102] M. L. Mehta, *Random Matrices* (Academic Press, 1990).

[103] T. Guhr, A. Müller–Groeling, and H. A. Weidenmüller, Phys. Rep. **299**, 189 (1998).

[104] V. Oganesyan and D. A. Huse, Phys. Rev. B **75**, 155111 (2007).

[105] Y. Y. Atas, E. Bogomolny, O. Giraud, and G. Roux, Phys. Rev. Lett. **110**, 1 (2013).

[106] M. P. Sörensen and T. Schneider, Zeitschrift für Phys. B Condens. Matter **82**, 115 (1991).

[107] E. J. Torres-Herrera, J. A. Méndez-Bermúdez, and L. F. Santos, Phys. Rev. E **100**, 022142 (2019).

[108] E. J. Torres-Herrera and L. F. Santos, Condens. Matter **5**, 7 (2020).

[109] G. Modugno, Reports Prog. Phys. **73**, 102401 (2010).

[110] N. Bogoliubov, J. Phys **11**, 23 (1947).

[111] L. D. Landau and E. M. Lifshitz, *Quantum Mechanics : Non-Relativistic Theory.* (Elsevier Science, 1977).

[112] E. P. Gross, Nuovo Cim. **20**, 454 (1961).

[113] L. P. Pitaevskii, Sov. Phys. JETP **13**, 451 (1961).

[114] L. Erdős, B. Schlein, and H.-T. Yau, Phys. Rev. Lett. **98**, 040404 (2007).

[115] L. Erdős, B. Schlein, and H.-T. Yau, Ann. Math. **172**, 291 (2010).

[116] F. Dalfovo, S. Giorgini, L. P. Pitaevskii, and S. Stringari, Rev. Mod. Phys. **71**, 463 (1999).

[117] C. J. Pethick and H. Smith, *Bose–Einstein condensation in dilute gases* (Cambridge University Press, 2008).

[118] L. Pitaevskii and S. Stringari, *Bose-Einstein Condensation and Superfluidity* (Oxford University Press, 2016).

[119] N. Bilas and N. Pavloff, Eur. Phys. J. D **40**, 387 (2006).

[120] P. Lugan, D. Clément, P. Bouyer, A. Aspect, and L. Sanchez-Palencia, Phys. Rev. Lett. **99**, 180402 (2007).

[121] T. Ernst, T. Paul, and P. Schlagheck, Phys. Rev. A **81**, 013631 (2010).

[122] P. Lugan and L. Sanchez-Palencia, Phys. Rev. A **84**, 013612 (2011).

[123] C. Gaul and C. A. Müller, Phys. Rev. A **83**, 063629 (2011).

[124] C. A. Müller and C. Gaul, New J. Phys. **14**, 075025 (2012).

[125] C. Gaul and C. A. Müller, Eur. Phys. J. Spec. Top. **217**, 69 (2013).

[126] H. F. Trotter, Proc. Am. Math. Soc. **10**, 545 (1959).

[127] M. Suzuki, J. Math. Phys. **26**, 601 (1985).

[128] R. C. Kuhn, O. Sigwarth, C. Miniatura, D. Delande, and C. A. Müller, New J. Phys. **9**, 161 (2007).

[129] D. L. Shepelyansky, Phys. Rev. Lett. **70**, 1787 (1993).

[130] G. Kopidakis, S. Komineas, S. Flach, and S. Aubry, Phys. Rev. Lett. **100**, 084103 (2008).

[131] A. S. Pikovsky and D. L. Shepelyansky, Phys. Rev. Lett. **100**, 094101 (2008).

[132] S. Flach, D. O. Krimer, and C. Skokos, Phys. Rev. Lett. **102**, 024101 (2009).

[133] D. O. Krimer, R. Khomeriki, and S. Flach, Phys. Rev. E **80**, 036201 (2009).

[134] C. Skokos, D. O. Krimer, S. Komineas, and S. Flach, Phys. Rev. E **79**, 056211 (2009).

[135] A. Iomin, Phys. Rev. E **81**, 017601 (2010).

[136] T. V. Laptyeva, J. D. Bodyfelt, D. O. Krimer, C. Skokos, and S. Flach, EPL (Europhysics Lett. **91**, 30001 (2010).

[137] B. Min, T. Li, M. Rosenkranz, and W. Bao, Phys. Rev. A **86**, 053612 (2012).

[138] N. Cherroret, B. Vermersch, J. C. Garreau, and D. Delande, Phys. Rev. Lett. **112**, 170603 (2014).

[139] I. Vakulchyk, M. V. Fistul, and S. Flach, Phys. Rev. Lett. **122**, 040501 (2019).

[140] A. Iomin, Comput. Math. with Appl. **73**, 914 (2017).

[141] D. Ben-Avraham and S. Havlin, *Diffusion and Reactions in Fractals and Disordered Systems* (Cambridge University Press, 2000).

[142] E. Lucioni, B. Deissler, L. Tanzi, G. Roati, M. Zaccanti, M. Modugno, M. Larcher, F. Dalfovo, M. Inguscio, and G. Modugno, Phys. Rev. Lett. **106**, 230403 (2011).

[143] T. Prat, D. Delande, and N. Cherroret, arXiv Prepr. (2017), arXiv:1704.05241v1 .

[144] P. Ehrenfest, Zeitschrift fur Phys. **45**, 455 (1927).

[145] B. C. Hall, *Quantum Theory for Mathematicians* (Springer, 2013).

[146] D. Vollhardt and P. Wölfle, Phys. Rev. Lett. **48**, 699 (1982).

[147] K. Efetov, *Supersymmetry in Disorder and Chaos* (Cambridge University Press, Cambridge, 1996).

[148] P. Ostrovsky, T. Nakayama, K. A. Muttalib, and P. Wölfle, New J. Phys. **15**, 055010 (2013).

[149] N. R. Goodman, Ann. Math. Stat. **34**, 152 (1963).

[150] D. Tse and P. Viswanath, *Fundamentals of Wireless Communication* (Cambridge University Press, Cambridge, 2005).

[151] T. Scoquart, T. Wellens, D. Delande, and N. Cherroret, Phys. Rev. Res. **2**, 033349 (2020).

[152] H. Prüfer, Math. Ann. **95**, 499 (1926).

[153] W. O. Amrein, A. M. Hinz, and D. B. Pearson, *Sturm-Liouville Theory* (Birkhäuser Basel, Basel, 2005).

[154] I. Y. Gol'dshtein, S. A. Molchanov, and L. A. Pastur, Funct. Anal. Its Appl. **11**, 1 (1977).

[155] P. Erdös and R. Herndon, Adv. Phys. **31**, 65 (1982).

[156] S. Kotani and B. Simon, Commun. Math. Phys. **112**, 103 (1987).

[157] P. Lugan, A. Aspect, L. Sanchez-Palencia, D. Delande, B. Grémaud, C. A. Müller, and C. Miniatura, Phys. Rev. A **80**, 023605 (2009).

[158] D. Adamova, J. Horejsi, and I. Ulehla, J. Phys. A. Math. Gen. **17**, 2621 (1984).

[159] E. H. Lieb and W. Liniger, Phys. Rev. **130**, 1605 (1963).

[160] B. Schmidt and M. Fleischhauer, Phys. Rev. A **75**, 021601 (2007).

[161] H. A. Gersch and G. C. Knollman, Phys. Rev. **129**, 959 (1963).

[162] M. P. A. Fisher, P. B. Weichman, G. Grinstein, and D. S. Fisher, Phys. Rev. B **40**, 546 (1989).

[163] T. D. Kühner and H. Monien, Phys. Rev. B **58**, R14741 (1998).

[164] M. Greiner, O. Mandel, T. Esslinger, T. W. Hänsch, and I. Bloch, Nat. 2002 4156867 **415**, 39 (2002).

[165] D. Jaksch, C. Bruder, J. I. Cirac, C. W. Gardiner, and P. Zoller, Phys. Rev. Lett. **81**, 3108 (1998).

[166] D. Jaksch and P. Zoller, Ann. Phys. (N. Y). **315**, 52 (2005).

[167] F. Verstraete, V. Murg, and J. Cirac, Adv. Phys. **57**, 143 (2008).

[168] U. Schollwöck, Ann. Phys. (N. Y). **326**, 96 (2011).

[169] S. Paeckel, T. Köhler, A. Swoboda, S. R. Manmana, U. Schollwöck, and C. Hubig, Ann. Phys. (N. Y). **411**, 167998 (2019).

[170] M. Suzuki, Commun. Math. Phys. **51**, 183 (1976).

[171] T. Barthel and Y. Zhang, Ann. Phys. (N. Y). **418**, 168165 (2020).

[172] D. Delande, K. Sacha, M. Płodzień, S. K. Avazbaev, and J. Zakrzewski, New J. Phys. **15**, 045021 (2013).

[173] K. Sacha, *Kondensat Bosego-Einsteina* (Instytut Fizyki im. M. Smoluchowskiego, Uniwersytet Jagielloński, Kraków, 2004).

[174] O. Penrose and L. Onsager, Phys. Rev. **104**, 576 (1956).

[175] C. N. Yang, Rev. Mod. Phys. **34**, 694 (1962).

[176] I. V. Gornyi, A. D. Mirlin, and D. G. Polyakov, Phys. Rev. Lett. **95**, 206603 (2005).

[177] D. Basko, I. Aleiner, and B. Altshuler, Ann. Phys. (N. Y). **321**, 1126 (2006).

[178] F. Alet and N. Laflorencie, Comptes Rendus Phys. **19**, 498 (2018).

[179] D. A. Abanin, E. Altman, I. Bloch, and M. Serbyn, Rev. Mod. Phys. **91**, 21001 (2019).

[180] M. Schreiber, S. S. Hodgman, P. Bordia, H. P. Luschen, M. H. Fischer, R. Vosk, E. Altman, U. Schneider, and I. Bloch, Science **349**, 842 (2015).

[181] S. S. Kondov, W. R. McGehee, W. Xu, and B. DeMarco, Phys. Rev. Lett. **114**, 083002 (2015).

[182] J.-Y. Choi, S. Hild, J. Zeiher, P. Schauss, A. Rubio-Abadal, T. Yefsah, V. Khemani, D. A. Huse, I. Bloch, and C. Gross, Science **352**, 1547 (2016).

[183] J. Smith, A. Lee, P. Richerme, B. Neyenhuis, P. W. Hess, P. Hauke, M. Heyl, D. A. Huse, and C. Monroe, Nat. Phys. **12**, 907 (2016).

[184] K. X. Wei, C. Ramanathan, and P. Cappellaro, Phys. Rev. Lett. **120**, 070501 (2018).

[185] M. Žnidarič, T. Prosen, and P. Prelovšek, Phys. Rev. B **77**, 064426 (2008).

[186] J. H. Bardarson, F. Pollmann, and J. E. Moore, Phys. Rev. Lett. **109**, 017202 (2012).

[187] M. Serbyn, Z. Papić, and D. A. Abanin, Phys. Rev. Lett. **110**, 260601 (2013).

[188] R. Vosk and E. Altman, Phys. Rev. Lett. **110**, 067204 (2013).

[189] P. Sierant, D. Delande, and J. Zakrzewski, Acta Phys. Pol. A **132**, 1707 (2017).

[190] P. Sierant and J. Zakrzewski, New J. Phys. **20**, 043032 (2018).

[191] M. Girardeau, J. Math. Phys. **1**, 516 (1960).

[192] M. D. Girardeau and E. M. Wright, Phys. Rev. Lett. **84**, 5691 (2000).

[193] M. A. Cazalilla, R. Citro, T. Giamarchi, E. Orignac, and M. Rigol, Rev. Mod. Phys. **83**, 1405 (2011).

[194] M. Olshanii, Phys. Rev. Lett. **81**, 938 (1998).

[195] B. Paredes, A. Widera, V. Murg, O. Mandel, S. Fölling, I. Cirac, G. V. Shlyapnikov, T. W. Hänsch, and I. Bloch, Nature **429**, 277 (2004).

[196] T. Kinoshita, T. Wenger, and D. S. Weiss, Science **305**, 1125 (2004).

[197] J. Radić, V. Bačić, D. Jukić, M. Segev, and H. Buljan, Phys. Rev. A **81**, 063639 (2010).

[198] D. Sen, Int. J. Mod. Phys. A **14**, 1789 (1999).

[199] T. Cheon and T. Shigehara, Phys. Rev. Lett. **82**, 2536 (1999).

[200] D. Sen, J. Phys. A. Math. Gen. **36**, 7517 (2003).

[201] H. Grosse, E. Langmann, and C. Paufler, J. Phys. A. Math. Gen. **37**, 4579 (2004).

[202] V. P. Michal, I. L. Aleiner, B. L. Altshuler, and G. V. Shlyapnikov, Proc. Natl. Acad. Sci. **113**, E4455 (2016).

[203] D. Petrosyan, B. Schmidt, J. R. Anglin, and M. Fleischhauer, Phys. Rev. A **76**, 033606 (2007).

[204] A. Rosch, D. Rasch, B. Binz, and M. Vojta, Phys. Rev. Lett. **101**, 265301 (2008).

[205] G. Carleo, F. Becca, M. Schiró, and M. Fabrizio, Sci. Rep. **2**, 243 (2012).

[206] J. Kopyciński, M. Łebek, M. Marciniak, R. Ołdziejewski, W. Górecki, and K. Pawłowski, arXiv Prepr. (2021), arXiv:2106.15289 .

Jakub Janarek **December 2021**

Quantum boomerang effect in disordered ultra-cold atomic gases

Abstract : In this thesis, we theoretically and numerically investigate the quantum boomerang effect – i.e. the return of a wave packet launched with a nonzero velocity to its initial position – in ultra-cold disordered atomic gases. We address three main problems. We study the effect of the time-reversal symmetry breaking on the existence of the quantum boomerang phenomenon. We show that time-reversal symmetry is not a necessary condition for the presence of the quantum boomerang. Next, we investigate the impact of interactions on the quantum boomerang effect, using the mean-field approximation. The interactions lead to partial destruction of the boomerang effect. Within the framework of the Gross-Pitaevskii equation, we identify a universal parameter that describes the observed destruction of the particle's return to the origin. Finally, we numerically study the effect of interactions using a quasi-exact approach. To this end, we study weakly interacting bosons, the Tonks-Girardeau gas, and strongly interacting bosons, which map to weakly interacting fermions. We find that weakly interacting bosons exhibit stronger destruction of the boomerang effect than in the case of the mean-field approach, thus that quantum fluctuations play a major role. Results for the Tonks-Girardeau gas show the existence of the full quantum boomerang phenomenon. Moreover, the results for strongly interacting bosons, where the boomerang is also only partial, provide evidence that the destruction of the quantum boomerang effect does not depend on the details of the interactions between particles.

Keywords : Anderson localization, quantum boomerang effect, time-reversal invariance, Gross-Pitaevskii equation, many-body interactions

Résumé: Nous étudions théoriquement et numériquement l'effet boomerang quantique - c'est-à-dire le retour à son point de départ d'un paquet d'ondes lancé avec une vitesse non nulle - dans les gaz atomiques désordonnés ultra-froids. Nous étudions tout d'abord l'effet d'une rupture de la symétrie par renversement du temps et montrons que, contrairement à ce qui était couramment admis, cette symétrie n'est pas une condition nécessaire à la présence de l'effet boomerang. Ensuite, nous étudions l'impact des interactions sur l'effet boomerang, en utilisant l'approximation de champ moyen. Dans le cadre de l'équation de Gross-Pitaevskii, nous montrons que les interactions conduisent à une destruction partielle de l'effet et identifions un paramètre universel qui décrit cette destruction. Enfin, nous étudions numériquement l'effet des interactions en utilisant une approche "many-body" quasi-exacte. À cette fin, nous étudions les bosons en interaction faible, le gaz de Tonks-Girardeau, et les bosons en interaction forte, qui correspondent à des fermions en interaction faible. Nous observons que les bosons faiblement interagissant présentent une destruction plus forte de l'effet boomerang que dans le cadre du champ moyen, ce qui signifie que les fluctuations quantiques jouent un rôle majeur. Pour le gaz de Tonks-Girardeau, nous montrons montrent que le phénomène de boomerang quantique est complet. Les bosons en forte interaction, où l'effet boomerang n'est que partiel, fournissent la preuve que la destruction de l'effet ne dépend pas des détails des interactions entre particules.

Mots clés : localisation d'Anderson, effet boomerang quantique, invariance par renversement du temps, equation de Gross-Pitaevskii, problème à N corps